UNIVERSITY OF SOUTHAMPTON

Interactions of Single-Crystal Lithium Niobate Surfaces with Ultra-Violet Laser Radiation

by

Alistair C Muir

A thesis submitted in partial fulfillment for the
degree of Doctor of Philosophy

in the
Faculty Of Engineering Science And Mathematics
Optoelectronics Research Centre

May 2008

Declaration of Authorship

I, Alistair Muir, declare that this thesis titled, 'Interactions of Single-Crystal Lithium Niobate Surfaces with Ultra-Violet Laser Radiation' and the work presented in it are my own. I confirm that:

- This work was done wholly or mainly while in candidature for a research degree at this University
- Where any part of this thesis has previously been submitted for a degree or any other qualification at this University or any other institution, this has been clearly stated
- Where I have consulted the published work of others, this is always clearly attributed
- Where I have quoted from the work of others, the source is always given. With the exception of such quotations, this thesis is entirely my own work
- I have acknowledged all main sources of help
- Where the thesis is based on work done by myself jointly with others, I have made clear exactly what was done by others and what I have contributed myself

Signed: _____

Date: _____

$$\mathcal{P}_{\mathrm{h}}\mathcal{D} = \sqrt{\frac{1}{0 \bigcup \infty} \int\limits_{\substack{\textit{naïvité}}}^{\textit{cynicism}} \left[\mathcal{P}_{\mathrm{anic}} + \mathcal{P}_{\mathrm{rocrastination}}\right]^2 \quad \mathrm{d}t} \tag{1}$$

A. Muir ‘07

UNIVERSITY OF SOUTHAMPTON

Abstract

Faculty Of Engineering Science And Mathematics
Optoelectronics Research Centre

Doctor of Philosophy

by Alistair C Muir

The aim of this thesis is to investigate the influence of ultraviolet laser light on single crystal lithium niobate surfaces with a focus on useful functionalisation. The investigations split naturally into three areas: effects on hydrophilicity by low intensity laser irradiation, effects on ferroelectric domain inversion by focussed laser irradiation, and modelling of the heating and subsequent lithium diffusion during focussed laser irradiation.

It was seen that irradiation of ultraviolet laser light with a photon energy greater than the bad gap of lithium niobate resulted in an increase to the hydrophilicity, or wettability, of the surface. The magnitude of the change was seen to be dependent upon both the conditions of laser intensity and exposure time and upon the environment in which exposures took place with a greater change seen with greater exposure time and/or intensity and with a greater environmental humidity. Under vacuum no change to the hydrophilicity was seen. It was shown that spatial structuring of the surface wettability could be achieved at the sub-micron level.

Irradiation of focused continuous wave ultraviolet laser light was seen to have two contrasting effects upon ferroelectric domain inversion. It was first seen that illumination of focussed laser light of high enough intensity could directly invert the ferroelectric polarity in the exposed region. The effect was characterised by chemical etching in hydrofluoric acid and by piezoresponse force microscopy and was seen to be most effective on the $-z$ face of the crystal. An explanation was proposed whereby photo-excited charges travel within a pyro-electric field, creating a space-charge field which locally inverts the spontaneous polarisation. The anisotropy in behaviour between the $+z$ and $-z$ faces was explained by the different mobilities of electrons and holes. It was also seen that if the crystal was electrically poled after illumination of the $+z$ face, domain inversion was inhibited in the illuminated region. The region of inhibited domain inversion was seen

to be greater than the region of direct poling and created domains with high quality surfaces. This was demonstrated to be a highly effective method for topographical surface microstructuring when followed by chemical etching.

The heating of lithium niobate by focussed continuous wave ultraviolet laser light was modelled. It was found that the temperature distributions created were highly localised to the beam spot and were independent of beam scan speeds for practically achievable speeds. The temperature dependence of the thermal diffusivity was included and seen to greatly increase the gradients of the temperature distributions at high temperatures. The diffusion of lithium ions due to the steep temperature gradients and, hence, ionic diffusivity gradient was modelled and it was found that lithium ions will diffuse from the surface, into the bulk of the crystal. This will leave a high refractive index surface layer through the dependence upon lithium concentration. The depth of the modelled lithium concentration profiles after the passage of the beam were found not to be sufficient to cause optical waveguiding.

Acknowledgements

The work in this thesis could not have happened without the help and collaboration of many people. I would first like to thank both my supervisor, Prof. Robert Eason, and my co-supervisor, Dr Sakellaris Mailis, for all the effort and encouragement they have put in to keep me going in the right direction. I would like to thank Dr Geoff Daniell for many enjoyable and fruitful conversations on mathematics and mathematical computing and also Professor Collin Please for further, patient, mathematical assistance. I would also like to thank the other members of the Non-linear & Microstructured Optical Materials group, both past and present, for all the help, encouragement, and correcting argument they have provided for me. So, thank you Dr Collin Sones, Dr Iain Wellington, Dr Chris Valdivia and Mr Tleyane Sono.

A little further afield from the ORC, I would like to thank our international collaborators without whom much work could not have accomplished, many lessons not learnt and friends not made. At the university of Bonn, Germany, I would like to thank Prof. Elisabeth Soergel, Dr Tobias Jungk and Dr **Á**kos Hoffmann for many hours spent at the PFM. From the Laboratoire Matériaux Optiques, Photonique et Systèmes at the University of Metz, France, I would like to thank Dr Aissa Harhira for the hours spent extracting Raman data from my samples.

Finally I would like to thank my wife, Helen, and my three gorgeous little girls, Anna-Marie, Nadine and Tamsin, for getting me through all this and reminding me that there is, in fact, a world outside of lithium niobate and little dark labs.

Contents

Abbreviations

LN	**L**ithium **N**iobate
UV	**U**ltra **V**iolet
SFG	**S**um **F**requency **G**eneration
DFG	**D**ifference **F**requency **G**eneration
OPG	**O**ptical **P**arametric **G**eneration
SHG	**S**econd **H**armonic **G**eneration
QPM	**Q**uasi **P**hase **M**atching
PPLN	**P**eriodically **P**oled **L**ithium **N**iobate
DC	**D**irect **C**urrent. [1]
TIR	**T**otal **I**nternal **R**eflection
SAW	**S**urface **A**coustic **W**ave
DI	**D**e- **I**onised
CCD	**C**harge **C**oupled **D**evice
RH	**R**elative **H**umidity
TEM	**T**ransmission **E**lectron **M**icroscopy
LT	**L**ithium **T**antalate
XPS	**X**-ray **P**hotoelectron **S**pectroscopy
AC	**A**ternating **C**urrent
AOP	**A**ll **O**ptical **P**oling
LAP	**L**ight **A**ssisted **P**oling
LLIP	**L**atent **L**ight **I**mpeded **P**oling
PFM	**P**iezoresponse **F**orce **M**icroscopy
HF	**H**dro**F**luoric
SEM	**S**canning **E**lectron **M**icroscope

[1] This is, however, used more generally within this thesis as a synonym for "'constant"'.

EFP	**E**lectric **F**ield **P**oling
AFM	**A**tomic **F**orce **M**icroscope
pdf	**p**robability **d**ensity **f**unction
IR	**I**nfra**R**ed
L3N	**L**ithium **3**(tri) **N**iobate

Physical Constants

Speed of Light	c	=	$2.997\ 924\ 58 \times 10^{8}$ $\mathrm{ms}^{-\mathrm{S}}$ (exact)
Elementary Charge	e	=	$1.602\ 176\ 462 \times 10^{-19}$ C
Permittivity of Vacuum	e	=	$8.854\ 187\ 817 \times 10^{-12}$ F m^{-1}
Planck Constant	h	=	$6.626\ 068\ 765 \times 10^{-34}$ J s
Reduced Planck Constant, $h/2\pi$	$\hbar$	=	$1.054\ 571\ 596 \times 10^{-34}$ J s
Avagadro Constant	N_A	=	$6.022\ 141\ 995 \times 10^{23}$ mol^{-1}
Boltzmann Constant	k_B	=	$1.380\ 650\ 324 \times 10^{23}$ J K^{-1}

Symbols

Symbol	Description	Unit
α	Optical intensity absorption coefficient	m^{-1}
β	Energy expansion coefficient	$\mathrm{J\ m^4\ C^{-2}\ K^{-1}}$
γ	Energy expansion coefficient	$\mathrm{J\ m^8\ C^{-4}}$
γ_{lv}	Liquid-vapour interfacial energy	$\mathrm{J\ m^{-2}}$
γ_{sv}	Solid-vapour interfacial energy	$\mathrm{J\ m^{-2}}$
γ_{sl}	Solid-Liquid interfacial energy	$\mathrm{J\ m^{-2}}$
γ_{so}	'Dry' Solid surface energy	$\mathrm{J\ m^{-2}}$
δ	Optical intensity absorption depth	m
ϵ	Electrical permittivity	$\mathrm{F\ m^{-1}}$
ϵ_r	Relative electrical permittivity	
ϵ''	Imaginary component of the refractive index	
$\boldsymbol{\epsilon}$	Electrical permittivity tensor	
η	Electron-hole recombination avoidance probability	
Θ	Linearised temperature	
θ_E	Equilibrium contact angle	
κ	Reciprocal permittivity	
κ	Rate of change of surface energy	s^{-1}
Λ	Domain width	m
Λ	Spatial period	m
λ	Wavelength	m
λ	Integration variable	
$\hat{\mu}_e$	Electron mobility	$\mathrm{m^2\ V^{-1}\ s^{-1}}$
$\hat{\mu}_h$	Hole mobility	$\mathrm{m^2\ V^{-1}\ s^{-1}}$

ρ	Mass density	Kg m^{-3}
τ	Time constant	s
$\chi^{(m)}$	Electric susceptibility tensor of order m	
Ω	Computational domain	
$\delta\Omega$	Computational domain boundary	
ω	Angular frequency	rad s^{-1}
a_1, a_2, a_3, c	Crystallographic axis directions	
a	Distance	m
a	Diffusivity function fitting parameter	K^{-1}
a	Diffusive jump length	m
b	Diffusivity function fitting parameter	K m^2 s^{-1}
C	Specific heat capacity	JKg^{-1}K^{-1}
$\mathbf{c}$	Elastic stiffness tensor	N m^{-2}
c_e	Electron concentration	m^{-3}
c_h	Hole concentration	m^{-3}
c	Particle concentration	m^{-3}
$\mathbf{D}$	Thermal diffusivity	m^{2}s^{-1}
$\mathbf{D^E}$	Electrical displacement	C m^{-2}
$\mathbf{d}$	Piezoelectric compliance tensor	C N^{-1}
dp	Positive charge distribution depth	m
dn	Negative charge distribution depth	m
$\mathbf{E}$	Electric field vector	V m^{-1}
E_{dep}	Electric depolarisation field	V m^{-1}
E_{scr}	Electric screening field	V m^{-1}
E_{net}	Net electric field	V m^{-1}
E_{sc-ph}	Photo-induced space-charge electric field	V m^{-1}
$\mathbf{e}$	Piezoelectric compliance tensor	N V^{-1} m^{-1}
F	Particle flux	s^{-1}
$\mathbf{g}$	Piezoelectric compliance tensor	V m N^{-1}
h	Finite difference spatial step size	
I	Light intensity	W m^{-2}

i, j, k, l, m, n	Integer variables	
J	Diffusive flux	$\mathrm{m}^{-2}\ \mathrm{s}^{-1}$
$\mathbf{K}$	Thermal conductivity tensor	J m$-1\mathrm{s}^{-1}\mathrm{K}^{-1}$
$\mathbf{k}$	Wavevector	m^{-1}
l	Computational domain length	
l	Length	m
l_c	Coherence length	m
N	Number of sampling points along the computational domain length	
N	Number density	
n	Number of particles	
n	Refractive index	
n_o	Ordinary refractive index	
n_e	Extraordinary refractive index	
n_i	Refractive index for polarisation along the i^{th} axis	
$\mathbf{P}$	Electric polarisation vector	$\mathrm{C\ m}^{-2}$
$\mathbf{P}^{NL}$	Non-linear component of the electric polarisation vector	$\mathrm{C\ m}^{-2}$
$\mathbf{P}_s$	Spontaneous electric polarisation vector	$\mathrm{C\ m}^{-2}$
P	Power	W
p	probability	
Q_e	Electron source function	$\mathrm{m}^{-3}\ \mathrm{s}^{-1}$
Q_h	Hole source function	$\mathrm{m}^{-3}\ \mathrm{s}^{-1}$
R	Reflectivity	
$\mathbf{r}$	Electrooptic tensor	$\mathrm{m\ V}^{-1}$
r	Diffusive jump rate	s^{-1}
S	Spreading coefficient	$\mathrm{J\ m}^{-2}$
S	Heat source function	$\mathrm{W\ m}^{-3}$
$\mathbf{s}$	Elastic compliance tensor	$\mathrm{m}^2\ \mathrm{N}^{-1}$
T	Temperature	K
T_c	Curie temperature	K
t	Time	s
v	Scanning velocity	$\mathrm{m\ s}^{-1}$

w	Beam spot size	m
$\mathbf{X}$	Mechanical stress tensor	N m^{-2}
X, Y, Z	Normalised coordinate axes in the rest frame of the scanning beam	
x	Mechanical strain tensor	
x, y, z	Cartesian axes	

To my wife Helen, who has endured the trials and tribulations of this PhD with me from naive beginning to cynical end, and to my girls, Anna-Marie, Nadine and Tamsin, who, thankfully, know of nothing else.

Chapter 1

Introduction

Lithium niobate (LN) is one of the most widely used dielectric materials available today. It has found use in areas of technology ranging from wireless humidity meters [1] to pyroelectric energy meters [2] to optical frequency converters [3] to electronic acoustic delay lines and filters, high speed optical modulators for telecoms systems [4, 5] and even desktop nuclear fusion [6]. This wide range of uses has led to, and been driven by, methods of large scale manufacture of crystals of extremely high quality with relatively low cost. Of course, LN has only found such a wide and extensive range of uses because it possesses many exploitable physical properties making it a highly functional material.

Many of the uses and applications of LN involve primarily, or exclusively, the LN surface. It is the aim of this thesis to examine ways in which the surface can be modified, primarily through ultraviolet (UV) laser irradiation, such that the functionality of this highly useful material can be increased even further.

All properties originate from the structure of the material and this is reviewed in chapter 1. Chapter 1 then goes on to outline some of these properties that are relevant to the work carried out in this thesis, with reference to some common devices that exploit the said properties. Large lists of numeric values of tensor components are not given as these can be found in the literature when needed, rather, the emphasis of the section is in highlighting the origins of the effects in a manner where the inter-relations of seemingly independent effects can be seen.

Chapter 2 investigates the effect of UV irradiation on the wetting properties, or more generally the hydrophilic properties, of the surface. In this chapter low intensity, defocussed, laser light is used to provide a large exposure area. The results are likely to apply, however, to higher intensity exposure conditions also. The change in the hydrophilicity is characterised by the contact angle of sessile drops of water for various

exposure conditions changing the incident power, exposure time, pulse duration (including c.w. exposure), and environmental humidity. A mechanism for the UV-induced hydrophilicity change is proposed whereby environmental H_2O molecules dissociatively adsorb onto the surface during illumination, thereby increasing the hydrophilicity. The ability of the increased wettability to create arbitrary liquid spreading paths is then investigated using scanned loosely focussed beams. Hydrophilic paths are written using a translation stage in various shapes including straight lines, s-bends and raster scans. The dependence upon track width of the spreading from macroscopic drops is also investigated. Finally the hydrophilicity is structured on the micron and sub-micron length scales and is shown to affect the condensation of liquids from vapour such that useful liquid structures can be made. The technological implications of the effect at each of these length scales in discussed.

Chapter 3 investigates the effect of focussed UV laser light, at a wavelength of 244 nm, on the local ferroelectric polarisation and shows that, at high enough intensity, UV laser light can directly invert the spontaneous polarisation. Investigations are carried out on both the $+z$ and $-z$ crystal faces and the resultant changes to the surfaces are characterised by both chemical etching and piezoresponse force microscopy. A model of the interaction is proposed whereby photo-excited charges travel within a pyro-electric field, creating a space-charge field which locally inverts the spontaneous polarisation. The anisotropy in behaviour between the $+z$ and $-z$ faces is investigated and is explained within the proposed model by the different mobilities of electrons and holes.

Chapter 4 extends the work of chapter 3 by investigating what effect the prior exposure of focussed UV laser light has during subsequent electric field poling. It is found that, when exposure is on the $+z$ face, domain inversion is inhibited within the exposed region to some depth below the surface. Again the effect is characterised by chemical etching and piezoresponse force microscopy and is explained within the framework of the model proposed in chapter 3. It is found to be a highly useful tool for topographical structuring, when combined with chemical etching, and the technological implications, along with limitations due to crystal symmetry, are discussed.

Chapter 5 looks theoretically at the heating of the crystal during focussed UV laser irradiation and develops both analytical and fully-numerical models to give the temperature distributions in the moving reference frame of the scanning beam. Through the use of an integral transform method the temperature dependence of the thermal diffusivity is included within the analytical model and results of this resultant non-linear model are compared to those of the linear case with constant thermal diffusivity. The importance of the inclusion of temperature dependence is discussed and the temperature distributions obtained under various conditions of beam spot size and power are analysed. The

effect on the temperature distributions of varying optical absorption coefficient is investigated and the implications for heating with CO_2 lasers is discussed. The numerical model is used to verify the techniques used in the analytical model since detailed experimental verification is technically very difficult. The numerical model is then used to further investigate the inclusion of temperature dependence in other thermal properties. A simple experiment is then carried out to test the model whereby the experimentally found conditions of beam power and spot size at the point at which melting occurs are compared with those predicted by the non-linear analytical model.

In chapter 6 a model is developed to describe the diffusion of lithium ions in the very steep temperature gradients seen during UV laser heating. Finite difference methods are used to solve the time-dependent equations in the reference frame of the crystal during the passage of heating beam with the temperatures being obtained from the heating model of chapter 5. The movement of lithium ions is shown to be essentially one-dimensional and directed perpendicular to the surface. The dependence of the resultant lithium concentration distribution on heating beam parameters of spot size, incident power, and scan speed and upon the optical absorption depth are investigated. The lithium concentration distributions are then converted into refractive index profiles through the Sellmeier equations for LN and these are tested for their waveguidance properties at optical wavelengths.

The work of the thesis is then summarised in chapter 7 and general conclusions are drawn. Suggestions for future work utilising and extending the results, models and methods of this thesis are then made in chapter 8.

1.1 The Structure of Lithium Niobate

Of the 32 crystal classes, 20 are seen to produce a spontaneous polarisation when subjected to an external stress and these are known as the piezoelectric classes. Of the 20 piezoelectric classes, 10 are characterised by the fact that they have at least one unique polar axis which retains a spontaneous polarisation without an external electric field or applied stress and these are known as the polar classes. Within the 10 classes of polar crystals some crystals are found that can reverse their direction of spontaneous polarisation under the application of an electric field such that the new direction is a stable state upon removal of the field. This property cannot be distinguished from the symmetry of the crystal structure alone and classification must so be done experimentally, however. These crystals are known as the ferroelectrics and it is within this group of crystals that we find LN.

LN is an artificial crystal that was first grown in 1937 [7] and has been intensively investigated since [7–9]. LN has the chemical formula (in the stoichiometric case) of $LiNbO_3$ and is composed of lithium, niobium and oxygen. In the Li_2O-Nb_2O_5 system LN melts congruently at 1550 K at a composition of 48.6 mol. % Li_2O and so this is the most frequently found composition. LN does, however, exist as a single crystal phase over a wide range of stoichiometries from 44.5 to 50.5 mol. % Li_2O at 1463 K [10]. The thermodynamically stable single-phase composition at room temperature is much narrower at $\sim$ 49 to 50.5 mol. % Li_2O, however room temperature ion kinetics prevent precipitation into secondary phases. Crystals with compositions of less than $\sim$ 49 mol. % Li_2O are then created when the crystal cools at a rate greater than that at which a second phase can precipitate and are thus only meta-stable at room temperature. For many applications this does not cause any problems but for others it can be a relevant consideration if heating occurs during later processing [7, 11–13]. Within the work of this thesis heating of the crystal will be frequent.

The crystal structure of LN is trigonal, meaning that it has a three-fold rotational symmetry about the polar axis. It also possesses a mirror plane parallel to the axis of rotation which places it in the crystal class 3m, in the Hermann-Mauguin notation, or C_{3v}, in the Schonflies notation [8]. The crystal structure consists of a sequence of close-packed, face sharing, oxygen octahedra stacked along the polar axis. The stacking of the oxygen octahedra is in a screw-like manner [7] which repeats after six oxygen planes along the polar axis. The oxygen tetrahedral interstices remain empty whilst the oxygen octahedra are filled with either lithium or niobium cations or vacancies along the positive polar direction (for perfect crystal structuring) in the following order: lithium, niobium, vacancy, lithium, niobium, vacancy... At temperatures above the Curie temperature, T_c, of $\approx$ 1490 K the crystal is paraelectric with the niobium cations located in the geometric

centres of their oxygen octahedra and the lithium cations at a position of ± 0.037 nm on either side of the oxygen plane with equal probability [8]. As the crystal cools through the Curie temperature the phase transition from paraelectric to ferroelectric takes place. This transition is of second order [8] since no abrupt change is seen at T_c. The niobium cations move away from the geometric centre of the oxygen octahedra and the lithium cations arrange co-operatively to the same side of the oxygen plane. Long range forces control the ordering of the movement from the paraelectric positions such that dipole moments of the individual unit cells align and a net spontaneous polarisation is obtained [7]. The position of the cations within the oxygen octahedra distorts the octahedra such that the oxygen-oxygen distance in the planes nearest the cations is less than that of the plane opposite. At room temperature the oxygen-oxygen distances are 0.3362 nm and 0.2879 nm in the planes nearest the lithium and niobium cations respectively. The niobium cation, then, has a larger effect upon the oxygen octahedra than does the lithium and this is also represented by the distances between the cation and the oxygen planes. The oxygen-lithium distance for the oxygen plane nearest the cation is 0.2068 nm and for the opposite plane is 0.2238 nm. The oxygen-niobium distance for the oxygen plane nearest the cation is, in contrast, just 0.1890 nm. The sum of the ionic radii of the oxygen and niobium ions is, however, 0.2010 nm which implies overlapping wavefunctions and strong ionic bonds. The breaking of these bonds will then form an energy barrier to polarisation reversal. The sum of the ionic radii of the oxygen and lithium ions is 0.2000 nm which, when compared with the oxygen-lithium distances, implies a weak bonding to the oxygen sub-lattice. However, for polarisation reversal the lithium cation must pass through the oxygen plane into the vacant octahedron. The oxygen-oxygen distance in this plane is 0.3362 nm which gives a space available for a sphere of radius 0.0620 nm. The ionic radius of the lithium ion is 0.0680 nm which means that it is difficult for the lithium to pass through the plane, which provides another energy barrier for domain inversion. [7]

It is thus the non-central positioning of the lithium and niobium cations that gives rise to the spontaneous polarisation, denoted $\mathbf{P}_s$, and the energy barriers for ionic movement that gives rise to the room temperature stability of this spontaneous polarisation. It is then from this stable spontaneous polarisation that many of the useful properties of LN are derived. The magnitude of the spontaneous polarisation of LN, with a value of $\approx 70\mu$C cm^{-2} [8], is around an order of magnitude larger than for most ferroelectrics. The positions of the atoms within the unit cell are well known at room temperature and are given in [14]. Figure 1.1 shows the arrangement of atoms within LN for a stack of oxygen octahedra along the polar axis. Also shown is the displacement of the lithium and niobium cations during polarisation reversal. Figure 1.2 shows the arrangement of atoms within the plane perpendicular to the polar axis. It can be seen here that the

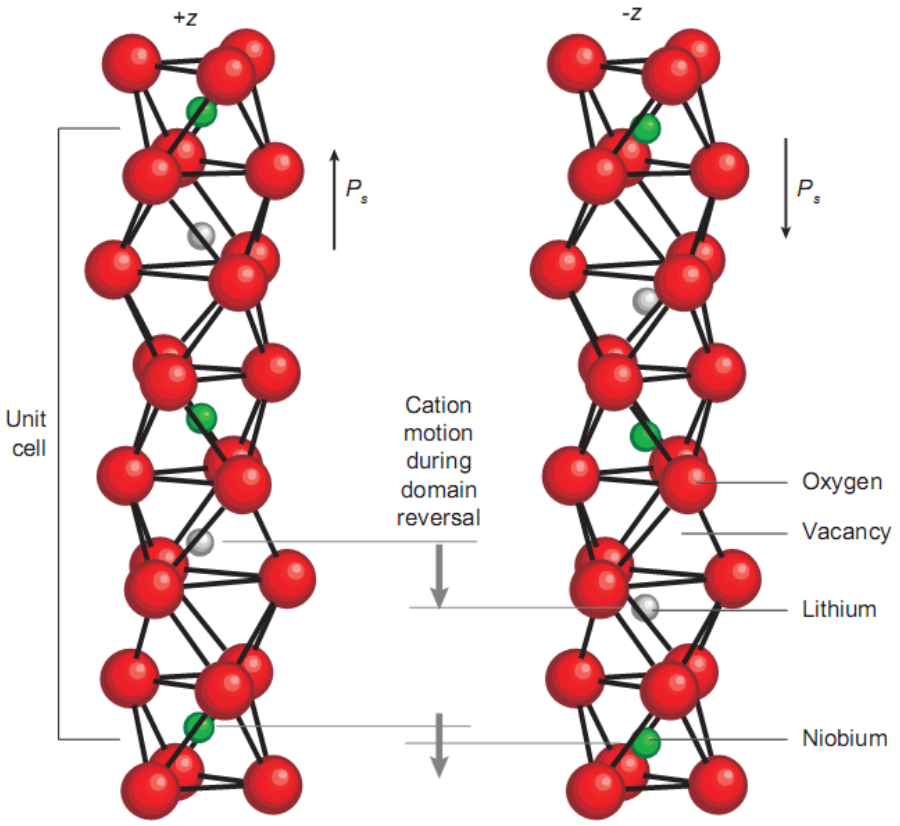

FIGURE 1.1: The crystal structure of LN showing the displacement of cations during polarisation reversal. After [15]

cations and vacancies are arranged such that each is surrounded by three of the other two.

The symmetry of LN lends itself well to a hexagonal coordinate system with axes (a_1,a_2,a_2,c) where c is the polar axis and the a_i axes are perpendicular to the mirror planes [14]. The coordinate system for the tensors that describe many properties of the crystal, however, is Cartesian. The accepted convention for relating the hexagonal axes to the Cartesian axes is as follows: The z axis is chosen to be parallel to the c axis. The x axis is chosen to coincide with any of the a_i axes and the y axis is perpendicular to the x axis and thus lies in a plane of mirror symmetry [14]. The direction of the $+z$ axis is defined as being directed outward from the face that becomes positive upon cooling [7] and negative upon compression [14]. The direction of the y axis is defined similarly as being directed out from the face which becomes negative upon compression [14].

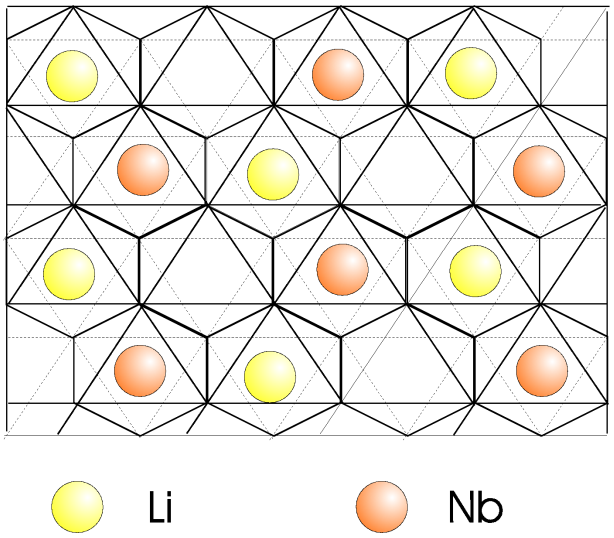

FIGURE 1.2: The crystal structure of LN in the plane perpendicular to the polar axis. Oxygen octahedra are shown as solid lines.

1.2 Exploitable Properties and Common Applications

1.2.1 Optical Transparency

LN has a wide transparency window over the visible part of the spectrum which makes it a very useful optical material. The transparency region starts in the infra-red between 5500 - 7000 nm and reaches the ultraviolet at between 320 - 350 nm. The transmission curve is extremely flat over this range with the only appreciable dip occurring at 2870 nm due to the presence of OH^- groups within the crystal. A typical transmission curve of un-doped congruent LN is shown in figure 1.3. The electronic band structure of LN around the Fermi level is determined mainly by the NbO_6 octahedra since the upper level of the valence band is formed by the oxygen 2p states and the lower level of the conduction band is formed by the niobium 4d states. The band gap of LN is around 3.7 - 3.9 eV [7]. The optical properties of LN in the UV region have been studied by Mamedov et al. [16] for photon energies between 0 and 35 eV. Since a large part of the work of this thesis relates to effects due to UV light the optical absorption data obtained in [16] is shown in figure 1.4. The work is mainly carried out at wavelengths of 244 nm and 266 nm which correspond to photon energies of 5.09 and 4.66 eV respectively. It can be seen in figure 1.4 that the optical absorption is rapidly increasing in this area which may have implications if the curve would shift with temperature, for example.

Whilst the main optical absorption characteristics are determined by the NbO_6 octahedra, weak absorption can also be caused by energy levels within the band-gap that are associated with either structural defects or extrinsic impurity ions. The absorption

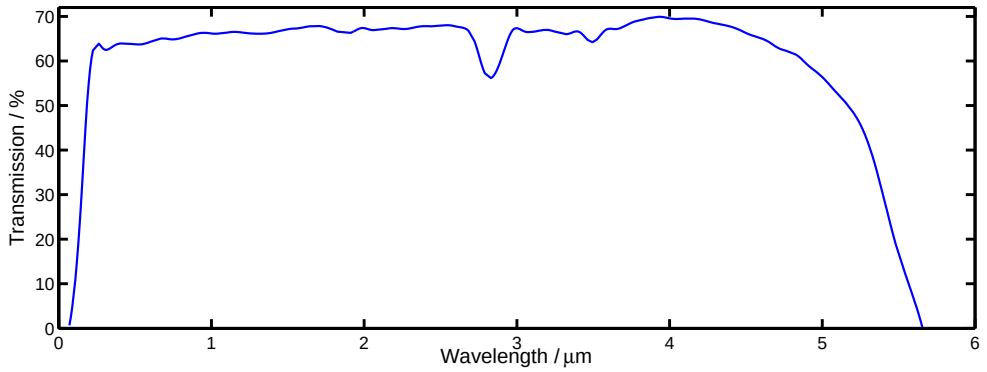

FIGURE 1.3: Optical transmission spectrum of LN. Data re-plotted after [7].

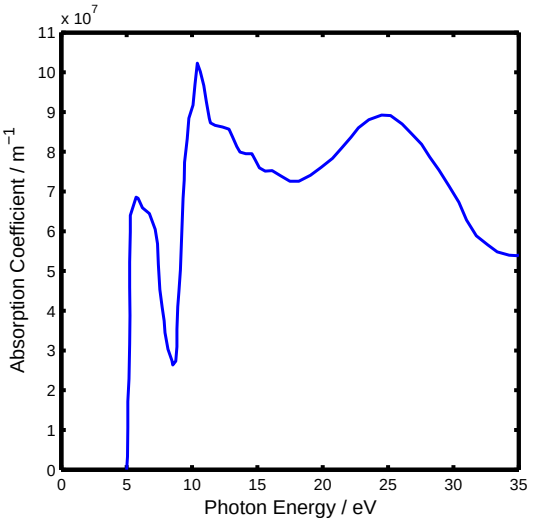

FIGURE 1.4: Optical absorption coefficient of LN in the UV region. Data re-plotted after [16].

due to these intra-band-gap energy levels does not significantly affect the overall transparency of the crystal at normal concentrations but are of great importance as sources and sinks of photo-excited charge. Figure 1.5 shows the positions within the band-gap of some experimentally verified and calculated energy levels corresponding to either F (or colour) centres which comprise electrons trapped at ionic vacancies, or extrinsic impurities such as iron. Some impurities, such as iron, are present even when doping is not intentional and are a main cause of photo-sensitivity.

1.2.2 $\chi^{(2)}$ Non-Linear Optical Properties

Second order, $\chi^{(2)}$, non-linearities form the basis of many of the common optical uses of LN, indeed it is precisely the fact that LN has large non-linear optical coefficients that

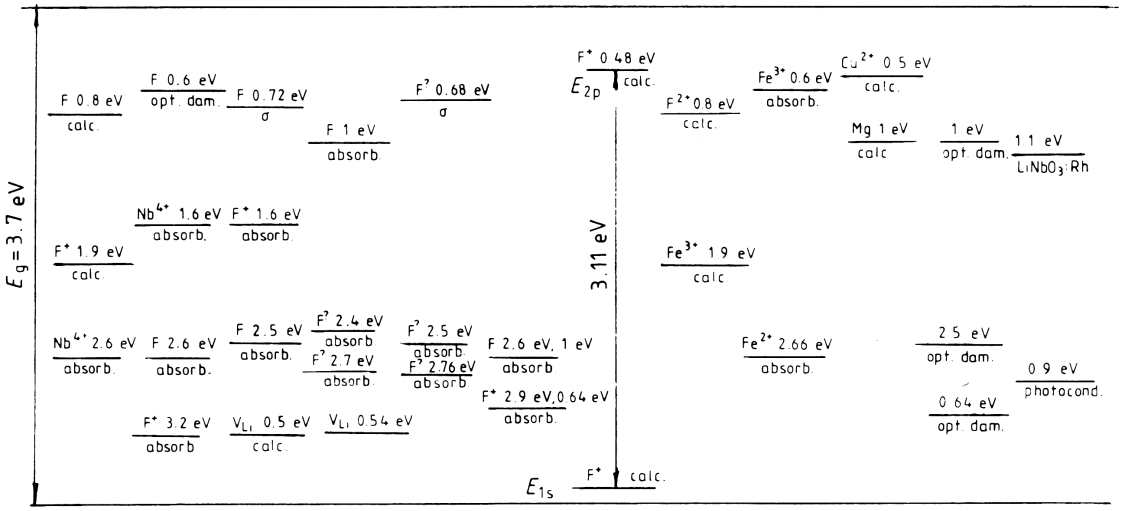

FIGURE 1.5: Intra-band-gap energy levels of some common F centres and impurity ions. After [7].

sets it apart from most other optical dielectrics. To understand these non-linearities it is first important, however, to examine how a system responds in the linear regime.

When light of frequency ω is transmitted through a transparent material the electric field of the light accelerates the loosely bound valance electrons, distorting the shape of the electron distribution. For most cases the restorative electrostatic forces that act to maintain the electron distribution are far greater than the distorting forces induced by the light and the magnitude of the distortion of the electron distribution is proportional to the applied electric field. The distortion of the electron distribution is referred to as the electrical polarisation $\mathbf{P}$ and is given in this linear regime, in tensor component form, as

$$P_i(\omega) = \epsilon_0 \sum_j \chi_{ij}(\omega) E_j(\omega) \qquad i, j = x, y, z \tag{1.1}$$

where $\mathbf{E}$ is the driving electric field, ω is the angular frequency of the oscillating electric field and χ is the electric susceptibility tensor. The product $\epsilon_0\chi$ is, of course, the derivative of $\mathbf{P}$ with respect to $\mathbf{E}$ and is related to the refractive index, n, as $n = \sqrt{1+\chi}$. Since the polarisation is linearly proportional to the applied field which oscillates at a frequency ω, the polarisation also oscillates at the frequency ω and will thus also re-radiate an electric field at this same frequency. The applicability of the assumption of linear behaviour will break down at high electric field strengths, however, when the linear response begins to saturate. At this point non-linear contributions to the polarisation must be taken into account. These non-linear contributions are always present, but are insignificant due to the extremely high values of the interatomic or crystalline electric field strengths which act to restore the spatial electron distributions. Externally applied

electric fields are usually relatively weak compared to these, even when focused laser light is used. In these situations the non-linearity is weak and it is legitimate to expand the polarisation as a Taylor series about $E = 0$ where the magnitude of terms decreases rapidly with order. The non-linear terms are then given by, to third order,

$$P_i^{NL} = \epsilon_0 \sum_{jk} \chi_{ijk}^{(2)} E_j E_k + \epsilon_0 \sum_{jkl} \chi_{ijkl}^{(3)} E_j E_k E_l + \dots \tag{1.2}$$

where $\chi^{(m)}$ is the mth order susceptibility tensor and the explicit dependence on ω has been dropped from the notation. In materials that are centro-symmetric, the second order non-linear coefficients must be zero or otherwise an inversion of the applied field would not result in an inversion of the polarisation, which is un-physical. Due to the ferroelectric nature of LN, however, there is no inversion symmetry to the z axis and so $\chi^{(2)}$ is non-zero.

In a scalar approximation, to make notation more legible, and assuming non-zero non-linear terms we can consider the non-linear polarisation

$$P^{NL} = \epsilon_0 \chi^{(2)} E^2 + \epsilon_0 \chi^{(3)} E^3 + \cdots \tag{1.3}$$

If the response of the polarisation to a harmonic electric field with two frequency components of the form

$$E = E_0 \sin \omega_0 t + E_1 \sin \omega_1 t \tag{1.4}$$

is considered

$$\begin{aligned} P^{NL} = \; & \epsilon_0 \chi^{(2)} \left\{ E_0^2 \sin^2 \omega_0 t + E_1^2 \sin^2 \omega_1 t + 2 E_0 E_1 \sin \omega_0 t \sin \omega_1 t \right\} \\ & + \epsilon_0 \chi^{(3)} \left\{ E_0 \sin \omega_0 t + E_1 \sin \omega_1 t \right\}^3 + \cdots \end{aligned} \tag{1.5}$$

where only the second order term has been expanded due to its greater relevance to the majority of practical uses. In the second order term we can see three factors which describe components of the time-dependent polarisation and hence the re-radiated field of the induced dipole. The first two terms are dependent only upon each of the components of the driving field individually, however the third term is dependent upon both components of the driving field and represents a component of the re-radiated field which is derived from a mixing of the two incident field components. Expanding the third term in equation 1.5 through standard trigonometric relations we obtain

$$P^{NL} = \epsilon_0 \chi^{(2)} E_0 E_1 \left\{ \cos\left(\omega_0 - \omega_1\right) t + \cos\left(\omega_0 + \omega_1\right) t \right\} + \cdots \tag{1.6}$$

where other factors, not arising from the third term in equation 1.5, have been omitted for clarity. It can then be seen that when an electric field which has two frequency

components is incident upon a non-centrosymmetric non-linear crystal, such as LN, the induced polarisation, and hence re-radiated field will contain frequency components that are either the sum or difference of the two incident field components. This effect is referred to as either sum frequency generation (SFG) of difference frequency generation (DFG), respectively, and forms the basis of optical parametric generation (OPG) techniques which are used extensively to create coherent light at wavelengths which are not otherwise easily available from lasing sources from wavelengths that are easily available [3, 17]. If we consider now the situation where a monochromatic field, with frequency ω and magnitude E, is present equation 1.5 becomes

$$P^{NL} = \frac{\epsilon_0 \chi^{(2)}}{2} E^2 \left(1 - \cos 2\omega t\right) + \cdots . \tag{1.7}$$

where, again, the third order term is omitted for clarity. It can be seen that, even when only a single frequency component is present in the incident field, the induced polarisation and hence re-radiated field contains a frequency component at twice the frequency of the incident field. This effect is known as second harmonic generation (SHG) and is widely employed to generate laser light at short wavelengths that are not otherwise available. In fact this is just a special case of SFG when ω_0 and ω_1 are degenerate. SHG will be used in the remainder of this section, however, to explore other properties of the parametric generation process, but the principles and conclusion obtained are applicable to all OPG techniques.

This far in the discussion, only the response of an isolated point has been considered and no discussion of travelling waves has been made. In reality optical materials are extended structures and we want the frequency conversion processes described above to continue in a constructive manner such that high intensity harmonics can be produced. This is hindered by dispersive qualities of the medium since the phase velocity is frequency dependent. Thus the two frequency components, the incident wave and the generated wave, will travel at different speeds within the material. The generated wave will always have a fixed phase relationship to the incident wave, however, so as the generated wave travels through the crystal from point a to point b the phase difference between the waves generated at each point will continually increase until destructive interference occurs and the amplitude of the generated wave decreases. The length over which this occurs is known as the coherence length, l_c, (not to be confused with the normal definition of the coherence length of laser light) and is given by

$$l_c = \frac{\pi}{\Delta k} \tag{1.8}$$

where Δk is the difference in wavevector of the generated wave and the incident wave. In certain circumstances the refractive indices of the two frequency components can

be made equal, through birefringent phase matching for example, and in this case the waves travel at equal velocity and the Δk drops to zero and the process is continually constructive.

Another method by which a generated wave of continuously increasing amplitude can be created is by quasi phase matching (QPM) [3]. It was mentioned above that the generated wave has a constant phase relationship to the incident wave, however if the polarity of the crystal is inverted, the sign of the relevant $\chi^{(2)}$ tensor coefficients invert also and the generated wave undergoes a phase shift of π relative to the wave that would have been created in the crystal of the original polarisation. The phase of existing waves is not affected by entering a region of inverted polarity since the first order susceptibility tensor is symmetric. Thus, if the polarity of the crystal is inverted at the point in which the pre-existing generated wave becomes out of phase with the newly generated wave, a π phase shift occurs to the newly generated wave and the two are again in phase and interfere constructively. This process is known as QPM and has resulted in the development of periodically poled lithium niobate (PPLN) as a highly efficient and flexible medium for frequency conversion. Thus by switching the polarity of the ferroelectric domain at a spatial frequency of ml_c, where m is an integer, efficient build-up of the second harmonic can occur. Although the efficiency of QPM is not as great as that of perfect phase matching, it does have the advantages over birefringent phase matching that the diagonal terms of the $\chi^{(2)}$ tensor are accessible and that phase matching can occur over a wider spectral range. Appendix A examines the build-up of the second harmonic in greater detail and figure 1.6 shows the evolution of the second harmonic intensity with distance through the crystal for the cases of; no phase matching, perfect phase matching, first order QPM with the domain inversion period $\Lambda = l_c$ and third order QPM with the domain inversion period $\Lambda = 3l_c$.

PPLN structures are not, however, limited to one dimensional gratings but have also been demonstrated as two dimensional hexagonally poled domain arrays [18] where multiple phase matching configurations are present due to the different lattice vectors of the domain array. This allows for multiple frequencies to be generated from a single beam, separated by angle, and much wider tuning ranges.

1.2.3 The Electro-Optic Effect

The electro-optic effect is one of the most exploited properties of LN due to its use in electro-optic modulators to directly alter the phase of a light signal. The electro-optic effect derives again from the non-centrosymmetric nature of LN and the non-zero $\chi^{(2)}$ susceptibility. Considering the second order term of equation 1.3 with the electric field

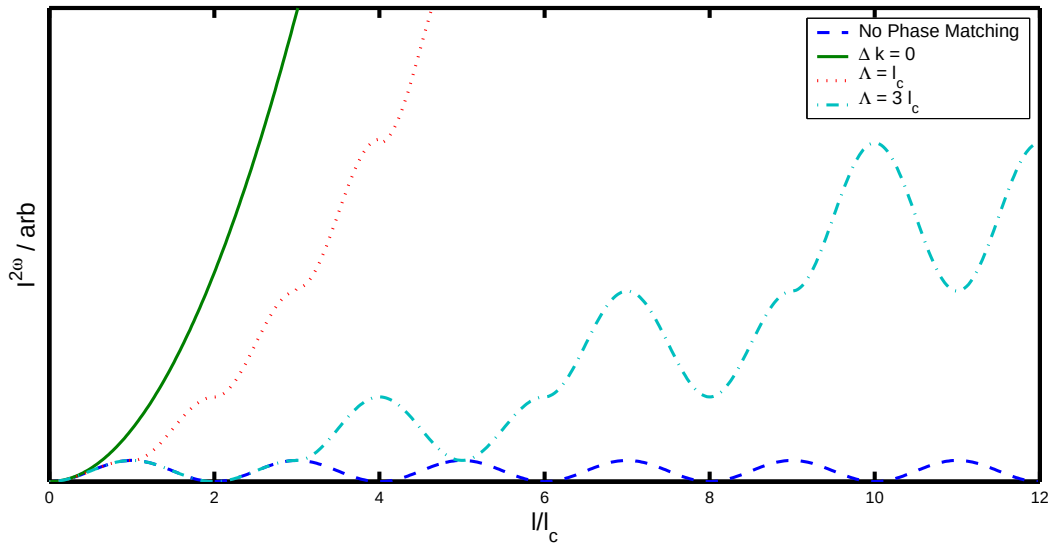

FIGURE 1.6: Variation of the second harmonic intensity with propagation distance for the situations of no phase matching, perfect phase matching and quasi phase matching with $\Lambda = l_c$ and $\Lambda = 3l_c$.

comprising a harmonic term and a non-harmonic DC term we obtain

$$\begin{aligned} P^{NL} &= \epsilon_0 \chi^{(2)} (E_0 \sin \omega t + E_{DC})^2 + \cdots \\ &= \epsilon_0 \chi^{(2)} (E_0^2 \sin^2 \omega t + E_{DC}^2 + 2E_{DC} E_0 \sin \omega t). + \cdots \end{aligned} \tag{1.9}$$

The third term of equation 1.9 then gives a component to the induced electrical polarisation at the frequency of the incident harmonic field whose magnitude depends upon the magnitude of the applied DC field. This component of the polarisation will then translate to a DC field induced change to the refractive index of the crystal at the frequency of the harmonic component. Since the electric fields are both vector quantities and the susceptibility is a tensor quantity, the scalar approximation above is a simplification and the induced refractive index change will depend upon the relative orientations of the two fields and the crystal axes. In full tensor component form the refractive index change is given by

$$\Delta \left(\frac{1}{n^2} \right)_{ij} = \sum_k r_{ijk} E_k \qquad i, j, k = x, y, z \tag{1.10}$$

where r is the electro-optic tensor and E_k are the components of the applied electric field vector. The electro-optic tensor is related to the change in the susceptibility, $\Delta\chi_{ijk}$, originating in the term in equation 1.9 discussed above by [19]

$$r_{ijk} E_k^{DC} = \frac{-\Delta\chi_{ijk}}{\epsilon_i' \epsilon_j'} \tag{1.11}$$

where E_k^{DC} is the k component of the applied DC field and $\epsilon_{i,j}$ are the linear permittivities in the i and j directions.

The electro-optic effect has been used to make a wide range of devices when combined with channel waveguides [5, 20] since both electrodes can be applied to the surface of the crystal with separations of just a few microns, allowing large electric fields to be generated from low voltages. The simplest device is a phase modulator that consists of two electrodes surrounding a channel waveguide. When a voltage is applied across the electrodes a field is present in the waveguide which changes the index, altering the velocity of light within the waveguide, and retards or advances the phase of the light exiting the guide. The modulation of the phase can be used to encode information onto the carrier light signal however the deciphering of the signal upon receiving can be challenging due to difficulties in measuring phase shifts and ambiguities between shifts π apart. However, once one can modulate the phase it is a simple matter to incorporate the phase shift into one arm of an interferometer and use the phase retardance in one arm to create either destructive or constructive interference when the split beams recombine such that the intensity is modulated and the encoded signal is easy to read. Another way in which this can be achieved is through the use of a directional coupler consisting of closely spaced waveguides where the coupling between them is controlled by the electro-optically induced index change.

The electro-optic effect can also be used to create useful devices in bulk crystals. This can be achieved in a similar way as QPM achieves high efficiency harmonic generation, by spatially structuring the ferroelectric crystal polarity. The sign of the index change produced by a given electric field is determined by both the relative orientation of the field and the electro-optic tensor as can be seen in equation 1.10. It has already been stated that when the polarity of the ferroelectric domain is inverted the sign of the $\chi^{(2)}$ tensor components invert also and so, through equation 1.11, so too do the sign of the r tensor components. This means that if a uniform field is applied across a boundary between two oppositely oriented ferroelectric domains then each domain will experience an index change in the opposite direction and an optical interface will be produced that can reflect and refract light waves. This has been used to produce electrically controllable lens arrays [21], beam deflectors [21–25], total internal reflection (TIR) switches [23–25] and Bragg diffraction gratings [26].

1.2.4 Photo-refractive Effect

The photo-refractive effect is a non-instant, non-local, light induced change to the refractive index that persists for some time after the illumination has stopped. The photo-refractive effect is due to three processes. First photo-ionisation of inter-band defects, in the case of visible light, or band to band photo-excitation, in the case of UV light creates free charges within the crystal. This is followed by charge transport through inter-band diffusion, electronic drift or photovoltaic current until charges are trapped in regions of low light intensity. This space-charge distribution creates electric fields within the crystal which can act upon the refractive index through the electro-optic effect. The photo-refractive effect in LN thus derives again from the non-centrosymmetric nature of LN and the non-zero $\chi^{(2)}$ susceptibility.

The photo-refractive effect is often a hindrance in optical applications since the modification of the refractive index across the beam front will cause the beam to fan, destroying the spatial profile. Doping the crystal with magnesium is commonly used to reduce photo-refractive effects [27]. The ability of light to influence the refractive index through the photo-refractive effect is used, however, in a wide range of useful applications from phase conjugation for beam clean-up and multi-wave mixing for power sharing between different quality beams to the creation of highly multiplexed volume holographic memories [28]. In the cases where photo-refractive effects are desirable the photo-refractive sensitivity is often increased by doping with either iron or copper[27]. Since the space-charge fields necessary for the photo-refractive effect will decay over time due to the dark conductivity of the crystal, methods have been developed to thermally fix the charge distributions [29]

1.2.5 Pyro-Electric Effect

At high temperatures, above T_c, LN is paraelectric with the niobium and lithium cations sitting in the centres of their respective oxygen octahedra. As the temperature drops below T_c, the lithium and niobium cations move away from the centres and a spontaneous polarisation develops. The displacement of the cations from their para-electric positions is a function of the energy of the system [8] and hence temperature. At a temperature below T_c a depolarisation field is present within the crystal due to the divergence of the spontaneous polarisation at the surface [8], either through the abrupt structural dislocation of the surface or due to a relaxation of the structure at the surface. This is compensated by the movement of free charges [8] and the alignment of dipolar defects [30] within the crystal. The compensating mechanisms are, however, slow to react to

changes in the spontaneous polarisation, which are themselves an almost instant reaction to changes in temperature. Thus when the temperature of the crystal changes over a time scale shorter than that at which the charge compensation mechanisms can react, the spontaneous polarisation is left over-compensated and an electric field develops within the crystal. This is known as the pyro-electric effect.

Thermodynamic phenomenological theories of ferroelectrics predict that the dependence upon spontaneous polarisation on temperature is of the form [8, 31]

$$P_s^2 = \beta(T_c - T)/\gamma \tag{1.12}$$

where β and γ are positive, temperature independant, constants. This behaviour has been seen in LT [31] which has a lower value of T_c, making experimental measurements much easier, but is isomorphous to LN and so should behave similarly. A dependence of similar character has also been seen in LN [32] although over a narrower temperature range that does not include T_c. It is clear, however, that the relationship between spontaneous polarisation and temperature is not linear as is stated in [14]. Over small temperature changes a linear approximation may be justified but in the work of this thesis the temperatures of interest shall range from room temperature to the melting point of LN near 1500 K.

Although commercial devices are made that utilise directly the pyro-electric effect, such as laser pulse energy meters and infra-red detectors [33], LN is not often chosen. The pyro-electric effect is seen, however to be highly influential upon the charge transport mechanisms in LN and has been shown to be the cause of electron emission [34, 35]. The production of high electric field strengths through the pyro-electric effect has also been used to drive a deuteron beam for use in fusion experiments [6].

1.2.6 Surface Optical Waveguides

Surface optical waveguide structures have been made in LN in a variety of different ways, either by altering the surface layer to obtain a higher refractive index or by modifying the crystal in a sub-surface layer such that the index of the sub-surface layer is reduced.

LN is a chemically stable single crystal over a wide stoichiometry range [10] and it is well known that the refractive index varies with stoichiometry over this range [36] with the extraordinary index increasing with decreasing Li concentration. It follows, then, that optical waveguiding structures may be created by the out-diffusion at high temperatures of volatile Li_2O. This has been investigated by Kaminow and Carruthers [37] and Carruthers et al. [38] and, indeed, guiding structures are produced. It is also

seen that these structures are of high quality and guide with low losses. The method of using vapour fluxes of Li_2O to vary the stoichiometry, and hence refractive index, has been extended by heating LN to high temperatures within a crucible made from either $LiNbO_3$ + Li_3NbO_4 or $LiNbO_3$ + $LiNb_3O_8$ which act as either a source or sink, respectively, for Li. Using this method it was also found that the vacuum environment of [37, 38] was not needed.

The in-diffusion of metals through the LN surface is also seen to produce a refractive index change that can be used for optical waveguiding. The metal atoms are easily accommodated in LN due to the high level of structural defects present, even in stoichiometric crystals. Many species have been investigated including Mg, Ni, Zn, Fe, Co, Cu, Cr, V and Ti. A thin film, 10 - 100 nm thick, of the metal is deposited onto the LN surface by either vacuum evaporation or sputtering and then the crystal is heated to a high temperature, around 1000°C, where diffusion can take place. Divalent species such such as Ni, Zn and Mg are seen to occupy Li vacancies within the crystal and cause a reduction of the extraordinary index. When Ni or Zn are diffused the ordinary index increases, however if Mg is used the ordinary index will decrease. Tri-valent or tetra-valent species such as Fe, Cr and Ti are seen to occupy niobium vacancies within the crystal and cause an increase to both the ordinary and extraordinary indices. [11] The diffusion of Ti is the most widely studied process due to the relatively large change in both the extraordinary and ordinary indices of < 0.02 and < 0.04 respectively allowing waveguides supporting both TE and TM modes. In the case of Ti in-diffusion it has been suggested by Sugii et al. [39] that the index change is due to the increased polarisability and photoelastic effect caused by the differing sizes of the Nb and Ti ions.

Proton exchange is another widely used method for changing the refractive index of the LN surface for the production of optical waveguides [11]. The method differs from metal in-diffusion since the LN samples are submerged within a solution containing the donor H^+ ions, often benzoic acid, which then substitute for Li ions within the crystal which can diffuse into the acid. The process takes place at temperatures of around 120 - 150°C which is far lower than those used in in-diffusion which are around 1000°C. The proton exchange process is seen to increase the extra-ordinary refractive index by around 0.12 [40] and to decrease the ordinary refractive index by around 0.05 [11]. These index changes are considerably higher than those that can be achieved through metal in-diffusion. It is seen that the proton exchange process can reduce the electro-optic [41] and acousto-optic [11] sensitivity of the crystal which may limit its utility, however post-exchange annealing can improve these piezoelectric and optical properties. The photo-refractive sensitivity of proton exchanged waveguides is greatly reduced with estimates of a reduction of four orders of magnitude compared to un-exchanged crystal. Due to the large refractive index change, proton exchange has been used in conjunction

with titanium in-diffused waveguides to create a number of useful devices such as lenses [42], polarisers [43] and Bragg gratings [44].

A further method of creating optical waveguiding structures in LN also employs the inclusion of other elements into the crystal, but in a very different manner to either metal in-diffusion or proton exchange. Ion implantation uses a high energy ionic beam to bombard the LN surface such that the ions penetrate the surface to a depth given by the energy and species of the ions [11]. When the ions initially enter the crystal they lose energy through electrostatic forces only and do not cause significant damage. When the ions have slowed sufficiently they lose their remaining energy through nuclear collisions and cause considerable damage to the crystal which lowers the refractive index. It is then the contrast in refractive index between the largely un-affected surface layer with this lower index sub-surface damaged layer that forms the waveguide. Many different ions can be employed for ion-implantation such as N, O, He, Ar, H and Ti. Due to the low damage level of the surface layer, the non-linear properties of the waveguide are well preserved. The index of the surface layer can also be raised when using He ions since bombardment encourages a loss of Li_2O from the surface. This is seen to be dependant upon both the ion dose and energy and can be used to help control the waveguide properties [11].

1.2.7 Piezoelectric and Converse-Piezoelectric Effect

The piezoelectric effect is the creation of an electric field by an applied stress. Since LN is ferroelectric it is also, by definition, piezoelectric. From a viewpoint of macroscopic phenomenology the piezoelectric effect can be described by the following coupled equations [8]

$$dE_i = -g_{ij}dX_i + \kappa_{ij}^X dD_j \tag{1.13}$$

$$dD_i = d_{ij}dX_j + \epsilon_{ij}^X dE_j \tag{1.14}$$

where **E** is the electric field vector, **D** is the electric displacement vector, **X** is the mechanical stress tensor, ϵ_{ij} and κ_{ij} are the electrical permittivity and reciprocal electrical permittivity tensors respectively and $g_{ij}\left(=\dfrac{\partial E_i}{\partial X_j}\right)$ and $d_{ij}\left(=\dfrac{\partial D_i}{\partial X_j}\right)$ are piezoelectric compliance tensors of third rank. The electric displacement is given by

$$dD_i = \epsilon_{ij}dE_j + dP_{si} \tag{1.15}$$

which, when substituted into equation 1.14, gives the linear relation

$$dP_{si} = d_{ij} dX_j \tag{1.16}$$

between the spontaneous polarisation and the applied stress.

The converse-piezoelectric effect, as the name suggests, is the creation of a mechanical strain due to an applied electric field. In the same manner as above the converse-piezoelectric effect can be described by the following coupled equations [8]

$$dX_i = c_{ij} dx_j - e_{ij} dE_j \tag{1.17}$$

$$dx_i = s^E_{ij} dX_j + d_{ij} dEj \tag{1.18}$$

where x is the mechanical strain tensor, $e_{ij}\left(=\dfrac{\partial X_i}{\partial E_j}\right)$ is a piezoelectric tensor of third rank and c^E_{ij} and s^E_{ij} are the third rank elastic stiffness and elastic compliance tensors, respectively, at constant electric field.

These two effects allow the transduction from mechanical energy into electrical energy and vice versa which gives rise to many useful applications. In LN the main application of the piezoelectric and converse-piezoelectric effect has been the creation, and scrutiny, of either bulk or surface acoustic waves (SAW) with the use of interdigital electrodes. The most widely used device employing SAW is the acoustic delay line filter which is found in many wireless communications devices and is produced in vast quantities by the electronics industry [45]. SAW are highly localised to the surface of the crystal and so their propagation is seen to be extremely sensitive to the surface conditions and this has led to a wide range of sensing applications from temperature [46] and humidity [47] sensors to gas composition [48] and flow [49] sensors to liquid conductivity sensors [50]. When liquids are concerned it has even been seen that SAW can be used to actuate and mix liquid drops along defined tracks within the acoustic delay line [51] adding further functionality to sensors which may allow for autonomous lab-on-a-chip devices.

The converse-piezoelectric effect has also been used to create piezoelectric actuators with LN [52–55] and forms the basis of piezo-response force microscopy which is widely used in the detection and characterisation of ferroelectric domain structures [56].

References

[1] R.D. Hollinger, A.R. Tellakula, C.-T. Li, V.V. Varadan, and V.K. Varadan. Wireless surface acoustic wave-based humidity sensor. *Proceedings of the SPIE - The International Society for Optical Engineering*, 3876:54 – 62, 1999.

[2] John H. Lehman, Katherine E. Hurst, Antonije M. Radojevic, Anne C. Dillon, and Jr. Richard M. Osgood. Multiwall carbon nanotube absorber on a thin-film lithium niobate pyroelectric detector. *Opt. Lett.*, 32(7):772–774, 2007.

[3] L. E. Myers and W. R. Bosenberg. Periodically poled lithium niobate and quasi-phase-matched optical parametric oscillators. *IEEE Journal of quantum electronics*, 33:1663–1672, 1997.

[4] F. Lucchi, D. Janner, M. Belmonte, S. Balsamo, M. Villa, S. Giurgola, P. Vergani, and V. Pruneri. Very low voltage single drive domain inverted $LiNbO_3$ integrated electro-optic modulator. *Optics Express*, 15(17):10739 – 10743, 2007.

[5] E.L. Wooten, K.M. Kissa, A. Yi-Yan, E.J. Murphy, D.A. Lafaw, P.F. Hallemeier, D. Maack, D.V. Attanasio, D.J. Fritz, G.J. McBrien, and D.E. Bossi. A review of lithium niobate modulators for fiber-optic communications systems. *IEEE Journal of Selected Topics in Quantum Electronics*, 6(1):69 – 82, 2000.

[6] B. Naranjo, J.K. Gimzewski, and S. Putterman. Observation of nuclear fusion driven by a pyroelectric crystal. *Nature*, 434(7037):1115–1117, April 2005.

[7] A. M. Prokhorov and Yu. S. Kuz'minov. *Physics and chemistry of crystalline lithium niobate*. Hilger, IOP Publishing Ltd, Bristol, BS1 6NX, England, 1990.

[8] M. E. Lines and A. M. Glass. *Principles and Application of Ferroelectrics and Related Materials*. Clarenon Press, 1977.

[9] K. K. Wong. *Properties Of Lithium Niobate*. EMIS Datareview. IEEE, 1989.

[10] L.O. Svaasand, M. Eriksrud, G. Nakken, and A.P. Grande. Solid-solution range of $LiNbO_3$. *Journal of Crystal Growth*, 22(3):230 – 2, 1974.

[11] M.N. Armenise. Fabrication techniques of lithium niobate waveguides. *IEE Proceedings J (Optoelectronics)*, 135(2):85 – 91, 1988.

[12] M. N. Armenise, C. Canali, M. De Sario, A. Carnera, P. Mazzoldi, and G. Celotti. Characterization of TiO_2, $LiNb_3O_8$, and $(Ti_{0.65}Nb_{0.35})O_2$ compound growth observed during Ti:$LiNbO_3$ optical waveguide fabrication. *Journal of Applied Physics*, 54(11):6223–6231, 1983.

[13] E. Born, J. Hornsteiner, T. Metzger, and E. Riha. Diffusion of niobium in congruent lithium niobate. *Physica Status Solidi A*, 177(2):393 – 400, 2000.

[14] R.S. Weis and T.K. Gaylord. Lithium niobate: summary of physical properties and crystal structure. *Applied Physics A (Solids and Surfaces)*, A37(4):191 – 203, 1985.

[15] Venkatraman Gopalan, Volkmar Dierolf, and David A. Scrymgeour. Defect-domain wall interactions in trigonal ferroelectrics. *Annual Review of Materials Research*, 37:449 – 489, 2007.

[16] A.M. Mamedov, L.S. Hajiyeva, I.S. Ibragimova, and B.S. Aliyeva. Vacuum ultraviolet (VUV) reflectivity and electron states in $LiNbO_3$. *Physica B &; C*, 128B+C: 61 – 8, 1985.

[17] R.L. Byer. Quasi-phasematched nonlinear interactions and devices. *Journal of Nonlinear Optical Physics and Materials*, 6(4):549 – 92, 1997.

[18] N.G.R. Broderick, G.W. Ross, H.L. Offerhaus, D.J. Richardson, and D.C. Hanna. Hexagonally poled lithium niobate: a two-dimensional nonlinear photonic crystal. *Physical Review Letters*, 84(19):4345 – 8, 2000.

[19] Chun-Ching Shih and A. Yariv. A theoretical model of the linear electro-optic effect. *Journal of Physics C (Solid State Physics)*, 15(4):825 – 46, 1982.

[20] R.C. Alferness. Waveguide electrooptic modulators. *IEEE Transactions on Microwave Theory and Techniques*, MTT-30(8):1121 – 37, 1982.

[21] M. Yamada, M. Saitoh, and H. Ooki. Electric-field induced cylindrical lens, switching and deflection devices composed of the inverted domains in $LiNbO_3$ crystals. *Applied Physics Letters*, 69(24):3659 – 3661, 1996.

[22] S.J. Barrington, A.J. Boyland, and R.W. Eason. Domain-engineered lithium niobate as a medium for an integrated solid-state two-dimensional color laser scanning system. *Applied Optics*, 43(8):1625 – 7, 2004/03/10.

[23] Stephen J. Barrington, Alexander J. Boyland, and Robert W. Eason. Resolution considerations in electro-optic, single interface deflectors. *Applied Optics*, 43(5): 1038 – 1043, 2004.

[24] A.J. Boyland, G.W. Ross, S. Mailis, P.G.R. Smith, and R.W. Eason. Total internal reflection switching in electro-optically addressable domain-engineered $LiNbO_3$. *Electronics Letters*, 37(9):585 – 587, 2001.

[25] R.W. Eason, A.J. Boyland, S. Mailis, and P.G.R. Smith. Electro-optically controlled beam deflection for grazing incidence geometry on a domain-engineered interface in $LiNbO_3$. *Optics Communications*, 197(1-3):201 – 7, 15 Sept. 2001.

[26] J.A. Abernethy, C.B.E. Gawith, R.W. Eason, and P.G.R. Smith. Demonstration and optical characteristics of electro-optic bragg modulators in periodically poled lithium niobate in the near-infrared. *Applied Physics Letters*, 81(14):2514 – 16, 30 Sept. 2002.

[27] K. Buse. Light-induced charge transport processes in photorefractive crystals. II. materials. *Applied Physics B (Lasers and Optics)*, B64(4):391 – 407, 1997.

[28] K. Buse. Light-induced charge transport processes in photorefractive crystals. I. models and experimental methods. *Applied Physics B (Lasers and Optics)*, B64(3): 273 – 91, 1997.

[29] K. Buse, S. Breer, K. Peithmann, S. Kapphan, M. Gao, and E. Kratzig. Origin of thermal fixing in photorefractive lithium niobate crystals. *Physical Review B (Condensed Matter)*, 56(3):1225 – 35, 1997.

[30] S. Kim, V. Gopalan, K. Kitamura, and Y. Furukawa. Domain reversal and nonstoichiometry in lithium tantalate. *Journal of Applied Physics*, 90(6):2949 –, 2001.

[31] A. M. Glass. Dielectric, thermal , and pyroelectric properties of ferroelectric $LiTaO_3$. *Physical Review*, 172:564–571, 1968.

[32] A. Savage. Pyroelectricity and spontaneous polarization in $LiNbO_3$. *Journal of Applied Physics*, 37(8):3071–3072, 1966.

[33] Tesfaye Gebre, Ashok K. Batra, Padmaja Guggilla, Mohan D. Aggarwal, and Ravindra B. Lal. Pyroelectric properties of pure and doped lithium niobate crystals for infrared sensors. *Ferroelectrics, Letters Section*, 31(5-6):131 – 139, 2004.

[34] E.M. Bourim, C.-W. Moon, S.-W. Lee, and In Kyeong Yoo. Investigation of pyroelectric electron emission from monodomain lithium niobate single crystals. *Physica B*, 383(2):171 – 82, 2006.

[35] G.I. Rozenman. Photoinduced exoemission from lithium niobate. *Soviet Physics - Solid State*, 30(8):1340 – 2, 1988.

[36] U. Schlarb and K. Betzler. Refractive indices of lithium niobate as a function of wavelength and composition. *Journal of Applied Physics*, 73(7):3472 –, 1993.

[37] I.P. Kaminow and J.R. Carruthers. Optical waveguiding layers in $LiNbO_3$ and $LiTaO_3$. *Applied Physics Letters*, 22(7):326 – 8, 1973.

[38] J.R. Carruthers, I.P. Kaminow, and L.W. Stulz. Diffusion kinetics and optical waveguiding properties of outdiffused layers in lithium niobate and lithium tantalate. *Applied Optics*, 13(10):2333 – 42, 1974.

[39] K. Sugii, M. Fukuma, and H. Iwasaki. A study of titanium diffusion into $LiNbO_3$ waveguides by electron probe analysis and X-ray diffraction methods. *Journal of Materials Science*, 13(3):523 – 33, 1978.

[40] J. L. Jackel, C. E. Rice, and J. J. Veselka. Proton exchange for high-index waveguides in $LiNbO_3$. *Applied Physics Letters*, 41(7):607–608, 1982.

[41] R. A. Becker. Comparison of guided-wave interferometric modulators fabricated on $LiNbO_3$ via Ti indiffusion and proton exchange. *Applied Physics Letters*, 43(2): 131–133, 1983.

[42] C. S. Tsai, D. Y. Zang, and P. Le. Acousto-optic bragg diffraction in a $LiNbO_3$ channel-planar composite waveguide with application to optical computing. *Applied Physics Letters*, 47(6):549–551, 1985.

[43] U. Hempelmann, H. Herrmann, G. Mrozynski, V. Reimann, and W. Sohler. Integrated optical proton exchanged tm-pass polarizers in $LiNbO_3$: modelling and experimental performance. *Lightwave Technology, Journal of*, 13(8):1750–1759, 1995.

[44] B.-E. Benkelfat, R. Ferriere, B. Wacogne, and P. Mollier. Technological implementation of bragg grating reflectors in Ti:$LiNbO_3$ waveguides by proton exchange. *Photonics Technology Letters, IEEE*, 14(10):1430–1432, 2002.

[45] D.P. Morgan. History of SAW devices. *Proceedings of the 1998 IEEE International Frequency Control Symposium (Cat. No.98CH36165)*, pages 439 – 60, 1998.

[46] X. Q. Bao, W. Burkhard, V. V. Varadan, and V. K. Varadan. SAW temperature sensor and remote reading system. *Ultrasonics Symposium Proceedings*, pages 583 – 585, 1987.

[47] T. Nomura, K. Oofuchi, T. Yasuda, and S. Furukawa. SAW humidity sensor using dielectric hygroscopic polymer film. *Proceedings of the IEEE Ultrasonics Symposium*, 1:503 – 506, 1994.

[48] J. Hechner, W. Soluch, and T. Wrobel. Methods of harmful effects limitation in SAW gas sensors. *Proceedings of the 1999 Joint Meeting of the European Frequency and Time Forum and the IEEE International Frequency Control Symposium (Cat. No.99CH36313)*, vol.2:1078 – 81, 1999.

[49] S.G. Joshi. Surface-acoustic-wave (SAW) flow sensor. *IEEE Transactions on Ultrasonics, Ferroelectrics and Frequency Control*, 38(2):148 – 54, 1991.

[50] Chi-Yen Shen, Yu-Tang Shen, and R.S. Horng. Chemical sensors using surface acoustic wave devices on proton-exchanged $LiNbO_3$. *1998 IEEE Ultrasonics Symposium. Proceedings (Cat. No. 98CH36102)*, vol.1:501 – 4, 1998.

[51] C.J. Strobl, Z. von Guttenberg, and A. Wixforth. Nano- and pico-dispensing of fluids on planar substrates using SAW. *IEEE Transactions on Ultrasonics, Ferroelectrics and Frequency Control*, 51(11):1432 – 6, 2004.

[52] Kiyoshi Nakamura and Hiroshi Shimizu. Local domain inversion in ferroelectric crystals and its application to piezoelectric devices. *Ultrasonics Symposium Proceedings*, 1:309 – 318, 1989.

[53] K. Nakamura and H. Shimizu. Hysteresis-free piezoelectric actuators using $LiNbO_3$ plates with a ferroelectric inversion layer. *Ferroelectrics*, 93:211 – 16, 1989.

[54] M. Ueda, H. Sawada, A. Tanaka, and N. Wakatsuki. Piezoelectric actuator using a $LiNbO_3$ bimorph for an optical switch. *IEEE 1990 Ultrasonics Symposium Proceedings (Cat. No.90CH2938-9)*, pages 1183 – 6, 1990.

[55] Hideki Yokoyama, Subaru Kudo, and Noboru Wakatsuki. Suppression of mechanical resonances of $LiNbO_3$ actuator with oppositely-polarized layers. *Japanese Journal of Applied Physics, Part 1: Regular Papers and Short Notes and Review Papers*, 38 (5 B):3334 – 3337, 1999.

[56] T Jungk, A Hoffmann, and E Soergel. Quantitative analysis of ferroelectric domain imaging with piezoresponse force microscopy. *Applied Physics Letters*, 89 (16):163507 –, 2006.

Chapter 2

Hydrophilic Surface Activation With Low Intensity UV Laser Light

2.1 Background and Motivation

Chapter 1 introduced LN as a material that has found many uses in the optoelectronics industry due to its large electro-optic, acousto-optic and non-linear coefficients. In many instances there is a requirement to perform a functionalisation of the surface such that further processing steps can be carried out [1–3] or to control an interaction of the crystal with a fluid in a finalised device [4]. Wafer bonding has been seen to be an important process in LN for either creating large area PPLN devices for power scaling [5], waveguide structures [2, 3, 6] and as an etch-stop for topographical structuring [1]. This has been carried out between LN wafers by functionalising the surface with solutions such as $NH_4OH + H_2O_2 + H_2O$[1–3, 6] which make the surface hydrophilic such that the hydrophilic-hydrophilic attraction can bond the wafers. This technique has been shown to not only bond wafers of differing doping [6] but also of different crystals such as LN to lithium tantalate (LT) [3] or even LN to GaAs [7]. Creation of structured hydrophobic surfaces has been achieved through depositing monolayers such as octadecyltrichlorosilane [4]. The structuring of these surface functionalisations, whether hydrophilic or hydrophobic, is currently achieved through the multiple processing steps of photolithography that may disrupt or further complicate the construction of other device components. The hydrophilic-hydrophilic attraction is not limited to planar macroscopic surfaces but also occurs between particles with hydrophilic surfaces. Thus a structured hydrophilic surface can form a template for attachment of hydrophilic, or

hydrophilic coated, particles such as many nano-particles or even biological molecules and cells.

In this chapter we show that it is possible to achieve a change of the inherent wetting properties of the crystal surface simply by exposing it to ultraviolet (UV) radiation at photon energies exceeding the band gap of the material. The surface energy of the crystal is seen to increase greatly such that the surface becomes super-hydrophilic. The change in the hydrophilicity of the surface is first investigated in section 2.2 using the contact angles of sessile drops of de-ionised (DI) water to characterise the effect in terms of the incident laser intensity and the exposure environment. In section 2.3 the use of the hydrophilicity change is investigated for the application of structured spreading of liquids as a novel deposition technique and in section 2.4 the hydrophilicity is structured on the micron and sub-micron scale for possible applications in the deposition of nano-particles or biological molecules or applications in environmental or chemical sensing.

2.2 Macro-scale Sessile Drop Contact Angle Investigation

2.2.1 Experimental Details

Experiments characterising the hydrophilicity change using sessile water drops have been carried out using a range of different lasers (with wavelengths (λ) of 244 nm, 248 nm and 266 nm) which were either pulsed, with pulse durations ranging from 130 fs to 20 ns, or continuous wave. Ultrafast laser exposures were carried out at $\lambda = 266$ nm using the third harmonic of a Coherent Mira oscillator - Legend amplifier system. The laser beam (pulse duration 130 fs, repetition rate 1 kHz) was expanded to give an energy fluence of 0.045 mJ cm^{-2} per pulse. Nanosecond laser exposures were carried out at $\lambda = 266$ nm (fourth harmonic of a Nd:YVO_4 laser, 20 ns pulse duration, 20 Hz repetition rate) and $\lambda = 248$ nm (KrF laser, pulse duration 20 ns, repetition rate 10 Hz). The $\lambda = 266$ nm beam was expanded to give an energy fluence of 2 mJ cm^{-2} per pulse and the $\lambda = 248$ nm beam was truncated by a 6 mm by 6 mm square aperture to give an energy fluence at the sample of 40 mJ cm^{-2} per pulse. The exposures using the femtosecond and nanosecond lasers were carried out under ambient laboratory conditions.

The continuous wave exposures were carried out at $\lambda = 244$ nm using a frequency doubled argon ion laser, and the slightly elliptical beam provided by the laser was expanded to give a spot with a major axis of 12 mm and minor axis of 10 mm. Exposures were carried out over a range of incident powers from 10 mW to 60 mW in an environmental chamber which provides a controlled environment of pressure, temperature and atmosphere. Large glass windows enabled optical monitoring of the surface for the contact

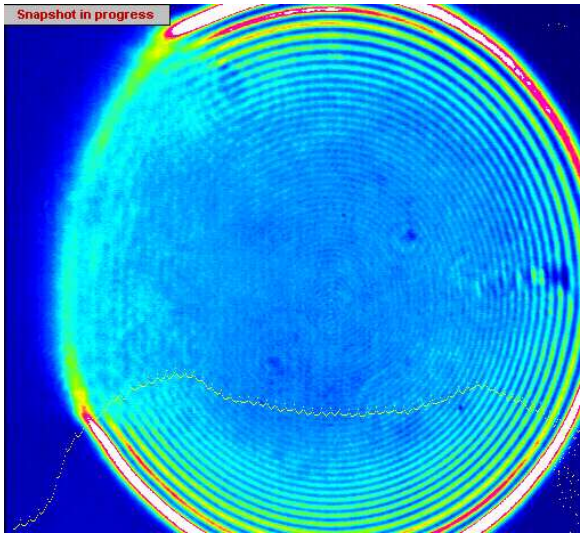

FIGURE 2.1: Beam profile of the continuous wave laser after expansion and spatial modulation through Fresnel diffraction of the lens aperture.

angle measurements. The UV illumination of the samples was performed through a fused silica window and the exposure time was controlled by a computer-controlled shutter.

The spatial profile of the beam is an important factor when considering the spreading of sessile drops since the contact angle is a function of the local surface energy at the contact line of the drop. The surface energy change is also a local function of the intensity and so as the contact angle decreases the contact line will move further into the lower intensity wings of the beam. The profile of the KrF laser beam was highly homogeneous, since only a small portion of the whole beam was used, the beams of the femtosecond laser and the nanosecond Nd:YVO_4 laser had Gaussian profiles. The beam from the continuous wave laser was expanded using a two lens arrangement which expanded the beam at the second lens to greater than the lens diameter. Thus Fresnel diffraction from the aperture formed by the lens occurred and was seen to increase the intensity at the edge of the beam. This had the effect that at very low contact angles, where the lateral size of the drop becomes large, the contact line is pinned at the high intensity edge. The beam profile from the continuous wave laser is shown in figure 2.1.

After UV exposure a 0.5 μl drop of de-ionised (DI) water was immediately placed on the surface and the drop profile was imaged and captured using a CCD camera. The contact angle was measured using ImageJ image analysis software[1] and the BIG Drop Shape Analysis plug-in[2].

[1]Image J: http://rsb.info.nih.gov/ij/
[2]Drop shape analysis plug-in: http://bigwww.epfl.ch/demo/dropanalysis/

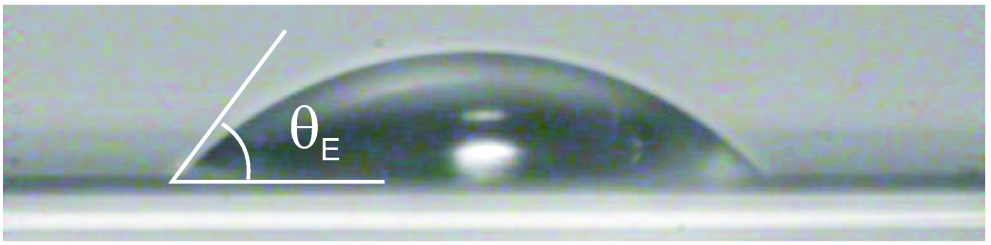

(a) Contact angle of a drop on an un-illuminated surface.

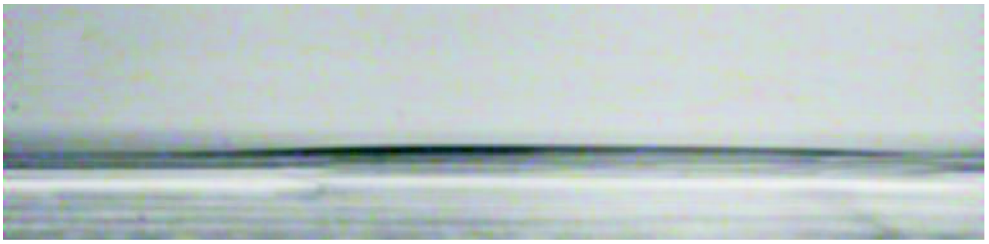

(b) A drop that has wetted the LN surface after exposure to UV light.

FIGURE 2.2: Effect of the contact angle (θ_E) of a DI water sessile drop on LN after exposure to UV light.

2.2.2 Results and Discussion

Figure 2.2 shows the effect of UV irradiation upon the contact angle of a sessile drop and defines the contact angle, θ_E, as the angle between the substrate surface and the tangent to the drop profile at the line where the solid, liquid and vapour phases meet. Figure 2.2(a) shows a drop of DI water on an un-illuminated surface and figure 2.2(b) shows a drop of the same volume on a pre-illuminated surface. After sufficient illumination, the contact angle of the drop decreases to a super-hydrophilic state ($\theta_E < 5°$) and the surface approaches complete wetting ($\theta_E = 0°$). As can be seen in figure 2.2(b), determination of the drop contact line becomes difficult at low contact angles with the visualisation method used here. Due to this difficulty, and subsequent high degree of error, such low contact angles, although observed, shall not be reported.

All lasers used were seen to produce a change in the hydrophilicity. The $\lambda = 244$ nm laser was chosen for the bulk of the investigation because of the superior quality of its beam profile. Exposures were carried out on both the positive and negative z faces but no significant difference in their behaviour was found.

Figure 2.3 shows the variation of the water contact angle on the $+z$ face as a function of exposure time with $\lambda = 244$ nm exposure, for powers (measured before the fused silica window of the chamber) of 10 mW (open circle), 20 mW (filled circle) and 60 mW (triangle). The exposures were carried out at a temperature T = 27 °C and relative humidity of 55 %. It can be seen from the figure that the contact angle change is not a

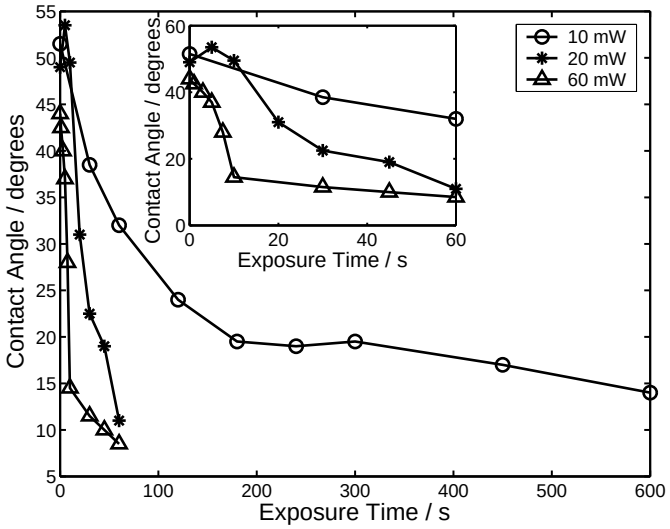

FIGURE 2.3: Change in water contact angle with increasing 244 nm exposure time for powers incident at the chamber of 10 mW, 20 mW and 60 mW. Insert shows an expanded view of the first minute. Lines added to guide the eye.

linear function of the total exposure, i.e. the integrated number of photons arriving at the surface, since doubling the incident power does not simply halve the time required to reach a given contact angle. Rather it is seen that the change is a function of both the total exposure and the incident intensity with higher intensities giving a greater change for equivalent exposure.

Charging of the surface was not seen to be a cause of contact angle change. Figure 2.4 shows the application of a 1μl drop of DI water to the surface of a sample which has been rinsed with acetone and blown dry with compressed air immediately before application. Due to the pyroelectric nature of LN the rapid cooling from the quickly evaporated acetone causes the surface to be strongly charged as can be seen by the strong attraction of the water droplet causing the drop to elongate toward the sample. Upon contacting the sample, however, no significant hydrophilicity is seen. This shows that surface charging is not the cause of the UV induced hydrophilicity. This attraction and deformation of a suspended drop toward the surface is also seen after exposures to UV in vacuum where no change to the contact angle is seen. The dependence of contact angle to atmospheric conditions will be described below.

The contact angle of olive oil was also measured before and after UV exposure however the surface was not seen to become oleophilic since no change in the contact angle was seen even after an exposure of 30 mW for 10 minutes. Prior to application, the drop was strongly pulled toward the sample, which was probably due to the photo-induced surface charging, however upon contacting the surface no significant change in contact angle was seen.

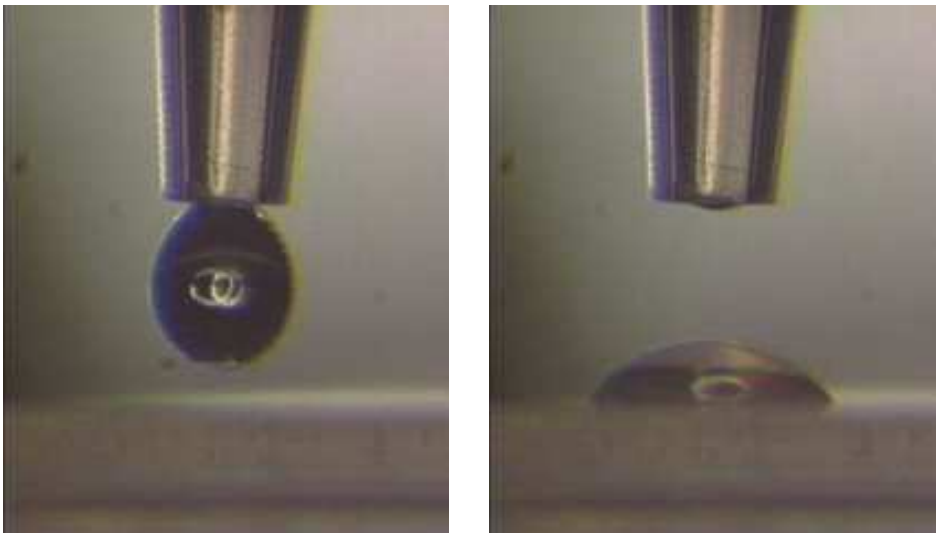

(a) A 1μl drop is strongly pulled toward the charged surface as can be seen by the drop elongation.

(b) Resultant contact angle of drop is not significantly changed by surface charging.

FIGURE 2.4: Effect of UV exposure on the wetting of LN by olive oil.

The atmosphere was observed to have a pronounced effect upon the hydrophilicity change. It was found that when illuminating with the chamber having been evacuated to a pressure of less than 2 mbar, no significant change to the contact angle was observed even for long exposures (15 minutes) at 45 mW. The humidity of the chamber during exposure was also seen to greatly influence the change in hydrophilicity, with a lesser effect occurring in dryer atmospheres. The relative humidity at constant temperature was lowered within the chamber by purging with dry nitrogen or increased by bubbling air through de-ionised water and measured with a thermohygrometer. The ambient relative humidity in the lab was 38 %. The samples were then illuminated under the desired humidity and then returned to atmospheric conditions for the contact angle measurement. As the humidity was increased the change in contact angle was greater for the same exposure. To keep the contact angle large enough to be measureable the exposure time was decresed as the humidity increased. This means that the change in the contact angle needs to be normalised in some way for analysis. Youngs equation relates the surface energies at the solid-liquid and solid-vapor interfaces to the contact angle of the three phase system as

$$\gamma_{lv}\cos(\theta_E) = \gamma_{sv} - \gamma_{sl} \tag{2.1}$$

where γ is the interfacial energy and the subscripts lv, sv and sl correspond to the liquid-vapor, solid-vapor and solid-liquid interfaces respectively. Since γ_{lv} is a property of the liquid alone, a change in the contact angle will come about only from a change

in $(\gamma_{sv} - \gamma_{sl})$. If it can be assumed that the rate of change of this quantity with UV exposure time is constant within our experimental conditions then so too will be $\cos(\theta_E)$ such that

$$\frac{d\ cos(\theta_E)}{dt} = \kappa(RH) \tag{2.2}$$

where κ is dependent upon the relative humidity (RH) and describes the strength of the contact angle change. This leads to

$$\kappa(RH) = \frac{cos(\theta_E) - cos(\theta_E(t=0))}{t} \tag{2.3}$$

where $\theta_E(t=0)$ is the contact angle of unexposed lithium niobate and t is the exposure time. Figure 2.5 shows the variation of the parameter $\kappa(RH)$ with relative humidity for exposures on the $+z$ face. The error was calculated from the standard deviation (σ) of repeated readings of the contact angle on cleaned unexposed samples, yielding a value of $\sigma = 2.8°$. Due to the large number of samples and exposures required to get error estimates over the full range of contact angles, it is assumed that the error is constant. In reality it is likely that the measurement error will increase with decreasing contact angle, but that the reproducibility will increase due to the lesser effect of deformations of the drop by the pipettor causing contact line pining. It can be seen in the figure that there is a linear trend, with the change in surface energy being proportional to the number of water molecules present in the atmosphere. The continuation of the trend beyond the ambient humidity, when nitrogen purging was no longer required, indicates that the decrease in UV sensitivity with lowering humidity is indeed due to a reduction in atmospheric water and not due to the displacement of other species by the nitrogen. The value at 95 % RH may be reduced due to condensation present upon the sample surface.

In order to study the recovery of the contact angle after exposure a number of samples were exposed at 45 mW for 60 s and then stored individually in polypropelene tubs in the dark. Figure 2.6 shows that the recovery to the initial contact angle takes around 20 days and that the recovery is not a linear function of time but proceeds at a continuously decreasing rate. If the surface energy change is due to the adsorption of water molecules on the crystal surface, as the humidity dependence suggests, and the thermal desorption of these molecules is a random process with constant probability, then the decay of the surface energy as measured by the cosine of the contact angle should be well modeled by an exponential decay. The decay of the cosine of the contact angle is shown in figure 2.7 with the best fit of the form $y = y_0 + y_1 \times exp(-t/\tau)$. The curve fits well and gives a value of $y_0 = 0.62$ corresponding to a final contact angle of 51.6° which is well within the range of measured unexposed contact angles. The other fit parameters are $y_1 = 0.37$ and $\tau = 2$ days.

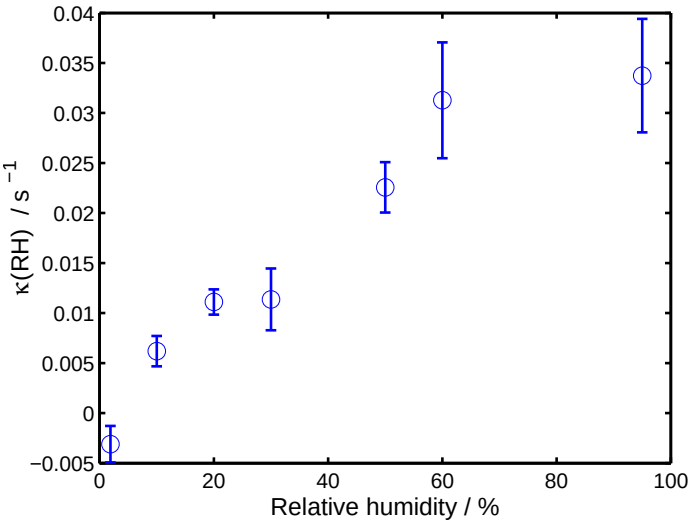

FIGURE 2.5: Change in the parameter $\kappa(RH)$, which describes the strength of the contact angle change, with relative humidity for exposures on the $+z$ face. Errors are calculated from an error in θ of $\pm 2.8°$. (Laser power P = 45 mW).

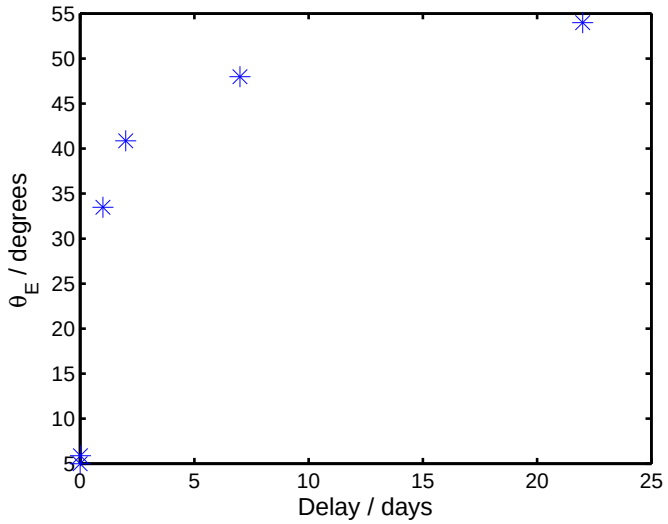

FIGURE 2.6: Recovery of the contact angle with time after exposure at 45 mW for 60 s.

From the observed dependence on humidity of the contact angle change after UV exposure it is proposed that the enhanced hydrophilicity is due to dissociative adsorption of atmospheric water onto photo-induced defects creating (hydrophilic) surface hydroxyl groups. The band gap of LN is determined primarily by the properties of the NbO_6 octahedra since the upper level of the valence band is formed by the oxygen electron 2p states while the lower level of the conduction band is formed by the d orbitals of the niobium ion [8]. Photons of energy approximately that of the band gap will thus be absorbed to create an electron-hole pair bound to a niobium and oxygen ion respectively.

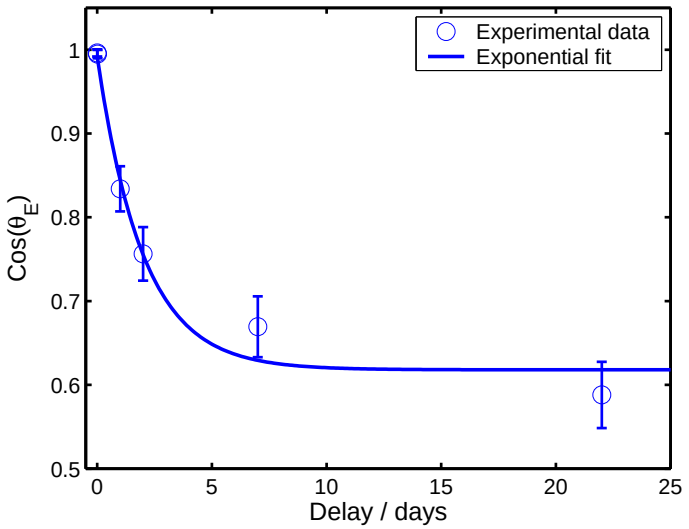

FIGURE 2.7: Decay of the cosine of the contact angle with time after exposure at 45 mW for 60 s. Errors are calculated from a constant error in θ of $\pm 2.8°$.

The dissociative adsorption will then proceed as follows [9]

$$\begin{aligned} Nb^{5+} + O^{2-} + h\nu &\rightarrow Nb^{4+} + O^{-} \\ Nb^{4+} + O^{-} + H_2O &\rightarrow Nb^{4+}O^{2-}H^{+} + O^{-}H^{+}. \end{aligned} \tag{2.4}$$

The reaction above is similar to that proposed for the UV induced hydrophilicity of TiO_2 [10, 11] and ZnO [12] by Watanabe and Hashimoto et al. Indeed the band structure of LN is similar to the band structure of TiO_2 since the main building blocks of each crystal are the BO_6 oxygen octahedra with the band gap of TiO_2 being formed by O 2p orbitals and Ti 3d orbitals and so one may expect the behaviour to be similar for $h\nu > E_g$ exposure. This simple hypothesis is, however, shown to be false in [13] where it is shown that $SrTiO_3$ has no UV-induced hydrophilic conversion despite being an ABO_3 oxygen-octahedral dielectric such as LN and having a band structure similar to both LN and TiO_2. One difference between $SrTiO_3$ and LN however is the stacking of the BO_6 octahedra; $SrTiO_3$ is a perovskite type dielectric that contains corner-sharing oxygen octahedra whereas the LN oxygen octahedra are face-sharing. The octahedra in TiO_2 are also face-sharing and so this may be another requirement for the hydrophilic conversion process. In [14] the origin of the UV-induced hydrophilic conversion in TiO_2 proposed by Watanabe and Hashimoto is disputed and attributed solely to the photocatalytic decomposition of organic contaminants which exposes the inherently hydrophilic TiO_2 surface. Although LN also shows a high photocatalytic activity under UV irradiation [15] our results concerning the humidity dependence of the contact angle change and the fact that no change occurs under vacuum do not support this hypothesis since we see no reason why the photocatalytic decomposition would not occur under these conditions

also. In comparison to the hydrophilic conversion in TiO_2 we find that the contact angle change in LN proceeds at a greater rate at the intensities used in this investigation. In [12] the contact angle change from the initial angle of 54° to 10° is seen to take around 5 minutes for a UV intensity of 50 mW cm^{-2} ($\lambda = 365$ nm) whereas we see in figure 2.3 that for an exposure of around 20 mW cm^{-2} the change from 55° to 10° is made in just 30 s ($\lambda = 244$ nm). In [14] the change from the initial contact angle (80°) to 15° is seen to take around 18 minutes for a UV exposure of 13.6 mW cm^{-2} ($\lambda = 254$ nm) with an initial slope of 4 ° min^{-1} whereas in figure 2 we see that for an intensity of around 10 mW cm^{-2} the change from 55° to 15° takes around 10 minutes with an initial slope (t < 200 s) of around 13° min^{-1}.

2.3 Structured Spreading

It has been shown in the previous section that after illumination with UV laser light, the surface of LN will become increasingly hydrophilic and a liquid drop will spread until the equilibrium contact angle, which may be zero for high UV doses, is reached. Thus if a drop of liquid is placed over an irradiated path, rather than a large region, the water will spread along the path until the equilibrium contact angle is reached. This may have application in the selective deposition of either liquid or solid substances (through evaporation of a carrier liquid) onto the LN surface.

2.3.1 Experimental Details

A computer-controlled stage system was used in conjunction with the frequency doubled argon ion continuous wave laser and the Nd:YVO_4 pulsed laser to translate the sample in the plane perpendicular to a focussed beam, thereby inscribing two dimensional paths of increased hydrophilicity across the surface. The KrF laser was used with a stencil to essentially print the path onto sample. This could only be done with the KrF laser due to its high energy per pulse and large beam spot size. The spreading behaviour of the water was recorded using a CCD camera and a computer video capture card.

The focusing control of the continuous wave laser was far greater than that of the Nd:YVO_4 pulsed laser and so this was used to create straight lines of varying width to identify the dimensions over which spreading would occur. The exposure of the irradiated regions was kept constant and so, for a given beam power, the velocity decreased as the beam spot size increased.

The Nd:YVO_4 pulsed laser was used to examine the qualitative behaviour of spreading along different path geometries with a beam spot diameter of around 1 mm as estimated

by eye. The path shapes investigated were cosine s-bends, cross-hatches, fans, square corners, and the ORC light logo, although only results from the square corners and s-bends will be shown here.

2.3.2 Results and Discussion

The patterned irradiation of the LN surface through the translation of a focused beam in the case of the frequency doubled argon ion continuous wave and Nd:YVO_4 pulsed lasers or the irradiation through a stencil in the case of the KrF laser did result in spreading along the written paths. Although the fluences used should have resulted in complete wetting, on many occasions the wetting film remained at a macroscopic thickness and did not spread across the whole of the treated path as may be expected. An array of cosine s-bends was written onto the LN surface following the pattern shown in figure 2.8 where the offset of the curve labelled 1 was 2 mm and the curve labelled 4 was a straight line. A drop of water was then applied to one end of each s-bend and the spreading of the drop was captured using a CCD camera. Figure 2.9 shows a comparative time series of the wetting of curves 1 and 4 with the wetting of curve 4 being shown uppermost in each subfigure. The time t=0 is given by the point at which the drop touches the surface in each application, thus figure 2.9 can be used to compare the velocity of the spreading drop in each case. It can be seen that the spreading along the bend of higher curvature was faster than that along the straight line since after 560 ms the drop on the straight line has not yet reached the end. Figure 2.10 shows the final spreading of the entire array in greater detail. It can be seen that the height of the deposited liquid track is not constant along the length of tracks 3 and 4 as may be expected for a final equilibrium state. However, at this volume scale, the drop shapes are determined by mainly surface energies and hydrostatic forces and not gravity, and so it is not inevitable that the the final spreading height should be constant. The remnant of the initial drop then remains on bends 3 and 4 since the contact line is pinned outside of the track. In tracks 1 and 2, where the spreading was more energetic, the contact line of the initial drop has been pulled inward to the exposed track. This relation between the size of the initial drop, the strength of the spreading and the size of any remnant will be important when considering deposition applications. The spreading co-efficient that describes the non-equilibrium wetting behaviour is given by [16]

$$S = \gamma_{so} - \gamma_{sl} - \gamma_{lv} \tag{2.5}$$

where γ_{so} is the energy associated with a 'dry' solid surface, γ_{sl} is the energy of the solid-liquid interface and γ_{lv} is the energy of the liquid-vapor interface. This shows that greater spreading will occur with a greater change to γ_{so} which we would expect

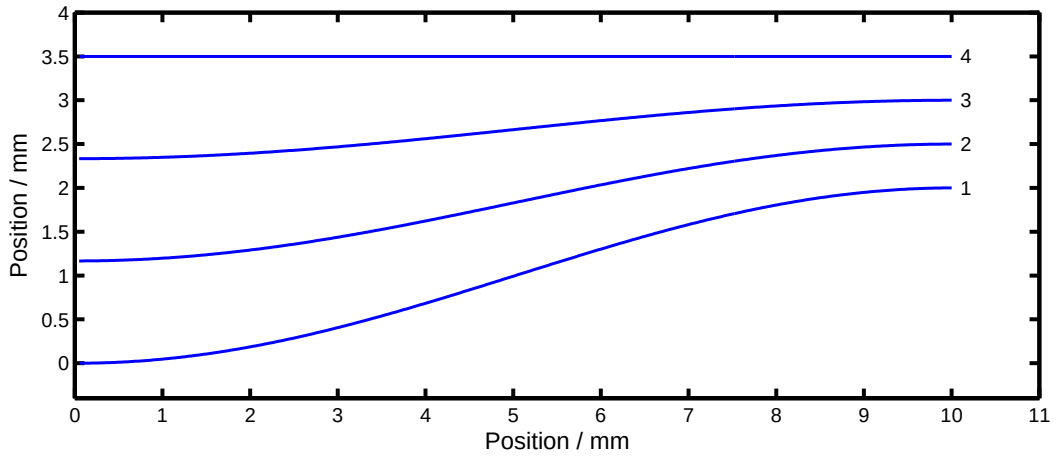

FIGURE 2.8: Diagram of the s-bend array exposure pattern.

to be a function of dwell time if saturation is not yet reached. This is believed to be the cause of the greater spreading in figure 2.9 at higher radii of curvature since the translation stages were required to make more changes to the velocity hence lowering the average speed and increasing the fluence. It was expected that the greater radii of curvature would have reduced the speed of the spreading drop due to inertial effects. The spreading of liquid films along pre-exposed tracks was not restricted to patterns with smoothly varying bends but also could flow around tight corners as can be seen in figure 2.11 in which water from the drop in the lower left hand corner has spread around two ninety-degree corners before finally coming to rest.

The width of the wetting strip was greater than the radius of the writing beam in all cases. This would be expected for two reasons. Firstly, the beams used to write the strips were not step-like top-hat beams but rather had an almost Gaussian profile. This would mean that there was not a sharp interface at the spot diameter and since the unexposed area is not hydrophobic (contact angle greater than 90 degrees) the initial drop will spread laterally some distance into the unexposed region before much of the volume can spread along the written path. The second consideration is for cases where the initial drop has a diameter greater than the exposed path. The typical writing spot radius was 1-2 mm and the drop volumes used in the initial wetting of the structure were 2-5 μl. The diameter of a spherical drop of volume 2 μl is 1.6 mm and the diameter of a 5 μl drop is 2.1 mm. The diameter of the pendant drop emerging from the syringe would not be too far from this and so it is likely that the initial drop was larger than the diameter of the structure in many cases. When this is the case, for spreading to occur only along the irradiated path it would be necessary to reduce the radius of curvature of the contact line within the path. The contact line has a tension and hence energy associated with it that increases with decreasing radius of curvature [17, 18] and so it

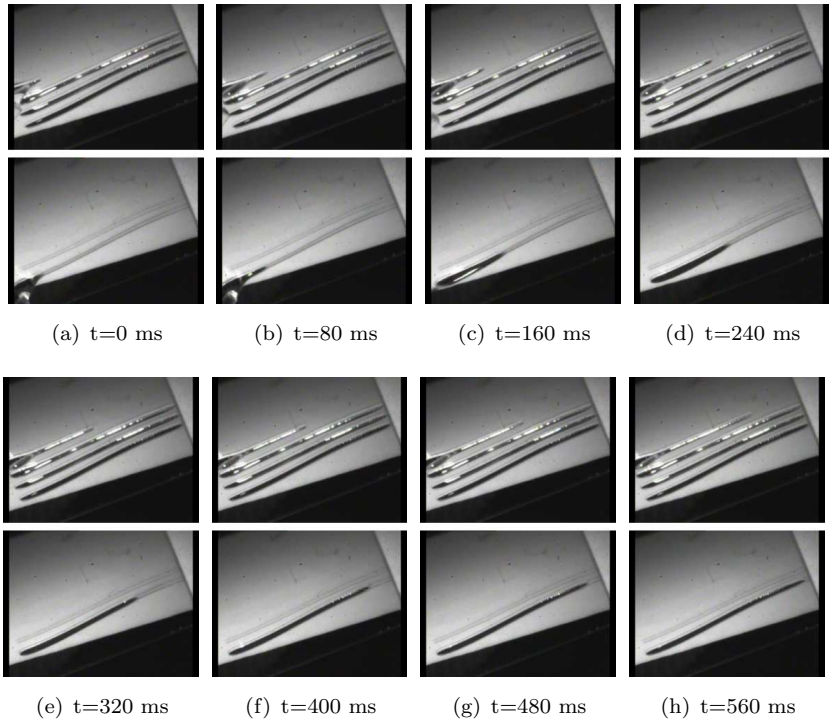

(a) t=0 ms (b) t=80 ms (c) t=160 ms (d) t=240 ms

(e) t=320 ms (f) t=400 ms (g) t=480 ms (h) t=560 ms

FIGURE 2.9: Time series comparison of the wetting of cosine s-bends 1 (lower frame of each subfigure) and 4 (upper frame of each subfigure).

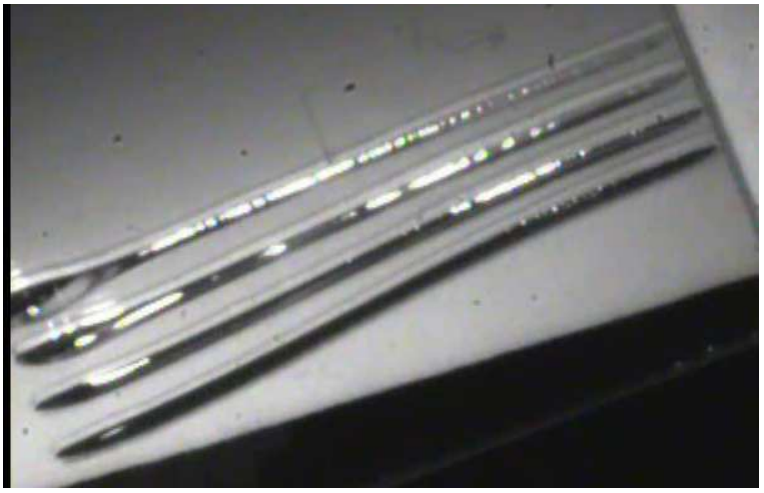

FIGURE 2.10: Screen capture from film of drop spreading on irradiated cosine s-bend patterns. The spreading speed increased with curvature, possibly due to increased fluence.

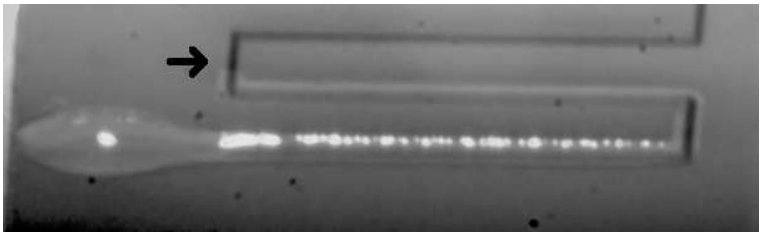

FIGURE 2.11: Screen capture from film of drop spreading on a scanned pattern with sharp corners. Arrow indicates point at which spreading stopped.

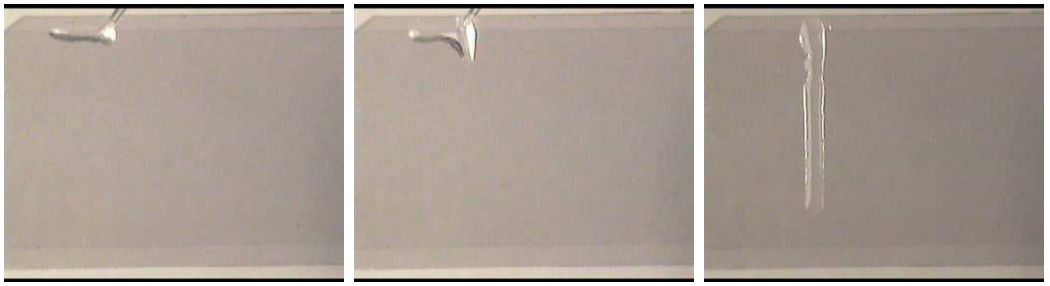

(a) No Spreading along 10 - 500 μm tracks.

(b) Drop begins to spread along 1 mm track.

(c) Drop spreads along 1 mm track, pulling water from non-irradiated area.

FIGURE 2.12: Screen captures from film of drop spreading on irradiated tracks of constant exposure but varying width. Spreading only occurred for the track with width approximately equal to the drop diameter.

may be energetically favourable to spread partly on the untreated region. Figure 2.12 shows a sample written at 244 nm composed of parallel lines written with equal exposure (obtained by varying both power and scan velocity) for beam diameters ranging from 10 μm to 1 mm. Spreading of a 2 μl drop only occurred for the line of diameter 1 mm. Deformations of the contact line of the sessile drop at the other lines were seen where part of the contact line was pulled but the energy gained by wetting the higher energy surface was not great enough to encourage complete wetting along the line.

2.4 Micro-scale Structured Surface wettability

Having investigated the behaviour of the UV induced hydrophilicity in LN, spatial structuring of the surface hydrophilicity, and thus wetting properties, was investigated also for possible application in micro-fluidic devices and sensors.

2.4.1 Experimental Details

Patterning on the micron scale was achieved by the use of transmission electron microscopy (TEM) hexagonal grids as absorption masks. The grids had hexagonal openings with a diameter of 40 μm (between parallel sides) at a periodicity of 60 μm. The grid was attached to the surface of the sample which was subsequently illuminated under ambient conditions with $\lambda = 244$ nm light from the frequency doubled argon ion laser.

Patterning at the sub-micron scale was achieved either through exposure with an interference pattern of two overlapping beams from the $\lambda = 266$ nm Nd:YVO_4 laser or by using a phase mask.

Exposures using phase masks were carried out with both the Nd:YVO_4 ($\lambda = 266$ nm) pulsed source and the $\lambda = 244$ nm c.w. source. The phase mask exposures were performed under the same conditions used in the sessile drop experiments. The phase mask used for the $\lambda = 244$ nm exposures had a period of 1136 nm and the masks used for the $\lambda = 266$ nm exposures had a period of 1076 nm. The beams used in both cases were divergent and not critically aligned. As such much of the zeroth order diffracted beam was present, which caused modulation of the light intensity pattern at the phase mask period due to interference between the zeroth and first orders as well as at half of this value due to interference of the two first order beams.

Visualisation of the patterning was achieved through the preferential creation of dew on the exposed areas by cooling the sample in a stream of humid air and visualising the dew pattern directly using a microscope. The existence of structures was also inferred from diffraction of a He-Ne laser beam from the grating formed by the dew.

2.4.2 Results and Discussion

Figure 2.13 shows an optical microscope image of the condensation formed on the +z face after an exposure through the TEM grid ($\lambda = 244$ nm, 45 mW for 2 minutes). The sample was cooled by a thermoelectric heat pump to a temperature close to the dew point. The hexagonal lattice which corresponds to the TEM grid pattern can clearly be seen as water vapour from the air preferentially condenses onto the exposed areas. Areas of significant condensation appear darker in the figure whilst dry areas remain bright. For these exposure conditions the condensation mechanism is seen to be dropwise rather than filmwise.

Figure 2.14(a) shows an optical microscopy image of the preferential condensation of water vapor onto a lithium niobate surface exposed with interfering beams from the

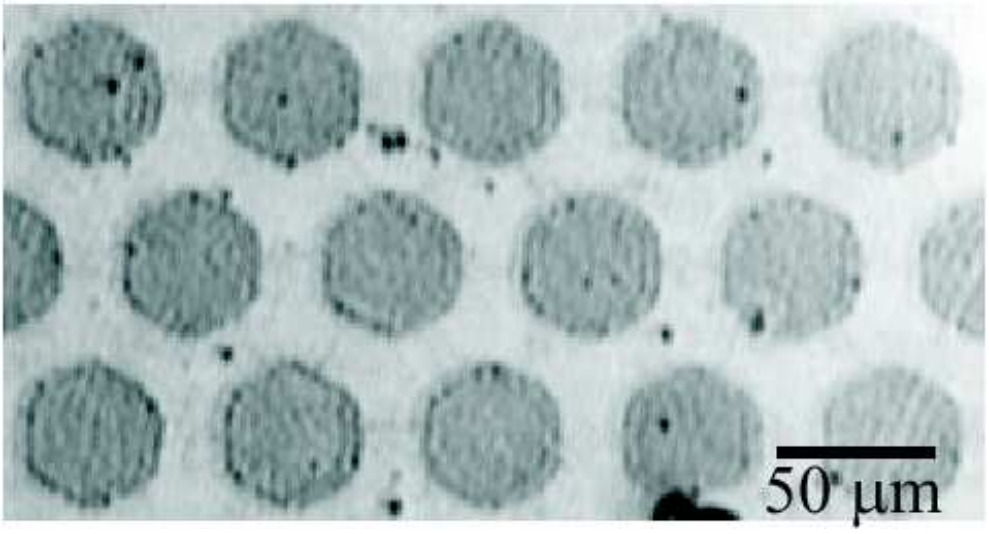

FIGURE 2.13: Condensation pattern formed after cooling in a humid atmosphere. Sample exposed through a TEM grid.

Nd:YVO_4 laser. The areas where water is condensing appear dark due to scattering while dry areas appear bright. In this instance it can be seen that the condensation mechanism appears to be filmwise as no discernible drop shapes are present in the condensing areas of the grating pattern. Whether the condensation proceeds as discreet drops or films depends upon the hydrophilicity change that has occurred upon the surface with filmwise condensation occurring for a completely hydrophilic surface ($\theta_E = 0$). Since the interfering beams have a Gaussian intensity profile however, it is possible to view a wide range of illuminating conditions on the same illuminated spot. For example, the microscope image of figure 2.14(b) shows the condensation formed in an area corresponding to lower intensity where the surface does not wet completely and so drops of condensation form. The contrast of the image has been enhanced for clarity and the preferential formation of the drops along the lines of the illuminating interference pattern can be seen clearly.

Diffraction of a He-Ne laser beam ($\lambda = 633$ nm) was also seen from the sub-micron structured surfaces due to spatially resolved condensation. The phase mask illuminations create interference patterns with periods of 1136 nm and 1076 nm for $\lambda = 244$ nm and $\lambda = 266$ nm illumination respectively giving feature sizes of the hydrophilic patterning of 500 nm. The probe laser beam was incident normally on the sample surface and the diffracted light was measured in transmission. The angles of the first diffracted order in each case were found to be 35.4° for the 1076 nm period mask and 33.9° for the 1136 nm period mask which are within measurement error of the theoretical values of 36.0° and 33.9° respectively.

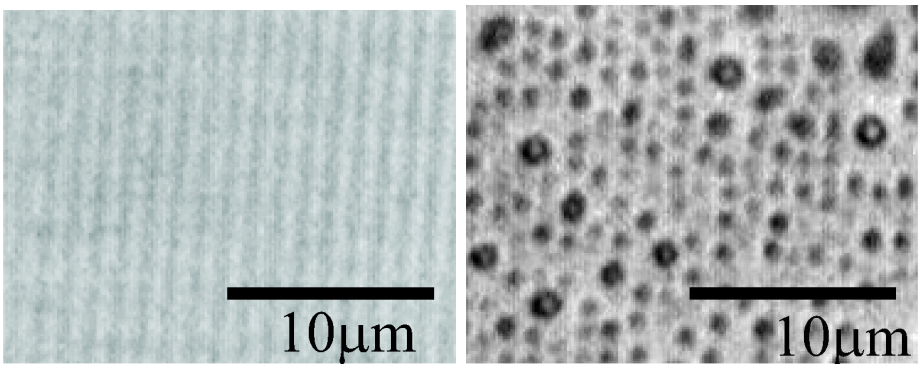

(a) High fluence region with filmwise condensation.

(b) Low fluence region with dropwise condensation.

FIGURE 2.14: Condensation patterns formed after an interference pattern exposure.

We envisage that spatial structuring of the wetting properties with this simple, one step, method will enable the creation of new microfluidic devices by creating fluid confinement with surface energy barriers, rather than physical barriers such as ridge structures or channels. Since no physical barriers will be present to scatter either optical or acoustic waves, device design can have the flexibility to take full advantage of the many non-linear optical and acoustic properties for which lithium niobate has become an indispensable material and help create true bio and chemical analysis lab-on-a-chip devices.

2.5 Summary and Conclusions

The hydrophilicity of LN has been seen to undergo a transition from mildly hydrophobic to super-hydrophilic under the influence of UV laser light. This has been investigated using the contact angles of 0.5 - 1 μl sessile drops under varying exposure intensities, times and environment. It was seen that the transition from a mildly hydrophobic to a hydrophilic state occurs more rapidly with higher incident light intensity however it was seen that the contact angle change is not simply a function of total exposure. It was seen that the change in hydrophilicity was strongly dependant upon the exposure environment, with the transition occurring faster in a high humidity environment and not occurring at all under vacuum conditions. From this observation it was proposed that the hydrophilicity change is due to the dissociative adsorption of atmospheric water molecules onto the crystal surface. The observation also indicated that the change was not due to the photo-catalytic decomposition of organic contaminants to the surface, as has been proposed for other photo-induced hydrophilicity changes [14], since this would also occur in vacuum. The dark decay of the hydrophilic change has been measured by producing identically exposed samples which were stored in sealed containers. It

was seen that the decay of the contact angle, and hence hydrophilicity change, fitted well a decaying exponential with a time constant of two days. This agrees with the hypothesis that the hydrophilicity change is due to adsorbed hydroxyl groups if the change is proportional to the hydroxyl density and thermal desorption occurs randomly with constant probability.

The spreading of liquid along defined hydrophilic tracks was also investigated as a method of deposition and it was seen that DI water did indeed spread with lateral confinement to exposed tracks. The velocity of the spreading water was seen to be dependant upon the exposure of the sample and hence upon the energy change of the surface. The geometry of the defined tracks was not seen to be important with spreading occurring along smooth bends and around tight corners. It was seen that the width of the wetting strip was greater than the width of the exposed region and this is likely to limit the extent to which spreading can occur along a track. The effect of the width of the exposed track was also investigated and it was seen that there was a lower limit of around 1 mm when applied drops had a volume of around 2 μl. This may be due to the extra energy required to decrease the radius of curvature of the contact line compensating for the energy of wetting the higher energy hydrophilic surface.

Structuring of the surface energy has been performed at the micron and sub-micron scale with the use of TEM grid amplitude masks and optical phase masks. The wetting characteristics were observed by the creation of dew on the surface since dew nucleation will occur preferentially in areas of high surface energy. It was seen that a large contrast to the wetting properties was easily achievable at these length scales and that, in the case of condensation of dew, the wetting mechanism could be tailored with the exposure such that condensation could occur in either a film-wise or drop-wise manner. The dew patterns were observed optically with a microscope and CCD camera and were inferred by the diffraction of a laser beam. In this investigation condensation from a vapour was employed, however other application methods could be used, such as aerosols or fine powders, that would allow the transfer of solid particles either directly or in a carrier liquid.

In conclusion we have shown that UV laser light can be used effectively as a simple, one step, method to control the hydrophilicity of the LN surface. On the micron and sub-micron scale this could have great application to the creation of sensor arrays using either biological molecules or hydrophilic nano-particles or quantum dots. On the millimetre scale it has been shown that this can be used as a structured deposition method of fluids, or colloidal solids within a liquid carrier, after placing a drop on the exposed track. It has also been shown that the hydrophilicity of macroscopic areas can be controlled which can allow for a simple method of wafer bonding. Indeed, following the publication of

the work presented in this chapter, Torchinsky and Rosenman [19] have achieved wafer bonding in lithium tantalate (LT), which is isomorphous to LN, through exactly this method. Furthermore in [19] it was shown through XPS measurements that the oxygen concentration on the surface increases during UV exposure as is expected under the model of dissociative water adsorption presented in this chapter.

UV induced hydrophilicity is then a useful form of surface functionalisation of LN which has already shown application for wafer bonding [19] and promises to show further application in a wide range of scientific disciplines.

References

[1] C. Sones, S. Mailis, V. Apostolopoulos, I.E. Barry, C. Gawith, P.G.R. Smith, and R.W. Eason. Fabrication of piezoelectric micro-cantilevers in domain-engineered $LiNbO_3$ single crystals. *Journal of Micromechanics and Microengineering*, 12(1):53 – 7, 2002.

[2] Y. Tomita, M. Sugimoto, and K. Eda. Direct bonding of $LiNbO_3$ single crystals for optical waveguides. *Applied Physics Letters*, 66(12):1484 – 5, 1995.

[3] Kazuo Eda, Masato Sugimoto, and Yoshihiro Tomita. Direct heterobonding of lithium niobate onto lithium tantalate. *Applied Physics Letters*, 66(7):827–829, 1995.

[4] C.J. Strobl, Z. von Guttenberg, and A. Wixforth. Nano- and pico-dispensing of fluids on planar substrates using SAW. *IEEE Transactions on Ultrasonics, Ferroelectrics and Frequency Control*, 51(11):1432 – 6, 2004.

[5] Mark J. Missey, Vince Dominic, Lawrence E. Myers, and Robert C. Eckardt. Diffusion-bonded stacks of periodically poled lithium niobate. *Opics Letters*, 23 (9):664–666, 1998.

[6] Corin B. E. Gawith, Ping Hua, Peter G. R. Smith, and Gary Cook. Nonreciprocal transmission in a direct-bonded photorefractive Fe:$LiNbO_3$ buried waveguide. *Applied Physics Letters*, 78(26):4106–4108, 2001.

[7] K. Hohakawa, K. Koh, C. Kaneshiro, Y. Aoki, C. Hong, and K. Komine. Fabrication process for semiconductor bonded SAW devices. *1999 IEEE Ultrasonics Symposium. Proceedings. International Symposium (Cat. No.99CH37027)*, vol.1:301 – 4, 1999.

[8] A. M. Prokhorov and Yu. S. Kuz'minov. *Physics and chemistry of crystalline lithium niobate*. Hilger, IOP Publishing Ltd, Bristol, BS1 6NX, England, 1990.

[9] M. Maeda, I. Suzuki, and K. Sakiyama. Humidity dependence of surface resistances of $LiNbO_3$ and $LiTaO_3$ single crystals. *Japanese Journal of Applied Physics, Part 1 (Regular Papers & Short Notes)*, 31(9B):3229 – 31, 1992.

[10] Rong Wang, Kazuhito Hashimoto, Akira Fujishima, Makota Chikuni, Eiichi Kojima, Atsushi Kitamura, Mitsuhide Shimohigoshi, and Toshiya Watanabe. Light-induced amphiphilic surfaces. *Nature*, 388(6641):431–432, July 1997.

[11] R. Wang, K. Hashimoto, A. Fujishima, M. Chikuni, E. Kojima, A. Kitamura, M. Shimohigoshi, and T. Watanabe. Photogeneration of highly amphiphilic TiO_2 surfaces. *Advanced Materials*, 10(2):135 – 8, 1998.

[12] R.-D. Sun, A. Nakajima, A. Fujishima, T. Watanabe, and K. Hashimoto. Photoinduced surface wettability conversion of ZnO and TiO_2 thin films. *Journal of Physical Chemistry B*, 105(10):1984 – 1990, 2001.

[13] M. Miyauchi, A. Nakajima, A. Fujishima, K. Hashimoto, and T. Watanabe. Photoinduced surface reactions on TiO_2 and $SrTiO_3$ films: Photocatalytic oxidation and photoinduced hydrophilicity. *Chemistry of Materials*, 12(1):3–5, 2000.

[14] A. Kanta, R. Sedev, and J. Ralston. Thermally- and photoinduced changes in the water wettability of low-surface-area silica and titania. *Langmuir*, 21(6):2400 – 2407, 2005.

[15] Zhaosheng Li, Tao Yu, Zhigang Zou, and Jinhua Ye. Degradation in photocatalytic activity induced by hydrogen-related defects in nano-$LiNbO_3$ material. *Applied Physics Letters*, 88(7):071917, 2006.

[16] P. G. de Gennes. Wetting: statics and dynamics. *Reviews of Modern Physics*, 57 (3):827–861, 1985.

[17] Arthur W. Adamson. *Physical Chemistry of Surfaces, page 348*. 1982.

[18] Abraham Marmur. Line tension and the intrinsic contact angle in solid-liquid-fluid systems. *Journal of Colliod and Interface Science*, 186:462–466, 1997.

[19] I. Torchinsky and G. Rosenman. Interface modification and bonding of lithium tantalate crystals. *Applied Physics Letters*, 92(5):052903, 2008.

Chapter 3

UV Continuous Wave All Optical Poling

3.1 Introduction: Light-Poling Interactions

As described in chapter 1 LN is a ferroelectric crystal with a spontaneous polarisation caused by the displacement of Li^+ and Nb^{5+} cations along the crystallographic c-axis, thus giving rise to 180° anti-parallel domains. The orientation of the spontaneous polarisation can be reversed by the application of an external electric field, indeed it is precisely this property that defines LN as a ferroelectric rather than just a pyroelectric. The orientation of these domains determines the crystal response to many external stimuli, such as DC or AC externally applied electric fields, optical fields or even acids interacting with the crystal surface and so structuring and engineering these domains has become a key method toward functionalising LN and exploiting many of its key inherent properties. The range of applications that has been found for domain-engineered LN is vast, with examples in single-crystal piezoelectric actuators [1–3], voltage-controlled planar lens arrangements [4], beam deflectors [4–8], total internal reflection switches [6–8], Bragg gratings [9], ridge waveguides and fiber alignment grooves [10, 11], free-standing micro-cantilevers [12] and, of course, $\chi^{(2)}$ gratings for QPM of non-linear frequency conversion [13, 14].

The conventional method for domain engineering is to apply an electric field via structured electrodes or a structured dielectric coating with a homogeneous liquid electrode. In either case domain inversion occurs when the electric field inside the crystal exceeds that of the coercive field [15, pg. 103] of the crystal. However, the photo-lithography required for the structured deposition in each case is complex, expensive and requires

cleanroom environment and the field contrast achievable at small length-scales means that domain patterning at periods less than around 4μm is challenging [16]

To circumvent the problems associated with conventional electric field poling much work has been done recently using laser radiation to either pole the crystal directly, or to influence the poling characteristics under simultaneous electric field application. To date light-poling interaction experiments can be grouped under three headings, all optical poling (AOP)[17–20], light assisted poling (LAP)[21–32] and latent-LAP[33]. AOP involves illumination with high-energy, pulsed, UV laser light at fluences near the ablation threshold and has been seen to create complex self-assembled surface domain patterns [18, 20] or ordered domain inversion when using a phase mask [17, 19]. LAP involves the use of visible light in conjunction with an applied electric field to induce domain inversion in the illuminated regions at a field strength below the coercive field of the un-illuminated crystal and latent-LAP involves illumination with high intensity femtosecond visible laser pulses followed by a delayed application of an electric field. The parameter space available for light-poling interaction investigations is vast, consisting of the incident wavelength, power/intensity, choice of continuous wave or pulsed light with the corresponding choice of pulse duration and repetition rate, temperature, illumination face, crystal pre-treatment (e.g. pre-poling), crystal dopants, whether an electric field is applied and if so; the field strength, pulse duration and pulse shape, electrode type and so on. Although much of this parameter space remains unexplored, investigations have been carried out with applied electric fields over a large wavelength range from UV to IR with pulse durations ranging from c.w. to femtoseconds and light intensities ranging from 0.01 W cm^{-2} to 50 MW cm^{-2}, and without electric fields over a wavelength range of 248 nm to 532 nm. Appendix B summarises, in a tabular format, the majority of the published light-poling interaction investigations to date. Details of the experimental conditions and results are given and where authors have proposed interaction mechanisms, these are included also.

In this chapter the influence of focussed c.w. UV light is investigated for AOP and a new method of domain structuring of latent light impeded poling (LLIP), whereby domain inversion is seen to be inhibited in illuminated regions during a subsequent electric field poling step, is presented in the following chapter. In each case experimental results are presented and a qualitative model is proposed that accounts for the behaviour of both effects.

3.2 UV Continuous Wave All Optical Poling

AOP has previously been seen only during pulsed laser illumination close to the ablation threshold [17–20]. It has been assumed that the high peak power of a pulsed source is a pre-requisite for AOP, however recent results here show that AOP is also possible in the c.w. regime using focussed UV laser light at a wavelength of 244 nm.

The experimental method is outlined in section 3.3 and the results are presented and discussed in section 3.4. The written structures are interrogated using piezoresponse force microscopy (PFM) and by chemical etching in hydrofluoric (HF) acid followed by both surface profiling and scanning electron microscopy. Section 3.5 presents an outline of a possible mechanism by which domain inversion could occur under UV illumination and conclusions are made in section 3.6.

3.3 Experimental Method

A UV laser beam of wavelength 244 nm is provided by a frequency-doubled argon ion laser. The beam is expanded, spatially filtered and collimated before being focused onto a LN sample by a 40 mm focal length lens. The focused spot has a calculated radius of approximately 1.5 μm, however, from the size of damage features seen in a photo-resist covered slide we believe the actual spot radius to be approximately 2.5 μm. The LN samples (500 μm thick single crystal) are mounted upon a three axis computer-controlled stage system (Newport MM2000). The exposure was also controlled by a computer-controlled shutter such that the beam was present only when the stage velocity was constant to ensure uniform exposure along the written lines. The stages were translated to write lines along both the x and y axes at speeds between 50 to 300 μm s^{-1}. Exposures under the above conditions were made at incident powers between 20 and 30 mW, which corresponds to an intensity range of 100 - 150 kW cm^{-2}. At powers below $\sim$ 20 mW no significant effect is seen and at powers higher than $\sim$ 30 mW, although the effect is seen, excessive melting and thermal damage occur. Exposures were carried out on both the positive and negative z faces of iron-doped (0.1 mol % and 0.01 mol %) and un-doped crystals and in duplicate such that identical samples could be analysed by PFM and by etching. Exposures were also carried out on the $-z$ face only of titanium in-diffused crystals.

For PFM analysis an atomic force microscope with a conducting tip was used to measure the piezoresponse of the exposed surface by applying an electric field to the surface with a metal coated silicon tip whilst measuring the induced strain by the tip deflection. An overview of the principles of PFM can be found in [34, 35].

Chemical etching in hydrofluoric (HF) acid is a well-established method of domain visualisation in LN due to the fact that the $-z$ face etches readily whilst the $+z$ face does not etch at all [36]. Thus if domains are inverted during UV laser irradiation they will present as either a raised ridge in the case of $-z$ face exposures or as an etched trench in $+z$ face exposures. A number of un-doped samples were etched at room temperature in HF acid of 48% aqueous solution for consecutive intervals of 5 minutes, between which they were imaged with an optical microscope and profiled using a KLA-Tencor stylus profilometer. After a cumulative etching time of 1 hr these samples were imaged with a scanning electron microscope (SEM). Other un-doped samples, and both the titanium in-diffused and iron doped samples, were etched for around 15 minutes only before being imaged with an SEM.

Further exposures were performed on a periodically poled LN (PPLN) sample which was analysed by PFM as the PPLN structure gave a benchmark against which to compare any UV laser-induced PFM signal.

3.4 Results and Discussion

3.4.1 Pre-Etching Examination

Before etching the samples were inspected using optical microscopy and surface profilometry. Figures 3.1(a) and 3.1(b) show optical microscope images of an un-etched $+z$ sample exposed at 30mW and 22mW, respectively, with a scan speed of 50 μm s^{-1}. It can be seen that at the higher power damage has occurred and the exposed area is composed of two regions; an outer region where the crystal has experienced thermal deformation and cracking and a second region, within the first, in which the crystal appears to be darker. The darkened region may, however, indicate a change in the refractive index of the crystal, as was observed following UV illumination by Mailis et al. [37]. The line of the cracks in the high power exposure are not seen to follow the direction of any of the crystal axes. In the lower power exposure no physical damage is seen to occur, however the darkening persists. This agrees with thermal modelling of the heating of LN by UV laser light carried out in chapter 5 which shows that melting would not occur for a spot size of 2.5 μm up to a power of 24mW. Figure 3.2 shows the variation of width of the two regions mentioned above with incident power for identical scanning speeds.

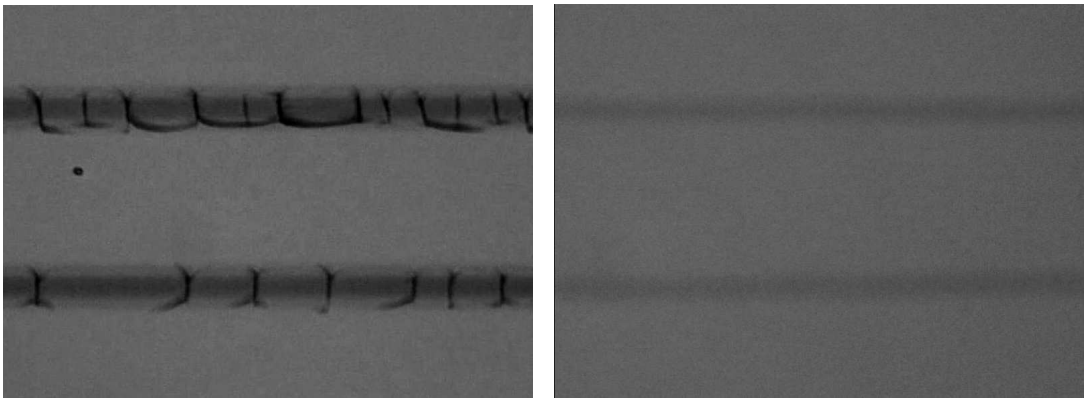

(a) High power, 30 mW. (b) Low power, 22 mW.

FIGURE 3.1: Optical microscope images of un-etched, directly written structures. Scan speed of 50 μm s^{-1} for both exposures.

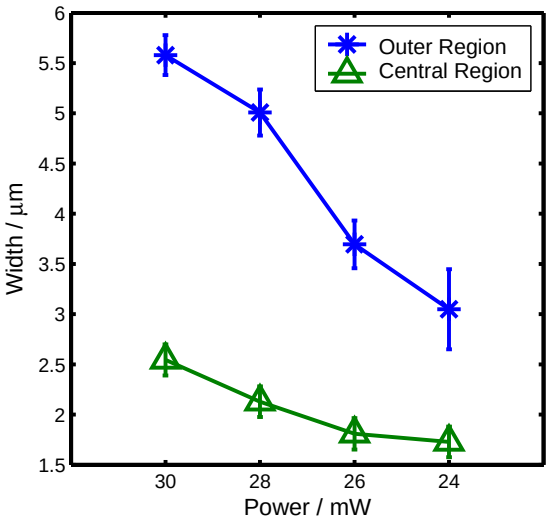

FIGURE 3.2: Variation with incident power of the width of the two regions observed in the UV written structures before etching. Error bars obtained as standard deviation of repeated measurements.

Profiling of the un-etched exposures shows that the crystal expands in the regions of obvious damage and that the surface height increases by up to ∼50 nm on the exposed face, regardless of polarity. Figure 3.3 shows a profilometer trace across a 30mW exposure on the $+z$ face. The peaks correspond to pairs of lines written at different speeds with low speeds on the left of the plot and faster speeds on the right, ranging from 50 to 300 μm s^{-1}. The direction of the trace is perpendicular to the lines. No dependence upon the scanning velocity is evident. The points at which the beam is incident corresponds to the narrow peaks, the width of which agrees with the $\sim 5\mu$m diameter of the beam, spaced 20 μm apart for identical speeds. However, across the base of each pair of peaks, an extra expansion of $\sim$ 10 nm can be seen that extends over a width of around 40 μm. The origin of this extended structure is unclear but may be due to mechanical strain from thermally induced stress or could be debris from the central damaged region. Figure 3.4 shows a corresponding scan of an exposure carried out at the same velocities but an incident power of 22 mW. It can be seen that the sharp peaks are not present whilst the shallow, extended, expansion remains. This associates the sharp peak with physical damage and the shallow expansion with another effect which is likely related to the thermal stress field created during laser heating which would extend beyond the heated region. Interestingly the shallow expansion in the low power scan are roughly half the width of the shallow expansions in the high power scan. In the high power scan the shallow expansions can clearly be seen to be the sum of two shallow expansions, centred on each scan line, as is particularly evident in the right most pair of peaks. In the low power scan, however, the shallow expansions are roughly half the width of that seen at high power. Since the scan lines are separated by the same distance in each case, this incongruity between the two results then suggests two possibilities; the expansion is due to a of superposition of effects associated with each scan and so would form mainly in the centre or that, since the beam is scanning in different directions during each scan in a peak pair, that there is a non-reciprocity in the effect when scanning along the positive and negative directions such that, at this low power, the effect is only seen in one direction. The first suggestion seems unlikely and can be partly ruled out by observation of the high power results in which a dip in the centre of the shallow peak can be observed, indicating that two shallow peaks are centred on the scan lines. The second proposition cannot be proved by the data set presented here and would require further investigation, however non-reciprocity in the behaviour of LN to scanning laser beams has recently been reported [38].

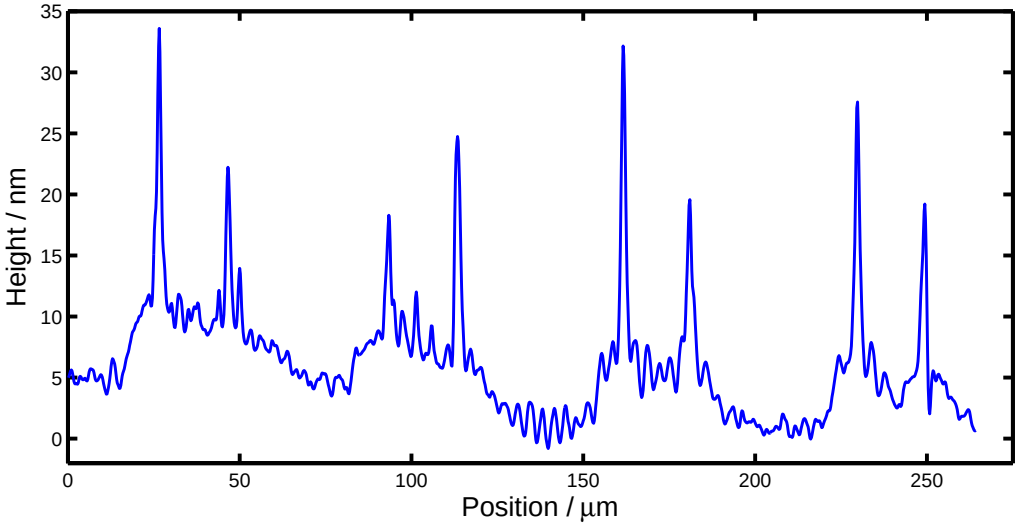

FIGURE 3.3: Profilometer scan of an un-etched exposure at 30 mW. Peaks correspond to pairs of lines written at the different speeds with low speeds on the left of the plot and faster speeds on the right.

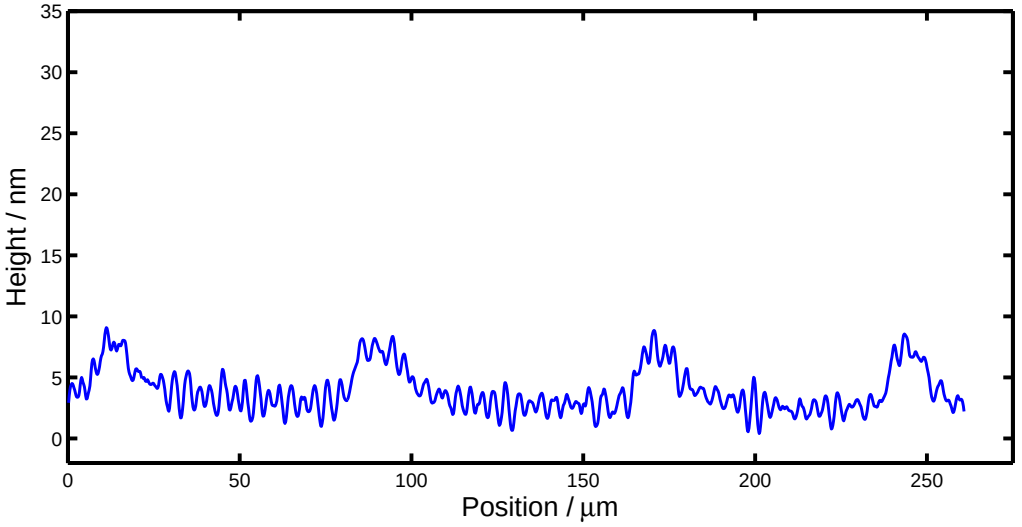

FIGURE 3.4: Profilometer scan of an un-etched exposure at 22 mW. Peaks correspond to pairs of lines written at the different speeds with low speeds on the left of the plot and faster speeds on the right. Vertical scale identical to that in 3.3 for ease of comparison.

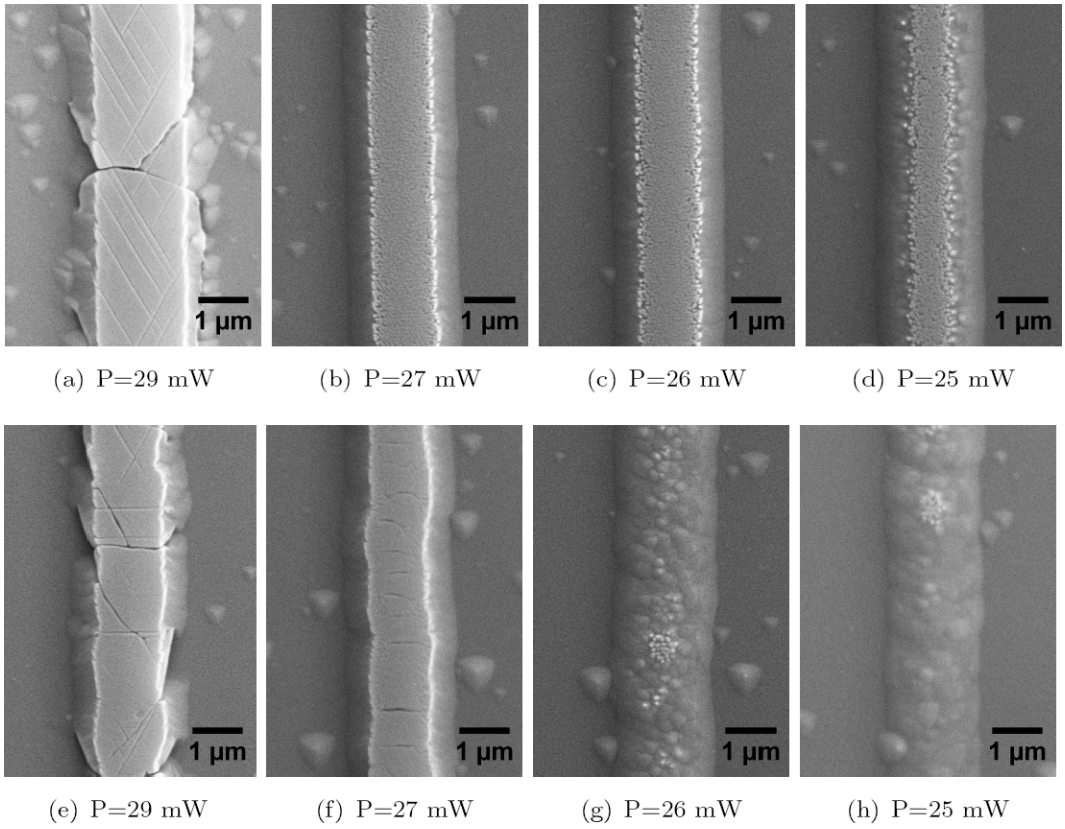

Figure 3.5: Variation with power of the UV laser-induced layer on the -z face. Lines scanned along the crystallographic y direction. SEM images of structures revealed by HF etching for 15 minutes. (a-d) Scan speed 50 µm s^{-1}. (e-h) Scan speed 200 µm s^{-1}.

3.4.2 Etching Results

Figure 3.5 shows SEM images after etching of exposed areas on the -z face of un-doped congruent LN with scan speeds of 50 (a-d) and 200 (e-h) µm s^{-1}. It is clear to see that the behaviour is strongly dependent upon exposure conditions with an abrupt qualitative change occurring at the highest power, splitting the behaviour into two regimes. These two regimes will be referred to as the high power regime and the low power regime, with the understanding that the terms are relative to the somewhat narrow power window of the main investigation. As was mentioned earlier, the effect is seen to occur at higher powers above 30 mW, but is considerably below 20 mW. The narrow width of the power window is believed to be due to the strong temperature dependence of the effect and the steep rate of change of temperature with power for these beam parameters which shall be shown in chapter 5. In the high power regime the UV exposed region is seen to be smooth and resists etching in the crystallographic z direction. The surface contains cracks, due to thermal damage, and is decorated with thin lines that extend along the x axes of the crystal. These features will be discussed in detail later.

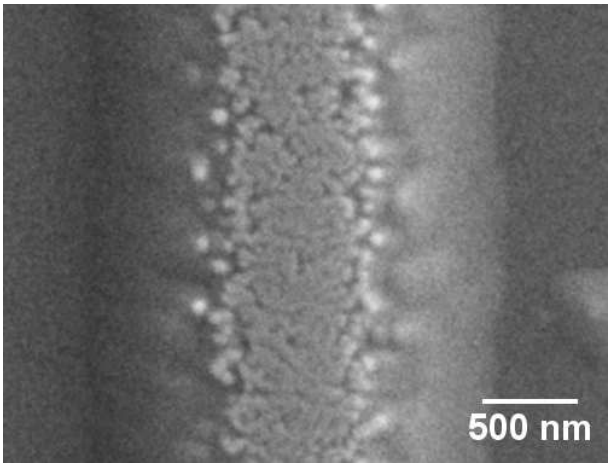

FIGURE 3.6: SEM image of the discrete features seen on the upper surface of the $-z$ face in the low power regime.

In the low power regime it is seen that etching is also resisted in the exposed regions, resulting in a raised ridge structure. The upper surface of the ridges is seen to consist of densely packed discrete features that have dimensions of around 50-100 nm and an example of this is shown in high magnification in figure 3.6. These features are believed to be $+z$ nano-domains formed during the UV illumination since they resist etching in the vertical direction whilst the $-z$ face they are embedded within does not. Thus the surrounding material etches and the nano-domains are revealed.

The change in height with cumulative etching time of the ridges, with respect to the unexposed background $-z$ face, is shown in figure 3.7. The slope of the curve gives the differential etch rate between exposed and unexposed regions. In the high power (solid blue) curve it can be seen that the gradient is constant and has a value which agrees with the etch rate of virgin LN [36]. This indicates that the ridge does not etch at all. As the power decreases it is seen that the etch resistance lasts for a time dependent upon the power and scan speed, but this time decreases with decreasing power or increasing velocity, until features etch at the same rate as the unexposed regions. This agrees with the hypothesis that the discrete features formed during lower power illuminations are $+z$ nano-domains since, as the surrounding $-z$ material is etched, the sides of these nano-domains are exposed to the etchant. At this point the nano-domains will begin to side-etch as the acid attacks the $-y$ faces. The ease at which etchant can enter between the nano-domains and attack the sides will, of course, depend upon the packing density. When the side etched distance reaches the radius of the nano-domains they will begin to reduce in height and the differential etch rate between the $-z$ crystal face and the exposed region will reduce. At the point at which the entire depth of these nano-features is revealed and side-etching has removed them completely the differential etch rate goes to zero and the height of the ridge is preserved.

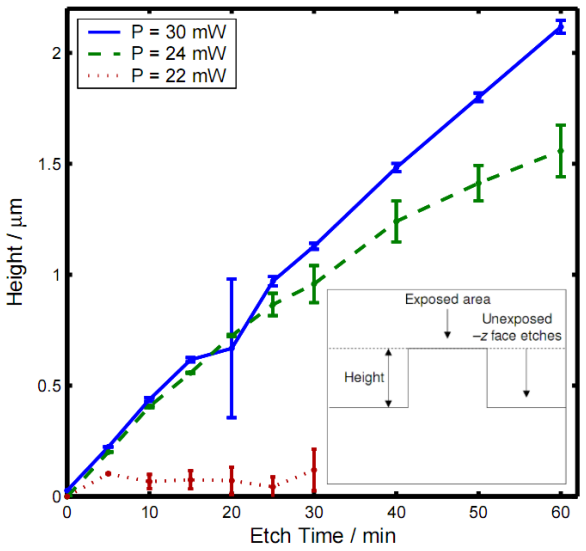

FIGURE 3.7: Change in feature height above $-z$ face with etch time for different power exposures at a scan speed of 100 μm s^{-1}. Flat gradient shows no etch resistance. Error bars obtained as standard deviations of repeated measurements. Insert shows how the height is defined.

The width of the upper surface of the ridges after 15 mins etching is plotted in figure 3.8 as a function of scan speed for laser powers of 29, 27, 26 and 25 mW. It can be seen that the width is strongly dependent upon the incident intensity and only weakly dependent upon the scan speed with the width increasing with increasing power and decreasing with increasing scan speed. Whilst, for a particular scan speed, it is seen that the width of the upper layer decreases with decreasing power, the overall width of the ridge left after etching is essentially constant (not shown in figure 3.8). This indicates that this entire width was initially covered in a capping layer of the $+z$ nano-domains described above, but that either the density, size and/or depth of the nano-domains decreased with distance from the centre of the beam path such that the outer nano-domains were removed by the time the measurements were taken. Figure 3.8 then shows that the density, size and depth of the nano-domains in the capping layer vary strongly with power and also vary with scan speed.

In the high power regime, exposures on the $-z$ face (figure 3.5(a)) are seen to result in an etch resistant layer of quite different topography as compared to low power exposures. The surface of the layer is seen to be very flat and smooth as compared to the low power regime where it consisted of discrete features that are believed to be $+z$ nano-domains. The edges of the layer are also seen to be sharp and well-defined. Some cracks are present due to thermal damage and these generally span the surface without particular alignment to crystal axes. Since the density of the features believed to be $+z$ nano-domains was seen earlier to increase with increasing laser intensity, it is believed that

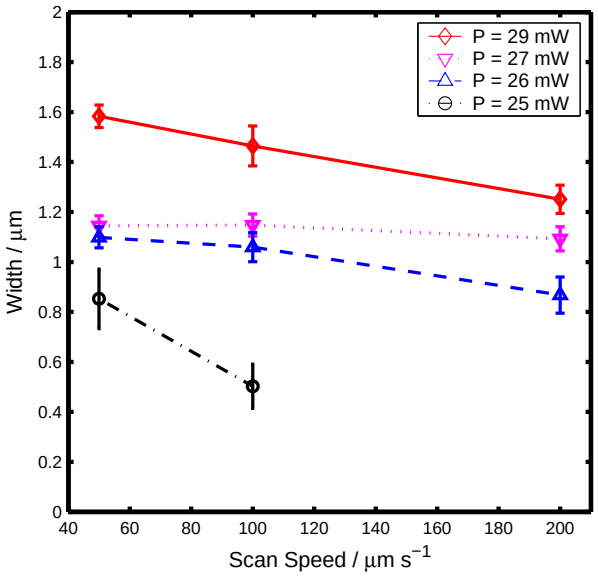

FIGURE 3.8: Variation in the width of the upper surface of the etched ridges with power and scan speed. Error bars obtained as standard deviations of repeated measurements.

the well-defined and smooth surface produced in the high power regime is due to the merging of the nano-domains to form a continuous $+z$ domain. Further evidence for this will be presented.

Figure 3.9 shows an SEM image of a high-power exposure after 1 hr etching where the affected layer can be seen to extend to a depth of around 1 μm, whilst the total height of the ridge is just over 2 μm. To investigate better the topography of the features the sample was tilted with respect to the electron beam, about the long axis of the line. The layer is seen to resist etching in the depth direction completely up to etching times of 1 hr as can be seen in figure 3.7, however figure 3.9 shows that the upper layer does etch in the vertical direction from *underneath* as can be seen from the voids where etchant has been permitted to enter through the thermally induced cracks. Furthermore it can be seen from the symmetric shape of the voids that the etch rate of the layer from underneath, toward the surface, is very similar to that of the unaffected crystal beneath. This indicates that the affected layer is a region of crystalline LN with an inverted polarity from the following reasoning. A domain inverted layer on the $-z$ face would present a $+z$ face to the etchant and so would resist etching in the inward surface normal direction. If etchant was permitted within or below this inverted layer it would see in the outward surface normal direction a $-z$ face and would so etch accordingly. If etchant is present at the head-to-head boundary between a positive surface domain and an underlying negative bulk domain it would be presented with two $-z$ faces and so would etch in the directions both away from and toward the surface, at the same time as etching sideways, and so a void would be formed. The void would be diamond-shaped

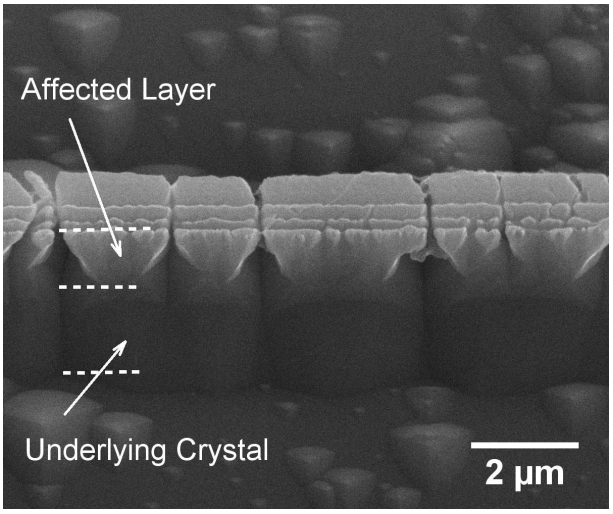

FIGURE 3.9: SEM image of typical features on the $-z$ face after high power UV exposure revealed after 1 hr etching. The x axis of the crystal runs along the direction of the ridge. Sample tilted at 30° to the electron beam, about the x axis. The areas indicated by annotations form the upstanding ridge structure and are both in relief of the crystal surface.

in cross-section with opposite vertices on the line parallel to the surface indicating the depth of the surface domain. This is seen in figure 3.9 and gives the approximate depth of the surface domains as $\sim 1\mu$m.

The etching behaviour along the x and y axes of the exposed ridges can also be used to indicate the polarity of the affected surface layer in relation to the underlying bulk material. Once a domain inverted layer is revealed by the etching of the surrounding crystal, thus forming a ridge structure, it would present either y or x faces to the etchant depending upon the scanning direction and hence geometry of the newly formed ridge. In the case that the beam is scanned along the y axis and the x faces are then presented to the etchant there would be no asymmetry of the etching since the x axis etches at the same rate along both the positive and negative directions. This is the behaviour seen in figure 3.10. In the case that the y faces of the crystal are presented to the etchant, however, an asymmetry is expected since the y axis etches differentially, with the -y faces etching at a far greater rate than the $+y$ faces [39]. The direction of the y axis is of course coupled to the direction of the z axis such that when the z axis is inverted the y axis inverts also [39]. This asymmetry of the etching in the y direction was seen in figure 3.11 which, through the argument above, identifies the y axis of the ridge structure as pointing upward in the figure. The direction of the y axis of the underlying and unexposed LN points downward in the figure. The asymmetries of the etch behaviour thus show that the exposed region is still crystalline and that the direction of the z and y axes is opposite to that of the unexposed crystal.

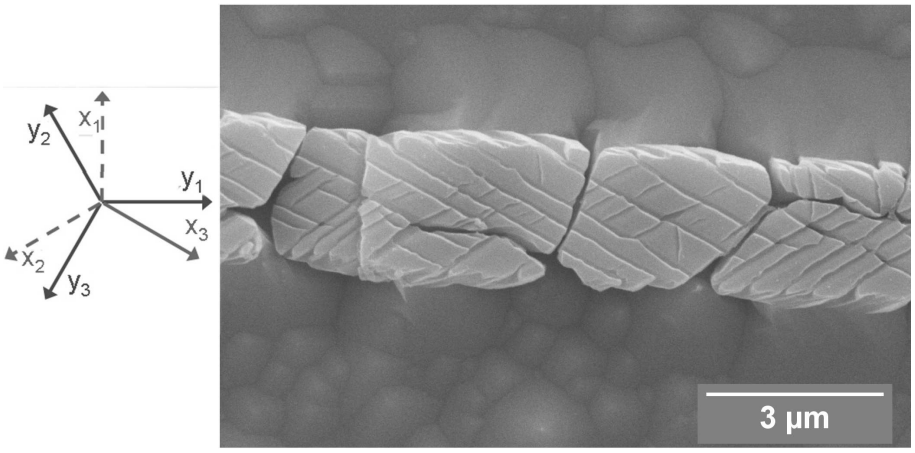

FIGURE 3.10: SEM image of a high-power exposure after 1 hr etching viewed from directly above. The two side faces presented to the etchant are x faces and so no differential etching is seen and the polarity cannot be ascertained. Insert shows axes of the underlying crystal.

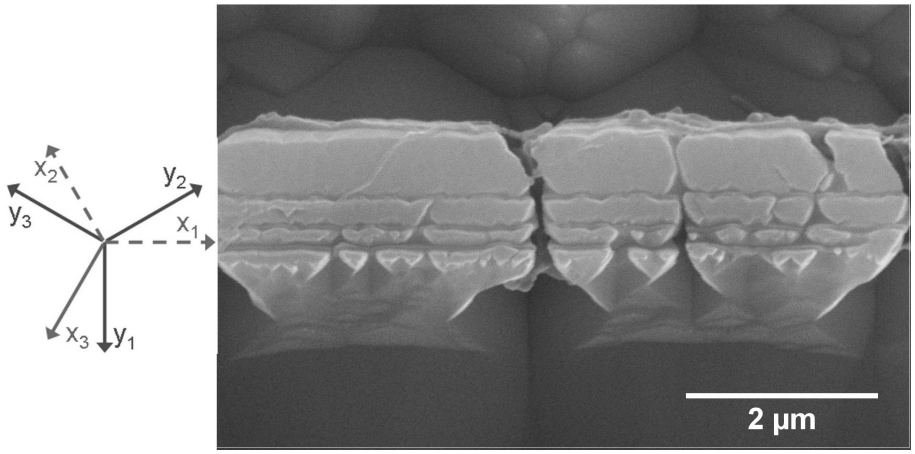

FIGURE 3.11: SEM image of a high-power exposure after 1 hr etching viewed from directly above. The polarity of the affected layer is seen through the differential y etching indicating that the affected layer is of the opposite polarity to the surrounding crystal. Insert shows axes of the underlying crystal.

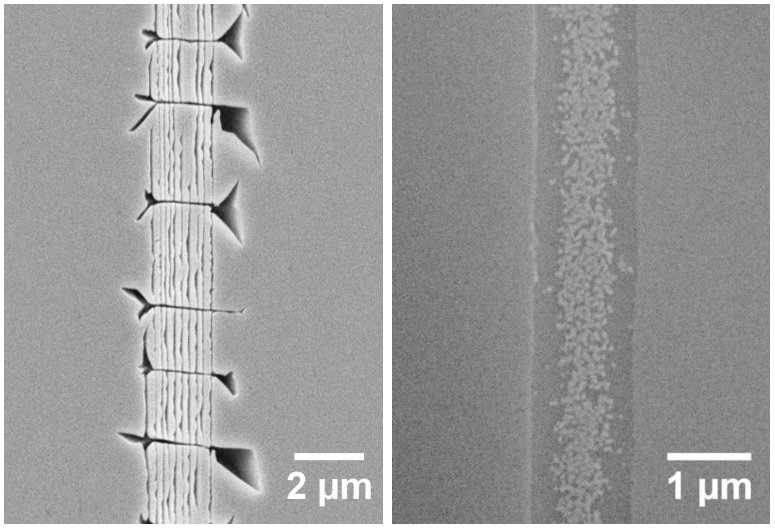

(a) High power (b) Low power

FIGURE 3.12: Typical behaviour of $+z$ exposures in the high and low power regimes. Beams scanned along the crystallographic x direction.

Exposures to the $+z$ face also showed strong intensity dependence, splitting the behaviour again into a low and high power regime. The distinction between a high and low power regime was seen to be made at the same incident powers on the $+z$ face of the crystal as on the -z face. In the low power regime $+z$ face exposures were seen to produce trenches after etching as can be seen in figure 3.12(b). These may be due to the etching of a shallow -z domain until the underlying $+z$ domain is reached. For powers in the intermediate region between the high and low power regimes, remnant features appear in the centre of the tracks that resist etching, however they disappear at the lowest powers. The depth of these trenches, as measured by a surface profiler, was seen to be inversely proportional to the scan speed. The measured depths of the trenches reached some tens of nanometers, however the true depth may be greater since the tip of the surface profiler has a large radius of curvature which makes probing narrow structures difficult. Figure 3.13 shows the variation in height of the exposed areas, relative to the unexposed face, with etching time for different incident powers and scan speeds. It can be seen that in the higher power case, figure 3.13(a), the height is constant within the error. In the lowest power, figure 3.13(c), the depth decreases rapidly to a value that is constant within the error. The ultimate depth of the trenches in figure 3.13(c) is clearly inversely proportional to the scan speed with deeper trenches being formed with slower scans and thus greater exposure. In the intermediate power region, figure 3.13(b), it can be seen that the ultimate depth of the trenches is greater than that of the lower power exposures, but that this depth is reached at a slower rate. This is most likely to be due to the remnant features in the centre of the trenches taking longer to etch away and thus reveal the depth of the trench. A trend with scan speed can also

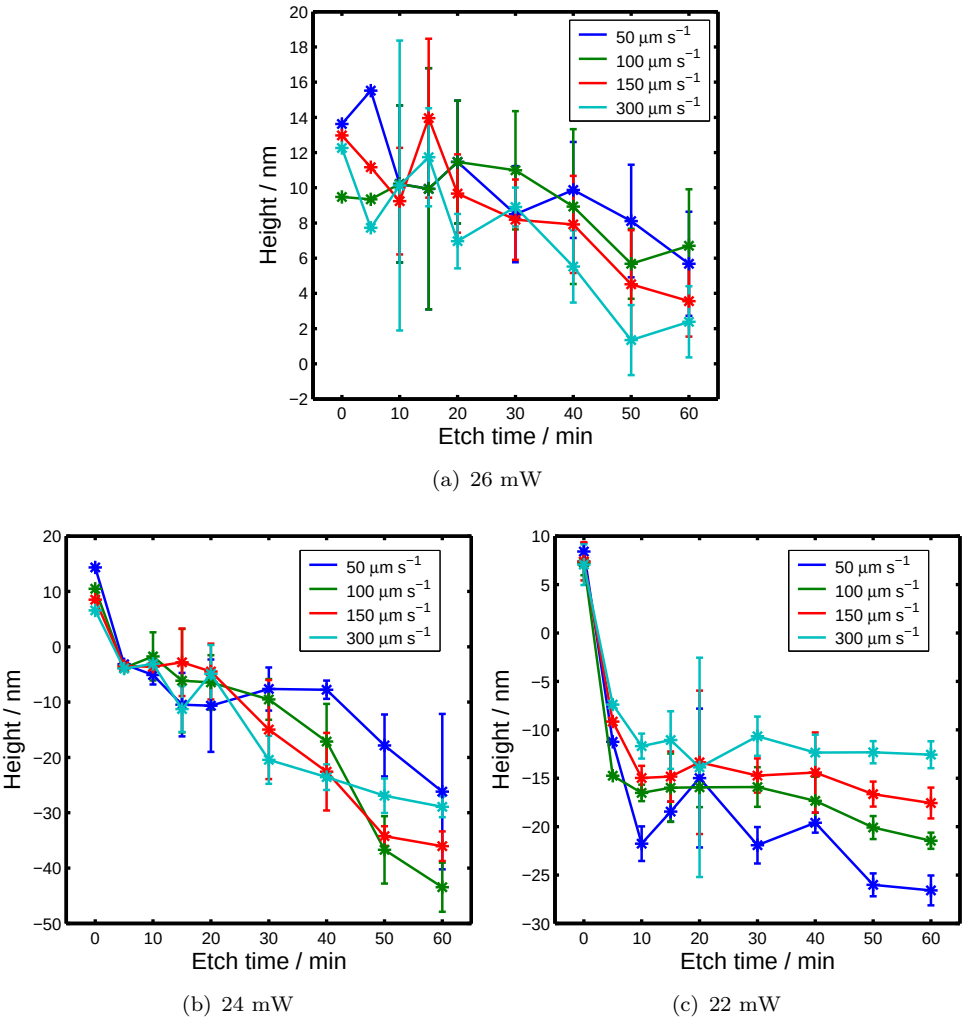

(a) 26 mW

(b) 24 mW

(c) 22 mW

FIGURE 3.13: Height of the exposed regions (relative to the un-exposed) against etch time for various scan speeds and powers. Error bars obtained from standard deviation of repeated scans where available.

be seen in figure 3.13(b) where the ultimate depth of the trenches increases with slower scan speed, but takes a greater time to get there due to a greater density of remnant features requiring a greater time for removal through side etching. The exception of this in figure 3.13(b) is the slowest scan speed which is likely to have the greatest density of remnant features. The ultimate depth of the trenches would give an indication of the depth of the domains formed, if indeed this is what they are. This would mean that the UV directly written domains reach only a depth of a few tens of nano-meters on the $+z$ face, which would limit their application to practical optical devices. They are however controllable structures that may still find application in other areas such as plasmonics. Figure 3.14 shows a surface profiler scan corresponding to the rightmost points in figure 3.13(c) where the velocity dependence, and hence controllability, is clearly seen.

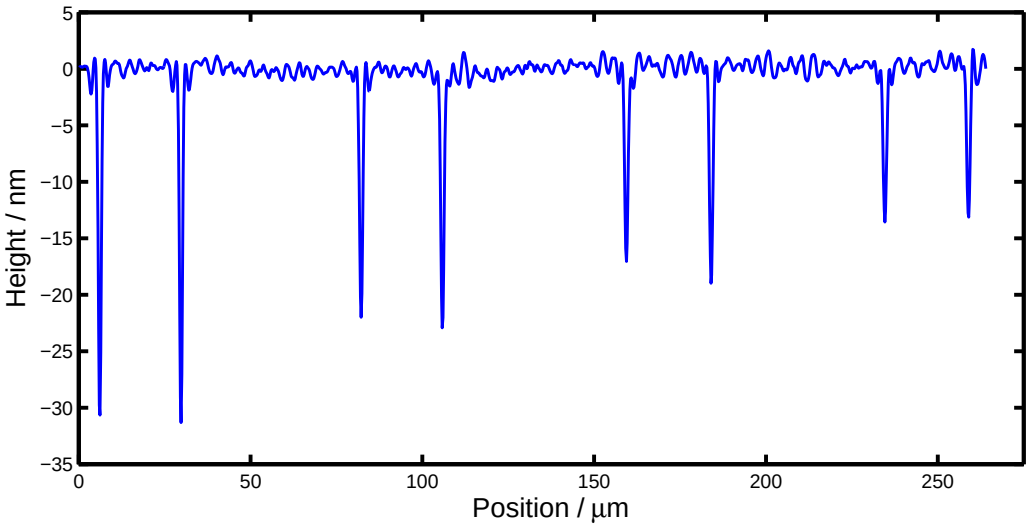

FIGURE 3.14: Surface profiler scan across exposures at a constant power of 22 mW with varying scan speed after an hours etching. From left to right, peak pair scan speed; 50 μm s^{-1}, 100 μm s^{-1}, 150 μm s^{-1}, 300 μm s^{-1}.

The behaviour of the $+z$ face in the high power regime is different. At high powers etching is not seen to occur over the entire exposed area. This can be seen in figure 3.12(a) that shows an exposure after 1 hr etching. Large cracks (seen horizontally in figure 3.12(a)) caused by thermal effects can be seen (also visible before etching). In the high power regime, on both the $+z$ and $-z$ face, long, narrow, features are formed within the exposed area that etch in contrast to their surrounding material as would $-z$ domains in a $+z$ background. These have widths of around 50-100 nm and are aligned strictly along the crystal x axes. Such aligned features should not exist in an amorphous material and so further confirms the crystalline nature of the surface. Due to the symmetry of the crystal structure, LN has three pairs of orthogonal x and y axes. The particular x axis that the features dominantly align to depends on the scan direction of the beam. When the beam scans along the y_1 axis, features are seen to appear along the x_2 and x_3 axes but are not seen along x_1, as shown in figures 3.15(a,c) for both the positive and negative z faces. When the beam is translated along the x_1 direction, the features are seen to align to the x_1 axis only as seen in figures 3.15(b,d). It is believed that these features are formed by the nucleation of a nanodomain followed by one dimensional growth along the x axis. It is interesting to note that these features span the cracks formed by thermal damage indicating that they were formed before the crystal cracked since any effect within the crystal would not traverse a void. That the domain is seen to grow along the x axes differentiates the behaviour from that seen in previous AOP studies [17–20] in which long, narrow, domains have grown along the y axes. This implies a different mechanism to the correlated nucleation due to incomplete screening proposed in [40]. The fact that these domains are forming with walls parallel to

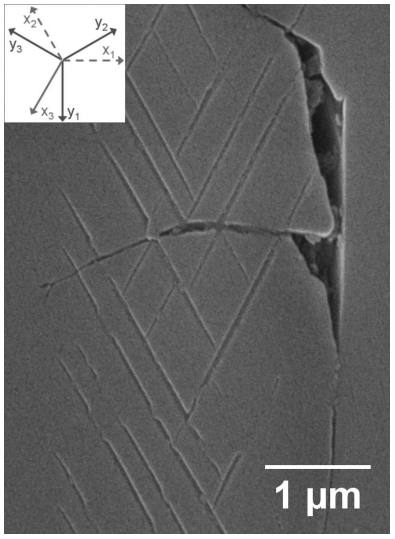

(a) Iron doped $+z$ exposure, scanned along y

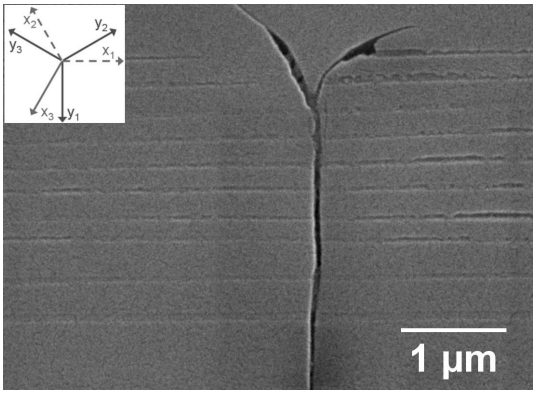

(b) Iron doped $+z$ exposure, scanned along x.

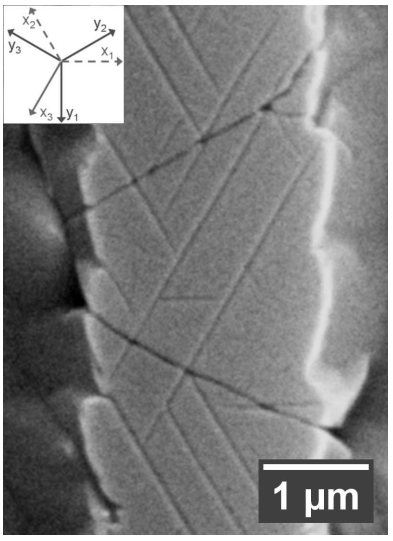

(c) Un-doped $-z$ exposure, scanned along y.

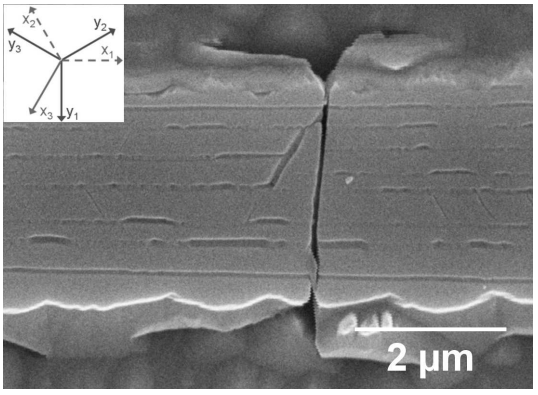

(d) Iron doped $-z$ exposure, scanned along x.

FIGURE 3.15: SEM images showing alignment to the x axes of features exposed by etching on the positive and negative z faces after UV exposure in the high power regime.

the x axis is also interesting since x walls have a normal in-plane polarisation and so are a higher energy configuration than y walls [41]. On the $+z$ face this may represent the only poled region in the exposed area. On the $-z$ face the lines appear as on the $+z$ face strengthening the hypothesis that the polarity of the $-z$ exposed regions has inverted and that the line features are caused by a fast one dimensional domain growth on the $+z$ face. Self organised domain growth along crystal axes has been seen in previous AOP studies where the growth was along the y axes and had much larger feature size and a larger distance of closest approach of around 1.5 μm [18, 20]. Structures similar to those

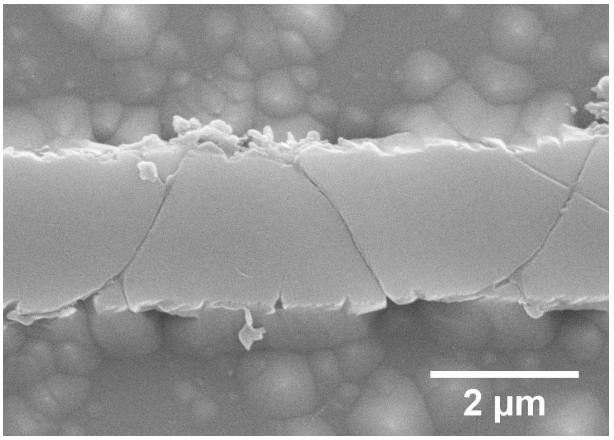

FIGURE 3.16: Typical behaviour of $-z$ exposures in the high power regime on titanium in-diffused LN. Beam scanned along the crystallographic y direction.

seen in this paper have been seen during spontaneous backswitching during electric field poling where the alignment has been along either the x or y axes with a feature size of tens of nm [42].

No difference was seen in the etch behaviour of iron doped samples as compared to un-doped samples since the same corresponding surface topography was present in both the high and low power regimes. This observation suggests dopants and defects with energy levels within the band-gap play little role and that the effect is dominated by band-band transitions.

Figure 3.16 shows an SEM image of a $-z$ face exposure, in the high power regime, on a titanium in-diffused sample after etching in HF acid. It can be seen that the etch behaviour is again similar to that of the exposures on un-doped LN, with a raised ridge being formed. The cracks due to thermal damage can again be seen, however the features that align to the x axes, that were seen earlier on iron-doped and un-doped LN, are seen with a much lower density. The quality of the edges is reduced due to remnant titanium oxide on the surface.

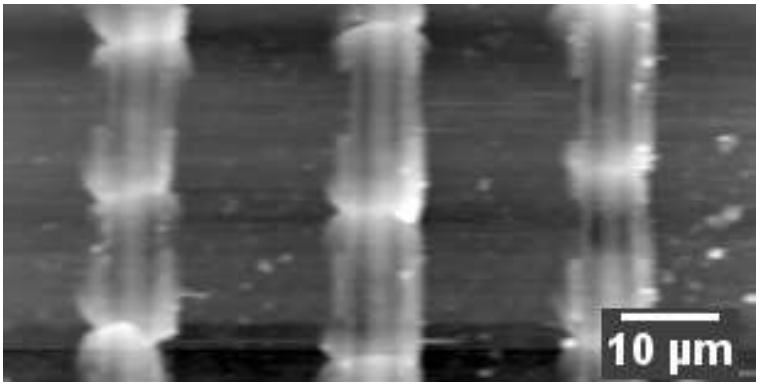

(a) Topography

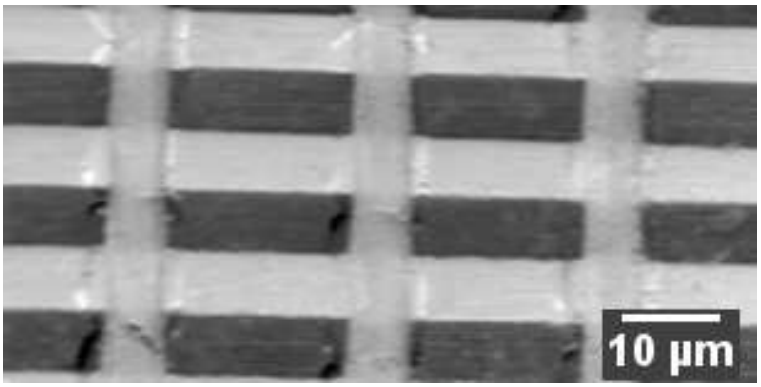

(b) PFM Image

FIGURE 3.17: Topography and PFM amplitude of a scanned UV exposure over PPLN. PPLN domains run horizontally in the images and UV written lines run vertically. In the PFM image $-z$ domains appear black and $+z$ domains appear white. UV scans are seen to invert $-z$ areas of PPLN.

3.4.3 PFM Results

Piezoresponse force microscopy utilises the converse piezoelectric effect to determine the polarity of ferroelectric domains [34]. An electric field is applied to the sample through a conducting atomic force microscopy tip which limits the depth resolution of the technique since the field within the crystal extends to approximately two times the radius of curvature of the tip. In our case this corresponds to a depth of around 100 nm. Any domain features with depth greater than this will be seen as bulk domains and show the full piezoresponse amplitude contrast. Domain features with depth less than 100 nm, however, will give the integrated piezoresponse of the sampling volume. This makes identification of shallow domains difficult since both shallow inverted domains and regions of non-piezoelectric material can give the same net PFM response.

Figure 3.17 shows the topography (a) and PFM amplitude (b) of a scanned exposure over a PPLN sample. The PPLN domains run horizontally over the image whilst the UV scanned lines run vertically. The full PFM contrast is clearly visible due to the

PPLN structure with black areas indicating a $-z$ face and white areas indicating a $+z$ face. The immediate observation is that the UV exposed areas show similar contrast to the $+z$ areas of the PPLN. Figure 3.18(b) shows a line plot of the PFM intensity across the line indicated in figure 3.18(a). The different areas of the crystal can clearly be identified in the line plot of the experimental data. The average piezoresponse over each area has been overlaid as a horizontal line as follows; -z face (green dotted line), $+z$ face (purple dashed line), the UV affected, initially -z, region (light blue dash-dot line) and the mid-level or null piezoresponse (red solid line). It can be seen that the piezoresponse in the UV scanned region is not identical to the piezoresponse of the $+z$ region, however it is significantly greater than the mid-level response between -z and $+z$ regions. This is a crucial observation since it indicates that there must be material present within the PFM sampling volume that has a $+z$ polarity. The reduced piezoresponse, as compared to the bulk -z material, could be due to many reasons such as a layer of damaged material, or an increased defect density or opposite nano-domains with reversed polarity within the resolution of the scan or even simply that the domains are shallow within the PFM sampling volume. Figure 3.17(b) also shows that, in the high power regime, the $+z$ areas of the crystal remain $+z$ after illumination. This agrees with the etching behaviour of the high power exposures as was seen in figure 3.12(a). Figure 3.19 plots the piezoresponse across the line indicated and shows the effect of the UV beam on an area which was initially $+z$. The domain polarity is not seen to change however it is interesting to note that the piezoresponse is not greatly reduced either. When compared with the reduction of the peizoresponse, compared to the bulk value, of the illuminated region in figure 3.18(b) it is clear that the reduction of the piezoresponse in figure 3.18(b) is not due to an amorphous layer. If this were so the reduction would be present equally on both the $+z$ and -z regions and result in equal reductions to the piezoresponse.

A second important observation to be made from figure 3.17 is that the area seen to be affected by the beam is much wider in the topographical image than in the piezoresponse image. This is similar to the behaviour seen optically in section 3.4.1 where a darkened region could be seen within the region of damage. It can also be seen that the area is more well-defined by straight edges in the piezoresponse image. Both of these observations act to decouple the physical thermal damage from any possible light-induced domain reversal.

The depth resolution of the PFM gives an estimate of the minimum depth of the domain formed on the $-z$ as ~ 100 nm. A greater estimate of the depth, which may be taken as an upper limit, has been given earlier in section 3.4.2 as $\sim 1\mu$m. Although methods exist to measure the depth of domains, such as side-polishing and etching [42] and x

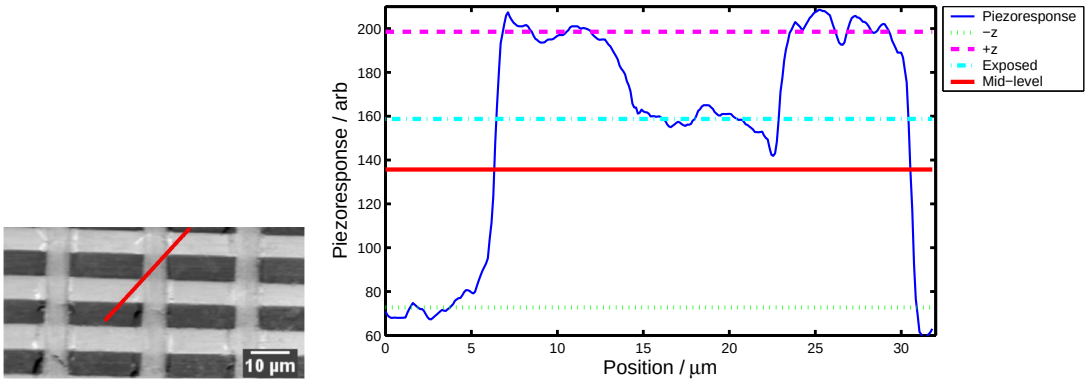

(a) PFM image (b) Piezoresponse plot of line indicated in red in (a)

FIGURE 3.18: Line plot of the piezoresponse across a path in the PPLN crystal encompassing bulk *+z* and *-z* domains and the area of *-z* domain which appears to be inverted by UV writing. The path is marked in (a) by a red line. Horizontal lines in (b) indicate the average piezoresponse of the *-z* face (green dotted line), *+z* face (purple dashed line), the UV affected, initially *-z*, region (light blue dash-dot line) and the mid-level or null piezoresponse (red solid line).

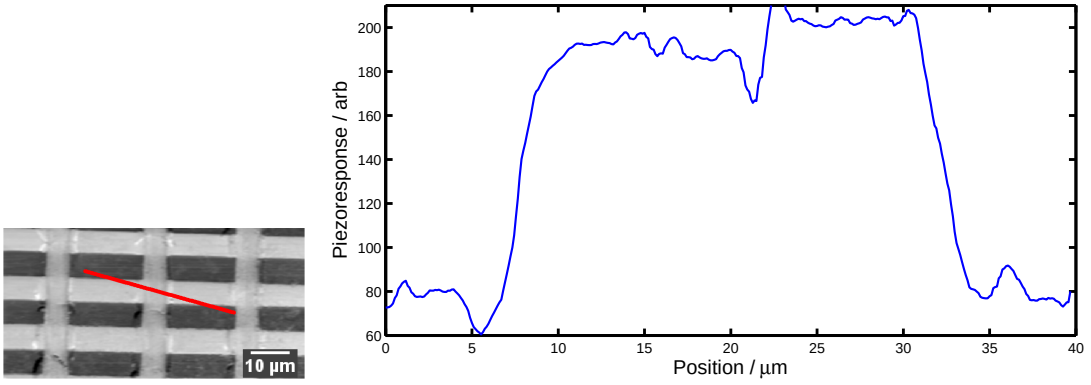

(a) PFM image (b) Piezoresponse plot of line indicated in red in (a)

FIGURE 3.19: Line plot of the piezoresponse across a path in the PPLN crystal encompassing bulk *+z* and *-z* domains and the area of *+z* domain scanned with the UV beam. The path is marked in (a) by a red line.

or *y* face PFM [43] it is not believe that these are suitable in this instance due to the presumed shallow depth of the structures and the influence of surface damage.

3.5 Model Hypothesis

The results presented earlier suggest that inverted ferroelectric domains are being formed during UV illumination. The UV laser induced ferroelectric domain inversion can be explained by considering an electric field formed by the separation of photo excited charges under the following reasoning.

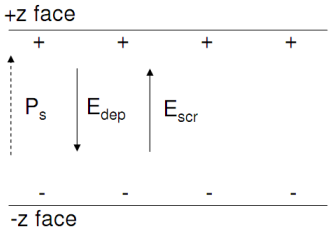

(a) Room temperature equilibrium

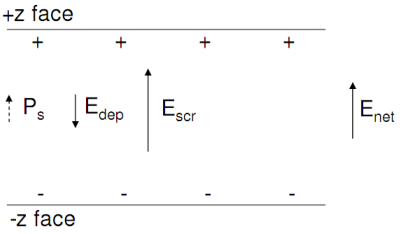

(b) Local heating reduces P_s and hence E_{dep}. E_{scr} is slow to react, thus leaving a net field E_{net}.

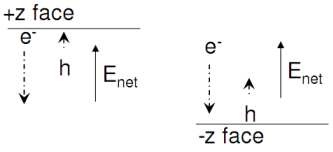

(c) Photo-excited charges at surface move in E_{net}. Electrons trapped at $-z$ face, holes trapped at $+z$ face.

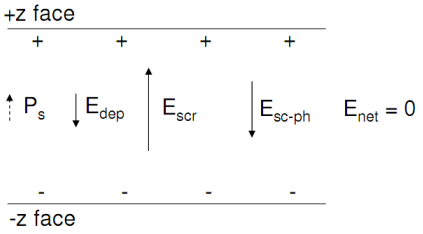

(d) Charge separation produces E_{sc-ph}. Equilibrium reached when $E_{net} = 0$

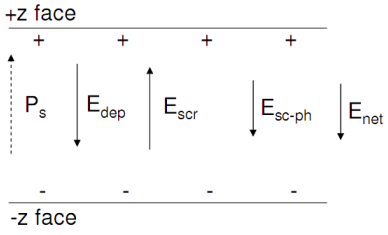

(e) When cool, P_s and hence E_{dep} increase, leaving a net field anti-parallel to P_s.

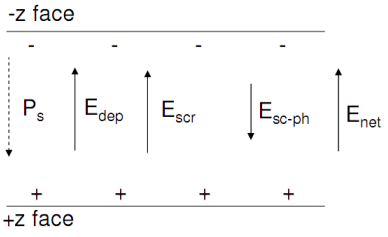

(f) If $E_{sc-ph} > E_c$ then P_s inverts.

FIGURE 3.20: Schematic of the proposed mechanism for domain inversion. Solid arrows represent electric field vectors. Other vectors represented by broken arrows for clarity.

LN is ferroelectric and so possesses a spontaneous electric polarization P_s which has associated with it an electric depolarisation field E_{dep}. At room temperature the unexposed crystal is in equilibrium and E_{dep} is screened by free charges and defects within the crystal [15] which create a compensation field, E_{scr}, with equal magnitude to E_{dep} and aligned parallel to P_s. This is shown schematically in figure 3.20(a). When the UV beam enters the crystal the energy is absorbed within the upper 50 nm ($1/e^2$ intensity absorption depth $\approx$ 30 nm) [44] and is mostly converted into heat, creating temperature distributions with spatial extents of the order of the beam width [45]. When the crystal is heated, P_s and consequently E_{dep} are decreased as the Li and Nb cations move toward the para-electric positions. E_{scr} is very slow to react [15] to changes in P_s and so a net field is left as E_{scr} now overcompensates E_{dep}, as shown in figure 3.20(b). At the same time, since the photon energy of the UV beam (5.1 eV) is greater than the LN band gap ($\approx$ 4 eV), photo-excitation occurs creating electron-hole pairs. Most will

re-combine and release their energy as heat. However, a fraction will survive and be free to travel within the crystal under the influence of both electric fields and concentration gradients. These photo-excited charges will see the net electric field, E_{net}, and will drift under its influence with holes moving toward the $+z$ face and electrons moving toward the $-z$ face, as shown in figure 3.20(c). It is worth noting here that charges excited between intrinsic energy bands in LN are not accelerated in the same way as those from defect levels and do not contribute to the bulk photovoltaic currents [46] as do impurity defects with energies within the band gap. The separated photo-excited charges will thus create a photo-induced space-charge field, E_{sc-ph}, anti-parallel to E_{scr}. If drift were the only driving force a maximum steady-state photo-induced field would be created that was equal to the vector sum of the E_{dep} and E_{scr} however charges also move by diffusion under the influence of concentration, and possibly thermal [45], gradients which may increase the magnitude of the photo-induced field. The field may also be increased by thermal [47] or photo-induced emission [48] of electrons from the surface. As the beam moves on, the crystal cools and P_s and, consequently, E_{dep} again increase. E_{dep} and E_{scr} now cancel leaving the net field in the crystal equal to E_{sc-ph}. If E_{sc-ph} is high enough it is energetically favourable for the spontaneous polarisation to align with the photo-induced field and the polarisation will be reversed. With reference to figure 3.20(e), in the boundaries of this simple model, domain inversion should occur only for $E_{sc-ph} > E_{scr}$ such that alignment of P_s with E_{sc-ph} would lower the total energy of the system. In the model above where E_{scr} remains constant, with magnitude equal to the room temperature depolarisation field, the estimate of the coercive field is the magnitude of E_{dep} and is given by

$$E_c = \frac{P_s}{\epsilon} \tag{3.1}$$

where ϵ is the permittivity along the z axis. The estimate of the coercive field above evaluates to 28,235 kV cm^{-1} using $\epsilon = 30\epsilon_0$ and $P_s = 0.75$ C m^{-2}. This is clearly greater than the experimentally determined coercive field of 210 kV cm^{-1} [15]. The experimentally determined coercive field does not in general agree with descriptions of ideal crystals but is found to be highly dependent upon defects within the crystal [49, 50], the existence of domain walls [49] or residual nanodomains [42] and upon behaviour of screening processes within the crystal [42]. In our case we also have the additional factor of a highly increased temperature which is known to alter the dynamics of both the defects [51, 52] and the intrinsic poling process. Thus it is highly likely that poling can be achieved even when E_{scr} is not completely compensated by E_{sc-ph} (figure 3.20(f)).

This model agrees well with the previously observed dependence of the domain width on speed and power as shown in figure 3.8. It was seen that the width of the domain inverted region had only a weak dependence upon scan speed but a very strong dependence upon power, which indicates that the effect is not simply a function of exposure. Although the

model requires photo-excited charges, the number density of which will be a function of exposure, the driving force for charge movement originates from the temperature distribution created by the heating laser. The temperature distribution has been shown in chapter 5 to be independent of scan speed for speeds below around 20 cm s^{-1} and hence independent of exposure. The strong temperature dependence and the requirement to be reasonably near the melting point can be understood with the model above by considering the steep change of P_s with temperature near the Curie point since $P_s \propto (T_c - T)^{1/2}$ [15] where T_c is the curie temperature.

Anisotropy between the behaviour on the two faces is expected under the following reasoning. The optical absorption depth is around 30 nm at the writing wavelength and so photo-excited charges can only be created within this depth. Thus the source of free charges able to create E_{sc-ph} is essentially two dimensional and located at the surface in a plane parallel to the surface. As can be seen in figure 3.20(c) the field E_{net} in which the photo-excited charges move is directed parallel to P_s regardless of which face is heated. Thus when heating the $+z$ face photo-excited holes will be trapped at the surface whilst photo-excited electrons will drift into the bulk of the crystal and, conversely, when the $-z$ face is heated photo-excited holes will drift into the bulk whilst photo-excited electrons will be trapped at the surface. If the mobilities of both electrons and holes were equal then the two situations would be similar and the same E_{sc-ph} would result. However, electron and hole mobilities are in general different with electrons being more mobile than holes with typical semiconductor mobility ratios of 3 (Si) to 23 (GaAs). Thus even from relatively simple consideration an anisotropy between the behaviour on the two z faces is expected.

In the experimental work and modelling described above, a laser wavelength of 244 nm has either been used or assumed for the incident light. As previously mentioned this wavelength has an optical absorption depth of 30 nm [44], which has two pertinent consequences with regard to the model described above. The first of these is that the length scale of the temperature distributions created by the beam are given by the beam radius, since the absorption depth is much less than the beam radius. The second is that the region in which photo-excited charges can be created is, of course, limited to the absorption depth. Since the ratio of the absorption depth to the beam radius is ≈ 80 the source of charges that can create the field E_{sc-ph} is essentially two dimensional and located at the surface. The limited depth of the charge source limits the distance over which charge separation can occur and hence the depth over which E_{sc-ph} extends. This then, ultimately, result in a limit to the depth of the domain formed. If a laser wavelength at which the optical absorption depth within the crystal is greater than the 30 nm optical absorption depth at $\lambda = 244$ nm, and that still has a photon energy greater than the band-gap, then the charge source will become extended in the depth direction and deeper

domains may be able to be formed. The optical absorption coefficient increases rapidly with decreasing wavelength near $\lambda = 244$ nm, so increasing the wavelength will increase the depth of the charge source. The temperature distributions within the crystal, and hence charge driving forces, would remain unchanged until the absorption depth was of equal magnitude to the beam radius.

A full numerical investigation of the charge and electric fields produced during UV laser exposure is required for validation of this qualitative model. Unfortunately, time has not allowed this within the duration of this thesis and this must be left as future work. The equations governing the charge transport have, however, been derived and this derivation is given in appendix C. The three coupled equations that govern the movement of optically excited charges are given below as

$$\frac{\mathrm{d}c_e}{\mathrm{d}t} = \frac{\hat{\mu}_e k_B T}{e}\nabla \cdot T\nabla c_e + \hat{\mu}_e \nabla \cdot c_e \mathbf{E} + Q_e \tag{3.2}$$

$$\frac{\mathrm{d}c_h}{\mathrm{d}t} = \frac{\hat{\mu}_h k_B T}{e}\nabla \cdot T\nabla c_h - \hat{\mu}_h \nabla \cdot c_h \mathbf{E} + Q_h. \tag{3.3}$$

and

$$\nabla \cdot \epsilon \mathbf{E} + \nabla \cdot \mathbf{P}_s = e(c_h - c_e) \tag{3.4}$$

where $c_{e,h}$ are the electron and hole concentrations, $\hat{\mu}_{e,h}$ are the electron and hole mobilities, k_B is the Boltzmann constant, T is the temperature, $Q_{e,h}$ are the source terms for electrons and holes, $\mathbf{E}$ is the electric field within the crystal, ϵ is the electrical permittivity tensor and $\mathbf{P}_s$ is the spontaneous polarisation vector. The electric field through the solution of the scalar potential and this is described in appendix C also. The source functions may be given by

$$Q^{e,h} = \frac{\eta I}{hc/\lambda} \tag{3.5}$$

where I is the local light intensity, h is Planck's constant, c is the speed of light, λ the wavelength of the light and η is a numerical factor describing the probability that an excited electron-hole pair avoid re-combination. The temperature can be treated as being independent from either the electric field or charge concentrations and may be calculated using the method described in chapter 5. As was described in the qualitative model above, the main driving force is provided by the temperature dependence of the spontaneous polarisation and this is given by the second term in equation 3.4. The precise form of the temperature dependence of the spontaneous polarisation is not quantified for LN fully between room temperature and the melting point, however phenomenological Landau theory [15, 53] predicts that near the Curie temperature the magnitude of the spontaneous polarisation should vary as

$$P_s = \beta(T_c - T)^{\frac{1}{2}} \tag{3.6}$$

where β is an experimentally determined constant. This function has been found to fit well to LT near T_c [53] and so should also be suitable for LN. An alternative, similar, expression has also been found as [54, pg. 185]

$$\frac{3}{2}\left(\frac{P_s}{P_0}\right)^2 = \left[1 + \frac{3}{4}\frac{(T_c - T)}{\Delta T_0}\right]^{\frac{1}{2}} - 1 \tag{3.7}$$

where $P_0 = 0.71$ C m^2 and $\Delta T_0 = 90$ °C. Solving equations 3.2, 3.3 and 3.4 in three spatial dimensions and time will be a demanding task, although some simplification may be possible from changing reference frames as was carried out in chapter 5.

In short we believe that domain formation is due to a space-charge field created by the combined effects of photo-excitation of charge and drift within an electric field, caused by the decrease of spontaneous polarisation at elevated temperatures, and that the different behaviour of the two faces is due to the different mobilities of electrons and holes.

3.6 Conclusion

In conclusion, it has been demonstrated domain inversion in congruent lithium niobate, iron-doped congruent lithium niobate and titanium in-diffused lithium niobate by a scanning continuous wave ultra-violet laser operating at a wavelength of 244 nm. The domain structures obtained have been analysed using piezoresponse force microscopy and by chemical etching in hydrofluoric acid, followed by surface profiling and scanning electron microscopy. The positive domains formed on the $-z$ face are also seen to contain self aligned nano-domains of negative polarity aligned along the x axes of the crystal. On the $+z$ face domain inversion can be seen at low powers, over the width of the exposed area, by etching. At higher powers domain inversion is not seen over the entire width of the exposure, however aligned nano-domains are seen within the exposed area. The domains formed on the $-z$ face at high powers have also been investigated by piezoresponse force microscopy. The piezoresponse of the UV written domains is seen to be reduced in comparison to bulk domains of the same polarity, however this has been shown not to be a result of surface melting but may be due to inhomogeneity or limited depth within the PFM sampling volume. A model is proposed whereby domain inversion is obtained through the action of a space-charge field of photo-excited charges and the differences of behaviour on the positive and negative faces can be explained by different electron and hole mobilities. Although not solved, the equations governing the model are derived.

Although we were unable to perform the experiments, we believe that by varying the illuminating laser wavelength to tune the optical absorption depth to a greater value the

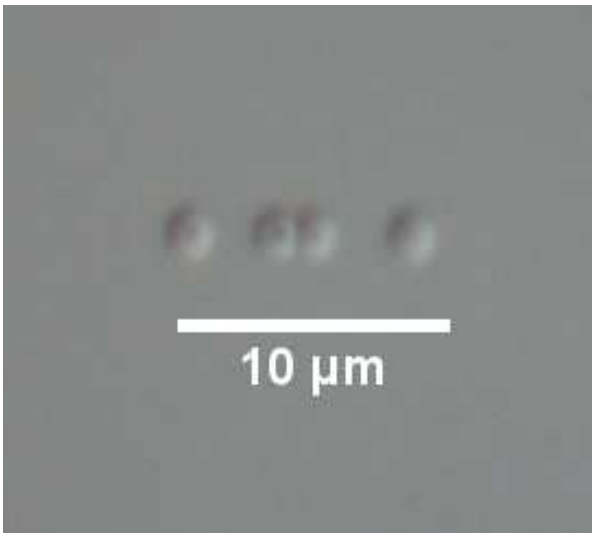

FIGURE 3.21: Micro-holes formed after laser illumination and etching.

depth of the domains will be increased. To increase the depth of the structure would certainly extend the range of possible application of domains written in this manner. Presently, the depth is too shallow for use in optical frequency generation through QPM, even when waveguide geometries are used. There are however uses that the technology can be applied to. It has certainly been shown that surface domain formation followed by chemical etching provides a simple and quick method for surface structuring which can itself be put to a wide variety of uses. The demonstration of etched ridge structures on titanium in-diffused planar waveguides makes possible the fabrication of strip-loaded waveguides [55] with no photolithography. The creation of shallow trenches on the $+z$ face could also be advantages to fields such as plasmonics due to the high etch resistance of the $+z$ face ensuring a high surface quality. Of course extended trenches are not the only structures that can be made as shown in figure 3.21 which shows an optical microscope image micro-holes ($< 2\mu$m) dots that have been created using the optical arrangement described in this chapter. The size of the dots is less than that of the beam that made them indicating that, with tighter focussing, small dots could be made that could usefully pattern substrates for uses in areas such as plasmonics. There is much work still to be done in the field of continuous wave AOP and, hopefully, the work carried out here has provided a substantial foundation.

References

[1] K. Nakamura and H. Shimizu. Hysteresis-free piezoelectric actuators using $LiNbO_3$ plates with a ferroelectric inversion layer. *Ferroelectrics*, 93:211 – 16, 1989.

[2] M. Ueda, H. Sawada, A. Tanaka, and N. Wakatsuki. Piezoelectric actuator using a $LiNbO_3$ bimorph for an optical switch. *IEEE 1990 Ultrasonics Symposium Proceedings (Cat. No.90CH2938-9)*, pages 1183 – 6, 1990.

[3] Hideki Yokoyama, Subaru Kudo, and Noboru Wakatsuki. Suppression of mechanical resonances of $LiNbO_3$ actuator with oppositely-polarized layers. *Japanese Journal of Applied Physics, Part 1: Regular Papers and Short Notes and Review Papers*, 38 (5 B):3334 – 3337, 1999.

[4] M. Yamada, M. Saitoh, and H. Ooki. Electric-field induced cylindrical lens, switching and deflection devices composed of the inverted domains in $LiNbO_3$ crystals. *Applied Physics Letters*, 69(24):3659 – 3661, 1996.

[5] S.J. Barrington, A.J. Boyland, and R.W. Eason. Domain-engineered lithium niobate as a medium for an integrated solid-state two-dimensional color laser scanning system. *Applied Optics*, 43(8):1625 – 7, 2004/03/10.

[6] Stephen J. Barrington, Alexander J. Boyland, and Robert W. Eason. Resolution considerations in electro-optic, single interface deflectors. *Applied Optics*, 43(5): 1038 – 1043, 2004.

[7] A.J. Boyland, G.W. Ross, S. Mailis, P.G.R. Smith, and R.W. Eason. Total internal reflection switching in electro-optically addressable domain-engineered $LiNbO_3$. *Electronics Letters*, 37(9):585 – 587, 2001.

[8] R.W. Eason, A.J. Boyland, S. Mailis, and P.G.R. Smith. Electro-optically controlled beam deflection for grazing incidence geometry on a domain-engineered interface in $LiNbO_3$. *Optics Communications*, 197(1-3):201 – 7, 15 Sept. 2001.

[9] J.A. Abernethy, C.B.E. Gawith, R.W. Eason, and P.G.R. Smith. Demonstration and optical characteristics of electro-optic bragg modulators in periodically poled lithium niobate in the near-infrared. *Applied Physics Letters*, 81(14):2514 – 16, 30 Sept. 2002.

[10] I.E. Barry, G.W. Ross, P.G.R. Smith, and R.W. Eason. Ridge waveguides in lithium niobate fabricated by differential etching following spatially selective domain inversion. *Applied Physics Letters*, 74(10):1487 – 8, 1999/03/08.

[11] I.E. Barry, G.W. Ross, P.G.R. Smith, R.W. Eason, and G. Cook. Microstructuring of lithium niobate using differential etch-rate between inverted and non-inverted ferroelectric domains. *Materials Letters*, 37(4-5):246 – 54, 1998/11/.

[12] C. Sones, S. Mailis, V. Apostolopoulos, I.E. Barry, C. Gawith, P.G.R. Smith, and R.W. Eason. Fabrication of piezoelectric micro-cantilevers in domain-engineered $LiNbO_3$ single crystals. *Journal of Micromechanics and Microengineering*, 12(1):53 – 7, 2002.

[13] L. E. Myers and W. R. Bosenberg. Periodically poled lithium niobate and quasi-phase-matched optical parametric oscillators. *IEEE Journal of quantum electronics*, 33:1663–1672, 1997.

[14] N.G.R. Broderick, G.W. Ross, H.L. Offerhaus, D.J. Richardson, and D.C. Hanna. Hexagonally poled lithium niobate: a two-dimensional nonlinear photonic crystal. *Physical Review Letters*, 84(19):4345 – 8, 2000.

[15] M. E. Lines and A. M. Glass. *Principles and Application of Ferroelectrics and Related Materials*. Clarenon Press, 1977.

[16] A.C. Busacca, C.L. Sones, V. Apostolopoulos, R.W. Eason, and S. Mailis. Surface domain engineering in congruent lithium niobate single crystals: A route to submicron periodic poling. *Applied Physics Letters*, 81(26):4946 – 4948, 2002.

[17] I.T. Wellington, C.E. Valdivia, T.J. Sono, C.L. Sones, S. Mailis, and R.W. Eason. Ordered nano-scale domains in lithium niobate single crystals via phase-mask assisted all-optical poling. *Applied Surface Science*, 253(9):4215 – 4219, 2007.

[18] C.E. Valdivia, C.L. Sones, J.G. Scott, S. Mailis, R.W. Eason, D.A. Scrymgeour, V. Gopalan, T. Jungk, E. Soergel, and I. Clark. Nanoscale surface domain formation on the +z face of lithium niobate by pulsed ultraviolet laser illumination. *Applied Physics Letters*, 86(2):022906 – 1, 2005.

[19] C.L. Sones, C.E. Valdivia, J.G. Scott, S. Mailis, R.W. Eason, D.A. Scrymgeour, V. Gopalan, T. Jungk, and E. Soergel. Ultraviolet laser-induced sub-micron periodic domain formation in congruent undoped lithium niobate crystals. *Applied Physics B: Lasers and Optics*, 80(3):341 – 344, 2005.

[20] V.Y. Shur, D.K. Kuznetsov, A.I. Lobov, E.V. Nikolaeva, M.A. Dolbilov, A.N. Orlov, and V.V. Osipov. Formation of self-similar surface nano-domain structures in lithium niobate under highly nonequilibrium conditions. *Ferroelectrics*, 341:85 – 93, 2006.

[21] C.L. Sones, M.C. Wengler, C.E. Valdivia, S. Mailis, R.W. Eason, and K. Buse. Light-induced order-of-magnitude decrease in the electric field for domain nucleation in MgO-doped lithium niobate crystals. *Applied Physics Letters*, 86(21): 212901 –, 2005.

[22] V. Dierolf and C. Sandmann. Direct-write method for domain inversion patterns in $LiNbO_3$. *Applied Physics Letters*, 84(20):3987 – 9, 2004/05/17.

[23] Christian Sandmann and Volkmar Dierolf. The role of defects in light induced domain inversion in lithium niobate. *Physica Status Solidi C: Conferences*, 2(1): 136 – 140, 2005.

[24] G.W. Ross, P.G.R. Smith, and R.W. Eason. Optical control of electric field poling in $LiTaO_3$. *Applied Physics Letters*, 71(3):309 – 11, 1997.

[25] M.C. Wengler, M. Muller, E. Soergel, and K. Buse. Poling dynamics of lithium niobate crystals. *Applied Physics B: Lasers and Optics*, 76(4):393 – 396, 2003.

[26] M.C. Wengler, B. Fassbender, E. Soergel, and K. Buse. Impact of ultraviolet light on coercive field, poling dynamics and poling quality of various lithium niobate crystals from different sources. *Journal of Applied Physics*, 96(5):2816 – 2820, 2004.

[27] M. Muller, E. Soergel, and K. Buse. Influence of ultraviolet illumination on the poling characteristics of lithium niobate crystals. *Applied Physics Letters*, 83(9): 1824 – 6, 2003.

[28] M.C. Wengler, U. Heinemeyer, E. Soergel, and K. Buse. Ultraviolet light-assisted domain inversion in magnesium-doped lithium niobate crystals. *Journal of Applied Physics*, 98(6):064104 –, 2005.

[29] H.A. Eggert, F. Kalkum, M.C. Wengler, U. Heinemeyer, and K. Buse. Light-assisted generation of tailored ferroelectric domain structures. *Ferroelectrics*, 340: 63 – 7, 2006.

[30] M. Fujimura, T. Sohmura, and T. Suhara. Fabrication of domain-inverted gratings in MgO:$LiNbO_3$ by applying voltage under ultraviolet irradiation through photomask at room temperature. *Electronics Letters*, 39(9):719 – 721, 2003.

[31] M. Houe and P.D. Townsend. Thermal polarization reversal of lithium niobate. *Applied Physics Letters*, 66(20):2667 – 9, 1995.

[32] C.E. Valdivia, C.L. Sones, S. Mailis, J.D. Mills, and R.W. Eason. Ultrashort-pulse optically-assisted domain engineering in lithium niobate. *Ferroelectrics*, 340:75 – 82, 2006.

[33] S. Mailis, C. E. Valdivia, C. L Sones, A. C. Muir, and R. W. Eason. Latent ultrafast laser-assisted domain inversion in congruent lithium niobate. In *CLEO-Europe/IQEC. CE7-2-THU*, 2007.

[34] T. Jungk, A. Hoffmann, and E. Soergel. Quantitative analysis of ferroelectric domain imaging with piezoresponse force microscopy. *Applied Physics Letters*, 89(16): 163507 –, 2006.

[35] E. Soergel. Visualization of ferroelectric domains in bulk single crystals. *Applied Physics B: Lasers and Optics*, 81(6):729 – 752, 2005.

[36] C. L. Sones, S. Mailis, W. S. Brocklesby, R. W. Eason, and J. R. Owen. Differential etch rates in z-cut $LiNbO_3$ for variable HF/HNO_3 concentrations. *J. Mater. Chem*, 12:295–298, 2002.

[37] S. Mailis, C. Riziotis, I.T. Wellington, P.G.R. Smith, C.B.E. Gawith, and R.W. Eason. Direct ultraviolet writing of channel waveguides in congruent lithium niobate single crystals. *Optics Letters*, 28(16):1433 – 1435, 2003.

[38] W Yang, P. G. Kazansky, and Y. P. Svirko. Non-reciprocal ultrafast laser writing. *Nature Photonics*, Online, 2008.

[39] T.J. Sono, J.G. Scott, C.L. Sones, C.E. Valdivia, S. Mailis, R.W. Eason, J.G. Frey, and L. Danos. Reflection second harmonic generation on a z-cut congruent lithium niobate crystal. *Physical Review B (Condensed Matter and Materials Physics)*, 74 (20):205424 – 1, 2006.

[40] V.Ya. Shur, E.L. Rumyantsev, E.V. Nikolaeva, E.I. Shishkin, D.V. Fursov, R.G. Batchko, L.A. Eyres, M.M. Fejer, and R.L. Byer. Nanoscale backswitched domain patterning in lithium niobate. *Applied Physics Letters*, 76(2):143 – 145, 2000.

[41] D.A. Scrymgeour, V. Gopalan, A. Itagi, A. Saxena, and P.J. Swart. Phenomenological theory of a single domain wall in uniaxial trigonal ferroelectrics: lithium niobate and lithium tantalate. *Physical Review B (Condensed Matter and Materials Physics)*, 71(18):184110 – 1, 2005.

[42] V. Y. Shur. Kinetics of ferroelectric domains: Application of general approach to $LiNbO_3$ and $LiTaO_3$. *Journal of Materials Science*, 41(1):199 – 210, 2006.

[43] T. Jungk, A. Hoffmann, and E. Soergel. Contrast mechanism for the detection of ferroelectric domains on the non-polar faces of $LiNbO_3$ using piezoresponse force microscopy. *arXiv*, cond-mat 0803.0171, 2008.

[44] A.M. Mamedov. Optical properties (VUV region) of $LiNbO_3$. *Optics and Spectroscopy*, 56(6):645 – 9, 1984.

[45] A.C. Muir, G.J. Daniell, C.P. Please, I.T. Wellington, S. Mailis, and R.W. Eason. Modelling the formation of optical waveguides produced in LiNbO $_3$ by laser induced thermal diffusion of lithium ions. *Applied Physics A: Materials Science and Processing*, 83(3):389 – 396, 2006.

[46] K. Buse. Light-induced charge transport processes in photorefractive crystals. I. models and experimental methods. *Applied Physics B (Lasers and Optics)*, B64(3): 273 – 91, 1997.

[47] E.M. Bourim, C.-W. Moon, S.-W. Lee, and In Kyeong Yoo. Investigation of pyroelectric electron emission from monodomain lithium niobate single crystals. *Physica B*, 383(2):171 – 82, 2006.

[48] G.I. Rozenman. Photoinduced exoemission from lithium niobate. *Soviet Physics - Solid State*, 30(8):1340 – 2, 1988.

[49] Sungwon Kim, V. Gopalan, and A. Gruverman. Coercive fields in ferroelectrics: A case study in lithium niobate and lithium tantalate. *Applied Physics Letters*, 80 (15):2740 – 2, 2002.

[50] A.K. Bandyopadhyay and P.C. Ray. Perturbation analysis and memory in ferroelectric materials. *Journal of Applied Physics*, 95(1):226 – 30, 2004.

[51] A.V. Yatsenko, E.N. Ivanova, and N.A. Sergeev. NMR study of intrinsic defects in congruent $LiNbO_3$. 1. "unoverlapping" defects. *Physica B*, 240(3):254 – 62, 1997.

[52] A.V. Yatsenko, H.M. Ivanova-Maksimova, and N.A. Sergeev. NMR study of intrinsic defects in congruent $LiNbO_3$. 2. "overlapping" defects. *Physica B*, 254(3-4):256 – 9, 1998.

[53] A. M. Glass. Dielectric, thermal , and pyroelectric properties of ferroelectric $LiTaO_3$. *Physical Review*, 172:564–571, 1968.

[54] A. M. Prokhorov and Yu. S. Kuz'minov. *Physics and chemistry of crystalline lithium niobate*. Hilger, IOP Publishing Ltd, Bristol, BS1 6NX, England, 1990.

[55] Naoya Uchida. Optical waveguide loaded with high refractive-index strip film. *Appl. Opt.*, 15(1):179, 1976.

Chapter 4

UV Continuous Wave Latent Light-Impeded Poling

The previous chapter has shown that focussed UV laser light can of produce space-charge fields within the crystal that are capable of ferroelectric domain inversion. In this chapter the interaction of the induced space charge field with domains created during a subsequent electric field poling step is investigated. It is seen that when the $+z$ face is illuminated and then subsequently poled using a conventional electric field poling arrangement, the illuminated regions remain as $+z$ islands within a background of newly poled -z domain. It is seen that the inhibited domains are not restricted in their shape or alignment by the crystal axes. The formation of these inhibited domains is seen to be dependent upon not only the illumination conditions but also the dynamics of the poling step.

The experimental method is outlined in section 4.1 and the results are presented and analysed in section 4.2. The poling process is visualised using an optical method, and recorded via a CCD camera, and the structures are interrogated using PFM and by etching in HF acid followed by optical microscopy and SEM. In section 4.3 the experimental results are discussed with reference to the domain interactions with the charge distributions that would be produced under the model of section 3.5. Conclusions are made in section 4.4.

4.1 Experimental Method

A beam from a frequency-doubled Ar-ion laser was focused to a spot size of 2.5 μm on the +z or -z face of either an un-doped congruent or 5 mol % MgO-doped LN crystal.

Positioning and exposure control of the crystal was achieved by a computer-controlled, three-axis stage system coupled with a mechanical shutter. For dynamic exposures, sets of parallel lines were drawn on the z faces of the crystals along the crystallographic x or y directions by moving the stages at speeds ranging from 0.05 - 0.3 mm s^{-1}. For static exposures, arrays of illuminated spots with identical exposure times, ranging from a few milliseconds to a few tens of seconds, were formed. The separation between the edges of adjacent illuminated spots in the arrays varied from zero to 6 μm which permitted us to verify if any proximity effect existed such as that observed in pulsed laser direct poling [1] where the closest approach observed there was of order $\sim 1.5\mu$m, irrespective of illuminated pattern resolution. For both types of exposure, the power was varied between 20 - 28 mW. Each set of illumination conditions was duplicated for both +z and -z face illumination, to allow a direct comparison of the resultant effects on each of these polar faces. The samples were then poled using the electric field poling (EFP) set-up described in reference [2]. Using this arrangement in-situ monitoring of the poling process was available using crossed polarisers and the induced birefringence at domain walls to track the wall movement. This was recorded to computer using a CCD camera. The voltage was ramped at 2 kV/min to a value of ~10.1 kV, corresponding to an electric field of 20.2 kV/mm across the 0.5 mm thick sample. This value of the applied electric field ensures that domain inversion occurs slowly, which is desirable since the kinetics of the domain wall motion is seen to influence greatly the shape and quality of the resultant structures. Etching of the poled crystal in aqueous HF acid solution then allows visualisation of the formed domain structures through the different etch rates of the two z faces [3]. PFM was also used to verify the domain nature of these structures. Lastly, the samples were imaged using SEM and optical microscopy.

4.2 Experimental Results

4.2.1 -*z* Face Illumination

Illumination of the -*z* face was not seen to result in domain inhibition but rather was seen to initiate nucleation of domains. The growth of the domains after nucleation, however, was seen to be greatly affected by the illumination of the surface. For an unexposed crystal, during nucleation and growth of a domain, our visualisation method would initially show a small black domain dot which would then resolve into a hexagonally shaped domain. This domain would then grow through two dimensional domain wall growth as described in [4]. This was not seen to occur when the -*z* face had been illuminated. Figure 4.1 shows the visualised domains after growth initiated at a nucleation site in an illuminated region. The region to the left contains 4 sets of 8 lines spaced 50μm apart

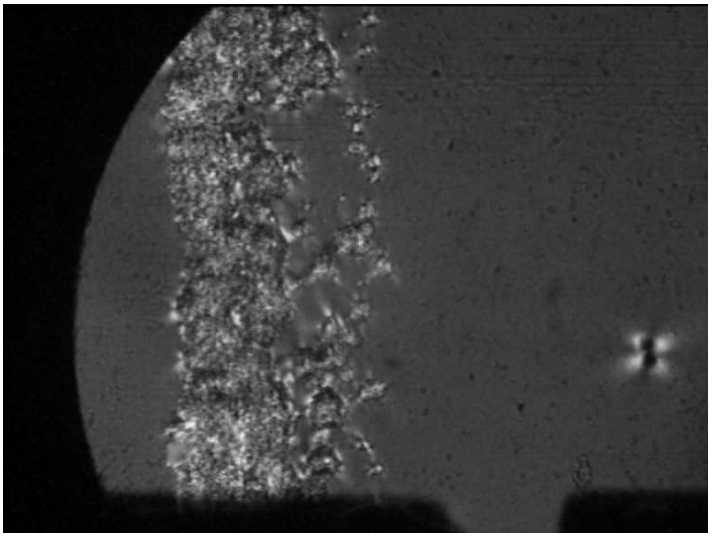

FIGURE 4.1: Captured video frame of poling process viewed under crossed polarisers. Area to the left corresponds to domains nucleated on the exposed regions after subsequent random growth. Width of area to left ~ 2 mm.

with sets spaced by 100μm and so extends around 2 mm in width. The growth of the domains seems random and un-correlated and does not follow the symmetry of the crystal structure at all. It is interesting that this behaviour extends far from the illuminated region both laterally from the exposed area and in depth. It can clearly be seen that nucleation occurs preferentially in the illuminated area. Figures 4.2(a) and 4.2(b) show microscope images of the illuminated faces after brief etching in HF for around 15 mins where positive domains appear smooth and bright and -z domains appear rough and dull. The crystal was not poled completely since the electric field was removed before this occurred and in the sample imaged in figure 4.2 domains were not seen to reach the $+z$.

4.2.2 $+z$ Face Exposures

Figure 4.3 shows the first observation of the latent light impeded poling effect. Whilst applying a voltage to try to push the directly written domains of the previous chapter (chapter 3) deeper within the crystal some small areas were seen to pole as bulk domains. The field was removed and the sample etched to investigate whether the directly written domains were indeed pushed deeper and it was seen that where bulk domains had formed in exposed areas positive domains were left where the beam had been scanned. Further exposures were then made to study this effect in its own right.

Arrays of dots were produced covering the same are of the crystal ($100 \times 100\mu$m) and with the same exposure conditions of incident power, 26 mW, and dwell time, 100 ms,

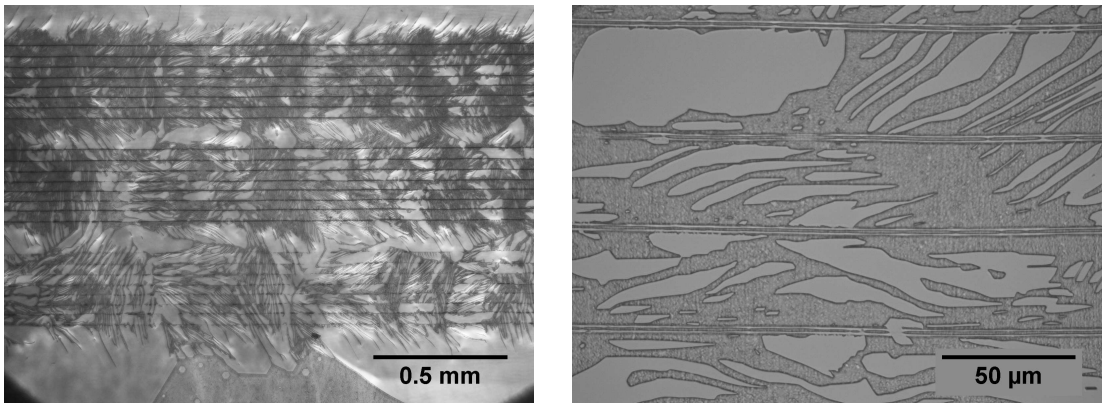

(a) Low magnification (b) High magnification

FIGURE 4.2: Optical microscope images of -z exposures between 20 and 24 mW at a velocity of 100μm s^{-1} after poling and brief etching.

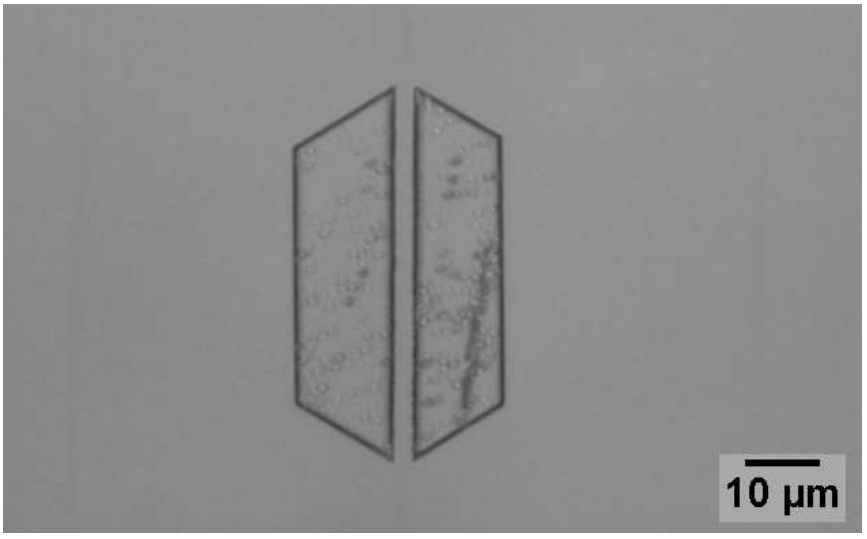

FIGURE 4.3: First observation of latent light impeded poling. The impeded poling region can clearly be seen as the line of positive domain within the small hexagonal negative domain that has been revealed by etching.

but with different dot separations of 4, 6, 8, 10 and 12 μm. Figures 4.4 and 4.5 show two SEM images of dot arrays after poling and etching. There was no interaction observed between neighbouring dots in as much as no significant deviation of either size or shape was observed with varying distance between exposures. This allows structuring on extremely small scales as can be seen in figure 4.5 where separations of less than one micron can be seen. As the exposures overlap, so too do the resultant domains and this can be seen on the left edge of figure 4.4.

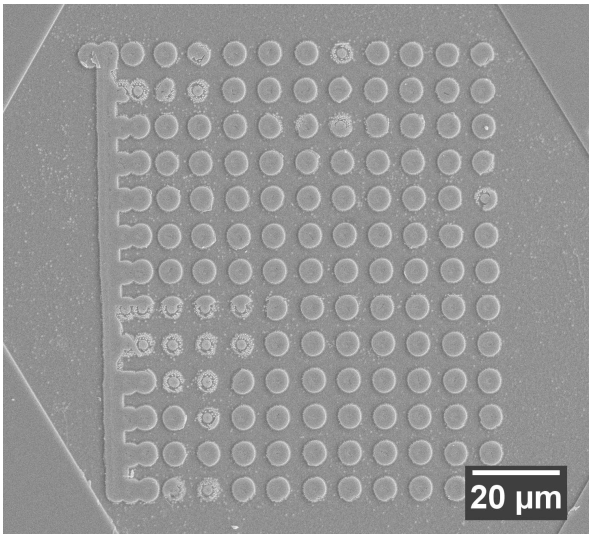

FIGURE 4.4: SEM image of a poling inhibited dot array

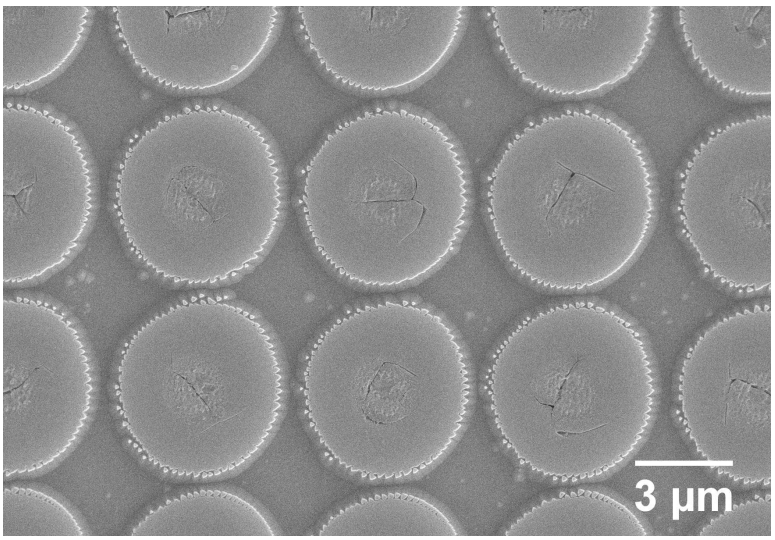

FIGURE 4.5: High magnification SEM image of a poling inhibited dot array

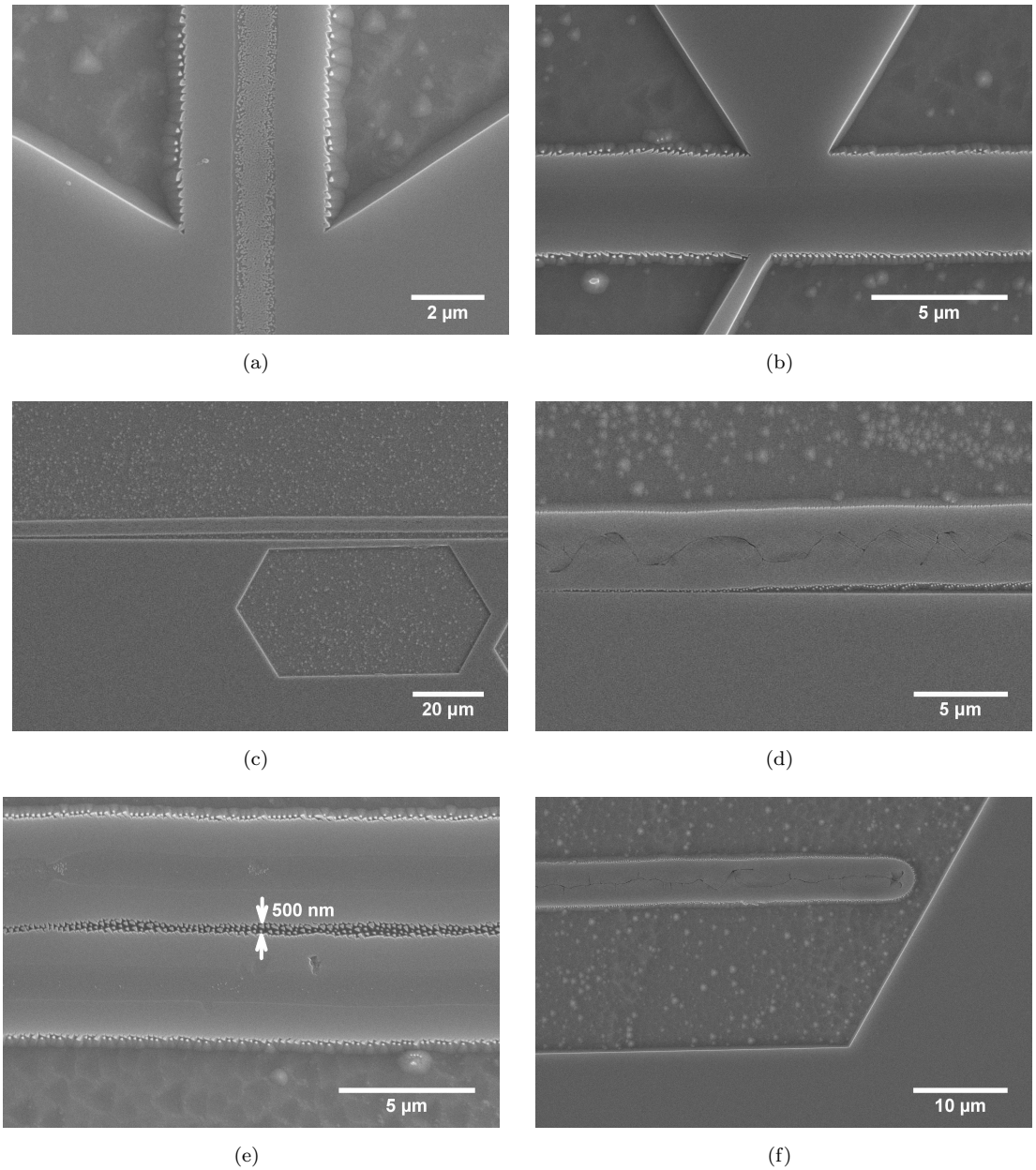

(a) (b)

(c) (d)

(e) (f)

FIGURE 4.6: SEM images of poling inhibited regions caused by scanning exposures.

Scanned exposures were also investigated and SEM images of some examples after poling and brief etching are shown in figure 4.6. In figures 4.6(a), 4.6(b), 4.6(c), 4.6(d) and 4.6(f) bulk positive domains can be seen, since the poling field was removed before the crystal could pole completely, and these can be differentiated from the poling inhibited regions from their characteristic smooth walls. All exposures are of similar conditions to those of the previous subsection, sec 3.2, and so the first thing to notice is that the features seen during exposures on the $+z$ face during direct pole experiments are, of course, still present. Trenches corresponding to low power direct optical poling can be seen in figures 4.6(b) and 4.6(e) and the cracks and domain-like features aligned to the x-axes can be seen in figures 4.6(d) and 4.6(f). It can be seen that the impeded poling effect extends further than the direct poling effect, with the width of the poling impeded structures being approximately three times that of the direct-pole features seen in the centre of the exposures. Similar to static exposures, structures could be written with arbitrary separations. Figure 4.6(e) shows the structure created after scanning two lines such that the exposures nearly overlap. The negative domain left between the two poling inhibited domains measures just 500 nm in width. Similarly small distances can be seen between the poling impeded domains and the regular bulk domains in figures 4.6(c) and 4.6(d). These figures also show that the impeded poling domains do not need to align along the crystal axes since the line of the impeded domain is seen to divert away from the wall of the bulk domain, which is directed strictly along the y axis [5]. It was seen throughout the impeded poling experiments that bulk domains would often be pinned at the scanned exposed lines such as in figure 4.6(c) and that, once a domain had encountered a scanned line, subsequent growth of the domains tended to be along the length of the scanned line, leading to asymmetric domains rather than the regular-hexagonal domains favoured by the virgin material. This can be seen in figure 4.7 which shows a video still sequence captured during a poling cycle. It can be seen in the figure that the nucleation is occurring nearly entirely along the illuminated lines and that the growth has a very preferential direction along the length of the lines. The figure also gives a good indication of the time scales of the poling process that was found to be optimal. The growth of the domains was not seen to proceed at a constant rate, particularly when the domain size became large. This can be seen in figures 4.7(h-i) where the domain in the lower right has grown suddenly as compared to its previous growth rate. The non-regular hexagonal shape of the domains is also clear to see, although the shape remains a six-sided polygon with sides aligned to the y axes of the crystal.

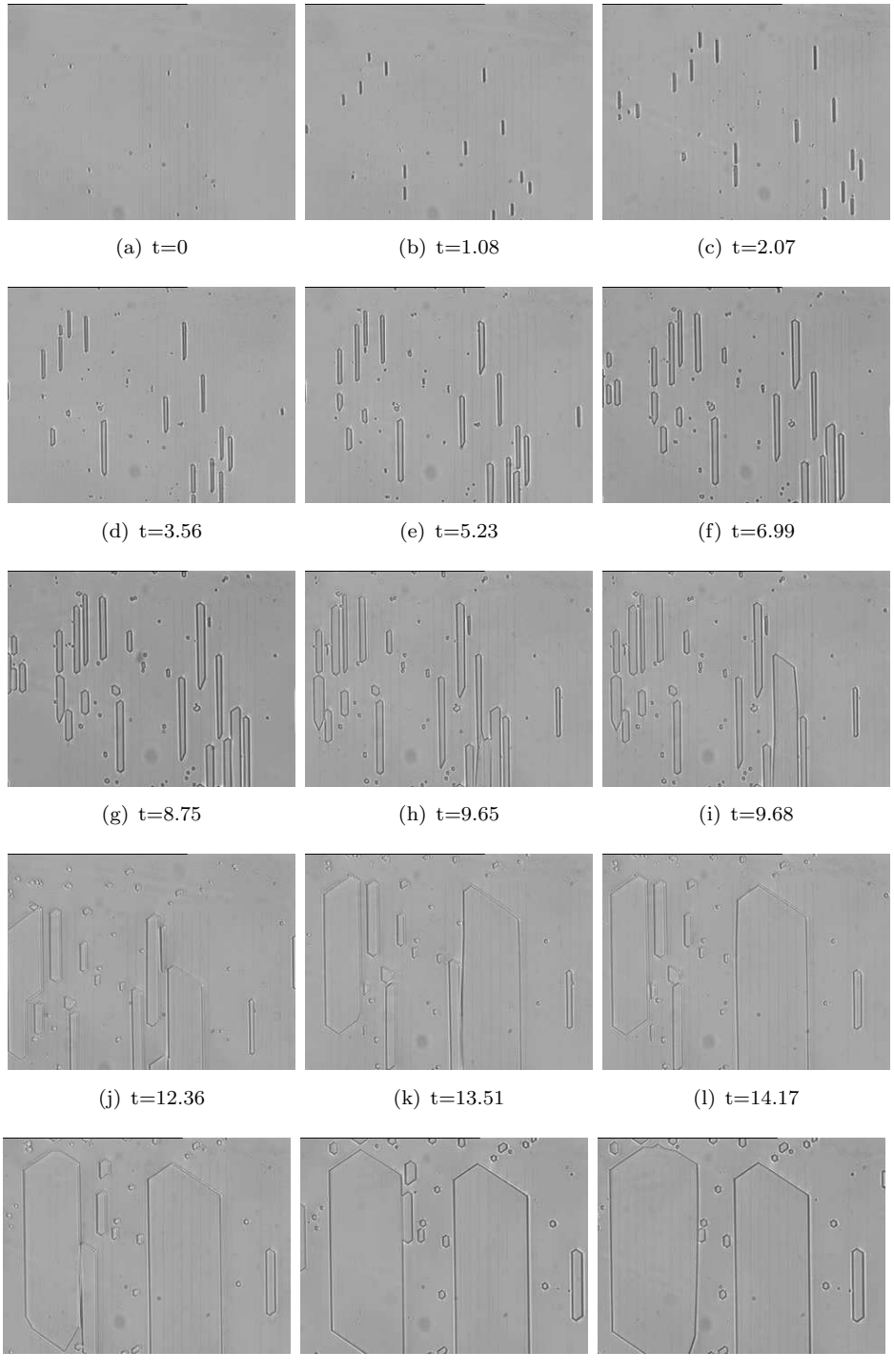

(a) t=0 (b) t=1.08 (c) t=2.07

(d) t=3.56 (e) t=5.23 (f) t=6.99

(g) t=8.75 (h) t=9.65 (i) t=9.68

(j) t=12.36 (k) t=13.51 (l) t=14.17

(m) t=18.12 (n) t=20.35 (o) t=21.40

FIGURE 4.7: Video stills showing the influence of scanned UV exposures on the $+z$ face on the poling process. Time (t) in minutes.

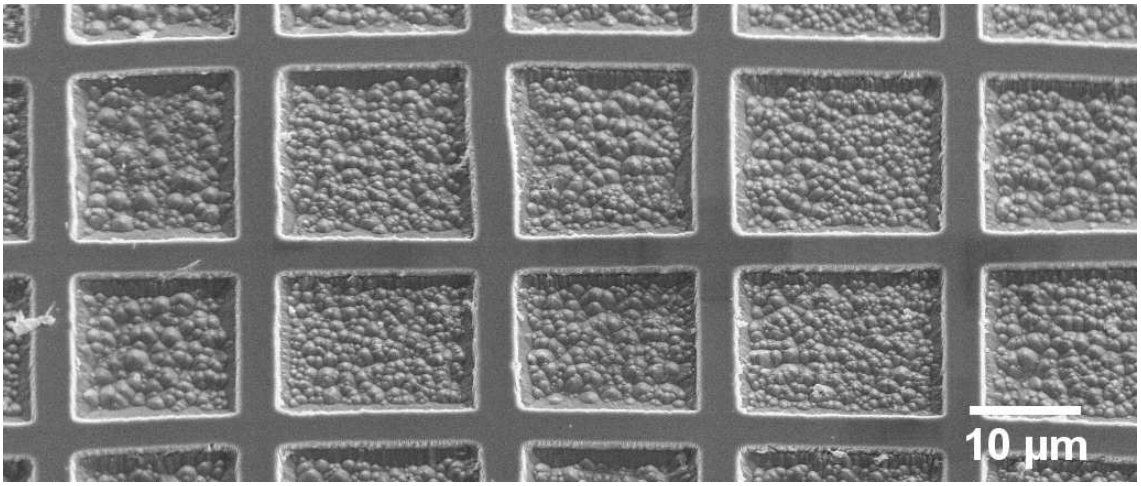

FIGURE 4.8: SEM image of a poling inhibited cross hatched pattern with lines written along the x and y axes.

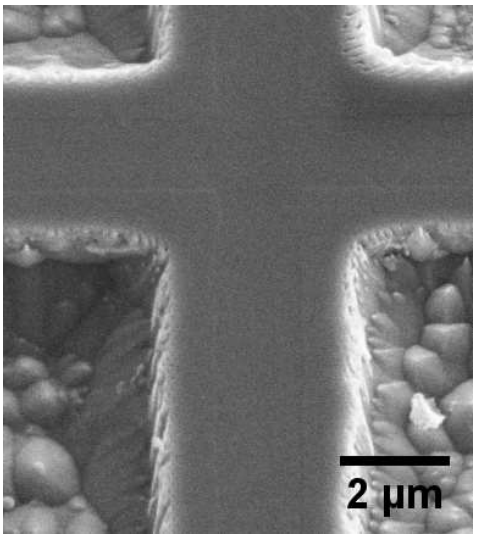

FIGURE 4.9: High magnification SEM image of a crossing region in the poling inhibited cross hatched pattern shown in figure 4.8.

Additional scanned UV exposure of a specific area was not observed to produce any further effect. This can be seen in figure 4.8 where a cross-hatched pattern is shown as a result of sequential line scans along the x and y crystallographic axes. A higher magnification SEM image that shows the quality of the overlapped exposure is shown in figure 4.9. The sample was tilted by 30 during the SEM scan which allows the observation of the quality of the side wall of the pole-inhibited domain.

The polarity of the inhibited domains was further investigated by PFM which confirmed the observations deduced by chemical etching. Figure 4.10 shows a PFM image of an area of the crystal that carries a set of static dot illuminations. Again, the poling

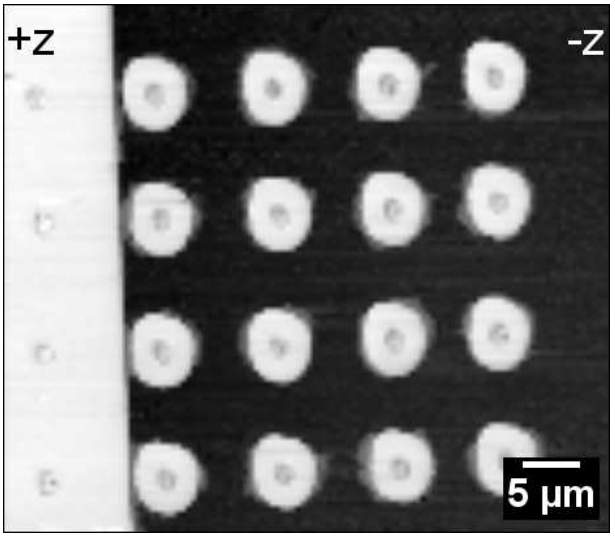

FIGURE 4.10: PFM image of poling inhibited dot array. White = *+z* face, black = *-z* face as indicated. White area to left of image is an un-poled bulk domain.

field was removed before complete inversion of the crystal could take place and so both positive and negative bulk domains are present as is required for the full calibration of the PFM scan. Full contrast is associated with opposite ferroelectric domains where a +z face appears white (left section of the image) while a -z face appears black (right larger section of the image). The dots which appear white in a black background of the PFM image correspond to the UV exposed areas which have maintained their original domain orientation (+z) while the surrounding area has been inverted (-z) and appears black. PFM measurements were made on static exposures with powers ranging from 24.5 to 26.5 mW and exposure times ranging from 50 to 500 ms and the full contrast was seen in all. To make it easier to identify the exposed areas the sample was etched very briefly in HF. This gave a surface relief of only around 80 nm but enabled verification of whether the entire region of etch resistance was, in fact, a positive domain since PFM also records topographic information. Figure 4.11 shows the piezoresponse and topography across the line indicated in figure 4.12. The correlation between the two signals is very good, indicating that the entire area that resists etching is indeed due to a retainment of the original polarisation during poling.

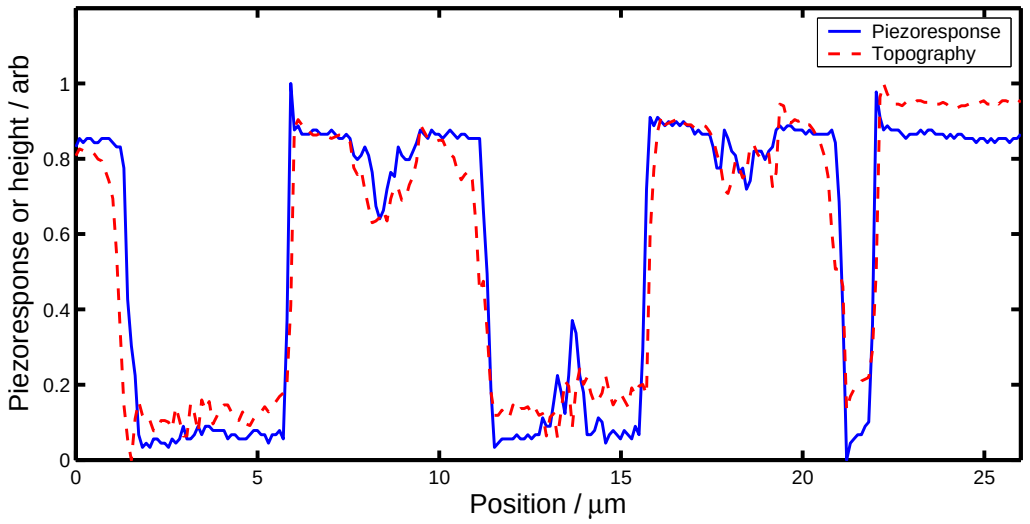

FIGURE 4.11: Comparison of the piezoresponse and topography signals from the PFM across the line shown in figure 4.12.

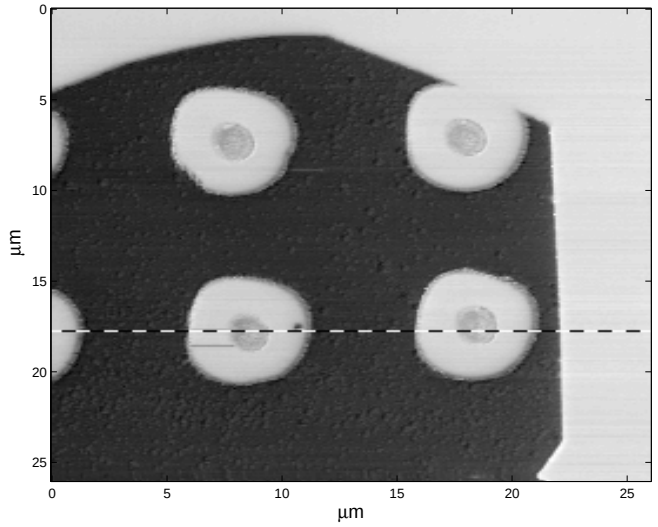

FIGURE 4.12: Piezoresponse image showing the area used in comparing the piezoresponse and topography in figure 4.11.

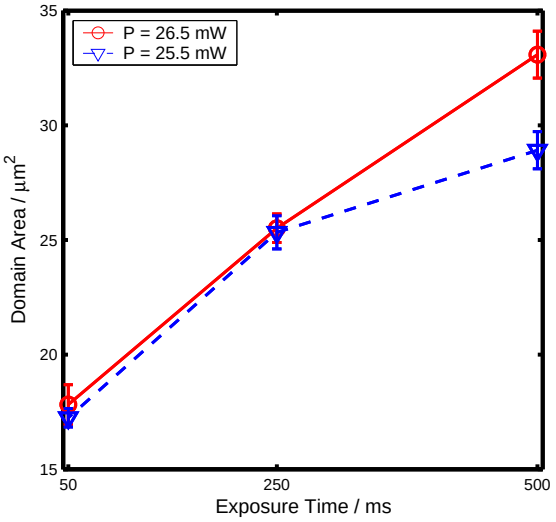

FIGURE 4.13: Variation in inhibited domain area from static exposures as measured from piezoresponse images. Error bars show standard deviations from repeat measurements.

The width of the area over which inhibition occurs is seen to be dependent upon both the incident power and the dwell time or scanning velocity of the beam with larger domains formed for longer dwell or lower scan speeds. Figure 4.13 shows the variation of the area of poling inhibited dots with exposure time for two different powers as measured from the piezoresponse images. In the figure the dependence upon the exposure time is clear, but the dependence upon power is less distinct due to the small difference in the powers used. It is interesting to note, however, that static and scanned exposures with equivalent exposures have not produced equivalent domain widths. A scanned exposure with a power of 24 mW and velocity of 100 μm s^{-1} gives a domain with width of 3.6 μm and corresponds to an exposure time of 5 μm/100 μm s^{-1} = 50 ms. A corresponding static exposure with a power of 24 mW results in a circular domain spot with diameter of 4.7 μm. To achieve the same domain width in a static exposure at 100 μm s^{-1} a power of around 28 mW must be used.

Attempts were made to measure the depth of the domain inhibited regions through cutting, polishing and then etching the y faces of the exposed regions. Unfortunately, the results were inconclusive due to the damage to the upper edge during polishing. This prevented a thorough characterisation but did allow an estimate of the upper limit to the depth to be made of $\sim 1\mu$m. A lower limit to the depth of the inhibited domains is given by PFM as it has a depth sensitivity of $\sim$100 nm as stated in chapter 3. Since the inhibited domains give a full contrast, 100 nm can be taken as a lower limit to their depth.

The quality of the poling inhibited regions was observed to be highly dependant upon

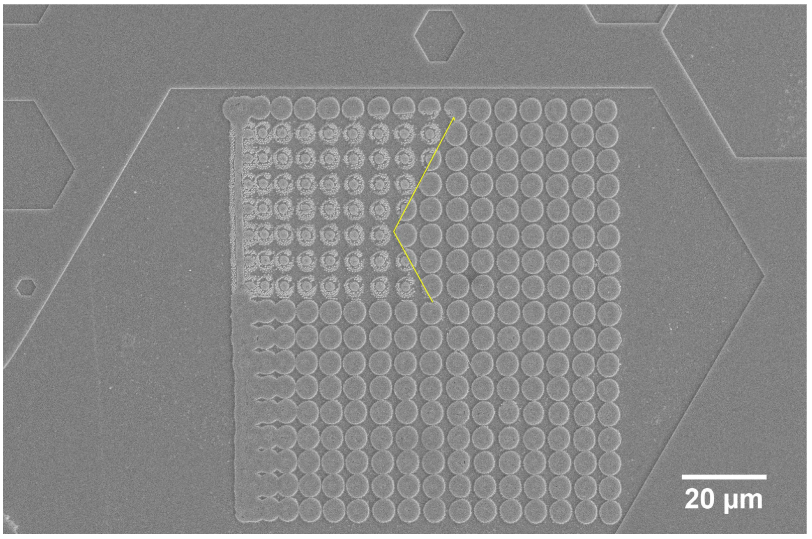

FIGURE 4.14: SEM image of a static dot array exposure. Region to the top left where dot domains are fragmented corresponds to a region of fast bulk domain growth. Line indicates the position of the domain labelled A in figure 4.15(a).

the domain wall kinetics during the EFP step. It was seen that when the wall movement was smooth and reasonably slow, the inhibition process produced continuous domains, when the domain wall movement was fast the domain inhibition occurred only partially or did not occur at all. Figure 4.14 shows an SEM image of the resultant domain pattern for a situation in which two domains have joined in a fast 'gulping' [4] manner and figure 4.15 shows video stills of the poling process. Where the two domains have previously grown slowly, the inhibited domains are fully formed as can be seen in figure 4.14, corresponding to times before figure 4.15(b). The position of the walls of the domain labelled A in figure 4.15(a) is shown in figure 4.14 where the distinction between fully inhibited and fragmented domains can be seen. The fast movement of the walls during the rapid merging of the domains between figures 4.15(b) and 4.15(d), which are successive frames taken at a frame rate of 30 frames per second giving a domain wall velocity during this stage of approximately 1.5 mm s^{-1}, can then be seen to correspond to the region of fragmented domain inhibition in figure 4.14. As the domain wall movement slows, the domain inhibition becomes complete again as can be seen at the top of dot array in figure 4.14.

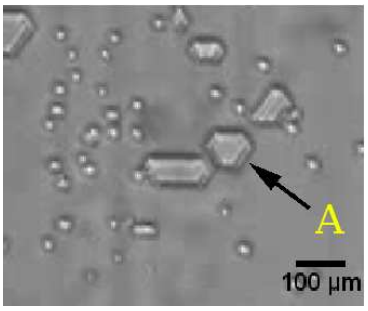

(a) t=0

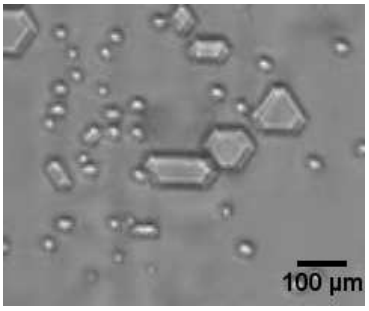

(b) t=69.400

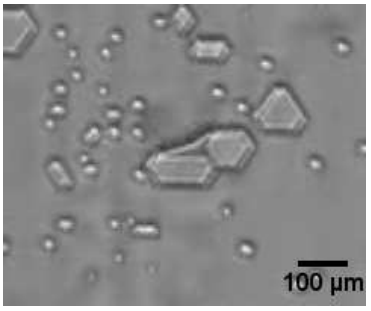

(c) t=69.433

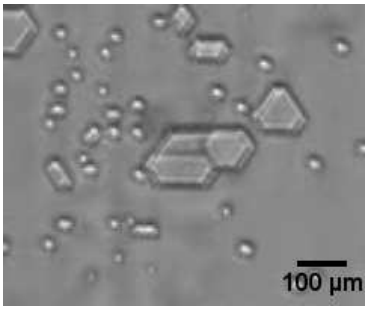

(d) t=70.467

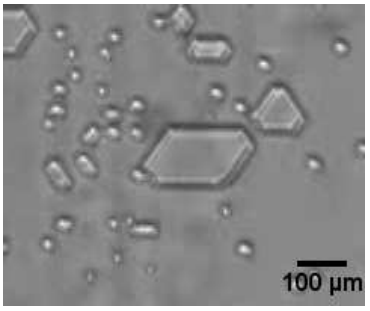

(e) t=80

FIGURE 4.15: Video stills sequence of fast domain movement leading to fragmentation of inhibited domains seen in figure 4.14. Time is measured in seconds relative to the first frame.

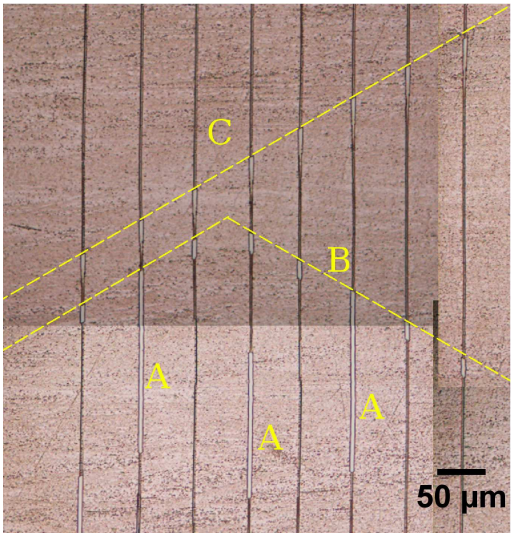

FIGURE 4.16: Optical microscope image of domain inhibited regions after higher voltage EFP. A - initial slow growth domains. B - bounding line of first fast growth. C - bounding line of second fast growth.

In congruent crystals the domain wall movement can often progress in a 'jerky' manner [4, 6]. As it was previously shown, this leads to an incomplete domain inhibition or no inhibition at all. This effect was seen to be increasingly prominent at higher poling voltages and hence led to the realisation that low voltage, slow, poling was essential. Figure 4.16 shows the results obtained when a higher poling voltage is used, leading to more energetic domain wall movement. Three distinct domain growth features can clearly be seen in the figure. The initial domains that have grown along the lines, as in figure 4.7, are labelled as A. In these areas the initial growth was slow and inhibition is complete. A sudden domain growth, with fast wall movement, has occurred to merge the initially separate A domains and possibly others not visible in the figure to form a domain bounded by the line B. During the fast motion of the wall, domain inversion is not inhibited at all but at the end of the motion the domain wall decelerates, allowing the inhibition process to occur. At a later time the domain bounded by line B grows through fast wall motion to form a domain bounded by the line C. Possibly due to the larger size of the domain, the wall deceleration appears to be more gradual, and a smoother transition from non-inhibiting to inhibiting behaviour can be seen as a tapering of the inhibited domain. This is shown in higher magnification in figure 4.17. In each of these figures the alignment of the domain walls can clearly be seen from the shape of the ends of the inhibited domains. In MgO doped crystals where EFP is known to be slower [7, 8] and smoother, the inhibited domains appeared to be smooth and continuous everywhere.

In the areas where the inhibition process was seen to be only partially effective, complex

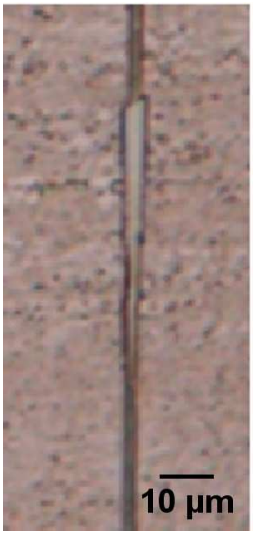

FIGURE 4.17: Optical microscope image of an inhibited domain formed at the end of a fast wall movement. Taper of inhibited domain illustrates deceleration of the domain wall.

patterns were seen, some of which are shown in figure 4.18. The origin of these patterns is not yet clear and may arise as a self correlated behaviour as in similar patterns seen during backswitched poling [4] or may represent an underlying modulation of the sub-surface charge distribution which modulates the local domain inhibition threshold. Similar patterns are seen at the edges of the fully inhibited regions, pointing toward this behaviour as being transitional between inhibition and normal poling. This can be seen, for example, in figure 4.6 where it presents mostly as arrays of quasi-periodic triangular dot domains. Similar patterns to those shown in 4.18 have also been observed during backswitched poling [4]. In this case, however, a large field is applied to the crystal using structured electrodes such that the domains spread outside of the electrode area, underneath an insulating dielectric. The backswitching then occurs when the external field is removed abruptly such that the screening mechanisms are retarded, leaving the domain unstable. In our case there is no abrupt field removal since the ramp rates of the external field are extremely slow. An equivalent of the abrupt field removal, however, may be the fast movement of the switching front of the domain wall across the exposed area. In the case where the wall movement is fast it may be that additional energy, associated with the velocity of the wall, allows the exposed area to pole initially, however the same conditions that inhibit domain inversion at slower wall velocities lead to the newly switched domain being unstable, and so backswitching occurs and stability is found through an inhomogeneous domain state within the exposed area. With further investigation this effect may prove to be highly useful due to the high spatial period patterning achievable.

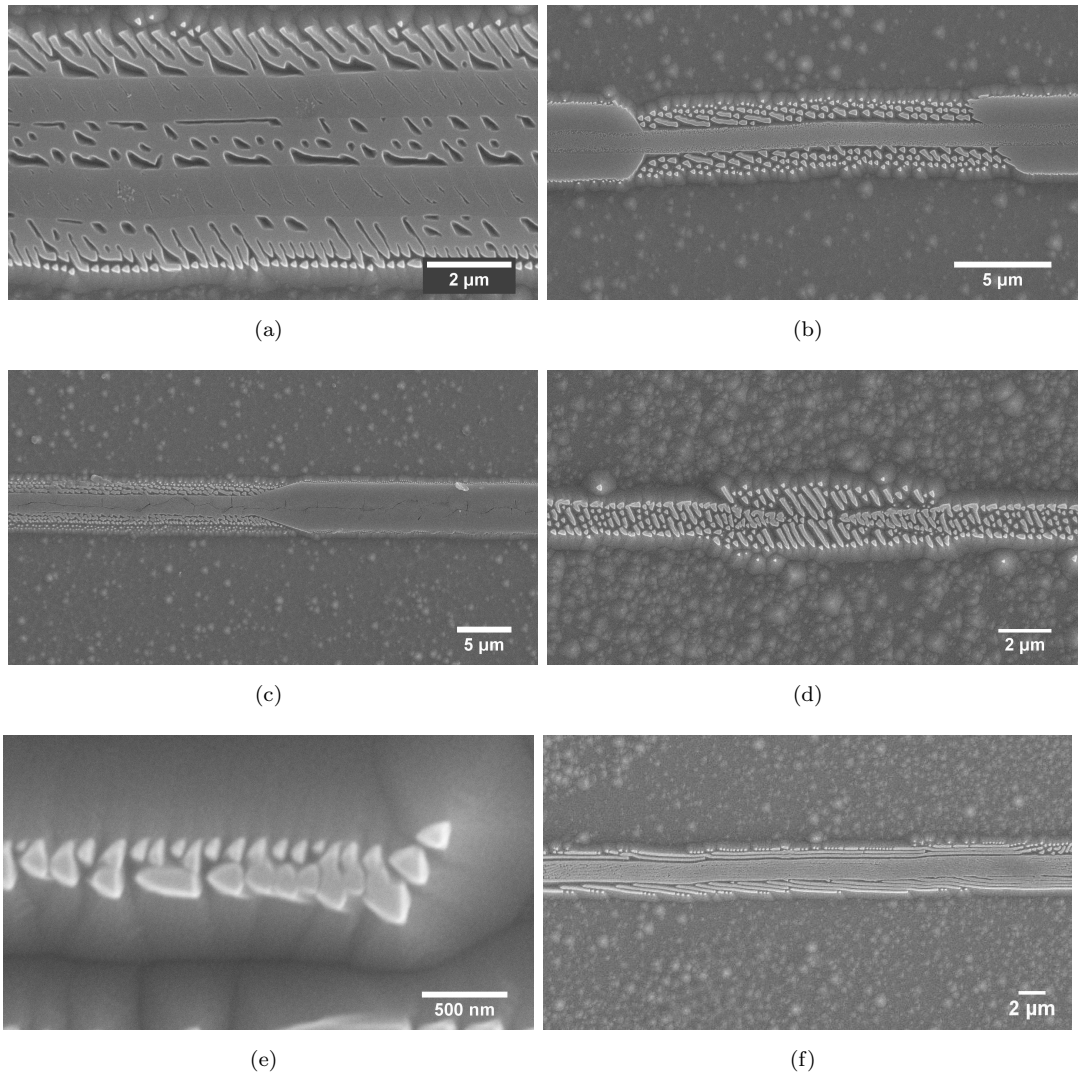

FIGURE 4.18: SEM images of complex structures seen during incomplete domain inhibition.

In order to investigate the stability of the inhibited domains the crystal was thermally annealed for 1 hr at 215°C after the EFP step of the process. SEM investigation of the HF etched annealed crystal showed that the poling inhibited domains survived the brief annealing process without any significant change.

Domain inhibited structures have been etched for an extended period of time to prove their applicability for surface structuring. Figure 4.19 shows the same cross hatched structure shown previously in figure 4.8 after 39 hrs etching in HF. The high-aspect ratio achieved is clearly evident in the figure. As was described in the previous chapter, the particular crystal faces that are presented to the etchant as the background -z crystal etches will affect the overall shape of the surface relief structures through the different etch rates of the x and $+y$ and -y axes. When the beam is scanned along y axis, the

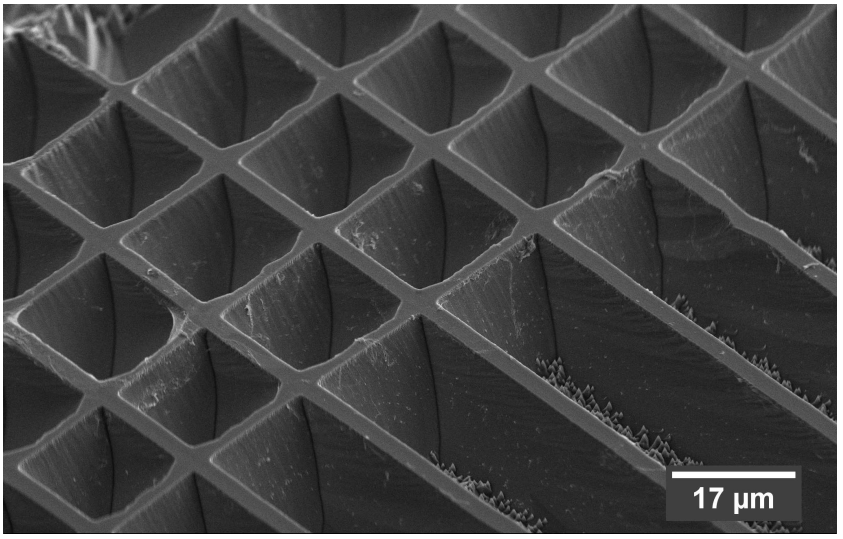

FIGURE 4.19: SEM image of domain inhibited cross hatched pattern after 39 hrs etching in HF. Sample tilted to 45°.

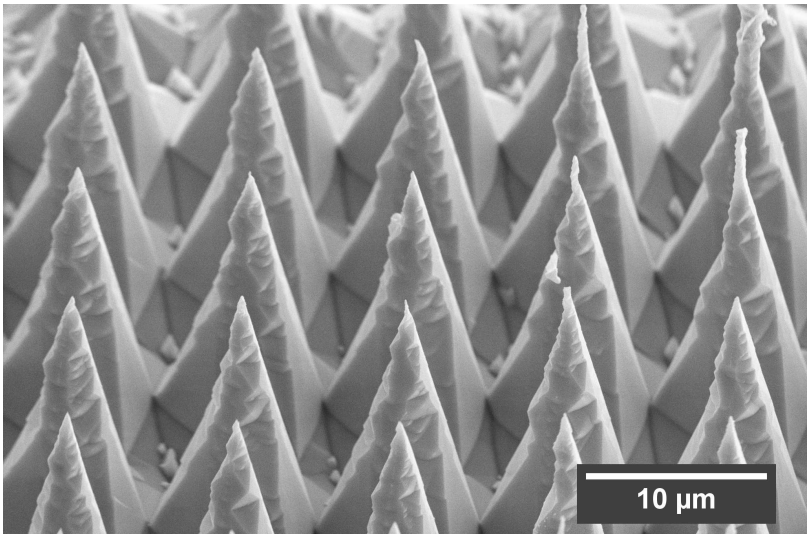

FIGURE 4.20: SEM image of domain inhibited dot array after 60 hrs etching in HF. Sample tilted to 45°.

ridge structure formed by etching will present x faces to the acid. Since the x faces are highly resistant to etching high aspect ratio, symmetric, ridges can be formed and are the most useful for applications such as ridge waveguides. Figure 4.20 shows an SEM image of an array of static dot exposures after etching at room temperature for 60 hrs where it can be seen that, as well as two dimensional structures, three dimensional structures such as sharp tips can be formed that may have uses for applications such as surface enhanced Raman scattering or even as atomic force microscope (AFM) tips.

The etch behaviour of the structures can be used to deduce the depth profile of the

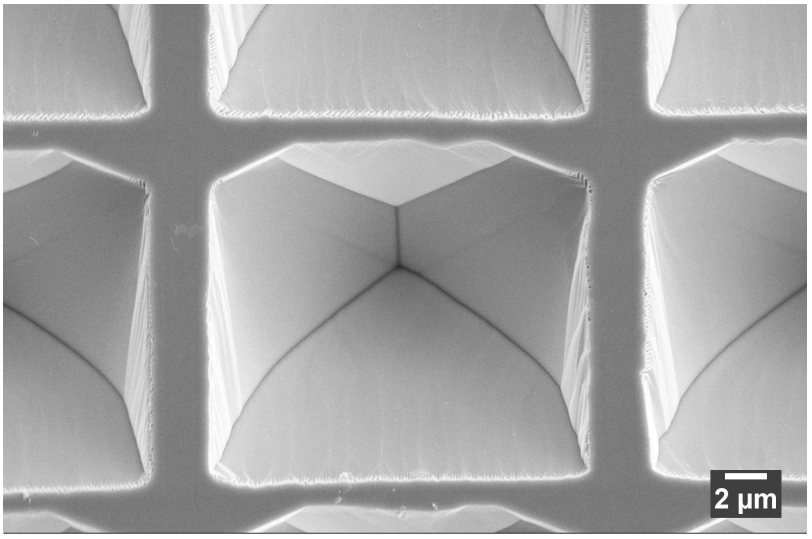

FIGURE 4.21: SEM image of a void in the cross hatched inhibited domain pattern shown in figure 4.19 viewed from directly above. An x axis runs horizontally in the figure and a y axis runs vertically.

domain inhibited layer in the following way. In figure 4.19 it can be seen that the width of the structures written along the y axes, such that x faces are revealed as the structures etch, retain their width as the crystal etches in the z direction whilst the structures written along the x direction become increasingly thinner. At first sight the etch behaviour of the structures written along x seems to indicate that the y axis of the domain inhibited layer has not inverted, however this is not the case and in fact may tell us something of the depth profile of inhibited domains. This can best be begun with reference to figure 4.21 which shows a void of the cross hatched inhibited domain pattern, after 39 hrs etching, viewed from directly above. The void contains four faces, to the left and right are the two x faces which etch at the same rate and hence show equal gradients and meet in the horizontal centre of the void. To the top and bottom are the negative and positive y faces respectively which do not etch at the same rate and hence have different gradients resulting in the faces approaching at a point above the vertical centre of the void. The upper edge shows the greatest gradient since this face has been etching as the $-z$ face has been etching in the depth direction. The question now is; if the domain orientation at the surface of the cross hatched lines has inverted, which inverts y as well as z, why has the inverse etching behaviour not occurred to this layer? And more specifically, why has the upper edge of the horizontal lines not seemed to have etched at all? The answer to these questions reveals information about the depth profile of the domain inverted layer and shows that the depth of the domain inhibited layer must decrease in depth to zero at its edge. If the depth of the domain goes smoothly to zero, when the $-z$ face etches it is the y face of the bulk material that is presented always to the etchant, and not the y face of the domain inhibited region. When the $+y$ face

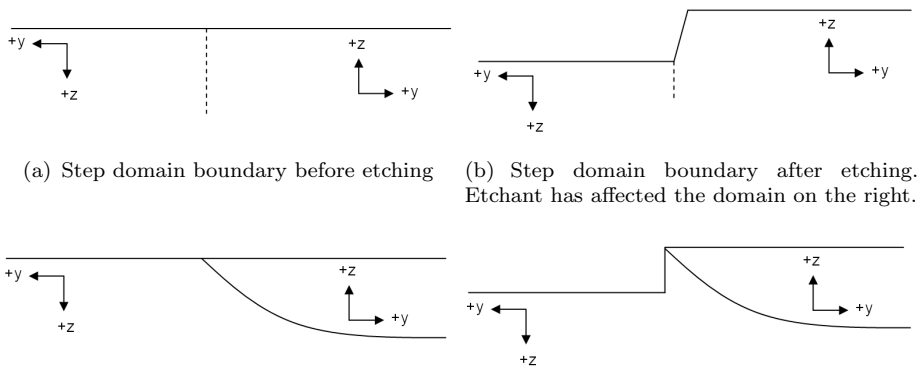

(a) Step domain boundary before etching

(b) Step domain boundary after etching. Etchant has affected the domain on the right.

(c) Smoothly varying domain boundary before etching

(d) Smoothly varying domain boundary after etching. The bulk crystal has shielded the -y face of the right hand domain, preventing it from etching.

FIGURE 4.22: Variation of etch behaviour between domains with smoothly varying depth and a step depth profile.

of the bulk crystal is presented it shields the -y face of the inhibited domain from the etchant, as can be seen in figure 4.22, and so etching of the inhibited domain does not occur. This is the situation of the upper edge of the horizontal line in figure 4.21, where the inhibited domain does not etch even though it is a -y face. The situation of the lower edge of the horizontal line in figure 4.21 can be similarly explained. The -y face of the bulk crystal is presented as the crystal etches in the z direction. The bulk crystal will then etch until the positive y face of the domain inverted layer is revealed, at which point sideways etching will stop. However, the etching in the y direction undercuts the inhibited domain if its thickness goes smoothly to zero and so the -z face of the inhibited domain will be presented in the undercut region. This will then readily etch and the inhibited domain will be removed. This situation is shown schematically in figure 4.23. Hence the inhibited layer takes on the apparent etch characteristics of the underlying material.

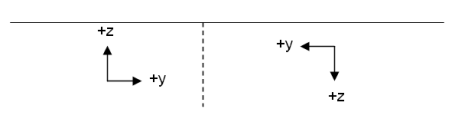

(a) Step domain boundary before etching

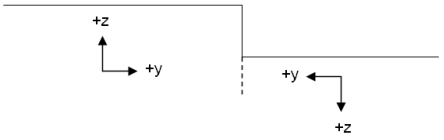

(b) Step domain boundary after etching. Etchant has reached the domain on the right where a $+y$ face is presented.

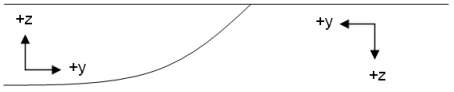

(c) Smoothly varying domain boundary before etching

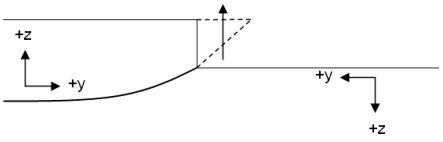

(d) Smoothly varying domain boundary after etching. The bulk crystal has etched in the z direction revealing a $-y$ face of the bulk crystal which etches and undercuts the domain on the left. This then presents the $-z$ face of the domain on the left which etches away in the direction indicated by the arrow. The region of the left domain removed by etching is indicated by the dashed lines.

FIGURE 4.23: Variation of etch behaviour between domains with smoothly varying depth and a step depth profile.

4.3 Discussion of Results

The experimental results presented in the previous subsection leave little doubt that the structures produced by UV laser exposure followed by EFP are indeed ferroelectric domains, where the process of domain inversion has been inhibited during the EFP step. It is seen that, using the EFP method and apparatus of reference [2], nucleation occurs always on the -z face which has important consequences for the poling behaviour after exposure on either the positive or negative z faces. When exposure was on the -z face the exposed areas acted as sites of nucleation. However as the nucleated domain attempted to propagate into the crystal, although not inhibited, the domain propagation was severely affected by the exposure, leading to a highly disordered domain. When the exposure was on the $+z$ face the domain which nucleated on the -z face, although with some spatial preference directly opposite the exposed area, and then propagated through the crystal freely until approaching the $+z$ face. At this point the propagation of the domain front is hindered in the exposed region, leaving the area un-poled. In section 3.2 a model was proposed for the mechanism responsible for direct poling during UV laser exposure, and since the inhibited domain effect described in this section is simply a further step after nearly identical exposures to section 3.2, the model proposed should account for the behaviour seen here. It was proposed that the direct pole behaviour is due to a laser initiated charge separation whereby; on the -z face, electrons are trapped at the surface and holes driven into the bulk and, on the $+z$ face holes are trapped on the surface and electrons are driven into the bulk. In the area between the two regions of opposite net charge, there then exists an electric field which is oriented appropriately to pole the crystal. However, when charges are separated in this way, an electric field is also produced. This electric field will have the characteristics of that formed by a simple charge dipole and will thus change direction (along the dipole axis) when measured either within or without the dipole. Thus if a charge distribution induces domain inversion within the dipole it shall also inhibit inversion outside of the dipole. In order to explore this further numerically, without evaluating the full time dependent charge transport model, positive and negative charges are distributed following a likely probability density function (pdf) and the resultant scalar potential and vector electric field distributions are calculated. The pdf used for the positive charge distribution after exposure on the $+z$ face is given by

$$p(z) \propto \mathrm{erfc}(z/dp) \tag{4.1}$$

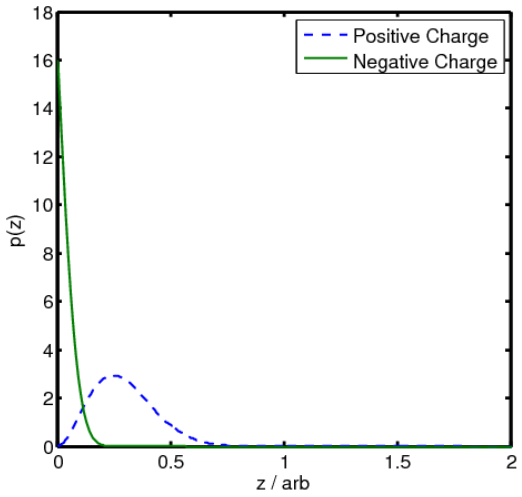

FIGURE 4.24: Probability density functions of the positions of randomly placed point charges.

where erfc(z) is the complimentary error function and dp describes the width of the distribution. For the negative charge distribution the pdf

$$p(z) \propto z^2 \text{erfc}(z/dn) \tag{4.2}$$

is used where, again, dn describes the width of the distribution. Both distributions are normalised in the calculations by normalising the corresponding cumulative density functions. Figure 4.24 illustrates the two pdfs and figures 4.25(a) and 4.25(b) show the distributions of 10,000 randomly distributed positive and negative charges. A Gaussian pdf has been used in the direction perpendicular to z. The scalar potential fields of each charge distribution are shown in figures 4.26(a) and 4.26(b) and scalar potential of the overall charge distribution is shown in figure 4.27(a). The electric field is given by the gradient of the potential field and this is shown in figure 4.27(b). The two different regions of opposite field orientation can clearly be seen, with the region of positive field localised to the surface, which would be responsible for direct poling, and the region of negative field extending further into the crystal, which would be responsible for inhibiting the poling process. This differing of the depths of the fields involved in the two processes may account for the inability of the PFM measurements to view directly poled domains on the $+z$ face whilst inhibited domains are clearly seen.

A similar effect has been seen during LAP whilst illuminating with a confocal microscope [9, 10]. In this instance a confocal microscope produced a high intensity (50 MW cm^{-2}) focal region with a spot size of ∼500 nm using light with a wavelength of 488 nm. An electric field was applied during illumination in the direction required to pole. The

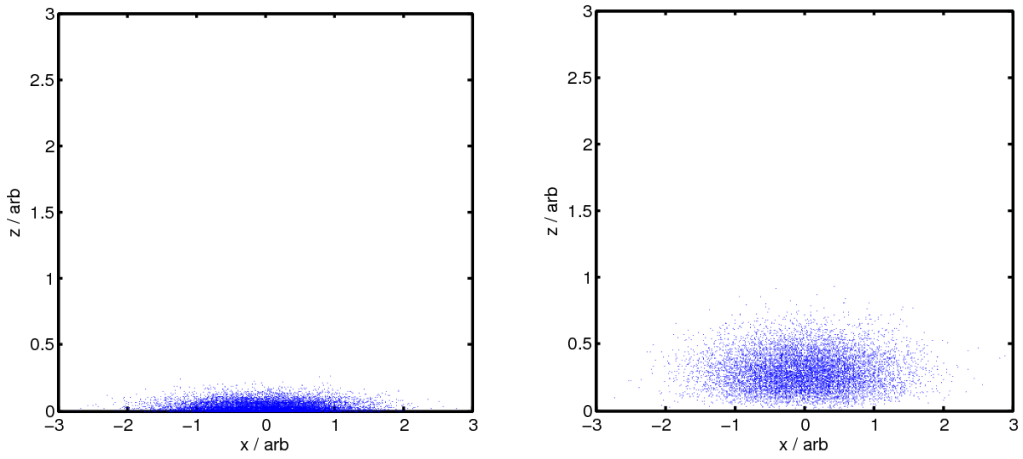

(a) Positive charge. (b) Negative charge.

FIGURE 4.25: Distributions of 10,000 randomly placed positive and negative charges following pdfs shown in figure 4.24 in depth and a Gaussian pdf in the transverse direction.

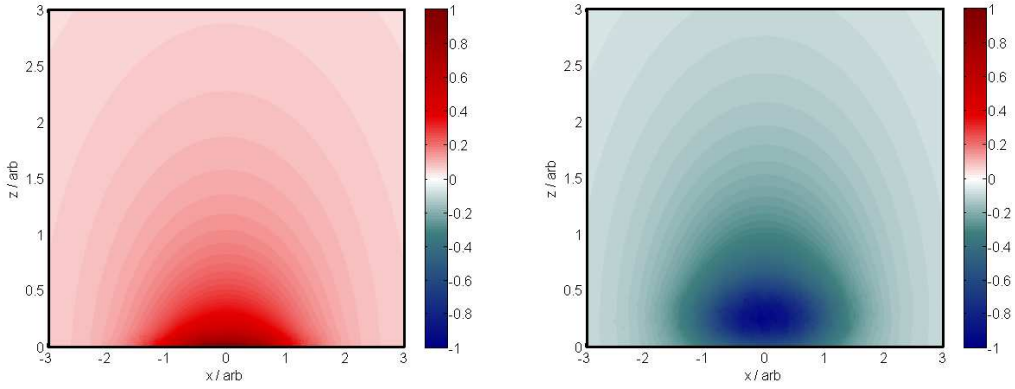

(a) Positive charge potential. (b) Negative charge potential.

FIGURE 4.26: Scalar electrical potential fields of the charge distributions shown in figure 4.25. Colour bars show field magnitudes in arbitrary units.

photoexcited charges excited in the focal region re-distribute to produce a zero net field in the focal region. Thus the electric field in the focal region, due to the photoexcited charges only, is directed opposite to the external field and so outside the focal region the field is directed parallel to the external field and hence aids domain inversion. Two differences between this and the results presented in this section then are the direction of the charge driving field and the asymmetry introduced by the localisation to the surface due to the high absorption in the UV region, however the basic reasoning is the same. This suggests that a similar inhibition effect could also be achieved using visible light with an externally applied, reverse bias, field. In [10] it was shown that charges from

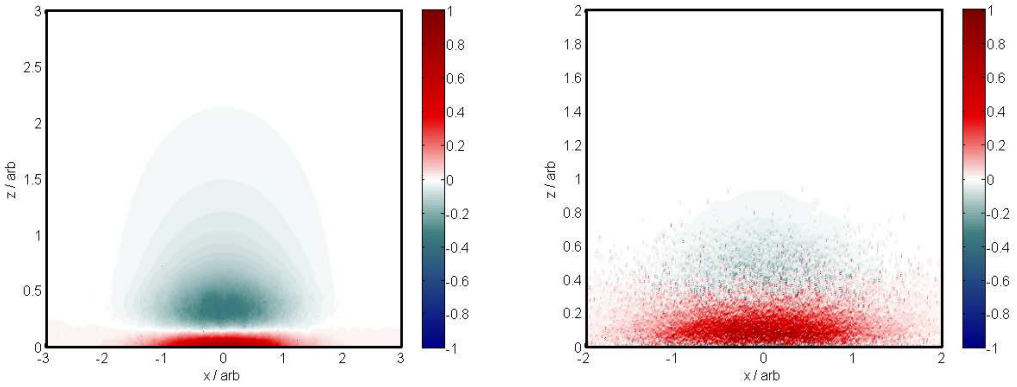

(a) Net scalar electrical potential.

(b) z component of the electric field.

FIGURE 4.27: Scalar electrical potential field of the combined charge distributions shown in figure 4.25 and the z component of the electric field. The length scale in figure 4.27(b) has been reduced for greater clarity. Colour bars show field magnitudes in arbitrary units.

traps of different depths within the bandgap were involved, and that only the effect of the deeper traps endured after the external field was switched off. Due to this it is likely that this effect will only work with high intensity pulsed light such that multi-photon absorption can excite charges from either deep traps or from the valence band to the conduction band. A femtosecond source would thus be preferable. In this way it would be possible to tailor the depth at which the inhibition takes place, and even to structure domains within the depth direction, producing gratings along the z axis.

The results of this chapter have shown that the kinetics of the poling process are crucial for the domain inhibition, which influences the way process should be viewed. In many LAP studies, it is sufficient to think of how light may influence the local coercive field of the crystal. However, the use of the term 'coercive field' implies that the effect is described entirely by the local region of the crystal and is not dependant upon the wall kinetics. In the case of inhibited domains it is better to think of an interaction of the moving, charged, domain wall with the electric field caused by the re-distributed charges. This may then include an analogy to momentum of the domain wall which could account for the overcoming by the moving domain of the inhibiting electric field in areas of fast wall movement.

4.4 Conclusion

A new method of light assisted domain engineering in lithium niobate has been demonstrated that is fundamentally different to that of either conventional LAP or AOP. In this

method illumination of focussed c.w. UV light on the $+z$ face leads to a local inhibition of domain inversion in the illuminated areas during a subsequent EFP step. The mechanism proposed is that, during illumination, the absorbed UV radiation heats the crystal and produces a pyro-electric field which drives photo-excited charges to leave a dipolar charge distribution after the passage of the beam. This dipolar charge distribution is arranged such that a charged domain wall approaching the region will be influenced by an electric field that will repel the wall and hence inhibit poling in the illuminated area. The extent to which the domain inversion is inhibited is seen to be dependent upon the kinetics of the domain walls during the EFP step and these can be controlled by some amount by the magnitude of the external field applied during the EFP step. When wall movement is slow, inhibition is seen to be complete and when wall movement is very fast inhibition does not occur. In the intermediary points, however, partial inhibition is seen which results in complex, self assembled, sub-micron scale domain patterning which shows promise for high spatial frequency patterning unachievable through conventional EFP and thus warrants further investigation. The ferroelectric nature of these inhibited domains has been confirmed by PFM.

As a method of surface structuring, UV poling inhibition followed by etching has been shown to be highly successful with high aspect ratio structures demonstrated with no loss of quality of the upper face. The shape/size and the quality of the fabricated structures is determined by the incident exposure conditions, in combination with the subsequent EFP parameters and the annealing steps respectively. Additionally, as the crystallographic symmetry is not observed to impose limitations on the orientations of the created structures, any desired shapes can be achieved. This may lead to a wide variety of useful structures from ridge wave-guides to diffraction gratings.

The depth of the inhibited domains has not yet been conclusively ascertained, however a lower limit to the depth has been given by PFM as around 100 nm and initial indications from side etching indicate depths of the order of a micron. To be useful for optical applications, the depth of the domains would need to be around 5 - 10 μm so that they could be used in waveguide applications. This may be achievable through variation of the exposure conditions, such as wavelength or spot size, or by having an external field present during illumination or possibly by cycling the EFP step. Such an investigation, along with a thorough and systematic study depth under current conditions must be left for future work.

The application of the technique to ultrafast visible pulsed lasers, where multiphoton absorption provides photo-excited charges from either deep traps or band to band transitions and an external electric field facilitates charge separation, has also been proposed

for future work as a direct consequence of understanding gained during this investigation. In this way full three dimensional domain engineering will be possible.

References

[1] I.T. Wellington, C.E. Valdivia, T.J. Sono, C.L. Sones, S. Mailis, and R.W. Eason. Ordered nano-scale domains in lithium niobate single crystals via phase-mask assisted all-optical poling. *Applied Surface Science*, 253(9):4215 – 4219, 2007.

[2] C.L. Sones, M.C. Wengler, C.E. Valdivia, S. Mailis, R.W. Eason, and K. Buse. Light-induced order-of-magnitude decrease in the electric field for domain nucleation in MgO-doped lithium niobate crystals. *Applied Physics Letters*, 86(21): 212901 –, 2005.

[3] C. L. Sones, S. Mailis, W. S. Brocklesby, R. W. Eason, and J. R. Owen. Differential etch rates in z-cut $LiNbO_3$ for variable HF/HNO_3 concentrations. *J. Mater. Chem*, 12:295–298, 2002.

[4] V. Y. Shur. Kinetics of ferroelectric domains: Application of general approach to $LiNbO_3$ and $LiTaO_3$. *Journal of Materials Science*, 41(1):199 – 210, 2006.

[5] D.A. Scrymgeour, V. Gopalan, A. Itagi, A. Saxena, and P.J. Swart. Phenomenological theory of a single domain wall in uniaxial trigonal ferroelectrics: lithium niobate and lithium tantalate. *Physical Review B (Condensed Matter and Materials Physics)*, 71(18):184110 – 1, 2005.

[6] Venkatraman Gopalan, Q.X. Jia, and T.E. Mitchell. In situ video observation of 180°; domain kinetics in congruent $LiNbO_3$ crystals. *Applied Physics Letters*, 75 (16):2482 –, 1999.

[7] Atsuko Kuroda, Sunao Kurimura, and Yoshiaki Uesu. Domain inversion in ferroelectric MgO:$LiNbO_3$ by applying electric fields. *Applied Physics Letters*, 69(11): 1565 –, 1996.

[8] K. Nakamura, J. Kurz, K. Parameswaran, and M.M. Fejer. Periodic poling of magnesium-oxide-doped lithium niobate. *Journal of Applied Physics*, 91(7):4528 – 34, 2002.

[9] V. Dierolf and C. Sandmann. Direct-write method for domain inversion patterns in $LiNbO_3$. *Applied Physics Letters*, 84(20):3987 – 9, 2004/05/17.

[10] Christian Sandmann and Volkmar Dierolf. The role of defects in light induced domain inversion in lithium niobate. *Physica Status Solidi C: Conferences*, 2(1): 136 – 140, 2005.

Chapter 5

Modelling The Heating Of Lithium Niobate By a Focused Scanning Laser Beam

5.1 Background and Motivation

In chapters 3 and 4 it was shown that illumination of LN with a scanning, focussed, UV laser beam with a wavelength of 244 nm can either directly pole the crystal or create a region where poling is impeded in a subsequent EFP step. It was hypothesised that the main driving force for the effect was the temperature field caused by the high optical absorption at 244 nm[1] producing local heating, along with photoexcited charges. The full solution of the model is complex due to the electrostatic coupling of the charged mobile species and has not been permitted in the time scales of this thesis. Since the fundamental driving force is due to the temperature fields, however, the heating of LN by a scanning laser beam has been modelled here as a basis for the future application to the model in chapters 3 and 4 and to other investigations of focussed UV light - LN interactions. This modelling is carried out in this chapter using both non-linear analytical and numerical finite difference methods. In section 5.2 the thermal properties of LN are reviewed and in section 5.3 the temperature dependencies of some thermal properties are included into a non-linear analytical heat flow model. In section 5.4 a numerical model is constructed using the finite difference method and is used to validate the analytical method and explore further the effect of temperature dependent thermal properties. Section 5.5 presents some experimental verification of the model and conclusions are then drawn in section 5.6.

5.2 Thermal Properties Of LN

The important thermal properties that we shall consider here are the thermal conductivity **K**, the specific heat C and the thermal diffusivity **D**. The thermal diffusivity is defined in terms of the thermal conductivity, specific heat and mass density ρ as

$$\mathbf{D} = \frac{\mathbf{K}}{\rho C} \tag{5.1}$$

however it is often easier to measure the thermal diffusivity directly using the transit time of a heat pulse [2, 3]. The thermal conductivity, and hence thermal diffusivity, is a tensor quantity since the heat flow for given a temperature distribution will in general be different along different crystal axes. The thermal conductivity has been measured in LN for directions perpendicular and parallel to the z axis as a function of temperature by Zhdanova et al. [4] and is presented in [4, 5]. The measurements are shown in figure 5.1 where it can be seen that the anisotropy is small. Since the anisotropy is only around 5% it has been considered reasonable to treat LN as thermally isotropic during the analyses within this thesis. The heat capacity of LN has also been measured between the temperatures of 80 and 390 K by Zhdanova et al. [4] and is shown in figure 5.2. The data has been fitted to the Einstein model of heat capacity given by

$$C = 3Nk_B \left(\frac{\hbar\omega}{k_B T}\right)^2 \frac{\exp(\hbar\omega/k_B T)}{(\exp(\hbar\omega/k_B T) - 1)^2} \tag{5.2}$$

where N is the number density of atoms in LN, k_b is the Boltzmann constant, $\hbar$ is the Planck constant divided by 2π, T is the temperature and ω is the fitting parameter. N was calculated to be 2.03^{25} Kg^{-1} and ω was found to be 65THz for the best fit. The thermal diffusivity has been measured as a function of temperature using an interferometric method to trace a heat pulse in [3]. This data is shown in figure 5.3 ($\triangle$) along with the thermal diffusivity calculated using equation 5.1 from the thermal conductivity and heat capacity data in [4, 5] ($\bigtriangledown$) where heat capacity data has been interpolated onto the temperatures at which the conductivity has been measured. It can be seen that the diffusivity decreases with temperature with the thermal diffusivity at 800 K being less than half the room temperature value. The method in [3] was, unfortunately, unable to show the anisotropy of the thermal diffusivity and so the conductivity in the z direction from [4, 5] was used. Empirical fits to the diffusivity data will be made later in section 5.3.4.

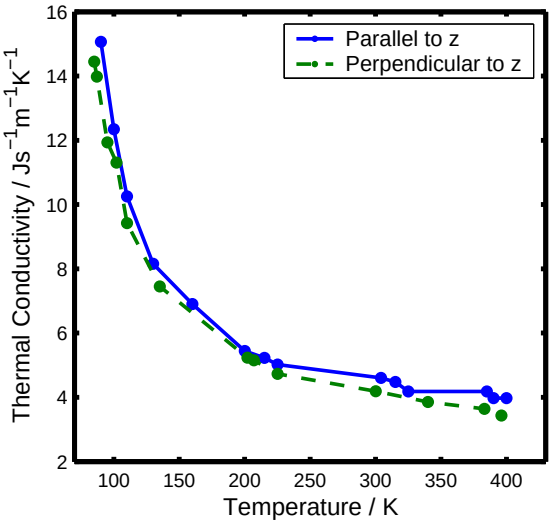

FIGURE 5.1: Thermal conductivity of LN as a function of temperature. Measurements taken from ([4, 5]). Solid line - heat flow directed along z axis. Dashed line - heat flow directed perpendicular to z axis.

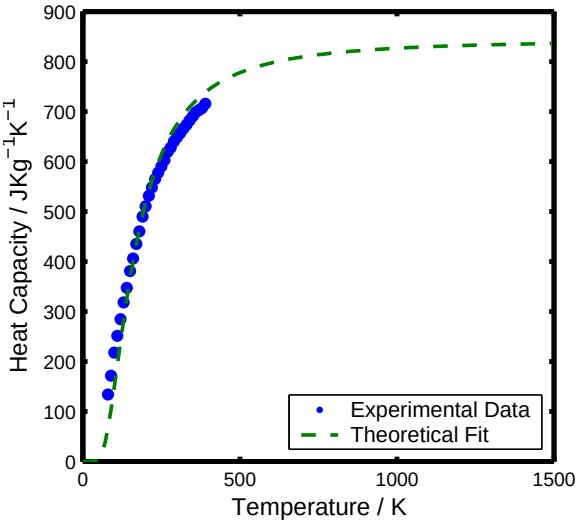

FIGURE 5.2: Heat Capacity of LN as a function of temperature. Measurements taken from ([4, 5]). Solid Dots - Experimental Data. Dashed line - Theoretical fit to Einstein's model of heat capacity, fitting parameter $\omega = 65$THz.

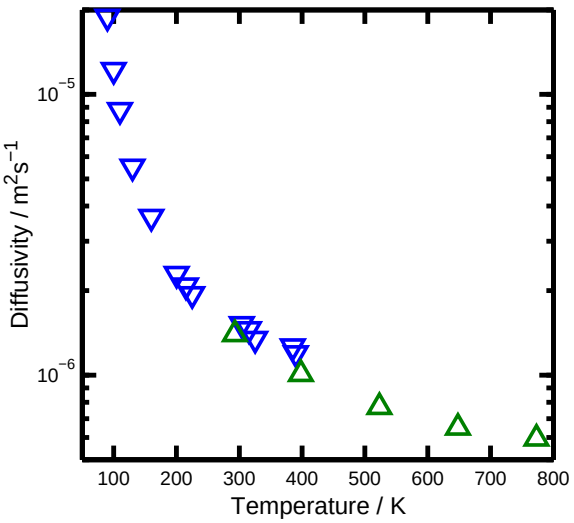

FIGURE 5.3: Thermal diffusivity of LN as a function of temperature. Measurements taken from [4, 5] (▽) and from [3] (△).

5.3 Non-Linear Analytical Modelling

5.3.1 System Description

The crystal was illuminated by a laser beam directed perpendicularly to the surface of the crystal. The beam had a $1/e^2$ spot radius of w, a power P and scans across the crystal surface at a velocity v in a direction we shall define to be the positive x direction in a Cartesian coordinate system with the positive z axis directed into the crystal. A dimensionless coordinate system is defined in the reference frame of the moving beam with origin at the point of contact between centre of the beam and the crystal surface by making the transformations $X = (x - vt)/w$, $Y = y/w$, $Z = z/w$. The coordinate systems are shown in figure 5.4.

5.3.2 Model Formulation

The starting point of the investigation is the heat equation

$$\rho C \frac{\partial T}{\partial t} - \nabla \cdot \mathbf{K} \nabla T = S(\mathbf{r}, t) \tag{5.3}$$

where ρ is the density of the material and $S(\mathbf{r}, t)$ is the heat source function. If the specific heat and density are assumed constant with respect to temperature the relation

$$\mathbf{D} = \frac{\mathbf{K}}{\rho C} \tag{5.4}$$

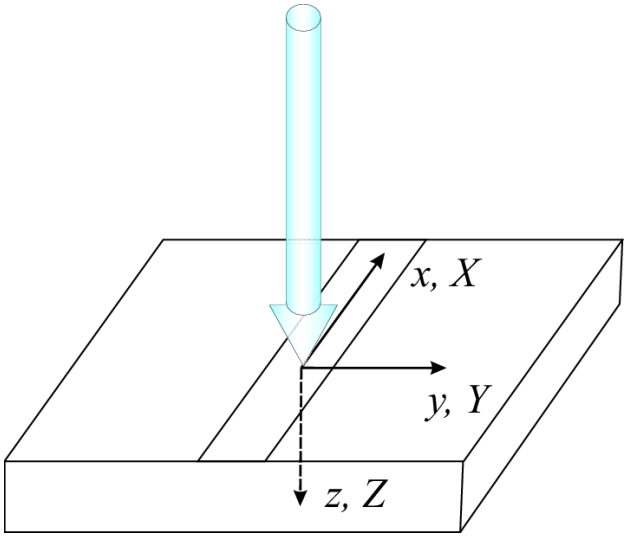

FIGURE 5.4: Coordinate systems used in the model. The coordinates x, y and z correspond to the reference frame of the crystal and have their origin at the center of the beam on the crystal surface at $t = 0$. X, Y and Z correspond to the reference frame of the moving beam and are normalised in units of the beam spot radius (w). The normalised coordinates have their origin at the centre of the beam on the crystal surface.

can be used. The heat equation can then be expressed in the isotropic case, where **D** is a function of temperature only, as

$$\frac{\partial T}{\partial t} - \nabla \cdot D(T)\nabla T = \frac{1}{\rho C} S(\mathbf{r}, t). \tag{5.5}$$

The heat source is the scanning UV Gaussian laser beam which is absorbed near the surface and converted into heat through phonon relaxation within the crystal. The Gaussian intensity profile of the scanning laser, and hence the heat source, is described by

$$S(x, y, z, t) = \frac{P(1-R)\alpha}{\pi w^2} \exp\left[-\frac{2((x-vt)^2 + y^2)}{w^2}\right] \exp\left[-\alpha|z|\right] \tag{5.6}$$

where P is the incident optical power, R is the intensity reflectivity at the writing wavelength and α is the optical absorption coefficient.

At the plane $z = 0$ we have the boundary between the crystal and the air above. The transfer of heat from the crystal surface to the air, however, shall depend upon the ability of the air to absorb heat and transport it from the surface. At the small length scales used in this investigation the effects of the viscosity of the air dominate convection and the heat transfer is due almost entirely to conduction [6]. Since the thermal conductivity of air is much less than that of LN we shall treat the heat loss from the surface to the air as being negligible and impose a boundary condition of zero heat flux. A simple way to impose this is to reflect the system about the plane $z = 0$ and solve for the entire

space $-\infty < z < \infty$, replacing the heat source of equation 5.6 for

$$S(x,y,z,t) = \frac{2P(1-R)\alpha}{\pi w^2} \exp\left[-\frac{2((x-vt)^2+y^2)}{w^2}\right] \exp\left[-\alpha|z|\right] \tag{5.7}$$

which includes a factor 2 outside of the exponential to account for the extra power required to heat the extra half-space $z < 0$.

5.3.3 Model Solution

The Kirchhoff transform [7] is derived in appendix D with the result

$$\Theta(T) = \Theta(T_0) + \frac{1}{D(T_0)} \int_{T_0}^{T} D(T')dT' \tag{5.8}$$

and is used to encompass the temperature dependence of the thermal diffusivity into a new temperature variable Θ. The value of $\Theta(T_0)$ in equation 5.8 is arbitrary and so can be defined to be zero. Equation 5.5 is then expressed in terms of the temperature variable Θ in the reference frame of the moving beam as

$$\frac{vw}{D(T(\Theta))}\frac{\partial\Theta}{\partial X} - \nabla^2\Theta = \frac{w^2 S(X,Y,Z)}{D(T_0)\rho C}. \tag{5.9}$$

If

$$\frac{vw}{D(T)} \ll 1 \tag{5.10}$$

the first term of equation 5.5 has a negligible effect. This can be written as a condition on v;

$$v \ll \frac{D(T)}{w}. \tag{5.11}$$

The thermal diffusivity of LN between room temperature and the melting point is typically of the order 10^{-6} $\mathrm{m^2 s^{-1}}$ [3] and the range of spot sizes used in reference [8] is between 1.75 μm and 6.6 μm. If a typical spot size of 5 μm is taken it can be seen that the first term will be negligible if

$$v \ll 0.2 \text{ m s}^{-1}. \tag{5.12}$$

The maximum scanning velocity used in [8] was 12 mm $\mathrm{s^{-1}}$ which is clearly much less than this limit of around 200 mm $\mathrm{s^{-1}}$ and so in re-creating the conditions of [8] the first term of equation 5.9 can be neglected. The heat equation can then be written as

$$\nabla^2\Theta = -\frac{w^2 S(X,Y,Z)}{D(T_0)\rho C}. \tag{5.13}$$

This is a form of Poisson's equation which has the familiar solution [9]

$$\Theta(\mathbf{r}) = \frac{w^2}{4\pi D(T_0)\rho C} \int \frac{S(\mathbf{r}')}{|\mathbf{r} - \mathbf{r}'|} d^3\mathbf{r}'. \tag{5.14}$$

The full solution of equation 5.14, after the substitution of equation 5.7 (re-expressed in the reference frame of the moving beam), is given in appendix E. The solution can be written as a single integral

$$\Theta(X, Y, Z, \lambda) = \frac{P(1-R)\alpha}{\pi\rho C D(T_0)} \int_0^\infty \frac{1}{1+8\lambda} g(X, Y, \lambda) h(Z, \lambda) d\lambda. \tag{5.15}$$

The function $g(X, Y, \lambda)$ is given by

$$g(X, Y, \lambda) = \exp\left[-\frac{2(X^2 + Y^2)}{1+8\lambda}\right] \tag{5.16}$$

and the function $h(Z, \lambda)$ is given by

$$\begin{aligned} h(Z, \lambda) = \exp&\left(\frac{-Z^2}{4\lambda}\right) \\ &\left(\exp\left[\left(\alpha w - \frac{Z}{2\lambda}\right)^2 \lambda\right] \operatorname{erfc}\left[\left(\alpha w - \frac{Z}{2\lambda}\right)\sqrt{\lambda}\right] + \right. \\ &\left. \exp\left[\left(\alpha w + \frac{Z}{2\lambda}\right)^2 \lambda\right] \operatorname{erfc}\left[\left(\alpha w + \frac{Z}{2\lambda}\right)\sqrt{\lambda}\right]\right). \end{aligned} \tag{5.17}$$

The final integral must be calculated numerically.

5.3.4 Fitting The Thermal Diffusivity

Having obtained a solution for the temperature in terms of Θ it is necessary to use the Kirchhoff transform again to convert to the real temperature T and so a function $D(T)$ must be generated empirically from experimental data. For an analytical solution for $T(\Theta)$ it is required upon integration of the function $D(T')$ in equation 5.8 that $\Theta(T)$ must be a linear one-to-one function of T for $T > T_0$. This considerably limits our choices for a fitting function and rules out many that may have a physical reasoning. Figure 5.5 shows the thermal diffusivity data from [3] which has been fitted with two different functions. The first fit is an exponential decay of the form

$$D(T) = D_0 + D_1 \exp(-aT) \tag{5.18}$$

and the second is a fit to the inverse temperature given by

$$D(T) = \frac{b}{T} \tag{5.19}$$

where D_0, D_1, a and b are fitting parameters. These are found to be for best fit: $D_0 = 5.3973 \times 10^{-7}$ m^{2}s^{-1}, $D_1 = 4.6392 \times 10^{-6}$ m^{2}s^{-1}, $a = 5.748 \times 10^{-3}$ K^{-1} and $b = 4.173 \times 10^{-4}$ m^{2}s^{-1}K respectively. Both are a good fit to the data but the real difference between the two can be seen when the curves are extrapolated to higher temperatures. Here we can see that the behaviour of the two functions differs considerably with the inverse temperature fit giving values at high temperatures roughly half that of the exponential fit. From the quality of the fit at high temperatures and from simple intuition one would want to choose the exponential function, however upon integration

$$\int_{T_0}^{T} \left(D_0 + D_1 \exp(-aT')\right) \mathrm{d}T' = f(T_0) + D_0 T - \frac{D_1 \exp(-aT)}{a} \tag{5.20}$$

where $f(t)$ is a function of T_0 only. This is not a linear one-to-one function and so is incompatible with equation 5.8. This forces us to use the inverse temperature function as a fit for D which integrates suitably and, after substitution into equation 5.8 we obtain the relation between the linearised temperature scale Θ and the real temperature T as

$$T(\Theta) = T_0 \exp\left(\frac{\Theta}{T_0}\right). \tag{5.21}$$

Equations 5.15 and 5.21 can now be solved numerically to give the temperature in the rest frame of the scanning beam at any arbitrary point.

5.3.5 Simulation Results

To investigate the effect of the Kirchhoff transform we can solve the linear heat equation

$$\nabla^2 T = -\frac{w^2 S(X,Y,Z)}{D_{lin}\rho C}. \tag{5.22}$$

where D_{lin} is a linear approximation to the thermal diffusivity i.e. a constant. Equation 5.22 can then be solved in the same manner as equation 5.13. Solutions from equation 5.22 will be referred to as originating from the linear model and those from equation 5.13 in which the thermal diffusivity is temperature dependent will be referred to as originating from the non-linear model. As a sensible choice of D_{lin} we can take the average value, or arithmetic mean, of the reciprocal of temperature approximation to the thermal diffusivity (eqn 5.19) between 290 K and 1500 K. The average is found to be $D_{lin} = 5.67 \times 10^{-7}$ m^{2}s^{-1} which is approximately D(736K). Similarly as a value of the constant heat capacity we take the arithmetic mean of the Einstein heat capacity fit

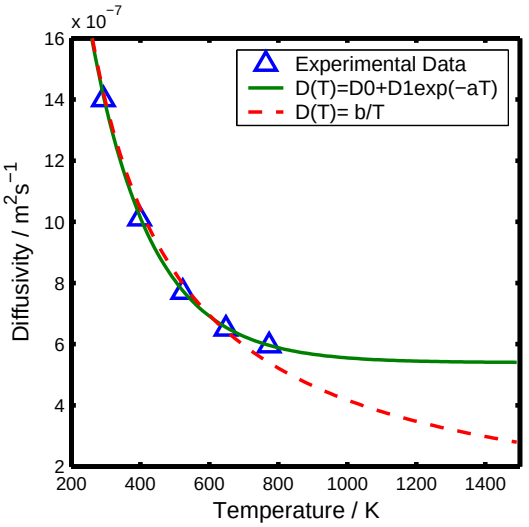

FIGURE 5.5: Thermal diffusivity of LN as a function of temperature. Measurements taken from [3]. Sold line shows fit of the form $D(T) = D_0 + D_1 \exp(-aT)$ with $D_0 = 5.3973 \times 10^{-7}$ m^{2}s^{-1}, $D_1 = 4.6392 \times 10^{-6}$ m^{2}s^{-1} and $a = 5.748 \times 10^{-3}$ K^{-1}. Dashed line shows fit of the form $D(T) = \frac{b}{T}$ with $b = 4.173 \times 10^{-4}$ m^{2}s^{-1}K.

between 290 K and 1500 K. This average is found to be $C = 806$ JKg^{-1}K^{-1} and will be used throughout this thesis. Figure 5.6(a) shows the temperature distribution obtained on the surface of the crystal at a relatively low power of 20 mW for both linear and non-linear models. The spot size w is 2.5 μm and the absorption coefficient corresponds to that at 244 nm. It can be seen that at low powers, and hence temperatures, the linear models underestimation of the thermal diffusivity leads to decreased heat flow and a subsequent temperature increase compared to the non-linear model. This is also shown in figure 5.6(b) which presents the corresponding temperature distributions from a higher power of 26 mW. Although the central temperatures are in agreement it can be seen that the distribution obtained from the non-linear model is considerably narrower due to the higher values of the thermal diffusivity in the cooler edges of the distribution. The variation of the central surface temperature with power is shown in figure 5.7 where the non-linear response is clearly seen.

Using the experimental exposure conditions of [8], simulations have been performed, unless otherwise stated, with the absorption coefficient α at a wavelength of 244 nm which is $\alpha = 3.3 \times 10^7$ m^{-1} [10]. Figure 5.8(a) shows the temperature distribution along the X axis for three different sets of spot size and laser power. Figure 5.8(b) shows the temperature distribution along the Z axis for the same parameters. The combinations of spot size and laser power were chosen to produce the same peak temperature. Figure 5.8 shows that in all cases the temperature changes are highly localised to the beam spot with the distributions dropping to around one third of the peak temperature rise in the direction parallel to the surface, and around one fifth in the direction normal

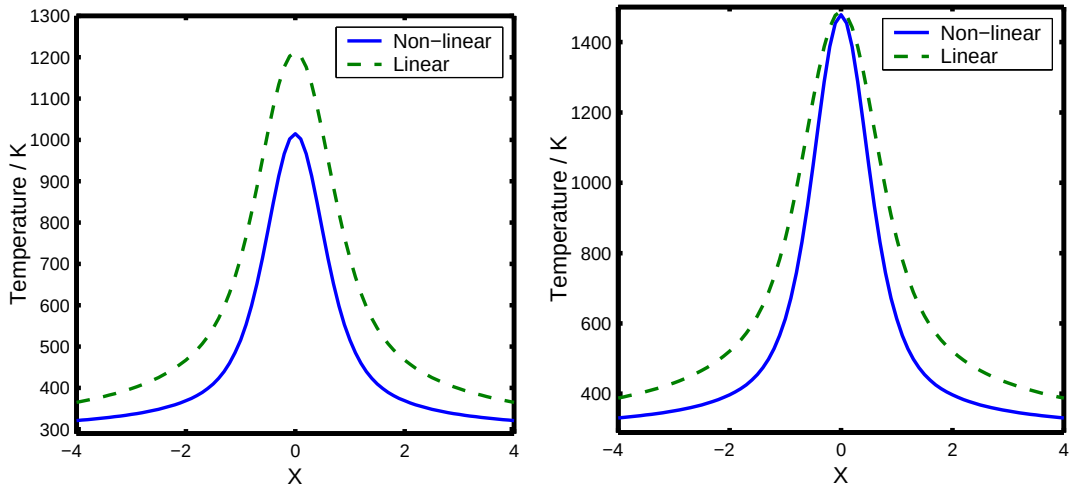

(a) $P = 20$ mW, $w = 2.5$ μm, $\alpha = 3.3 \times 10^7$ m^{-1} (b) $P = 26$ mW, $w = 2.5$ μm, $\alpha = 3.3 \times 10^7$ m^{-1}

FIGURE 5.6: Effect of the temperature dependent thermal diffusivity in the non-linear model (solid curve) compared to the constant thermal diffusivity of the linear model (dashed curve). Temperature distributions along X at $Z = Y = 0$.

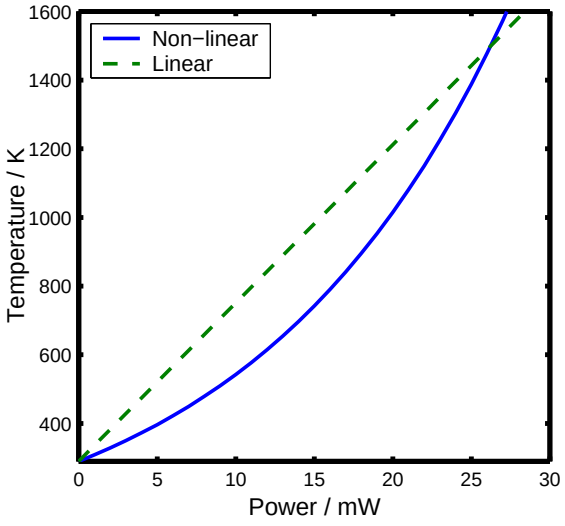

FIGURE 5.7: Variation of the surface temperature in the centre of the beam with incident power for both non-linear (solid curve) and linear (dashed curve) models. Beam parameters in both cases are $w = 2.5$ μm, $\alpha = 3.3 \times 10^7$ m^{-1}

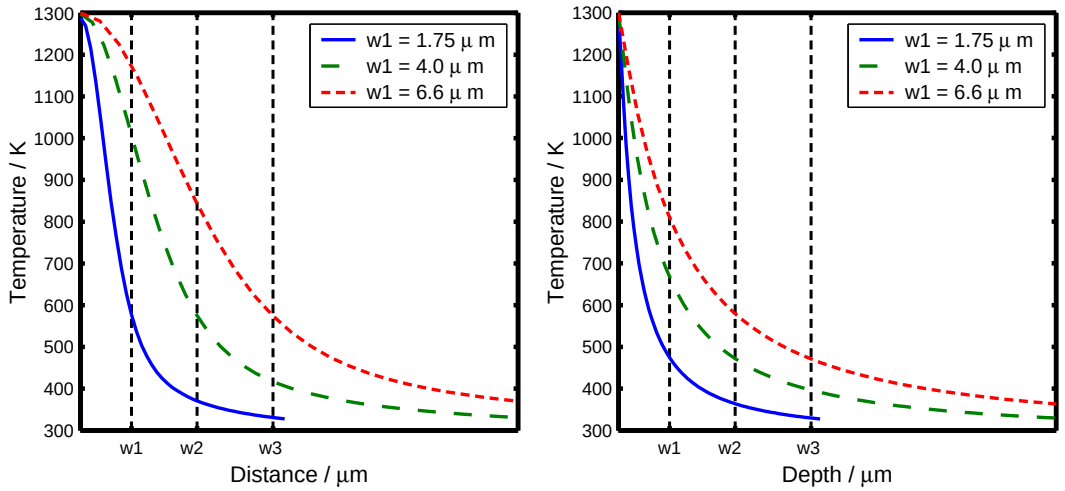

(a) Distribution on crystal surface.

(b) Distribution within the crystal, $X = Y = 0$.

FIGURE 5.8: Temperature rise as a function of distance from the centre of the beam for beam parameters $w = 1.75$ μm, $P = 16.8$ mW (solid line),$w = 4.0$ μm, $P = 38.0$ mW (dashed line), $w = 6.6$ μm, $P = 62.5$ mW (dotted line).

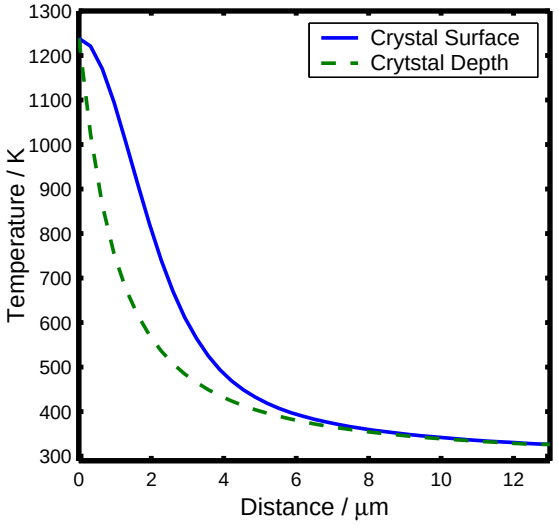

FIGURE 5.9: Temperature rise with depth (dashed line) and along the surface (solid line) in the moving frame of the beam for $w = 3.25$ μm, $P = 30$ mW.

to the surface, by a distance of one beam radius. The difference in character of the distributions in the two directions can be seen clearly in figure 5.9 which shows the temperature distributions along the X and Z axes. The temperature gradient in the Z direction is much greater than those parallel to the surface (X or Y) due to the fast decay of the z component of the heat source in equation 5.7. The localisation of the temperature changes to length scales of order w shows that the crystal is experiencing extremely steep spatial temperature gradients, with temperatures varying by nearly 1000K in a distance of around 10μm.

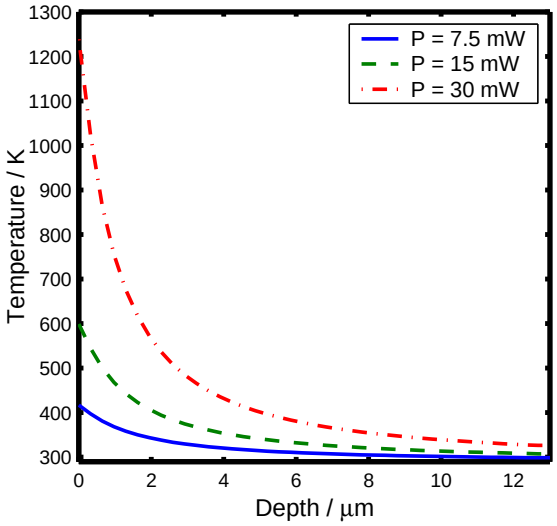

FIGURE 5.10: Temperature rise with depth. $w = 3.25$ μm, $P = 7.5$ mW, 15 mW, 30 mW.

Figure 5.10 shows the variation of the temperature distribution along the Z axis with incident laser power for a fixed spot size. It is seen that while the spatial extent of the temperature changes does not vary greatly with incident power, the peak temperature increases significantly and hence the corresponding temperature gradients increase also. For many physical processes it may be the gradient of the temperature rather than the temperature itself that is the driving parameter and so it is worthwhile to look at the variation of this also. The variation of the temperature gradient in the Z direction with power at the point $(X, Y, Z) = (0, 0, 0)$ is shown in figure 5.11. This can be understood with reference to figure 5.5 which shows the thermal diffusivity of LN as a function of temperature. This is of course the same effect as the narrowing of the temperature distribution in figure 5.6 since the thermal diffusivity decreases in areas of increased temperature.

The temperature distributions shown so far have been spatial distributions in the reference frame of the moving beam. These were shown mathematically to be essentially independent of the scanning velocity by the condition in equation 5.11. However, any physical changes to the crystal will occur in the rest frame of the crystal as the beam passes and so despite the temperature distribution being independent of the laser scan speed physical changes unlikely to be. Figure 5.12 shows the temporal temperature distribution in the crystal reference frame at the point $(x, y, z, t) = (0, 0, 0, t)$ for the maximum and minimum scan speed used in [8]. The figure shows clearly that at higher speeds the crystal will spend less time at elevated temperatures but what is also evident is that the heating and cooling rates increase with speed also. This is important when

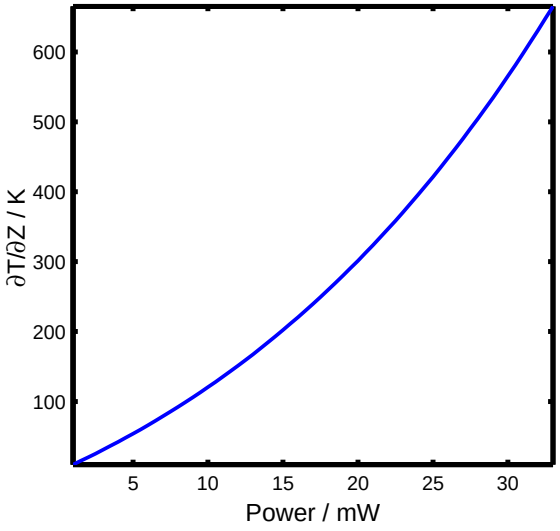

FIGURE 5.11: Variation of the temperature gradient in the Z direction with incident power at the point $(X, Y, Z) = (0, 0, 0)$. $w = 3.25$ μm.

considering relaxation processes that may occur within the crystal. One important relaxation process is the relaxation of internal and surface electric fields which arise during the heating of LN due to the pyroelectric nature of the crystal. Many mechanisms are present to compensate the pyroelectric fields that arise when heating, such as ionic and electronic movement within the crystal and the accumulation of surface charge from the atmosphere. The change in electric dipole moment as a function of temperature is a very fast process and so the extent of field compensation by the relatively slow movement of charges will depend upon the heating and cooling rates of the crystal. This could have a large effect on any electric field driven processes occurring within the crystal where it may be found that the effect is stronger during a fast scan due to high uncompensated pyroelectric fields. The results of such scans may run contrary to expections that slow scans would produce better results due to the longer dwell time of the beam.

Until now the laser heating simulations have been aimed at reproducing the conditions found in [8] where waveguides were written with a scanning UV laser with a wavelength of 244 nm. The model is not however limited to simulation in the UV region of the spectrum and in fact is relevant to any wavelength that is absorbed by the crystal. The only limit to the applicability of the model to physical situations is that the heating volume must be significantly smaller than the crystal such that the approximation of an infinite model domain holds. For the modelling of heating small crystals with weakly absorbing beams such that the absorption depth approaches that of the crystal depth the approximation breaks down and edge effects such as source reflections at interfaces must be considered. For the purposes of this thesis however, we shall restrict ourselves to strongly absorbing radiation and assume that the crystal is of large enough dimensions

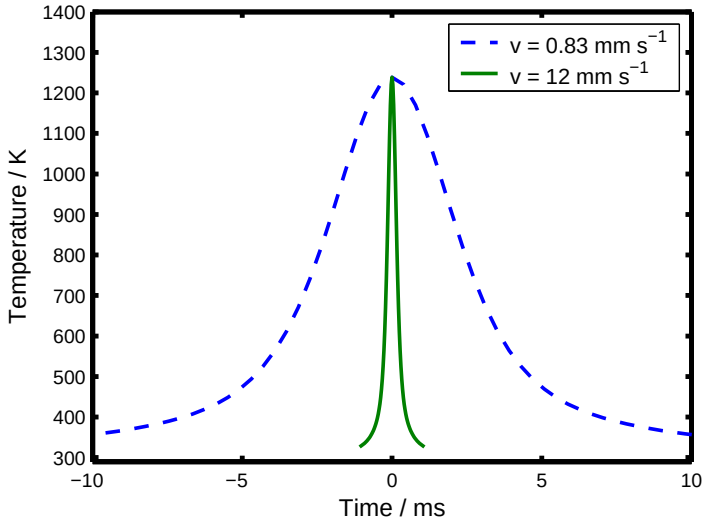

FIGURE 5.12: Temporal temperature distribution in the crystal frame at the point $(x, y, z, t) = (0, 0, 0, t)$ for the maximum and minimum scan speed used in [8]. $w = 3.25$ μm, $P = 30$ mW.

for the approximations to hold. The motivation for looking at wavelengths other than UV, where the absorption coefficient may not be as large, is the possibility to make use of lasers in the IR region with $\lambda < 5\mu$m where the crystal is also absorbing. Lasers such as the CO_2 laser that operate at $\lambda = 10.6\mu$m are widely available and can reach much higher powers, $\sim 10 - 100$W, than the available UV lasers that can reach around 500 mW. If the index change mechanism of [8] is indeed thermally driven then this should allow the production of larger structures of greater depth or the possibility of parallel writing.

To base the investigation on possible use of CO_2 lasers we take imaginary part of the refractive index, ϵ'', at 10μm as given in reference [11] as 0.05 for $\mathbf{E} \perp c$ and 0.04 for $\mathbf{E} \parallel c$. Using the definition

$$\alpha = \frac{4\pi\epsilon''}{\lambda} \tag{5.23}$$

we obtain absorption coefficients of $6.3\times10^4\text{m}^{-1}$ and $5.0\times10^4\text{m}^{-1}$ respectively for $\mathbf{E} \perp c$ and $\mathbf{E} \parallel c$ giving corresponding absorption depths $\delta = 1/\alpha$ of 15 and 20 μm.

For α significantly less than the spot size of the beam no variation of the temperature distribution is seen and the shape is set entirely by the spot size as demonstrated in figure 5.8. Figure 5.13(a) shows the temperature distribution with depth under the center of the beam in the reference frame of the beam as the optical absorption coefficient α is decreased. The spot size in figure 5.13 is 5 μm and the optical absorption coefficients are $\alpha = 5.0\times10^5\text{m}^{-1}, \alpha = 1.0\times10^5\text{m}^{-1}$ and $\alpha = 0.2\times10^5\text{m}^{-1}$ with corresponding absorption depths of 2, 10 and 50 μm respectively. As the absorption coefficient decreases and

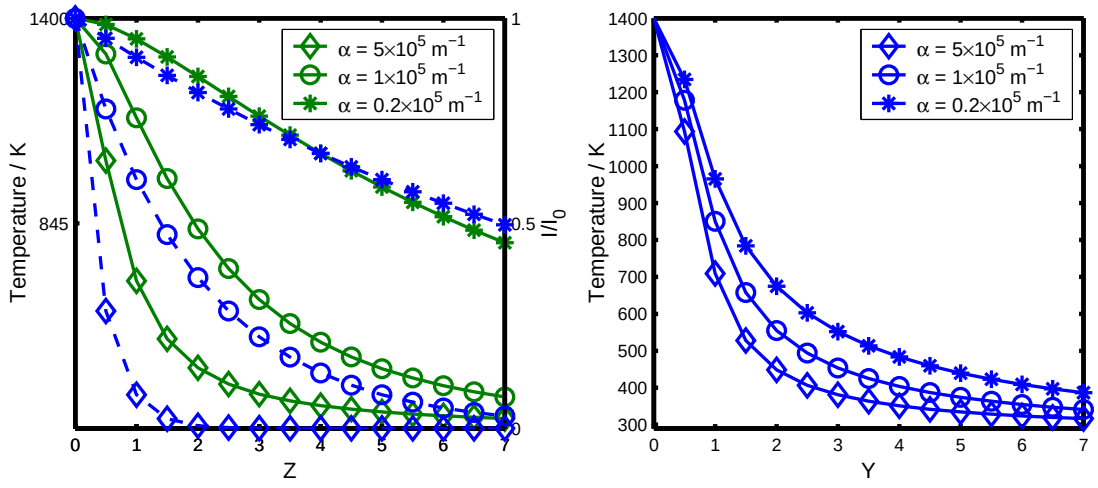

(a) Distribution with depth, $X = Y = 0$.

(b) Distribution on crystal surface, $X = Z = 0$.

FIGURE 5.13: Variation of the temperature distribution (solid curves) and optical intensity (dashed curves) with depth under the centre of the beam for various values of α. Power varied to maintain $T(X, Y, Z) = (0, 0, 0)$ constant at 1400 K. $w = 5.0$ μm, $P = 76$ mW (diamond), 153 mW (circle), 464 mW ($*$).

the absorption depth increases to be comparable to the beam spot size w it is α that has the greatest influence on the shape of the temperature distributions in the depth direction with the depth of the distribution being comparable then to the absorption depth. In the direction parallel to the surface the decrease of the absorption coefficient is seen to increase the width of the temperature distribution but to a far lesser extent than in the depth direction as can be seen in figure 5.13(b). Figure 5.14 illustrates the change in the temperature distribution with decreasing optical absorption by showing the temperature distribution in the plane perpendicular to the surface passing through the point $X = Y = 0$ for values of α (δ) of $5 \times 10^5 \mathrm{m}^{-1}$ (2 μm) figure 5.14(a) and of $0.2 \times 10^5 \mathrm{m}^{-1}$ (50 μm) figure 5.14(b). It can be seen in the figures referenced above that the power required to reach a given temperature increases due to the increased volume being heated by the beam. This would place restrictions on which lasers could be used for practical purposes but shows that CO_2 lasers would certainly be suitable. It is also worthy of note here that that if CO_2 lasers are to be used to locally heat LN the smallest possible focused spot size that could be achieved is around 5 μm. However, in an actual experiment the spot is likely to be many times this. In this case, despite the increased absorption depth compared to UV heating the shape of the temperature distributions will be determined by the spot size and not α.

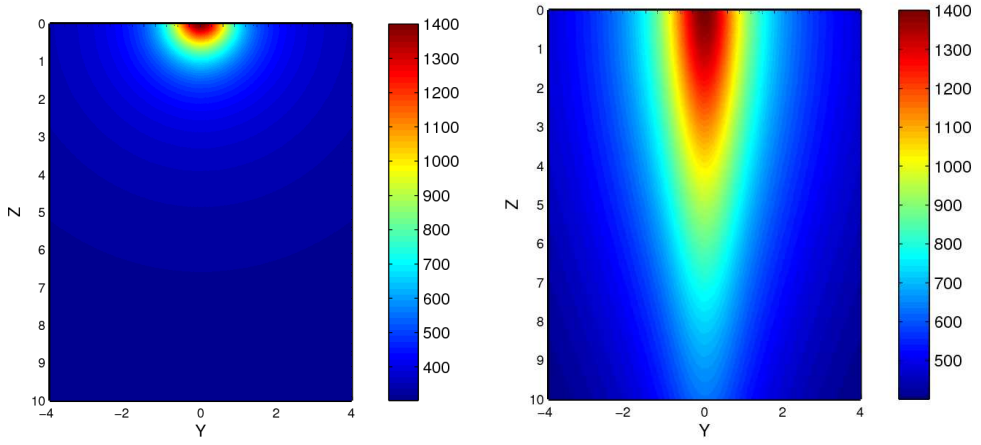

(a) $\alpha = 5 \times 10^5 \mathrm{m}^{-1}$. (b) $\alpha = 0.2 \times 10^5 \mathrm{m}^{-1}$.

FIGURE 5.14: Temperature distribution in the plane perpendicular to the surface through the point $X = Y = 0$.

5.4 Finite Difference Modelling

5.4.1 Motivation and Reasoning

Testing the analytical heat flow model against experiment is extremely challenging due to the inaccessibility of the inside of the crystal, the extremely small volumes being heated and the short time scales over which heating occurs. To test the analytical method we can however build a fully numerical model. This also allows us to test the effects of the approximations in the analytical model such as the constant heat capacity and the choice of fitting function to the thermal diffusivity. The finite difference method is suitable for this problem due to the simple geometry of the system and the simplicity of implementation. The problem itself is of the boundary value type since we are interested in the steady state behavior.

5.4.2 Approximation of Derivatives By Finite Differences

The definition of the derivative is

$$\frac{\mathrm{d}f}{\mathrm{d}x} = \lim_{h \to 0} \frac{f(x+h) - f(x-h)}{h} \tag{5.24}$$

and it is directly from this that the finite difference approximation arises. When we do not take the limit but take a small but finite value of h we obtain the approximation

$$\frac{\mathrm{d}f}{\mathrm{d}x} = \frac{f(x+h) - f(x)}{h} + O(h) \tag{5.25}$$

where the term $O(h)$ is the error of the approximation and in this instance is of the order of h. The forward difference approximation to the derivative is shown above but different approximations can also be made depending upon the suitability to the specific geometry of the domain being modelled or the physics of the system. For instance when we are at the most positive extent of a domain in the x direction to take a forward difference approximation does not have a physical meaning since the point $(x+h)$ does not exist. In this instance a backward difference approximation would be taken (equation 5.28). Similarly when one is interested in a system of the form

$$\begin{aligned} \frac{\mathrm{d}u}{\mathrm{d}t} &= \beta u \\ u(t_0) &= \gamma \end{aligned} \tag{5.26}$$

which models the temporal evolution of the variable u, a backward difference approximation in time would not be suitable since the initial values of u are given. The three most common difference approximations to the first and second derivatives are shown below

$$\frac{\mathrm{d}f(x)}{\mathrm{d}x} = \frac{f(x+h)-f(x)}{h} + O(h) \tag{5.27}$$

Forward difference

$$= \frac{f(x)-f(x-h)}{h} + O(h) \tag{5.28}$$

Backward difference

$$= \frac{f(x+h)-f(x-h)}{2h} + O(h^2) \tag{5.29}$$

Central difference

$$\frac{\mathrm{d}^2 f(x)}{\mathrm{d}x} = \frac{f(x+2h)-2f(x+h)+f(x)}{h^2} + O(h) \tag{5.30}$$

Forward difference

$$= \frac{f(x-2h)-2f(x)+f(x-2h)}{h^2} + O(h) \tag{5.31}$$

Backward difference

$$= \frac{f(x+h)-2f(x)+f(x-h)}{h^2} + O(h^2) \tag{5.32}$$

Central difference

It can be seen that the central difference approximation has a smaller error than the forward or backward differences. By considering the Taylor expansion of the function f about x_i an approximation to the derivatives of f can be made to arbitrary precision with arbitrary displacement forward or backwards ($(x \pm ih)$) with the formula

$$f^{(d)}(x) = \frac{d!}{h^d} \sum_{i=imin}^{imax} C_i f(x+ih) + O(h^p) \tag{5.33}$$

where d is the order of the derivative and p is the order of the error. The weights C_i are found by substituting the formal definition of the Taylor expansion for $f(x+ih)$

$$f(x+ih) = \sum_{n=o}^{\infty} i^n \frac{h^n}{n!} f^{(n)}(x) \tag{5.34}$$

into equation 5.33. Then

$$f^{(d)}(x) = \frac{d!}{h^d} \left(\sum_{i=imin}^{imax} C_i \right) \sum_{n=o}^{d+p-1} i^n \frac{h^n}{n!} f^{(n)}(x) + O(h^p) \tag{5.35}$$

To satisfy equation 5.35 it is necessary that

$$\sum_{i=imin}^{imax} i^n C_i = \begin{cases} 0, & 0 \leq n \leq d+p-1 \text{ and } n \neq p \\ 1, & n = d \end{cases} \tag{5.36}$$

This is a set of $d+p$ linear equations in $i_{max} - i_{min} + 1$ unknowns (C_i). Constraining the number of unknows to be $d+p$ gives the system a unique solution and the vector C can be found. Once C is found the approximation of equation 5.33 can be made.

5.4.3 Modelling With Finite Differences

To numerically model the heating of LN by a laser beam we shall take advantage of the symmetry of the low velocity temperature distributions and introduce two planes of symmetry in which we can apply a zero gradient boundary condition and reduce our domain to one octant of the cartesian space. The domain consists of a regular square mesh of nodes in which the temperatures will be sampled. The heat equation to solve is

$$-\nabla \cdot K \nabla T = S(\mathbf{r}, t) \tag{5.37}$$

where K is assumed isotropic and temperature dependent. Due to the finite sampling distance of the finite difference method and the very small optical absorption depth in the UV it is sensible to approximate the source term as a boundary flux rather than a volume source term as was used in the analytical model. As such we replace in equation 5.7 the exponential decay with a delta function and re-derive the constant of proportionality to give a source function

$$S_{fd} = \frac{4P(1-R)}{\pi w^2} \exp\left(-2(X^2+Y^2)\right)\delta(Z). \tag{5.38}$$

We apply the Neumann boundary conditions of zero temperature gradient on the symmetry boundaries and heat flux on the upper boundary and Dirichlet boundary conditions

TABLE 5.1: Boundary definitions for the finite difference problem.

Boundary Number, i	**Plane**
1	$Z = 0$
2	$Z = Z_{max}$
3	$X = 0$
4	$X = X_{max}$
5	$Y = 0$
6	$Y = Y_{max}$

on the remaining boundaries. This yields the differential equation problem to be solved as

$$\begin{cases} -\nabla \cdot K\nabla T &= 0 \quad \text{on } \Omega \\ -\nabla \cdot K\nabla T &= S_{fd} \quad \text{on } \partial\Omega_1 \\ \mathbf{n} \cdot K\nabla T &= 0 \quad \text{on } \partial\Omega_{1,3,5} \\ T &= T_0 \quad \text{on } \partial\Omega_{2,4,6} \end{cases} \tag{5.39}$$

where Ω is the computational domain, $\partial\Omega_i$ is the domain boundary and $\mathbf{n}$ is the inward normal to the boundary. The boundaries $\partial\Omega_i$ are defined as planes in X, Y, Z in table 5.1.

To enable solution of the term $T(X, Y, Z)$ whilst using central difference approximations (equations 5.29 and 5.32) we recast the derivative in equation 5.37 as

$$\nabla \cdot K\nabla T = K\nabla^2 T + \nabla K \cdot \nabla T. \tag{5.40}$$

Substituting the difference equations 5.29 and 5.32 for the derivatives above we obtain in Ω

$$\begin{aligned} T = \quad & \frac{1}{6-f} \quad \Big\{ \Big[T_{X+} + T_{X-} + T_{Y+} + T_{Y-} + T_{Z+} + T_{Z-} - fT \Big] \\ & + \frac{1}{4K} \quad \Big[(K_{X+} - K_{X-})(T_{X+} - T_{X-}) \\ & \qquad + (K_{Y+} - K_{Y-})(T_{Y+} - T_{Y-}) \\ & \qquad + (K_{Z+} - K_{Z-})(T_{Z+} - T_{Z-}) \Big] \Big\} \end{aligned} \tag{5.41}$$

where the shortened notation is used where $T(X, Y, Z) = T$ and a positive or negative sign coupled to a coordinate in the subscript represents a displacement of h, for example $T(X+h, Y, Z) = T_{X+}$. We have also included an over relaxation factor f to increase the speed of convergence. The problem is solved using point-by-point iteration throughout the computational domain evaluating either 5.41 or the relevant boundary condition from the equation set 5.39. The thermal conductivity K is a function of the temperature T and in the finite difference model can take any form to encompass the temperature dependencies found earlier for both D and C in section 5.2 through equation 5.1. The

computational domain is an N×N×N mesh of points, spaced a distance h apart. The boundary conditions imposed on $\partial\Omega_{2,4,6}$ are strictly only true at an infinite distance but are a good approximation at a distance of a few beam widths. For a fixed number of points however, increasing the domain size reduces the resolution of the model and may affect the convergence properties. Increasing the resolution, however, dramatically increases the number of points and hence numerical calculations to be done since an increase of the resolution by a factor of 2 increases the number of points, and hence computational time, by $2^3 = 8$. As a compromise we choose the length of the domain to be $l = \sqrt{N}$ and $h = l/N = 1/\sqrt{N}$.

5.4.4 Results and Comparison To Analytical Model

The first comparison to make is between the linear analytical model used in section 5.3.5 and the corresponding finite difference model. In this case we take

$$K = D_{lin} C \rho \tag{5.42}$$

using the previous numerical definitions. The temperature distributions with depth under the centre of the beam and with distance across the surface are shown in figure 5.15. The agreement between the two models is very good as can be seen by the plot of the difference $T_{fd} - T_{an}$ in figure 5.16 where T_{fd} is the temperature obtained with the finite difference model and T_{an} is the temperature obtained with the analytical model. It can be seen that there is some disparity between the two distributions in the surface layer where the finite difference model gives a higher temperature at the centre of the beam. This may be due to the use of the different source term to that in the analytical case, even though the delta function source term is the analytical limit of equation 5.7 as $\alpha \to \infty$. However, the peculiarity of the localisation to just the surface layer of the finite difference computational domain suggests that the difference is numerical in origin and not physical. In the finite difference model the boundary conditions pin the temperature to T_0 at a finite distance from the source whereas in the analytical model no pinning of the temperature is required since the domain is assumed to be infinite. This may be the cause for the general lowering of the temperatures seen in the finite difference model.

If we let the heat capacity and density remain constant, we can now test how well the Kirchoff transform has included the temperature dependence of the thermal diffusivity by using the reciprocal of temperature fit to the thermal diffusivity data defined earlier to calculate K. Figure 5.17 shows again the temperature distributions with depth and along the surface where again the agreement is seen to be generally good. The difference between the two is shown in figure 5.18 where it is seen that surface disparity of

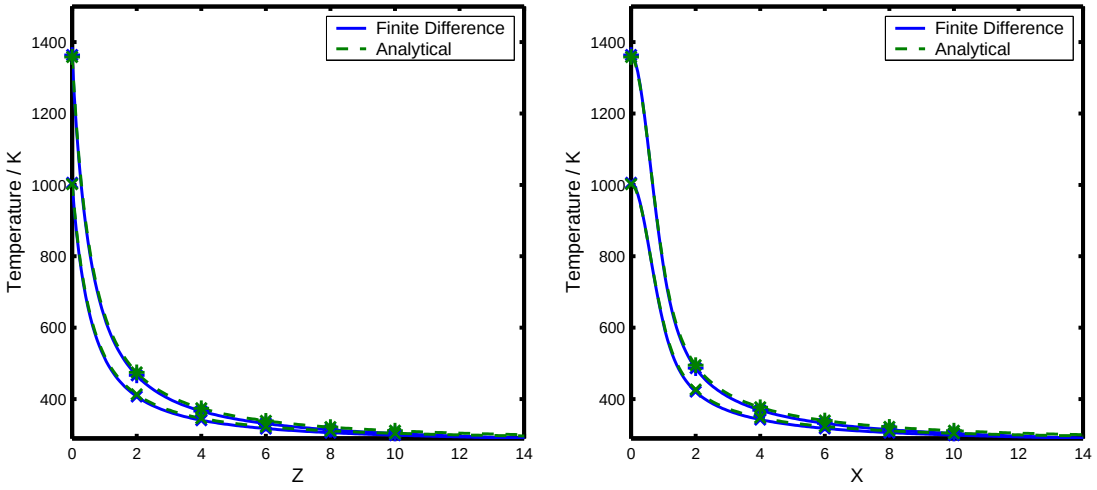

(a) Distribution with depth, $X = Y = 0$.

(b) Distribution on crystal surface, $Y = Z = 0$.

FIGURE 5.15: Comparison of the linear analytical (dashed curve) and finite difference (solid curve) models. $w = 3.25$ μm, $P = 30$ mW $(*)$,$P = 20$ mW $(\times)$, $D = D_{lin} = 5.67 \times 10^{-7}$ m^{2}s^{-1}, $C = 806$ Jkg^{-1}K^{-1}, finite difference domain length (samples) $N = 200$.

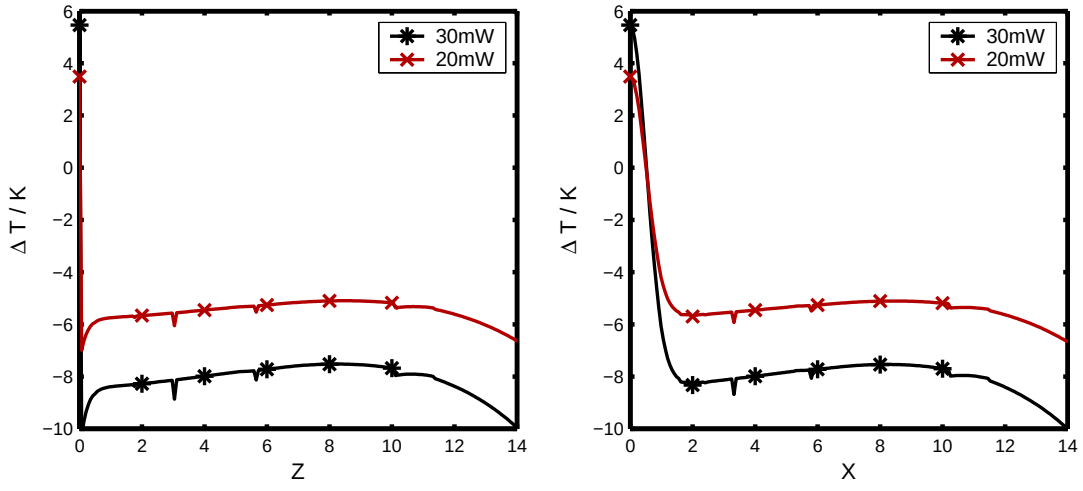

(a) Distribution with depth, $X = Y = 0$.

(b) Distribution on crystal surface, $Y = Z = 0$.

FIGURE 5.16: Temperature difference between the linear analytical and finite difference models. $\Delta T = T_{fd} - T_{an}$, $w = 3.25$ μm, $P = 30$ mW $(*)$, $P = 20$ mW $(\times)$, $D = D_{lin} = 5.67 \times 10^{-7}$ m^{2}s^{-1}, $C = 806$ Jkg^{-1}K^{-1}, finite difference domain length (samples) $N = 200$.

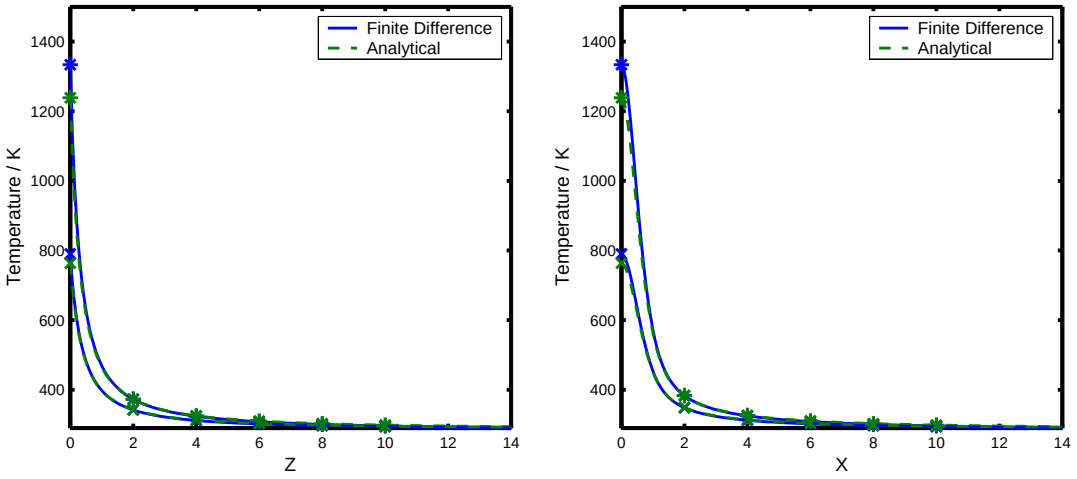

(a) Distribution with depth, $X = Y = 0$.

(b) Distribution on crystal surface, $Y = Z = 0$.

FIGURE 5.17: Comparison of the nonlinear analytical model (dashed curve) and finite difference model using the reciprocal fit for D (solid curve). $w = 3.25$ μm, $P = 30$ mW ($*$), $P = 20$ mW ($\times$), $D = (4.173{\times}10^{-4}/T)$ m^{2}s^{-1}, $C = 806$ Jkg^{-1}K^{-1}, finite difference domain length (samples) $N = 200$.

temperatures extends further into the crystal in this case, not being limited to to the upper layer of nodes in the finite difference model. However, at a power of 30 mW the difference between the temperatures obtained by the two models is only seen to be around 8% of the maximum temperature and the general trend of the two models is seen to be very similar. Again the effect of limiting the boundary temperatures can be seen although here the effect is less than in the linear case since the thermal diffusivity in these cooler regions is lower, concentrating heat near the centre of the beam.

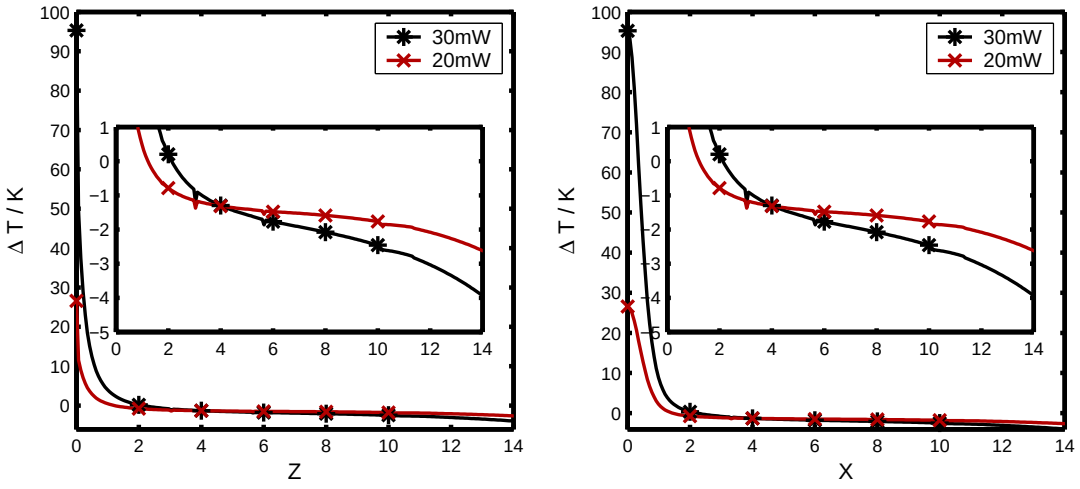

(a) Distribution with depth, $X = Y = 0$.

(b) Distribution on crystal surface, $Y = Z = 0$.

FIGURE 5.18: Temperature difference between the nonlinear analytical and finite difference models. $\Delta T = T_{fd} - T_{an}$, $w = 3.25$ μm, $P = 30$ mW $(*)$,$P = 20$ mW $(\times)$, $D = 4.173 \times 10^{-4}/T$ m^{2}s^{-1}, $C = 806$ Jkg^{-1}K^{-1}, finite difference domain length (samples) $N = 200$. Inserts show an expanded view to aid comparison.

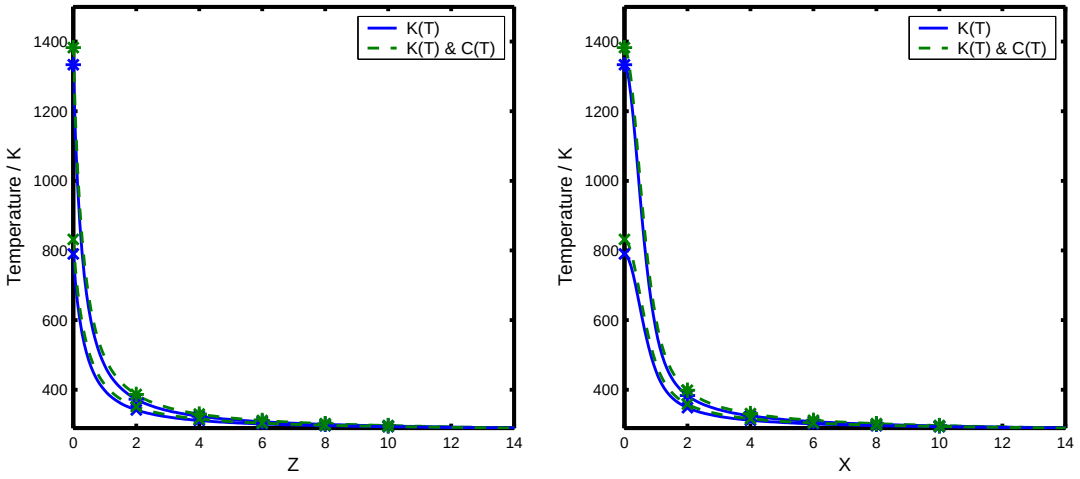

(a) Distribution with depth, $X = Y = 0$.

(b) Distribution on crystal surface, $Y = Z = 0$.

FIGURE 5.19: Effect of including temperature dependence of the heat capacity using the finite difference model. Linear heat capacity (solid curve) and temperature dependent heat capacity (dashed curve). $w = 3.25$ μm, $P = 30$ mW ($*$), $P = 20$ mW ($\times$), $D = (4.173 \times 10^{-4}/T)$ m^{2}s^{-1}, $C = 806$ Jkg^{-1}K^{-1}, finite difference domain length (samples) $N = 200$.

It has been shown that the methods used in the nonlinear analytical modelling are good since they agree to a high degree with the fully numerical model. During the construction of the analytical model we were, however, limited to how faithfully we could include nonlinear effects due to the requirement that the fitting function must integrate to give a one-to-one function in Θ for T and the limitation of only being able to fit to D and not also C. The finite difference model does not have this limitation and so can be used to accommodate a temperature-dependent C from equation 5.2 and the the alternative fitting function for D of equation 5.18.

To compare the effect of including a temperature-dependent heat capacity we use the finite difference model only so that any differences seen are due only to the heat capacity and not differences between the models. The temperature dependence of the thermal diffusivity is included using the reciprocal fit and the heat capacity is included as a fit to the Einstein equation 5.2.

Figures 5.19 and 5.20 show the temperature distributions and the difference in the temperature distributions respectively due to the temperature dependent heat capacity using equation 5.2. The inclusion of a temperature dependent C is seen to globally increase temperatures. This is due to the fact that the linear approximation of the heat capacity takes its value at approximately 670 K whilst the majority of the temperature distribution is below this temperature. In these low temperature regions the over estimation of the heat capacity in the models with constant C leads to a greater required energy to

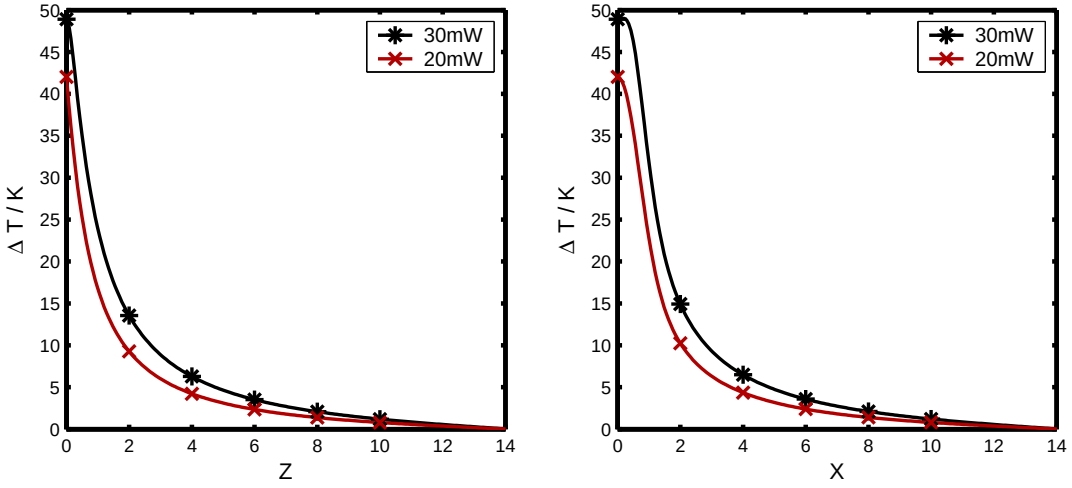

(a) Distribution with depth, $X = Y = 0$.

(b) Distribution on crystal surface, $Y = Z = 0$.

FIGURE 5.20: Temperature difference between the distributions obtained using linear and temperature dependent heat capacity. $\Delta T = T_{C(T)} - T_{C_{linear}}$, $C_{linear} = 806$ Jkg^{-1}K^{-1}, finite difference domain length (samples) $N = 200$.

raise the temperature by a given amount and hence with a fixed steady state energy flux equal to the source power the linear model predicts a lower temperature. However, the effect of including a temperature dependent heat capacity is small in comparison with the effect of including a temperature dependent diffusivity as shown in figure 5.6(b).

To compare the effect of the choice of thermal diffusivity fitting function we again use the finite difference model. The heat capacity is taken again to be constant at 806 J Kg^{-1}K^{-1} and the thermal diffusivity functions are taken from equations 5.18 and 5.19.

Figures 5.21 and 5.22 show temperature distributions and the difference in the temperature distributions respectively due to the different thermal diffusivity fits (C constant) both along the depth and along the surface. It is clear that the difference between the two cases is small for low temperatures. However, as the power, and hence temperatures at the centre of the beam, increase above 800 K the effect of the divergence between the two fits becomes apparent. The reciprocal of temperature function for the thermal diffusivity gives a rapidly decreasing value for D, leading to reduced heat flow and a subsequent rise in temperature compared to the exponential function for the thermal diffusivity model which gives a reasonably constant diffusivity after 800 K. It still remains to be seen which of the two is the most physically meaningful fit and so for the purposes of the thesis the reciprocal of temperature function for the thermal diffusivity will be used in the knowledge that for over half the temperature range practically available the difference is negligible.

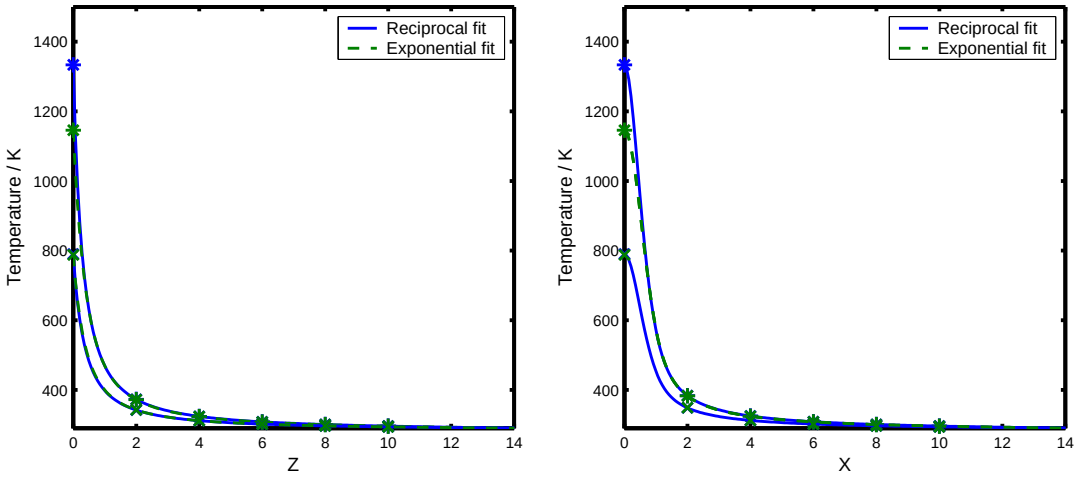

(a) Distribution with depth, $X = Y = 0$.

(b) Distribution on crystal surface, $Y = Z = 0$.

FIGURE 5.21: Effect of choice of thermal diffusivity fit. $w = 3.25$ μm, $P = 30$ mW ($*$), $P = 20$ mW ($\times$), $C = 806$ Jkg^{-1}K^{-1}, finite difference domain length (samples) $N = 200$.

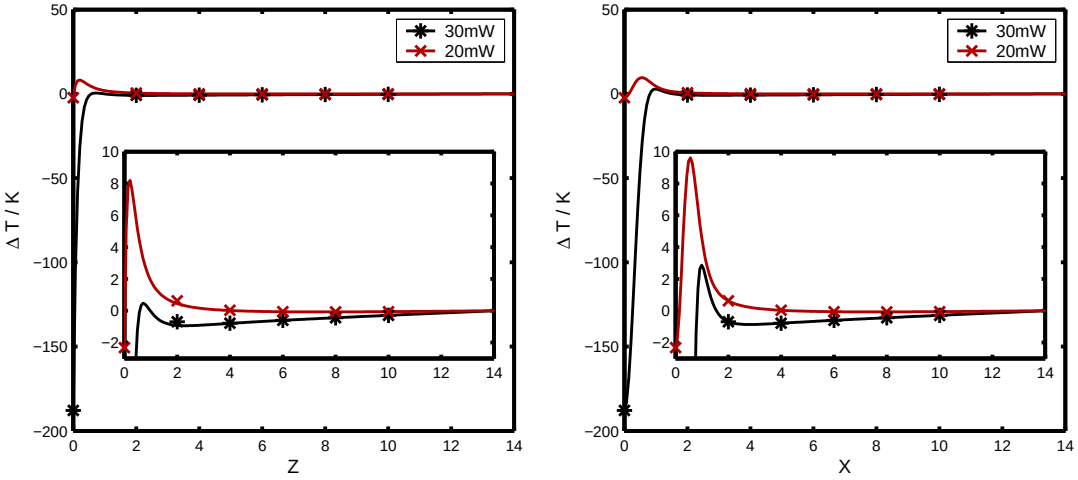

(a) Distribution with depth, $X = Y = 0$.

(b) Distribution on crystal surface, $Y = Z = 0$.

FIGURE 5.22: Temperature difference between the distributions obtained using reciprocal and exponential thermal diffusivity fits. $\Delta T = T_{exponential} - T_{reciprocal}$, $C = 806$ Jkg^{-1}K^{-1}, finite difference domain length (samples) $N = 200$. Inserts show an expanded view to aid comparison.

From the results of the finite difference modelling it has been seen that the method of the analytical model is good and does compare well with the numerical modelling. Some differences have been seen but it is difficult to say with certainty that they arise due to limitations of the analytical model and not from errors within the finite difference method. The primary source of temperature dependence of the system in equation 5.3 however, is the thermal diffusivity (or conductivity) hence the assumption in the analytical model of constant heat capacity is proved to be reasonable.

5.5 Experimental Verification

As was mentioned in the previous section it is extremely hard to find a handle with which the temperature of the crystal can be mapped while it is being heated to provide verification of the model. Both contact and IR thermometry are unsuitable due to the small volumes being heated and within the validity of the model no physical changes that can be imaged after wards take place. If the model were extended to include a phase change from solid to liquid we would be able to measure the resultant melt widths and pit depths to compare to theory. However this is a very involved task that would require the modelling of a highly complex system with phase changes from both solid to liquid and liquid to gas, moving boundaries and coupled convective and diffusive fluxes all with very little physical data to base it on. At the boundary between the two models there is however a point where both would be valid that could provide one datum for comparison. This point is the melt onset which will occur at a temperature of 1513 K.

5.5.1 Results

Figure 5.23 shows lines scanned at powers of 22, 24 and 26 mW as measured before the final focusing lens. Although a darkened region can be seen in all lines that is indicative of a refractive index change it was only at a power of 24 mW and above that any signs of melting were seen. The beam spot size in this instance was $\sim$2.5 μm as estimated from burn patterns on photoresist. This is a very crude method of obtaining a spot size and so the error may be large and perhaps of the order of 0.5 μ m. Figure 5.24 shows the power at which melting should occur for spot sizes of $w = 2, 2.5$ and 3 μm where very good agreement can be seen with the experimental results.

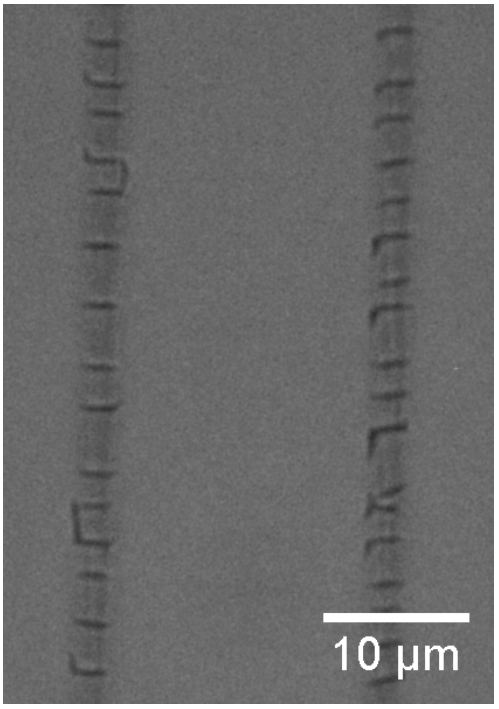

(a) p = 26 mW.

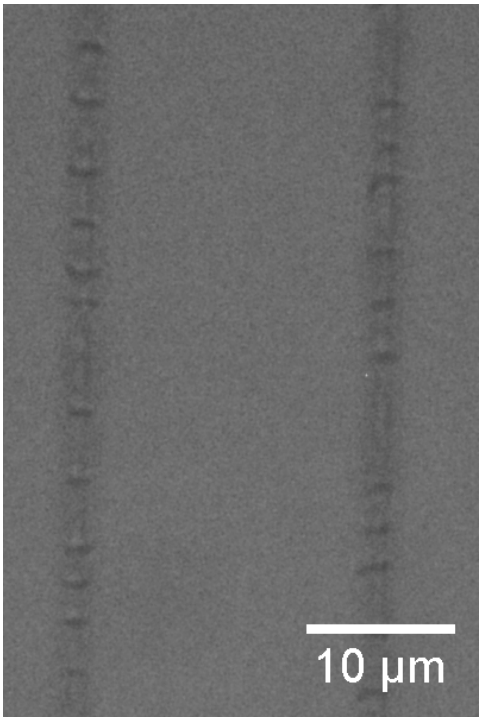

(b) p = 24 mW.

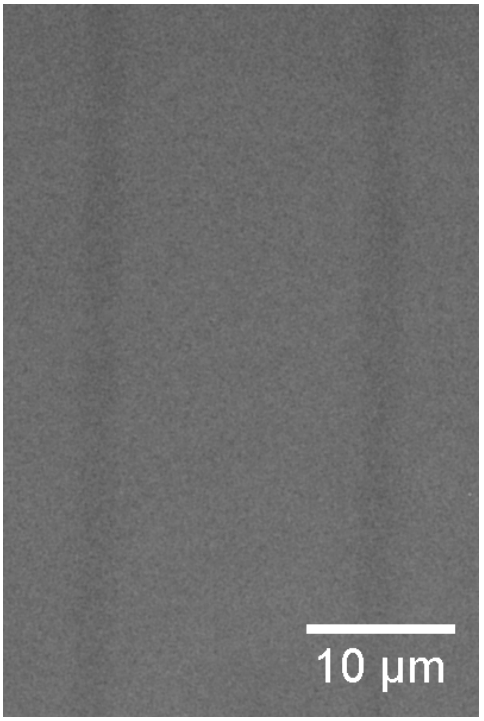

(c) p = 22 mW.

FIGURE 5.23: Optical microscope images of lines written in LN by 244 nm UV laser light. $w \approx 2.5\mu$m, scan speed $v = 300\mu\text{ms}^{-1}$.

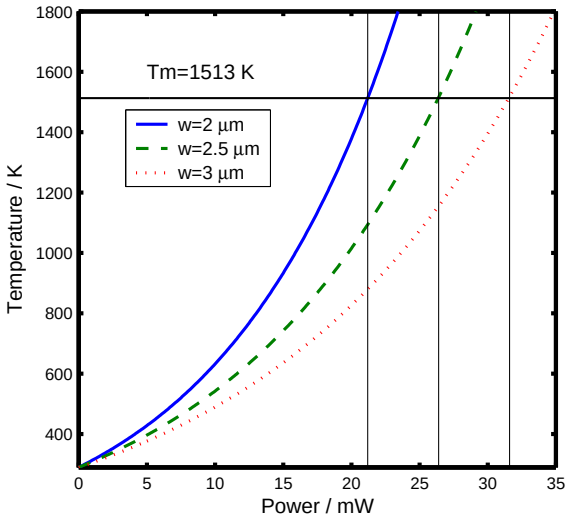

FIGURE 5.24: Temperature variation with power for $w = 2, 2.5$ and 3 μm at point $(X, Y, Z) = (0, 0, 0)$ obtained using the nonlinear analytical model. Horizontal line indicates the melting point of congruent LN.

5.6 Summary and Conclusions

The heating of lithium niobate by absorbing laser radiation has been modelled by both analytical and numerical methods as a first step in the understanding of the crystal heating by absorbed laser radiation. The analytical modelling included the temperature dependence of the thermal diffusivity in a new temperature variable by means of the Kirchhoff transform. This nonlinear analytical model was compared with its corresponding linear model and the inclusion of the temperature dependence of the thermal diffusivity was seen to have a significant effect upon the temperature distributions obtained. Particularly it was seen that the temperature distributions were narrowed, becoming more localised to the source. This was attributed to a higher diffusivity in cooler regions allowing a greater heat flow away from the source whilst in the hotter regions closer to the source the thermal diffusivity was decreased leading to a reduced heat flow and subsequent temperature rise. The anisotropy of the temperature distributions was examined and whilst, by definition of the fundamental equations, no anisotropy was seen parallel to the surface a strong anisotropy was seen between directions parallel and perpendicular to the surface. The model was constructed in the moving reference frame of the beam and it was found that the spatial temperature distributions were independent of the scan speed for practically achievable scanning speeds. The spatial temperature distribution in the rest frame of the crystal was transformed into the temporal temperature distribution in the rest frame of the crystal to show that this is highly dependent upon scan speed and the physical implications of this were discussed. The dependence of the temperature distribution in the moving frame on spot size, incident

power and optical absorption were investigated. It was found that the length scale of the temperature distribution in the depth direction was given by whichever was the larger of the spot size w and the absorption depth $\delta(= 1/\alpha)$ whilst the length scale of the temperature distribution parallel to the surface remains essentially fixed at the length scale w, broadening only slightly. The implications of this for heating with far infra-red sources which are slightly less absorbing than UV were discussed.

To test the validity of the analytical model and the assumptions therein two methods were used. Firstly, a fully numeric model using the finite difference method was constructed and secondly a crude practical experiment was used to find the power at which melting would onset. The finite difference model was first used to compare with a linear analytical model to find a benchmark against which the subsequent comparison of nonlinear models, to validate the use of the Kirchhoff transform, could be set. Some differences were seen which, although being relatively small, were localised to the top layer of surface nodes of the finite difference computational domain. Due to the sharp discontinuity of this difference it was attributed to be of a numerical source rather than physical and must be considered in the following comparisons. The comparison of the nonlinear analytical and finite difference models was carried out using the same empirical function for the thermal diffusivity with all other factors remaining linear. The comparison was favourable and even with the surface disparity mentioned previously the maximum difference seen between the two models for the high power simulation used was only around 8% persisting near this value for only a very small fraction of one beam width in depth. Having demonstrated that the analytical methods used are indeed valid the finite difference model was used to investigate the impact of neglecting the temperature dependence of the heat capacity and of the choice of empirical function for the thermal diffusivity. The temperature dependent heat capacity was found to cause a general increase of temperature however the increase was small and did not change the shape of the temperature distributions to any large degree. This demonstrated that the thermal diffusivity is indeed the prominant source of nonlinearity in the system. The effect of the choice of a reciprocal of temperature fit for the thermal diffusivity over an expontial fit was investigated and it was seen that where temperatures exceeded around 800 K, where the fit functions diverge, the reciprocal fit resulted in larger temperature rises. Due to the lack of physical data at high temperatures both models were concluded to be equally valid and the reciprocal fit is used in the remainder of this thesis. The results of all investigations were discussed qualitatively and related back to the expected behavior from the thermal properties.

The finite difference model and the analytical model have been shown to be complimentary and both certainly have their advantages. The analytical model benefits from the

ability to give temperatures at arbitrary points and distributions with arbitrary resolution but suffers from it's assumptions. The finite difference model on the other hand has very few assumptions and can include a wide range of physical dependencies but is limited in its resolution and practicality by the need to solve the entire computational domain which must extend far enough from the source for the boundary conditions to be valid. This places a large computational burden for which the cost is time. The speed of the finite difference simulations could be increased by taking the full rotational symmetry into account and recasting in polar coordinates, thereby reducing the computational domain to two dimensions. For historical reasons of the derivation this thought did not occur until after the work was completed.

A significant difficulty in the modelling carried out in this section has been the attainability of reliable physical data, particularly on the anisotropy and temperature dependence of the material. The majority of the thermal data, and only that which contains any anisotropy data, comes from Zhdanova et al. [4] and was completed almost forty years ago when the growth of LN was in its infancy and crystal quality was very different to that of today. Had a greater body of knowledge been available the model described here could have provided a fully anisotropic description. A constructive extension to the heat flow modelling would have been to include melting and the subsequent behaviour of the melt, however this problem is highly nonlinear and would almost certainly need numerical methods that could deal with both phase changes and moving boundaries. This has been done in other studies of materials such as steel where the material properties are well known over a large parameter space however the lack of data for LN would prohibit accurate models in our case. It is also not clear as to whether the benefit gained in understanding by including a phase change would be worth the expenditure of time and effort.

In conclusion, an analytical model of the heating of LN by a scanning laser beam has been developed, tested and found to be valid. This model can now be used as the basis of the investigation into the interaction of lithium niobate surfaces and highly absorbed continuous wave laser radiation.

References

[1] A.M. Mamedov, L.S. Hajiyeva, I.S. Ibragimova, and B.S. Aliyeva. Vacuum ultraviolet (VUV) reflectivity and electron states in $LiNbO_3$. *Physica B &; C*, 128B+C: 61 – 8, 1985.

[2] K. Kobayashi, T. Koike, Y. Imai, and H. Obara. Observation of anisotropic thermal diffusivities in yz $LiNbO_3$ using transient heat pulse diffusion measurement. In *Ultrasonics Symposium, 2001 IEEE*, volume 1, pages 451 – 454, Atlanta, GA, 2001.

[3] R.A. Morgan, K.I. Kang, C.C. Hsu, C.L. Koliopoulos, and N. Peyghambarian. Measurement of the thermal diffusivity of nonlinear anisotropic crystals using optical interferometry. *Applied Optics*, 26(24):5266 – 71, 1987.

[4] V. V. Zhdanova, V. P. Klyuev, V. V. Lemanov, I. A. Smirnov, and V. V. Tikhonov. Thermal properties of lithium niobate crystals. *Sov. Phys. -Solid State (USA)*, 10: 1360, 1968.

[5] K. K. Wong. *Properties Of Lithium Niobate*. EMIS Datareview. IEEE, 1989.

[6] Norbert Kockmann, editor. *Micro Process Engineering: Fundamentals, Devices, Fabrication, and Applications*. Wiley VCH, 2006.

[7] J.E. Moody and R.H. Hendel. Temperature profiles induced by a scanning cw laser beam. *Journal of Applied Physics*, 53(6):4364 – 71, 1982.

[8] S. Mailis, C. Riziotis, I.T. Wellington, P.G.R. Smith, C.B.E. Gawith, and R.W. Eason. Direct ultraviolet writing of channel waveguides in congruent lithium niobate single crystals. *Optics Letters*, 28(16):1433 – 1435, 2003.

[9] R. C. Clive. *Techniques In Partial Differential Equations*. McGraw-Hill, New York, 1971.

[10] A.M. Mamedov. Optical properties (VUV region) of $LiNbO_3$. *Optics and Spectroscopy*, 56(6):645 – 9, 1984.

[11] A. S. Jr Barker and R. Loudon. Dielectric properties and optical phonons in lithium niobate. *Physical Review*, 158:433, 1967.

Chapter 6

Modelling Of The Thermally Driven Diffusion of Lithium Ions In LN

6.1 Background and Motivation

In chapters 3 and 4 it was shown that illumination of LN with a scanning, focused, UV laser beam with a wavelength of 244 nm can either directly pole the crystal or create a region where poling is impeded in a subsequent EFP step. It was hypothesised that the main driving force for the effect was the temperature field caused by the high optical absorption at 244 nm[1] producing local heating, along with photoexcited charges. The full solution of the model is complex due to the electrostatic coupling of the charged mobile species and has not been permitted in the time scales of this thesis. Since the fundamental driving force is due to the temperature fields, however, the heating of LN by a scanning laser beam has been modelled in chapter 5 as a basis for the future solution of the model in chapters 3 and 4 and for other investigations of focussed UV light - LN interactions.

It was seen in [2] that optical waveguiding structures could be produced in LN by a scanning focused UV laser beam. The beam, of wavelength 244 nm, from a frequency doubled argon ion laser was focused to a $1/e^2$ spot radius ranging from 1.75 to 3.25 μm with energy fluences of 60 to 600 kW/cm^2 and scanned across the surface of the crystal. Due to the high absorption coefficient at this wavelength of 3.3 $\times 10^7$ m^1 [1] the optical energy is absorbed in a very thin layer (< 100 nm) at the surface. As such it was assumed that the effect giving rise to the refractive index change required for waveguiding could not be due to light directly as in the photorefractive effect but must instead be caused

by thermal effects. Indeed the creation of optical waveguides in LN following thermal treatments is not a new phenomenon [3, 4] although in most cases it is not used as a method in itself but presents as an unwanted by product during Ti-indiffusion [5, 6]. In these instances the change in refractive index is attributed to a decrease in lithium content due to out-diffusion from the surface since the refractive index is known to be a function of composition [7]. In the case of [2], however, the heating duration of a particular area of crystal is only for the few milliseconds that the beam spot takes to cross a given point, rather than the extended periods of hours used in [3, 4]. As such it was believed that the index change mechanism caused by the scanning UV beam, although related, must be of a different character and so requires an investigation of its own.

6.1.1 Possible Index Change Mechanisms and Limitations of Modelling

Many possible mechanisms exist to change the refractive index during laser heating with UV light, and more than one might be active in the results seen in [2]. Some of these are straightforwardly amenable to numerical modelling given the current knowledge of the physical properties of the crystal and from the deterministic nature of the mechanism. Others, however, are either too complex in their mechanism or require data on physical properties yet unknown or insufficiently characterised for LN. One such possible index change mechanism that will not be possible to model accurately is the strain induced index change following residual stresses caused by damage during the heating process. In this case some modelling could be carried out, using the standard stress-strain relations [8] and the known elastic constants and thermal expansion properties of LN [9], which would show the thermally induced stresses during laser heating, but this would only be valid in the linear regime and would not lead to residual stresses. Residual stresses would result, however, from high temperature fractures or dislocations which break the symmetry of the heating and cooling cycle. It is this knowledge of the fracture and dislocation mechanisms in LN that is missing from the literature, preventing a reliable model formulation. Stresses may arise from the mismatched re-solidification of a melt pool, however this too cannot be modelled due to incomplete knowledge of the thermal properties of the liquid phase of LN.

A further possibility that cannot be modelled, but should be considered, is the precipitation of neighbouring crystallographic phases. The Li_20-Nb_2O_5 system has many stable compositional phases with a wide stoichiometry range as can be seen from the phase diagram of the system in figure 6.1. Between a melt composition range of 37 mol. % to 60 mol. % Li_2O, $LiNbO_3$ is the first phase to form the melt and depending upon

the melt composition this may decompose into one of two other phases [10, chap. 1]. The first, which occurs on the lithium deficient side of the phase diagram, is lithium triniobate $LiNb_3O_8$ (L3N). L3N will decompose from LN as $3LiNbO_3 \rightarrow LiNb_3O_8 + Li_2O$ [11]. The crystal is mainly composed of oxygen octahedra, as is LN, however the arrangement of the cations is different giving the crystal a different point and space group [12]. The refractive indices of $LiNb_3O_8$ were measured at a wavelength of 633 nm to be; $n_1 = 2.28$, $n_2 = 2.36$, $n_3 = 2.4$. For comparison the refractive indeces of congruently melted LN at a wavelength of 633 nm are $n_o = 2.29$, $n_e = 2.208$ [13]. Since L3N is centrosymmetric it is not ferroelectric and so does not have the technologically useful properties of LN. The decomposition of LN into L3N can also occur during the heating of LN [10, Sect.1.4][14–18] both on the surface and in the bulk of the crystal for niobium rich stoichiometries. It has been shown in [14] that in fact the congruent composition of 48.6 mol. % Li_2O of LN is only metastable at low temperatures and that the decomposition is restricted by the energetics of niobium diffusion and not by thermodynamic stability arguments. Since the refractive indices of L3N are different to that of LN its precipitation may cause waveguiding structures. The n_2 and n_3 indices of L3N are greater than either n_e or n_o of LN whilst n_1 of L3N is smaller thus whether a waveguide can be formed for a particular light polarisation depends upon the orientation of the L3N precipitates relative to the LN host. In [19] L3N is precipitated during annealing of proton exchanged LN waveguides and upon precipitation of L3N in the guide a single mode of o-polarisation is seen to propagate, despite lowering of the host n_o by the proton exchange process [20], indicating an increase of n_o. A similar behaviour is seen in [18] where the birefringence increases with L3N growth. The waveguides in [2] were seen, however, to guide e-polarised light and not o-polarised light which reduces the likelihood of this being a major cause.

Another possible mechanism for changing the refractive index is an induced inhomogeneity of the crystal stoichiometry. Lithium niobate can exist as a single phase crystal over a wide stoichiometry range from around 45 % Li_2O to around 50 % Li_2O [14]. This can be seen from the phase diagrams in figure 6.1. Over this stoichiometry range the crystal has, of course, the same physical structure as is described in section 1.1 and is still ferroelectric, unlike the compositions in the adjoining regions of the phase diagram of $LiNb_3O_8$ and Li_2NbO_4. Although the general structure of the crystal remains the same over the stoichiometry range various properties of the crystal do change and one such property is the refractive index. The extraordinary refractive index of LN is known to increase with decreasing Li_2O content [3, 4, 7, 21] and so if the local concentration of Li_2O can be controlled, refractive index structures such as waveguides can be produced. This has been achieved simply by heating the crystal to temperatures corresponding to the region in the phase diagram where LN is stable over the required stoichiometry (see

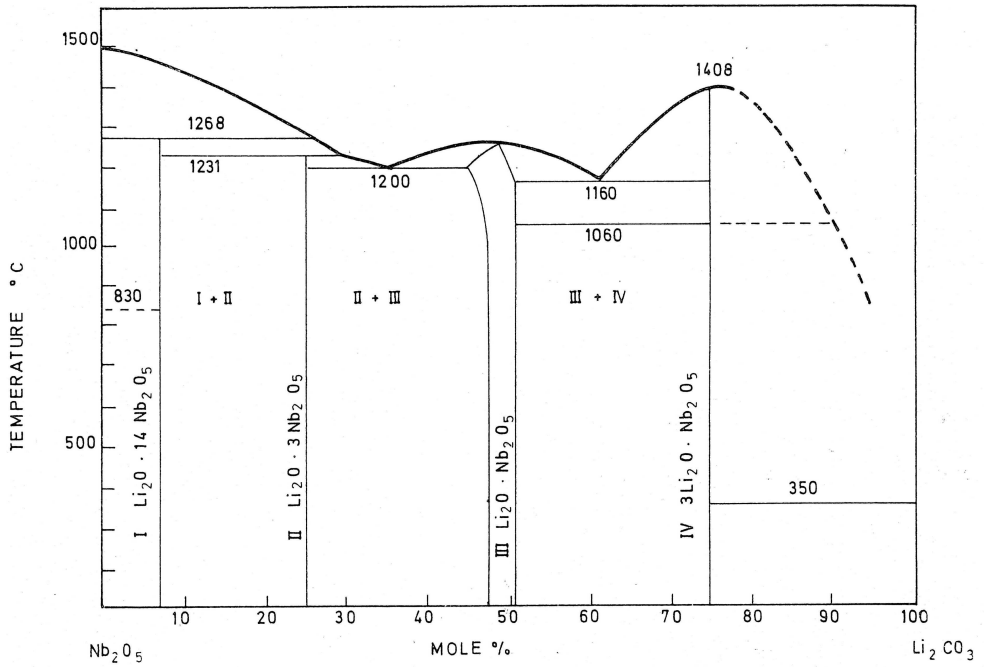

FIGURE 6.1: Phase-equilibrium diagram of the Li_2O - Nb_2O_5 system. After [11].

figure 6.1) for an extended period of time such that volatile Li_2O could evaporate from the surface [4]. During depletion of Li_2O from the outer surface a concentration gradient was created within the crystal that drove a flow of Li_2O to the surface, through a normal Fickian diffusion process, and a smooth variation of stoichiometry and hence refractive index was produced with depth into the crystal. This was seen to produce high quality, low loss, slab wave guides that guided e-polarised light.

The waveguides produced in [2] were seen to guide e-polarised light and not to guide o-polarised light, as were those seen in [3, 4]. This may suggest that the refractive index change seen in [2] is also due to a decrease of the lithium concentration in the exposed region. In contrast to residual thermal stress and the precipitation of new crystal phases, the diffusion of ionic species within the crystal is amenable to modelling and this task will form the remainder of this chapter.

6.2 Numerical Modelling with Finite Differences

The governing equations of the thermal diffusion of lithium ions in LN are derived under the assumptions that there is no electrostatic interaction between diffusing species and the vacancy density is constant. The equations are solved using finite difference methods and the temperature distributions obtained in chapter 5 to give the lithium concentration distribution in the y, z plane of the crystal after the passage of the illuminating

beam. The resultant lithium concentration distribution is converted to a refractive index distribution using the Sellmeier equations for LN. The waveguiding properties of the refractive index distributions are then modelled using a commercial waveguide modelling package for comparison with reference [2]. The lifetime of the lithium concentration distributions at room temperature are investigated and compared with the lifetimes of the experimental waveguides.

The refractive index of LN is dependent upon the concentration of lithium present [7] and waveguides have been produced through the out-diffusion at high temperatures of lithium from the surface of LN [3, 4]. However this requires durations of hours at temperatures near the melting point and so is inadequate for situations when heating is only observed for milliseconds. In reference [3, 4] the temperature was uniform throughout the volume of the LN crystal and so no temperature gradients were present but the heating process in reference [2] has been seen in chapter 5 to produce very steep temperature gradients and it is proposed that the waveguides observed in reference [2] were due to the thermal diffusion within the crystal of lithium away from the irradiated regions, driven by the steep temperature gradients.

6.2.1 Model Derivation

It is assumed that the ionic diffusivity is isotropic in uniform temperature fields as indicated in [22] and that concentration changes are small such that vacancies are always present for diffusing species to occupy.

Two sites separated by a distance a, as shown in fig 6.2, are considered. There are n_1 particles at site 1 and n_2 particles at site 2. The quantity r is defined to be a rate function that corresponds to the average number of times a particle jumps in any direction in unit time and is dependent upon temperature. In one dimension, the flux of particles from site 1 to site 2, and site 2 to site 1 are given by J_{12} and J_{21} respectively where

$$J_{12} = \frac{1}{6} r_1 n_1 \tag{6.1}$$

and

$$J_{21} = \frac{1}{6} r_2 n_2. \tag{6.2}$$

The factor 1/6 is present since, at any given point, the particles can jump in any of the six cartesian axis directions. We treat these with equal probability and consider only the net flow for one direction, which will be equivalent for all. The net flux between

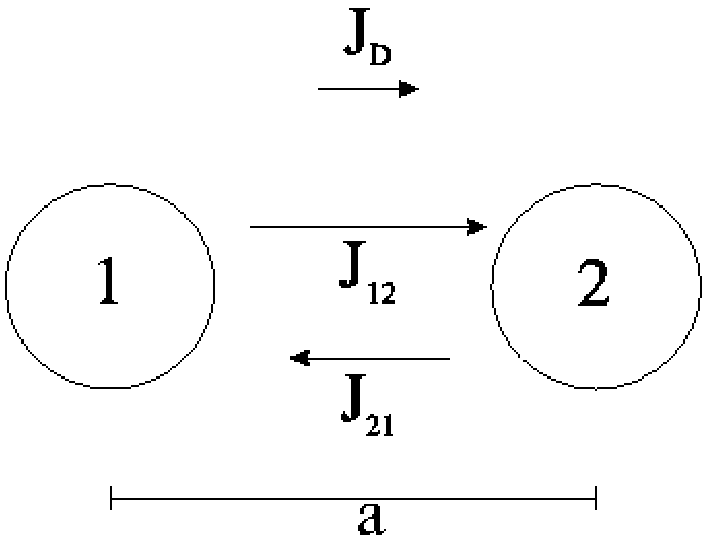

FIGURE 6.2: Schematic for diffusive flow between sites 1 and 2. J_D is the net flow from site 1 to 2 and J_{ij} is the flow from site i to site j. The two sites are separated by the discrete jump distance a.

sites 1 and 2 is then

$$\begin{aligned} J_D &= J_{12} - J_{21} \\ &= -\frac{1}{6}\left(r_2 n_2 - r_1 n_1\right). \end{aligned} \tag{6.3}$$

In terms of concentrations

$$J_D = -\frac{a^2}{6}\frac{\left(r_2 c_2 - r_1 c_1\right)}{a} \tag{6.4}$$

where c_1 and c_2 are the concentrations of particles at site 1 and 2 respectively. Taking the limit as $a \to 0$

$$J_D = -\frac{a^2}{6}\frac{\partial(rc)}{\partial x} \tag{6.5}$$

where c is the concentration which will be dependent upon position. In the limit where r is constant it can come out of the derivative and we return to the familiar Fick's first law

$$J_D = -D\frac{\partial c}{\partial x} \tag{6.6}$$

where D is given by $a^2 r/6$.

The rate of change of the concentration of particles within a volume can be found by balancing the fluxes through the test volume shown in figure 6.3. The flux of particles through the face $ABCD$ is

$$F_{ABCD} = 4dydz\left(J_{Dx} - \frac{\partial J_{Dx}}{\partial x}dx\right). \tag{6.7}$$

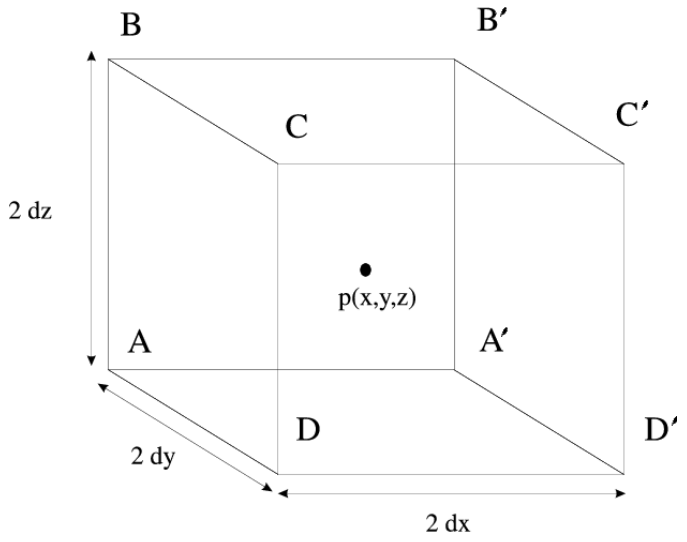

FIGURE 6.3: Test volume 8dxdydz.

where J_{Dx} is defined at the point p. The flux through the face $A'B'C'D'$ is

$$F_{A'B'C'D'} = 4dydz\left(J_{Dx} + \frac{\partial J_{Dx}}{\partial x}dx\right). \tag{6.8}$$

The net contribution in the x direction is then

$$F_{ABCD} - F_{A'B'C'D'} = Fx = -8dxdydz\frac{\partial J_{Dx}}{\partial x}. \tag{6.9}$$

The contributions from the y and z directions are similarly

$$Fy = -8dxdydz\frac{\partial J_{Dy}}{\partial y} \tag{6.10}$$

and

$$Fz = -8dxdydz\frac{\partial J_{Dz}}{\partial z}. \tag{6.11}$$

The net change of particle number in the volume is then

$$\begin{aligned} Fx + Fy + Fz &= -8dxdydz\left(\frac{\partial J_{Dx}}{\partial x} + \frac{\partial J_{Dy}}{\partial y} + \frac{\partial J_{Dz}}{\partial z}\right) \\ &= -8dxdydz\nabla J_D \end{aligned} \tag{6.12}$$

where $J_D = J_{Dx} + J_{Dy} + J_{Dz}$. The net change in particle number is also given by

$$\Delta n = 8dxdydz\frac{\partial c}{\partial t} \tag{6.13}$$

which gives us

$$\frac{\partial c}{\partial t} = -\nabla J_D. \tag{6.14}$$

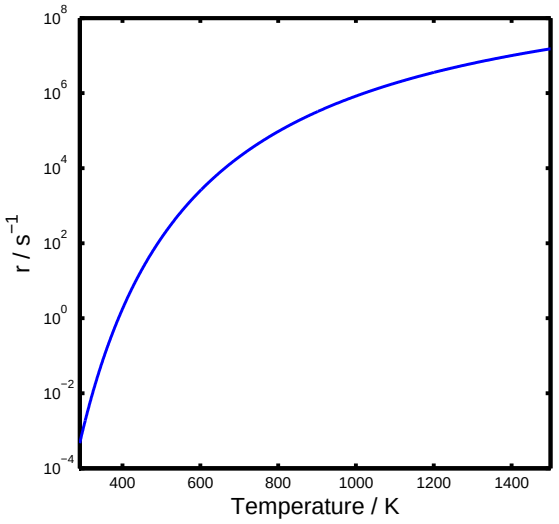

FIGURE 6.4: Variation of the rate function with temperature between room temperature and the melting point of LN.

Substituting equation 6.5

$$\frac{\partial c}{\partial t} = \frac{a^2}{6}\nabla^2(rc). \tag{6.15}$$

Again when r is taken to be constant we return to Fick's second law

$$\frac{\partial c}{\partial t} = D\nabla^2 c. \tag{6.16}$$

The temperature dependent expression for r is

$$r = r_0 \exp\left(-\frac{Q}{k_B T}\right) \tag{6.17}$$

where Q is the activation energy or the energy required for the ion to leave its present position and r_0 is the attempt rate. Q and r_0 were found to be 0.75 eV and 5.024×10^9 s^{-1} respectively as determined by nuclear magnetic resonance measurements [22]. Over the temperature range seen during laser heating r varies over five orders of magnitude as can be seen in figure 6.4.

6.2.2 Numerical Simulation

Finite difference techniques have been used to solve equation 6.15 with the boundary condition that no concentration change occurs at the edge of the temperature distributions. In the crystal rest frame the temperature distribution and hence r are time dependent since the beam is moving. This presents a three dimensional time dependent problem.

The boundary conditions at $|x|$, $|y|$ and $z \gg 0$ are that the concentration should smoothly go to the background value. The boundary at $z = 0$ however is a sharp boundary and the behaviour here is very different to that in the bulk. The boundary condition at $z = 0$ is that there is no flux of lithium through the surface. There is of course no flux into the crystal from the air and it is assumed that there is no significant out-diffusion due to the very short heating timescales of milliseconds.

The time scale for the diffusive motion is determined by the dwell time of the beam which is given approximately by

$$\Delta t = \frac{w}{v}. \tag{6.18}$$

This gives a corresponding characteristic diffusive distance of

$$\Delta z = \sqrt{\frac{a^2 r}{6}\Delta t} \tag{6.19}$$

If a is taken to be the lithium-lithium distance of 0.38 nm [22] and r taken to be $r(1000\text{ K})$, $w = 3.25$ μm and $v = 0.83$ mm s^{-1}, $\Delta z = 28$ nm. At this length scale the variation of rc is small everywhere except in the z direction at $z = 0$ therefore, from equation 6.5 the net flow of lithium will essentially only be away from the surface in the z direction across the length Δz. The one dimensional diffusion equation is then

$$\frac{\partial c}{\partial t} = \frac{a^2}{6}\frac{\partial^2 (rc)}{\partial z^2}. \tag{6.20}$$

This is approximated by finite differences as

$$\frac{c_i^{n+1} - c_i^n}{\delta t} = -\frac{Jz^n_{(i+1/2)} - Jz^n_{(i-1/2)}}{\delta z} \tag{6.21}$$

where

$$Jz^n_{(i+1/2)} = -\frac{a^2}{4}\frac{(rc)^n_{i+1} - (rc)^n_i}{\delta z}. \tag{6.22}$$

where the superscript n and subscript i refer to temporal and spatial steps respectively. It follows naturally from the derivation of the diffusive flux to take single forward difference approximations in the z direction. The second derivative of equation 6.20 is taken explicitly as two first order derivatives to include the crystal surface boundary condition in terms of a particle flux.

6.2.3 Results and Discussion

Using the model described in chapter 5 the lithium concentration distributions in the y, z plane after the passage of the writing beam were calculated. Figure 6.5 shows a

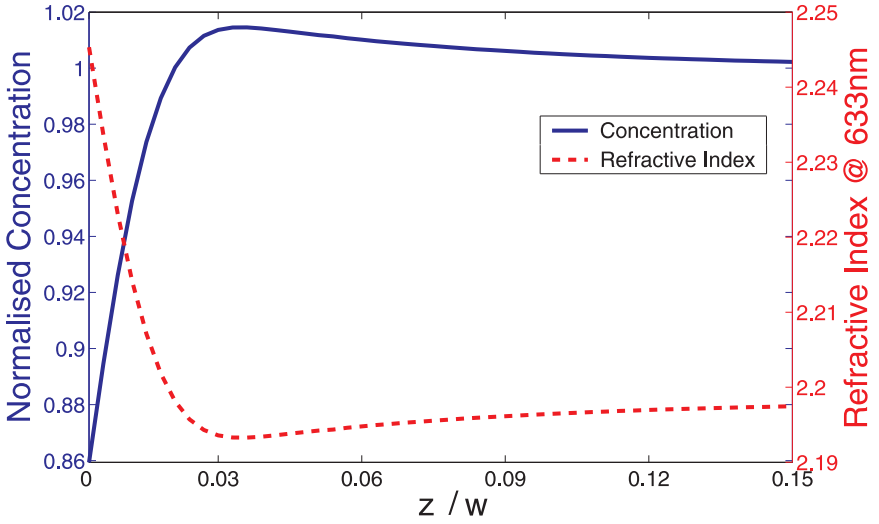

FIGURE 6.5: Resultant lithium concentration distribution and index distribution along z in the enter of the written channel. $P = 30$ mW, $w = 3.25$ μm, $v = 0.83$ mm s^{-1}.

typical lithium concentration distribution (solid line) along the z axis where the writing parameters $w = 3.25$ μm, $v = 0.83$ mm s^{-1}, $P = 30$ mW have been used. The background lithium concentration in LN has been normalised to unity for clarity of numbers. The lithium dependent refractive index calculated using the Sellmeier equations for LN [7] is also shown (dashed line in the same plot). It can be seen that there is indeed a region of decreased lithium concentration near the surface of the crystal which creates a region of increased refractive index and also that there is an increase in the lithium concentration at a depth of around $0.03w$ which creates a region of decreased refractive index. The magnitudes of the concentration changes are dependent upon the temperature distributions through equation 6.17 and hence on the exposure conditions. Figure 6.6 shows the lithium concentration distribution in the line along the surface of the crystal. It can be seen again that the dimensions of the concentration distribution are smaller than those of the temperature distribution. In the y direction however the difference between the width of the temperature distribution and lithium concentration distribution is much smaller in the z direction.

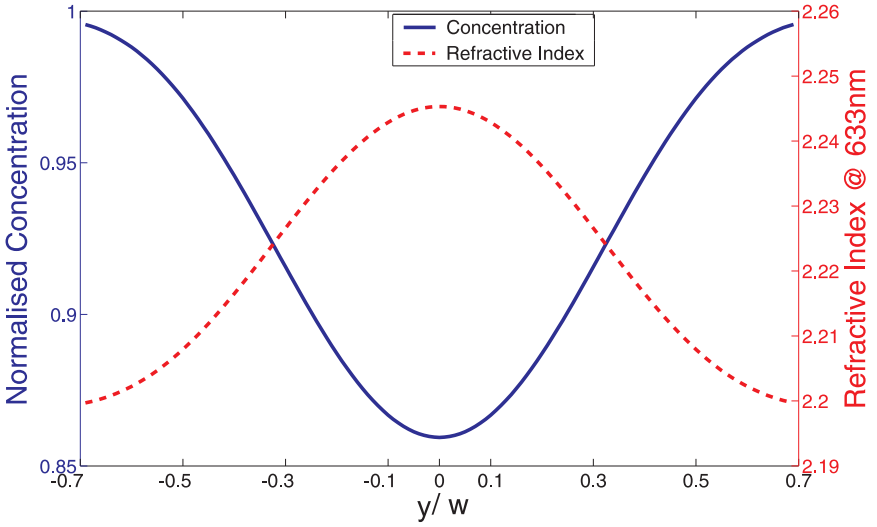

FIGURE 6.6: Resultant lithium concentration distribution and index distribution along y on the surface of the crystal. $P = 30$ mW, $w = 3.25$ μm, $v = 0.83$ mm s^{-1}.

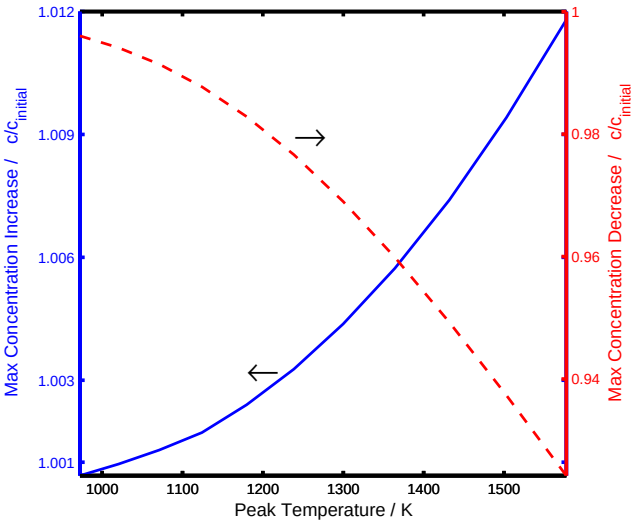

FIGURE 6.7: Variation of the maximum concentration increase and decrease with peak temperature. $w = 3.25\mu$m, $\alpha = 3.3 \times 10^7$ m^{-1}, $v = 0.83$ mm s^{-1}. Power varies from 25 to 35 mW.

Figure 6.7 shows the variation of the maximum concentration increase and decrease with peak temperature for beam parameters of $w = 3.25\mu$m, $\alpha = 3.3 \times 10^7$ m^{-1}, $v = 0.83$ mm s^{-1}. The temperature was changed by varying the power between 25 to 35 mW but the figure has been plotted with temperature for greater physical meaning. It can be seen that the magnitude of the change increases with temperature in a non-linear manner over the temperature range shown. The point of maximum concentration decrease is always located at the surface of the crystal, however the position of the point of maximum concentration increase is seen to move further into the crystal as the exposure increases. Figure 6.8 shows the movement of the position in depth of the maximum concentration increase, and hence the physical depth of the distribution, with increasing peak temperature. The change in position of the peak is of the same order as the step size of the model and so the outlying position of the second point is due to a rounding error. It can be seen that, although the physical depth of the concentration profile does increase with exposure, the change in physical distribution depth is only around 20 nm over the temperature range in the figure. Since the lithium movement is essentially in the depth direction only, the lateral size of the distributions scales with the beam spot size.

Figure 6.9 shows the variation of the lithium concentration distribution in the direction with depth as the spot size is changed. The power is varied such that the surface temperature under the centre of the beam remains at 1500 K. As the beam size increases, the depth of the concentration profile does not significantly increase. The magnitude of the concentration change is seen, however, to decrease with increasing spot size which is

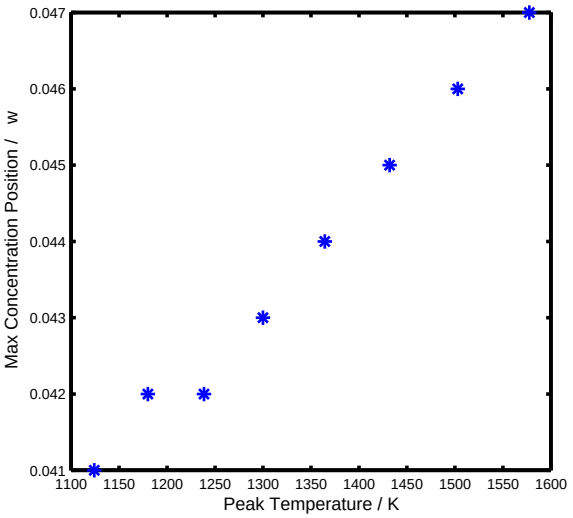

FIGURE 6.8: Variation of the depth of maximum concentration increase with peak temperature. $w = 3.25\mu$m, $\alpha = 3.3 \times 10^7$ m^{-1}, $v = 0.83$ mm s^{-1}. Power varies from 25 to 35 mW.

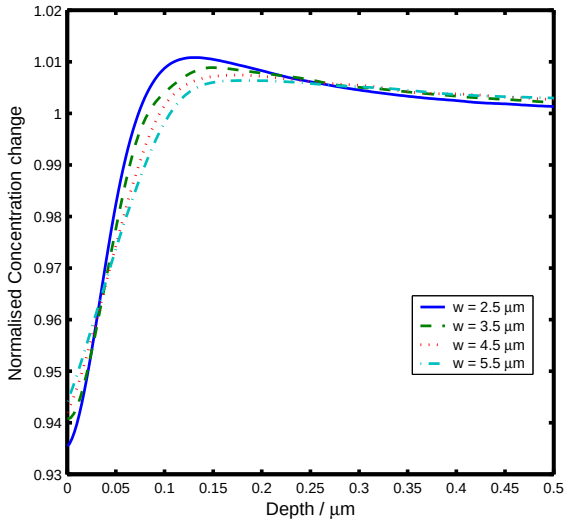

FIGURE 6.9: Variation of the concentration profile with depth with beam spot size. $\alpha = 3.3 \times 10^7$ m^{-1}, $v = 0.83$ mm s^{-1}. Power adjusted to keep the peak surface temperature at 1500 K.

due to the decrease in the spatial gradient of the r distribution. A similar effect is seen as the optical absorption is decreased, extending the temperature distributions in the depth of the crystal, as can be seen in figure 6.10. The magnitude of the concentration change was seen to depend strongly upon the scanning velocity of the beam as can be seen in figure 6.11. As the velocity decreases the concentration changes become large, such that some of the assumptions of the model such as constant vacancy density and no electrostatic coupling may no longer hold.

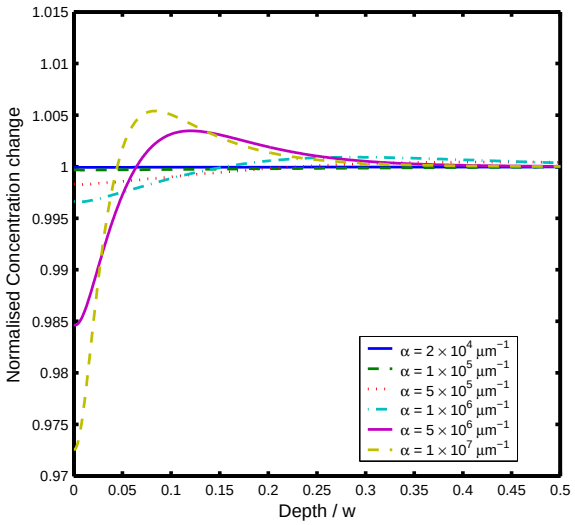

FIGURE 6.10: Variation of the concentration profile with depth with absorption coefficient. $w = 3.25\mu$m, $v = 0.83$ mm s^{-1}. Power adjusted to keep the peak surface temperature at 1500 K.

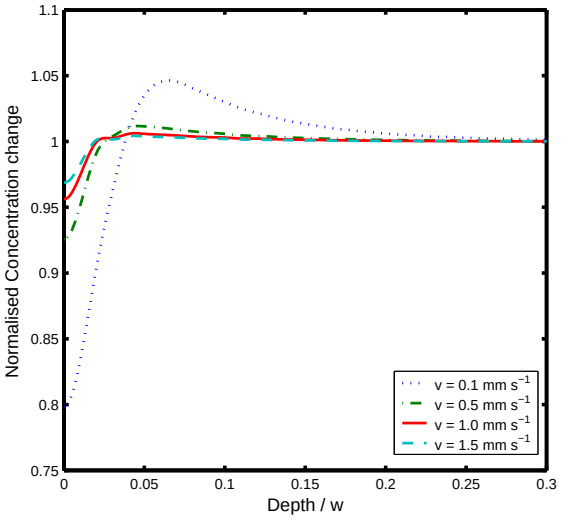

FIGURE 6.11: Variation of the concentration profile with depth for various scanning velocities. $\alpha = 3.3 \times 10^7$ m^{-1}, $w = 3.25\mu$m. Power adjusted to keep the peak surface temperature at 1500 K.

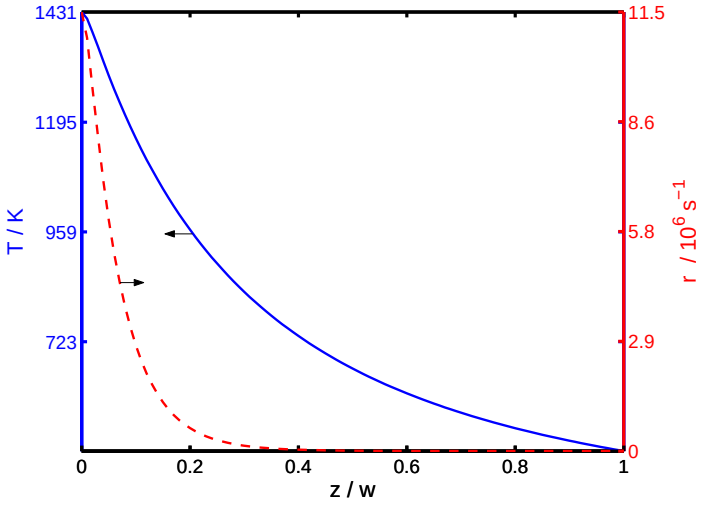

FIGURE 6.12: Temperature and corresponding diffusive jump rate distributions versus depth under the centre of the beam for beam parameters $p = 33$ mW, $w = 3.25$ μm and an optical absorption coefficient of 3.3 $\times 10^7$ m^{-1}.

The model predicts that the lithium ions do indeed move due to the temperature gradient, however, the concentration change distribution has a far smaller spatial extent than the corresponding temperature distribution. This is due to the rapidly changing rate function, r, as can be seen in figure 6.12 which shows a temperature distribution along z and its corresponding r distribution. Although the magnitude of r is certainly seen to drop quickly, it is actually the decrease in the gradient $\frac{\mathrm{d}r}{\mathrm{d}z}$ that limits the active depth for thermal diffusion and in figure 6.12 this is essentially zero by half a beam width in depth.

It is possible to include in the finite difference approximation the effects of diffusion in a direction other than z. This has been done for diffusion in the y direction and the correction to the one dimensional case for the same beam parameters as above is shown in figure 6.13. The form of the distribution is, as one would expect, showing movement of lithium from the hot central region to the cooler edges of the beam path. However, it can be seen that the magnitude of the concentration change caused only by diffusion along y is roughly 100 times smaller than that caused by diffusion along the z dimension, representing a maximum correction of only around 1% thus validating the assumption that the diffusive flow is essentially one-dimensional.

The finite difference model can also be used to predict the long term behaviour of the lithium concentration distributions by simulating their subsequent concentration gradient driven diffusion at room temperature following the writing process. The decay of the concentration distribution is shown in figure 6.14 where it can be seen that these distributions are not permanent and will decay on a time scale of months. This is

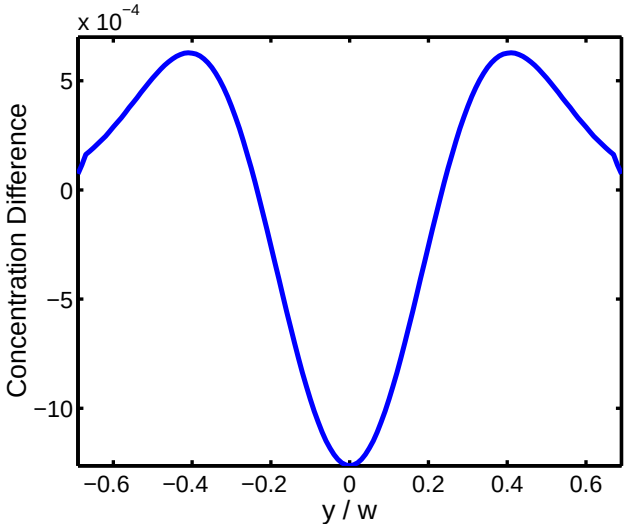

FIGURE 6.13: Correction to the concentration distribution of figure 6.6 due to the inclusion of flow in the y direction. $P = 30$ mW, $w = 3.25$ μm, $v = 0.83$ mm s^{-1}.

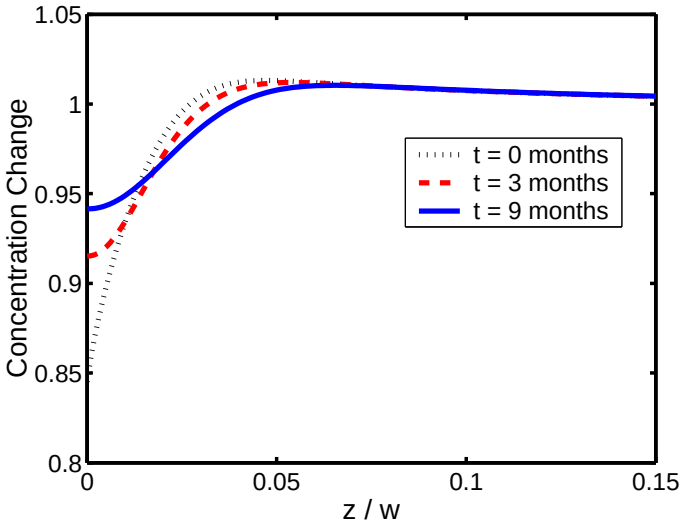

FIGURE 6.14: Decay of the concentration distribution at room temperature.

also seen experimentally with the physical guides which gives added strength to the proposition that lithium diffusion is responsible for the index changes seen in [2].

Both figures 6.5 and 6.6 show the correct refractive index structure for optical guiding: a high index core region surrounded by a lower index cladding region. Whether these refractive index distributions could support waveguide modes depends on both the magnitude of the refractive index difference between the two regions and the physical size of the high refractive index core region. The refractive index distributions predicted by the model were inserted into Selene Pro[1], a commercial beam propagation package, but were

[1]Selene Pro Version 4.2. Produced by BBV, now part of C2V (www.C2V.nl)

found however insufficient to support waveguide modes corresponding to those seen in reference [2]. For comparison it was found that a slab guide with a step index configuration of the minimum and maximum indexes of those seen from the model would require a depth of at least twice that produced by the model to support waveguide modes.

There are however many significant physical processes that could be occurring but are not included in the present model. If charge neutrality is not conserved locally a space charge field would be created in the lithium deficient region that could act upon the refractive index through the electro-optic effect. Another possible effect is photo-bleaching during the writing process that would dynamically increase the absorption depth across the beam spot. This would have the effect of pushing the active diffusion region further into the crystal hence increasing the depth of the index change structure.

From this point of view a factor of two in the difference in depth between a guiding and non-guiding structure is not strong enough to rule out thermally driven lithium movement as being the principle cause for the waveguides seen in [2] particularly as the structure lifetime is similar to that of the experimental waveguides.

6.3 Summary and Conclusions

Modelling of the formation of the of the UV direct-write waveguides in LN observed in reference [2] through thermal diffusion of lithium has been carried out. A model for thermal-diffusion in steep temperature gradients has been derived and applied to lithium ions in LN using the temperature distributions obtained in the heat flow model of chapter 5. It was seen that significant diffusive flow occurred in only a thin layer at the crystal surface and was directed along the z axis into the crystal.

The lithium concentration distributions predicted by the model have been translated into refractive index distributions through the Sellmeier equations for LN [7] and these have been imported into a commercial waveguide modelling package. Unfortunately, at this stage, the refractive index distributions are seen to be insufficient to support waveguide modes. Using a comparison of a step index slab waveguide it was seen that optical confinement would be produced by an increase to the depth of the distribution by a factor of around 2. With consideration of the fact that the diffusion model does not explicitly take into account the crystal structure or charge coupling of diffusing species and the assumption that the refractive index change is due only to lithium concentration changes with no contribution from any space-charge fields, a correction factor of only this small magnitude is encouraging. On the basis of this promising result the diffusion model was then used to investigate the decay rate of the lithium concentration distributions

through normal Fickian diffusion at room temperature and the decay is seen to agree well with the lifetimes of the experimental waveguides.

As well as the assumptions that have been made about the mechanics of both the heat and lithium flow it has also been assumed that the lithium concentration dependence of the refractive index is the only way in which the refractive index is changed, and this may well not be the case. LN is piezoelectric, and photoelastic which means that if there is any residual stress or strain, caused by either the density cycling through heating or compaction of the crystal after a decrease in lithium concentration, it will manifest itself in a change of refractive index. Also if charge is not conserved locally during the lithium diffusion an electric field will result between the diffused lithium ions and their vacancies that will also act upon the refractive index through the electro-optic effect. Of these two possibilities it is believed that the non-uniform charge distribution and associated electro-optic induced index change will be the larger perturbation. Hopefully with the inclusion of effects such as this we will obtain modelling results that will agree consistently with experiment.

Experimental evidence of the modelled lithium concentration profiles has, thus far, eluded us. The authors of reference [2] had tried to use secondary ion mass spectrometry however the results were inconclusive due to the limited transverse dimensions of the structures. During this investigation attempts were made to measure the lithium concentration in exposed regions with confocal micro-Raman spectroscopy using the known dependence of the width of the peaks at 153 and 254 cm^{-1}on lithium concentration [21, 23]. The scans were carried out at the Laboratoire Matériaux Optiques, Photonique et Systèmes at the University of Metz probing both from the upper z face and from a polished x face of the crystal. Scans performed from the z faces failed to show conclusively any broadening of the lines. If the results presented here do, however, represent the true nature of the process this might be expected since the dimensions of the confocal spot were around $0.5 \times 6\mu$m with the long dimension along the optical axis. This would mean that the region of concentration change, which has a depth or around 100 nm as can be seen in figure 6.9, would comprise just 1/60 of the free space sampling volume and would so give only a small signal above the background. Scans performed on the x face, which looked along the line of the written structures, should have been more successful than those performed on the z face since the concentration would have been constant over the length of the sampling volume and the depth of the lithium concentration distributions would have corresponded to the smaller dimension of the confocal spot. However, two problems arose here to render the results un-usable. The first was the difficulty in producing high quality polished edges at submicron distances from the upper surface. The faceting and roughness at these points changed the direction of the probe beam and introduces additional scatter which lowered the intensity of the Raman

scattered radiation. The second problem was the appearance of a second peak at 254 cm^{-1} which made width measurements of the peak at 238 cm^{-1} impossible. Some interesting features were noted, however, in the Raman scans in the illuminated areas since with each sample that was sent, new spectral lines were observed. As a possible origin the Raman lines of L3N [24] were compared but were not found to be the cause. This also reduces the likelihood that L3N precipitates are responsible for any index change seen in [2]. The new spectral lines must then be caused by other defects introduced during UV exposure, but their origin will not be explored here.

Future work would include the thermally driven diffusion of ionic species with the electronic charge transport model derived in chapter 3. In the present section it was assumed that any electric fields could be locally compensated by more mobile electronic charges on a time scale smaller than that required for ionic movement and so could be neglected. This may not be the case and so a full model should be investigated.

Our results lead us to believe that the thermal diffusion of lithium ions is a primary cause for the waveguides observed in reference [2]. However there has been no way to directly compare modelling with experiment other than to use a further modelling package to calculate waveguide modes. This means that the only comparison rests upon a great deal of assumptions.

References

[1] A.M. Mamedov, L.S. Hajiyeva, I.S. Ibragimova, and B.S. Aliyeva. Vacuum ultraviolet (VUV) reflectivity and electron states in $LiNbO_3$. *Physica B &; C*, 128B+C: 61 – 8, 1985.

[2] S. Mailis, C. Riziotis, I.T. Wellington, P.G.R. Smith, C.B.E. Gawith, and R.W. Eason. Direct ultraviolet writing of channel waveguides in congruent lithium niobate single crystals. *Optics Letters*, 28(16):1433 – 1435, 2003.

[3] J.R. Carruthers, I.P. Kaminow, and L.W. Stulz. Diffusion kinetics and optical waveguiding properties of outdiffused layers in lithium niobate and lithium tantalate. *Applied Optics*, 13(10):2333 – 42, 1974.

[4] I.P. Kaminow and J.R. Carruthers. Optical waveguiding layers in $LiNbO_3$ and $LiTaO_3$. *Applied Physics Letters*, 22(7):326 – 8, 1973.

[5] S.L. Kwiatkowski and A.R. Mickelson. Characterization of lithium out-diffused slab waveguides in $LiNbO_3$ as a function of fabrication conditions. In *Lasers and Electro-Optics Society Annual Meeting, 1993. LEOS '93 Conference Proceedings. IEEE*, pages 151 – 2, San Jose, CA, USA, 1993.

[6] J.L. Jackel, V. Ramaswamy, and S.P. Lyman. Elimination of out-diffused surface guiding in titanium-diffused $LiNbO_3$. *Applied Physics Letters*, 38(7):509 – 11, 1981.

[7] U. Schlarb and K. Betzler. Refractive indices of lithium niobate as a function of wavelength and composition. *Journal of Applied Physics*, 73(7):3472 –, 1993.

[8] C. Kittle. *Introduction To Solid State Physics, Fourth Edition.* John Wiley and Sons, New York, 1971.

[9] K. K. Wong. *Properties Of Lithium Niobate.* EMIS Datareview. IEEE, 1989.

[10] A. M. Prokhorov and Yu. S. Kuz'minov. *Physics and chemistry of crystalline lithium niobate.* Hilger, IOP Publishing Ltd, Bristol, BS1 6NX, England, 1990.

[11] L.O. Svaasand, M. Eriksrud, A.P. Grande, and F. Mo. Crystal growth and properties of $LiNb_3O_8$. *Journal of Crystal Growth*, 18(12):179 – 84, 1973.

[12] M Lundberg. The crystal structure of $LiNb_3O_8$. *Acta Chemica Scandinavica*, 25: 3337–3346, 1971.

[13] R.S. Weis and T.K. Gaylord. Lithium niobate: summary of physical properties and crystal structure. *Applied Physics A (Solids and Surfaces)*, A37(4):191 – 203, 1985.

[14] L.O. Svaasand, M. Eriksrud, G. Nakken, and A.P. Grande. Solid-solution range of $LiNbO_3$. *Journal of Crystal Growth*, 22(3):230 – 2, 1974.

[15] M. N. Armenise, C. Canali, M. De Sario, A. Carnera, P. Mazzoldi, and G. Celotti. Characterization of TiO_2, $LiNb_3O_8$, and $(Ti_{0.65}Nb_{0.35})O_2$ compound growth observed during Ti:$LiNbO_3$ optical waveguide fabrication. *Journal of Applied Physics*, 54(11):6223–6231, 1983.

[16] H. Akazawa and M. Shimada. Precipitation kinetics of $LiNbO_3$ and $LiNb_3O_8$ crystalline phases in thermally annealed amorphous $LiNbO_3$ thin films. *Physica Status Solidi A*, 203(11):2823 – 7, 2006.

[17] H. Akazawa and M. Shimada. Mechanism for $LiNb_3O_8$ phase formation during thermal annealing of crystalline and amorphous $LiNbO_3$ thin films. *Journal Of Materials Research*, 22(6):1726–1736, June 2007.

[18] E. Born, J. Hornsteiner, T. Metzger, and E. Riha. Diffusion of niobium in congruent lithium niobate. *Physica Status Solidi A*, 177(2):393 – 400, 2000.

[19] V. A. Ganshin and Yu. N. Korkisho. H:$LiNbO_3$ waveguides: effects of annealing. *Optics Communications*, 86:523–530, 1991.

[20] M.N. Armenise. Fabrication techniques of lithium niobate waveguides. *IEE Proceedings J (Optoelectronics)*, 135(2):85 – 91, 1988.

[21] U. Schlarb, S. Klaur, M Wesselman, K Betzler, and M. Wohlecke. Determination of the li/nb ratio in lithium niobate by means of birefringence and raman measurements. *Applied Physics A: Solids and Surfaces*, 56:311–315, 1993.

[22] D. Bork and P. Heitjans. Nmr investigations on ion dynamics and structure in nanocrystalline and polycrystalline $LiNbO_3$. *Journal of Physical Chemistry B*, 105 (38):9162 – 9170, 2001.

[23] Y. Zhang, L. Guilbert, P. Bourson, K. Polgar, and M.D. Fontana. Characterization of short-range heterogeneities in sub-congruent lithium niobate by micro-raman spectroscopy. *Journal of Physics: Condensed Matter*, 18(3):957 – 63, 2006.

[24] N.V. Sidorov, M.N. Palatnikov, and V.T. Kalinnikov. Raman spectra and features of the structure of lithium niobate crystals. *Optics and Spectroscopy*, 82(1):32 – 8, 1997.

Chapter 7

Summary and Conclusion

The work presented in this thesis has covered a varied range of topics with the unifying theme of illumination of the LN surface with UV laser light. The results that are summarised here illustrate how the functionality of LN can still be increased some 70 years after it was first grown, showing that this is still a highly fruitful material for original fundamental research.

In chapter 2 the hydrophilicity of LN was seen to undergo a transition from mildly hydrophobic to super-hydrophilic under the influence of low intensity UV laser light. This was investigated using the contact angles of 0.5 - 1 μl sessile drops under varying exposure intensities, times and environment. It was seen that hydrophilic transition occurs more rapidly with higher incident light intensity but, however, was seen not to be simply a function of total exposure since halving the incident power and doubling the exposure time did not result in the same contact angle change. It was seen that the change in hydrophilicity was strongly dependant upon the exposure environment with the transition occurring faster in a high humidity environment and not occurring at all under vacuum conditions. From this observation it was proposed that the hydrophilicity change was due to the dissociative adsorption of atmospheric water molecules onto the crystal surface. The observation also indicated that the change was not due to the photo-catalytic decomposition of organic contaminants to the surface, as has been proposed for other photo-induced hydrophilicity changes [1], since this would also occur in vacuum. The decay of the hydrophilic change was measured and was seen to fit well to a decaying exponential with a time constant of two days. This agreed with the hypothesis that the hydrophilicity change was due to adsorbed hydroxyl groups if the change was proportional to the hydroxyl density and thermal desorption occurs randomly with constant probability.

The spreading of liquid along defined hydrophilic tracks was also investigated as a method of deposition and it was seen that DI water did indeed spread with lateral confinement to exposed tracks. The velocity of the spreading water was seen to be dependant upon the exposure of the sample and hence upon the energy change of the surface. The geometry of the defined tracks was not seen to be important with spreading occurring along smooth bends and around tight corners. It was seen that the width of the wetting strip was greater than the width of the exposed region and this is likely to limit the extent to which spreading can occur along a track. The effect of the width of the exposed track was also investigated and it was seen that there was a lower limit of around 1 mm when applied drops had a volume of around 2 μl. This may be due to the extra energy required to decrease the radius of curvature of the contact line compensating for the energy of wetting the higher energy hydrophilic surface.

Structuring of the surface energy was performed at the micron and sub-micron scale with the use of TEM grid amplitude masks and optical phase masks. The wetting characteristics were observed by the creation of dew on the surface since dew nucleation will occur preferentially in areas of high surface energy. It was seen that a large contrast to the wetting properties was easily achievable at these length scales and that, in the case of condensation of dew, the wetting mechanism could be tailored with the exposure such that condensation could occur in either a film-wise or drop-wise manner. The dew patterns were observed optically with a microscope and CCD camera and were inferred by the diffraction of a laser beam.

In chapter 3 domain inversion in congruent lithium niobate, iron-doped congruent lithium niobate and titanium in-diffused lithium niobate under the influence of only a scanning continuous wave ultra-violet laser operating at a wavelength of 244 nm was shown. The domain structures obtained were analysed using piezoresponse force microscopy and by chemical etching in hydrofluoric acid, followed by surface profiling and scanning electron microscopy. The positive domains formed on the $-z$ face were seen to contain self-aligned nano-domains of negative polarity which are aligned along the x axes of the crystal. On the $+z$ face domain inversion was seen at low powers however at higher powers domain inversion was only seen as aligned nano-domains within the exposed area similar to those seen on the domains formed during exposure of the -z face. The piezoresponse of the UV-written domains was seen to be reduced in comparison to bulk domains of the same polarity and this was shown not to be a result of surface melting but may be due to inhomogeneity or limited depth within the PFM sampling volume. A qualitative model was proposed to explain the mechanism of domain inversion under UV illumination whereby the domain inversion is obtained through the action of a space-charge field of photo-excited charges. The differences of behaviour on the positive and

negative faces was then explained by the effect of different electron and hole mobilities. Although not evaluated, the equations governing the model were derived.

In chapter 4 a new method of light assisted domain engineering in lithium niobate was demonstrated. This method was quite different to that of either conventional LAP or AOP and presents an un-paralleled level of flexibility. Domain engineering was achieved by illumination of the LN surface by focussed c.w. UV light on the $+z$ face which lead to a local inhibition of domain inversion in the illuminated areas during a subsequent EFP step. The mechanism proposed was that, during illumination, photo-excited charges were driven by a pyro-electric field to leave a dipolar charge distribution within the crystal after the passage of the beam. This dipolar charge distribution was arranged such that a charged domain wall approaching the region would see an electric field that would repel the wall and hence inhibit the wall movement. Thus poling in the illuminated area did not occur, leaving a region of crystal in which domain inversion was inhibited. The extent to which the domain inversion was inhibited was seen to be dependent upon the kinetics of the domain walls during the EFP step and these could be controlled by the magnitude of the external field. When wall movement was slow, inhibition was seen to be complete and when wall movement was very fast inhibition did not occur at all. In the intermediary points, however, partial inhibition was seen which resulted in complex, self assembled, sub-micron scale domain patterning. Although this was not an intended result of the investigations, it shows promise for high spatial frequency patterning unachievable through conventional EFP and thus warrants further investigation. The ferroelectric nature of these inhibited domains was also confirmed by PFM. The depths of the inhibited domains has not yet been conclusively ascertained, however a lower limit to the depth was given by PFM as around 100 nm and initial investigations from side etching indicated depths of the order of a micron.

As a method of surface structuring, UV poling inhibition followed by etching was shown to be highly successful with high aspect ratio structures demonstrated with no loss of quality of the upper face. The shape/size and the quality of the fabricated structures was determined by the incident exposure conditions, in combination with the subsequent EFP parameters and the annealing steps respectively. Additionally, as the crystallographic symmetry was not observed to impose limitations on the orientations of the created structures, any desired shapes could be achieved.

In chapter 5 the heating of lithium niobate by absorbing laser radiation was modelled by both analytical and numerical methods as a first step in the understanding of the interactions between LN and highly absorbing, principally UV, laser radiation. The analytical modelling included the temperature dependence of the thermal diffusivity in a new temperature variable by means of the Kirchhoff transform. This nonlinear

analytical model was compared with its corresponding linear model and the inclusion of the temperature dependence of the thermal diffusivity was seen to have a marked effect upon the temperature distributions obtained. Particularly it was seen that the temperature distributions were narrowed, becoming more localised to the source. This was attributed to a higher diffusivity in cooler regions allowing a greater heat flow away from the source whilst in the hotter regions closer to the source the thermal diffusivity was decreased leading to a reduced heat flow and subsequent temperature rise.

The model was constructed in the moving reference frame of the beam and it was found that the spatial temperature distributions were independent of the scan speed for sensible scanning speeds. The spatial distribution in the rest frame of the crystal was transformed into the temporal temperature distribution in the rest frame of the crystal to show that, of course, this is highly dependent upon scan speed and the physical implications of this were discussed. The dependence of the temperature distribution in the beam frame on spot size, incident power and optical absorption strength were investigated. It was found that the length scale of the temperature distribution in the depth direction was given by whichever was the larger of the spot size w and the absorption depth $\delta(= 1/\alpha)$ whilst the length scale of the temperature distribution parallel to the surface remains essentially fixed at the length scale w, broadening only slightly with increasing absorption depth. The implications of this for heating with far infra-red sources which are slightly less absorbing than UV were discussed.

To test the validity of the analytical model and the assumptions therein two methods were used. Firstly a fully numeric model using the finite difference method was constructed and secondly a crude practical experiment was used to find the power at which melting would onset. The finite difference model was first used to compare with a linear analytical model to find a benchmark against which the subsequent comparison of nonlinear models, to validate the use of the Kirchhoff transform, could be set. Some differences were seen which, although being relatively small, were localised to the top layer of surface nodes of the finite difference computational domain. Due to the sharp discontinuity of this difference it was attributed to be of a numerical source rather than physical and must be considered in the following comparisons. The comparison of the nonlinear analytical and finite difference models was carried out using the same empirical function for the thermal diffusivity with all other factors remaining linear. The comparison was favorable and even with the surface disparity mentioned previously the maximum difference seen between the two models for the high power simulation used was only around 8% persisting near this value for only a very small fraction of one beam width in depth. Having demonstrated that the analytical methods used are indeed valid the finite difference model was used to investigate the impact of neglecting the temperature dependence of the heat capacity and of the choice of empirical function for the

thermal diffusivity. The effect of a temperature dependent heat capacity was found to be a general increase of temperature that was proportional to the temperature itself. The increase was small and did not change the shape of the temperature distributions to any large degree. This demonstrated that the thermal diffusivity is indeed the prominant source of nonlinearity in the system. The effect of the choice of a reciprocal of temperature fit for the thermal diffusivity over an expontial fit was investigated and it was seen that where temperatures exceeded around 800 K, where the fit functions diverge, the reciprocal fit resulted in larger temperature rises. Due to the lack of physical data at high tmperatures both models were concluded to be equally valid and the reciprocal fit was used in the remainder of this thesis. The results of all investigations were discussed qualitativly and related back to the expected behavior from the thermal properties.

In chapter 6 modelling of the thermal diffusion of lithium was carried out as a possible mechanism for the formation of the UV direct-write waveguides in LN observed in reference [2]. A model for thermal-diffusion in steep temperature gradients was derived and applied to lithium ions in LN using the temperature distributions obtained in the heat flow model of chapter 5. It was seen that significant diffusive flow occurred in only a thin layer at the crystal surface and was directed along the z axis into the crystal.

The lithium concentration distributions predicted by the model were translated into refractive index distributions through the Sellmeier equations for LN [3] and these have been imported into a commercial waveguide modelling package. The refractive index distributions were seen to be insufficient to support waveguide modes. Using a comparison of a step index slab waveguide it was seen that optical confinement would be produced by an increase to the depth of the distribution by a factor of around 2. With consideration of the fact that the diffusion model did not explicitly take into account the crystal structure or charge coupling of diffusing species and the assumption that the refractive index change was due only to its lithium concentration dependence, with no contribution from any space-charge fields, a correction factor of only this small magnitude is encouraging. On the basis of this promising result the diffusion model was then used to investigate the decay rate of the lithium concentration distributions through normal Fickian diffusion at room temperature and the decay was seen to agree well with the lifetimes of the experimental waveguides.

Attempts were made to measure the lithium concentration in exposed regions with confocal micro-Raman spectroscopy using the known dependence of the width of the peaks at 153 and 254 cm^{-1} on lithium concentration [4, 5]. The scans were carried out at the Laboratoire Matériaux Optiques, Photonique et Systèmes at the University of Metz probing both from the upper z face and from a polished x face of the crystal. Scans performed from the z faces failed to show conclusively any broadening of the lines. This

might be expected from the results of the diffusion modelling since the dimensions of the confocal spot are far greater than the predicted depth of the lithium distribution which would thus give only a small signal above the background. Scans performed on the x face, which looked into the line of the written structures, should have been more successful than those performed on the z face since the concentration would have been constant over the length of the sampling volume. However the results from the x face scans were un-usable due to the quality of the polished edges within the first micron from the crystal edge and the appearance of a second peak at 254 cm^{-1} which made width measurements of the peak at 238 cm^{-1} impossible. Some interesting features were noted, however, in the Raman scans in the illuminated areas since with each sample that was sent, new spectral lines were observed. As a possible origin the Raman lines of L3N [6] were compared but were not found to be the cause. This also reduces the likelihood that L3N precipitates are responsible for any index change seen in [2]. The new spectral lines must then be caused by other defects introduced during UV exposure, but their origin was not explored here.

In conclusion, the work presented in this thesis has both shown new ways in which the functionality of LN can be increased through the interactions of the LN surface with UV laser light and has contributed to the understanding of how absorbing radiation of both UV and IR wavelengths interacts with the material. The areas of investigation have ranged from wettability and thermodynamic surface energy structuring, the results of which may have far reaching implications and applicability to fields of wafer bonding, chemical sensing, environmental sensing, liquid actuation and even micro-structured deposition, to ferroelectric domain engineering, with application to surface topological structuring, optical frequency conversion and charged particle deposition. The work has been of a fundamental investigatory nature, rather than optimising previously found methods, and so shows a large scope for future investigation and it is hoped that this may then form the basis of other fruitful works.

References

[1] A. Kanta, R. Sedev, and J. Ralston. Thermally- and photoinduced changes in the water wettability of low-surface-area silica and titania. *Langmuir*, 21(6):2400 – 2407, 2005.

[2] S. Mailis, C. Riziotis, I.T. Wellington, P.G.R. Smith, C.B.E. Gawith, and R.W. Eason. Direct ultraviolet writing of channel waveguides in congruent lithium niobate single crystals. *Optics Letters*, 28(16):1433 – 1435, 2003.

[3] U. Schlarb and K. Betzler. Refractive indices of lithium niobate as a function of wavelength and composition. *Journal of Applied Physics*, 73(7):3472 –, 1993.

[4] U. Schlarb, S. Klaur, M Wesselman, K Betzler, and M. Wohlecke. Determination of the li/nb ratio in lithium niobate by means of birefringence and raman measurements. *Applied Physics A: Solids and Surfaces*, 56:311–315, 1993.

[5] Y. Zhang, L. Guilbert, P. Bourson, K. Polgar, and M.D. Fontana. Characterization of short-range heterogeneities in sub-congruent lithium niobate by micro-raman spectroscopy. *Journal of Physics: Condensed Matter*, 18(3):957 – 63, 2006.

[6] N.V. Sidorov, M.N. Palatnikov, and V.T. Kalinnikov. Raman spectra and features of the structure of lithium niobate crystals. *Optics and Spectroscopy*, 82(1):32 – 8, 1997.

Chapter 8

Future Work

The work carried out in this thesis has been wide-ranging and is of a generally fundamental investigatory nature, rather than being device led, which leaves many possibilities for future applied work. As always, further work can be carried out on the investigation of the effects seen either by increasing the parameter space used experimentally or by relaxing the constraints used in theoretical work, such as temperature independence or isotropy. Also the work carried out in this thesis used only LN and so an obvious extension would be to investigate whether any of the effects investigated here could occur in other materials with similar properties to LN, particularly other ferroelectrics. This choice of other relevant materials may not be as simple as it first appears as has already been highlighted in chapter 2 where it was seen that the UV-induced hydrophilic effect did not occur in $SrTiO_3$ despite the similarities in both the physical structure (both $SrTiO_3$ and $LiNbO_3$ have BO_6 octahedra as the main structural element) and the electronic band structure. It may also be found in other ferroelectrics that the heating by the laser destroys the ferroelectric ordering, since many have much lower Curie temperatures than LN, and that they do not return to a single domain, or even single crystal state, upon cooling.

The wavelength range of the laser light used in this investigation was reasonably limited, particularly in the c.w. regime where only 244 nm light was used. It would be fruitful to investigate a wider range of wavelengths in, especially, areas where the creation of photo-excited charges seems to be of importance such as the poling work of chapters 3 and 4. With reference to figure 1.4 it can be seen that the optical absorption coefficient decreases rapidly with decreasing photon energy below around 5.0 eV (photon energy at $\lambda = 244\ nm$ is 5.09 eV) changes very rapidly and so longer wavelengths than 244 nm could change greatly the extent of any photo-excited charge sources.

The remainder of this chapter shall look individually at each of the areas of investigation carried out within this thesis and identify some of the future work that could, or should, be carried out. Some will involve the extension of the fundamental investigations however devices that could be made that take advantage of the results of this thesis will also be proposed.

8.1 Hydrophilic UV Surface Activation

8.1.1 Composite Areas for Greater Control of Macroscopic Properties

In chapter 2 it was seen that the magnitude of the change in hydrophilicity, as measured by the contact angle of sessile drops, was strongly dependant upon the exposure conditions of beam intensity, exposure time and environmental humidity, and upon the initial cleaning of the surface. This made re-producability of non-saturated contact angles difficult. For applications where the macroscopic wettability needs to be controlled between the extremes of complete wetting and the unexposed state and particularly when structuring of the wettability over large areas is required we propose here the creation of a composite surface of microscopic areas of saturated change and no change at all. The macroscopic hydrophilicity change would then be given by the ratio of the areas. The structuring can be achieved through patterning of the incident light, as was seen in section 2.4 and it is simple to ensure that the effect is saturated in the exposed areas. The areas of work requiring investigation will then be to find the most appropriate method of controllably structuring the light, determining the relation between area ratio and wetability change and determining at what level the structuring of the surface affects the morphology of the liquid surface.

8.1.2 Investigation of Wettability of Other Liquids

During the study carried out in chapter 2 the main liquid used was DI water. The effect was also seen to work with acetone, however this was not investigated fully. The effect was not seen to work with olive oil, however this is a high viscosity oil and, most likely, quite complex and so may not be the best representative of this class of liquids. To better investigate the change in general wettability, and not just water wettability, a thorough investigation with a range of liquids of polar, non polar, acid and alkali chracteristics should be carried out. This will also help to ascertain the nature of the chemical change to the LN surface that is responsible for the change in hydrophilicity.

8.1.3 Variation of the Exposure Atmosphere

The present study concluded that the humidity of the exposure environment was highly influential upon the strength of the wettability change since the increased hydrophilicity was due to dissociative adsorption of water molecules. It may be that a similar effect could be seen during exposure in other gaseous environments. The experimental arrangement used here would easily accommodate such experiments since the exposure chamber can be evacuated before other gases are admitted. This may have application not only to changing the hydrophilicity of the surface, which could possibly be made more hydrophobic if carbon containing molecules can be adsorbed, but also to other applications where the surface reactivity could be structured by patterned adsorption of chemical groups.

8.1.4 Reversible Hydrophilicity

The work of chapter 2 has shown that UV laser light promotes the dissociative adsorption of water molecules onto the LN surface which increases the wetability through the interaction of the adsorbed molecules and those of liquid water. To make many useful devices, such as light-controlled liquid lenses, it would be highly desirable to find a way in which light could also be used to remove the adsorbed water molecules and return the surface to its initial, mildly hydrophobic, state. This might be accomplished by finding a wavelength of light that could couple efficiently to one of the vibrational modes of the adsorbed molecules, but would not be absorbed by the LN or cause much photo-refractive damage. In this case it may be possible to impart enough energy to the adsorbed molecules that they essentially boil away, leaving the original surface of the crystal. This may be achieved within the wavelength region of 2 - 4 μm where absorption bands of water exist but LN is still transparent. For the use in liquid lenses and other such devices, absorption by the liquid may be avoided by a careful choice of a liquid that is still affected by the hydrophilic surface treatment, but has different absorption properties to water. This would also allow for the actuation of liquid drops through structured light fields alone which may be highly desirable for chemical sensing chips.

8.1.5 Nano-Particle / Macro-Molecule Deposition

The structured deposition of either large molecular structures or nano-particles may be achieved if they can bind to the hydrophilic water molecules adsorbed onto the crystal surface. Many nano-particles are coated in hydrophilic ligands to make them soluble in water and many proteins contain hydrophilic amino acids. If the adhesion energy

between the nano-particle / molecule and the hydrophilic LN surface is greater than that between the nano-particle / molecule and the carrier liquid then the bonding may be efficient. Careful consideration of the carrier liquid may then be necessary which may also have implication on the stability of the nano-particles / molecules which are to be attached. If structured bonding on the length scales at which the surface hydrophilicity can be structured is achievable, many uses within chemical sensing could be found.

If hydrophilic nano-particle / molecule deposition is combined with the results of chapters 3 and 4 then a further method of efficient deposition may be possible. When a domain pattern is present upon the crystal surface, a change in temperature of the crystal will result in an electric field through the pyro-electric effect, as described in section 1.2.5, which will point either into or out of the surface depending upon the local polarity of the surface. Thus, if the nano-particles / molecules to be deposited are appropriately charged they will feel an electrostatic attraction to the surface of the crystal where the UV laser light has been used to influence the domain structure. This will cause the nano-particles / molecules to adhere to the surface efficiently and the hydrophilic interactions between the hydrophilic groups of the nano-particles / molecules and the LN surface will ensure a strong bond when the temperature returns to the initial value.

8.1.6 Environmental Sensing

UV induced hydrophilicty can be used to construct a range of sensors whereby the sensing area is controlled by the illumination, rather than layers of other substances applied to the surface which may affect the operation of the sensing mechanism. Two possible sensing mechanism could be the effect upon SAWs through attenuation and the effect upon light fields through diffraction.

The simplest sensor that could be made would be a humidity sensor whereby the condensation of water is monitored on the UV treated areas where the dew point is greater than the unexposed surface. In the case of optical interrogation the diffraction of light from a structured grating could be monitored where the diffraction efficiency would be a function of the volume of the condensate. By varying the temperature such that the diffraction efficiency remains constant at a low value the dew point, and hence humidity, can be measured. In the case of SAW sensors the condensation can be measured by the attenuating effect upon the SAW. By structuring the hydrophilicity, condensation can occur only on the high energy sections. This allows for long delay lines of arbitrary length since the attenuation of the signal is not dependent upon the total propagation distance, but only on the area of the exposed region, allowing for lower power levels to be utilised which is important for wireless devices.

The results of chapter 2 suggest that the wettability by oil is unaffected by the UV exposure and so a dual delay line sensor, with one delay line hydrophilicly structured, can act as a composition sensor for vapours composed of both water and oil. Oils will in general condense at a higher temperature that water and will affect the attenuation in both delay lines equally. Water will condense at a lower temperature and will preferentially affect the hydrophilicly structured delay line. The magnitude and ratio of the magnitudes of the attenuation in each arm can then give information on the concentrations of oil and water present in the vapour.

8.1.7 Micro-Lenses and Micro-Lens Arrays

When a liquid condenses on a surface such that a drop is formed the profile of the drop takes on a shape such that the surface area and hence surface energy is minimised. For a drop with a circular contact line the surface will have a single radius of curvature and a spherical cap will be formed and if the contact line if not circular multiple radii of curvature will be present. The surface of the liquid drop will be very smooth and so will be of high optical quality. Thus a drop of liquid can act as a high quality plano-convex lens with different focal lengths along different axes as dictated by the shape of the contact line. It has already been shown in chapter 2 that the initiation of condensation from vapour to liquid can be structured by UV illumination. Further to this it is seen that as the condensate mass increases the condensate forms a single drop encompassing the exposed area, with the contact line pinned at the edge of the exposed area. An example of this type of drop is shown in figure 8.1(a). The drop then forms a very short focal length lens which can be placed at any desired location on the LN surface. Also, since the contact line is pinned at the edge of the exposed area, the radius of curvature of the drop, and hence focal length of the lens, is variable by controlling either the environmental humidity or the substrate temperature to change the equilibrium, i.e. zero net mass flux, drop surface area. The strength of the pinning can be seen in figure 8.1(b) where the contact line is pinned despite the very low radius of curvature evident in the interference fringes. An initial area of application that we see for this is as an integrated lens for coupling into optical waveguides.

8.2 UV Laser Poling

8.2.1 Wavelength Combination

The work carried out in chapters 3 and 4 made use of a c.w. UV laser with a wavelength of 244 nm only. This was concluded to be successful since it fulfilled the two requirements

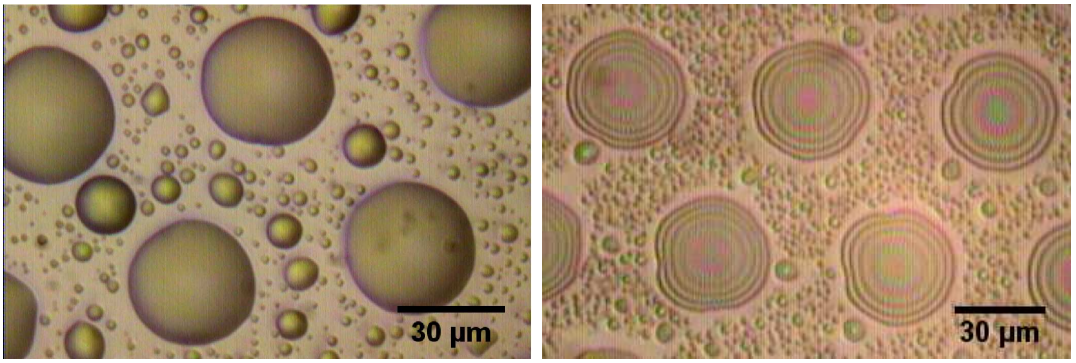

(a) Small focal length micro-lens array formed by structured condensation

(b) Large radius of curvature condensate drop due to high contact line pinning strength.

FIGURE 8.1: Micro-lenses formed by controlled condensation

of producing a spatially extended temperature distribution that was continuously present in the laser rest frame and producing free charges that could move within the crystal. However, even though the c.w. lasers available at a wavelength of 244 nm can do both jobs, it may be better to use two different lasers of different wavelengths to fulfil both requirements simultaneously in a more efficient manner. For example a c.w. carbon dioxide laser that operates in the infra-red region at 10.6 μm will heat efficiently and has a large enough output power to heat a large area and a nano- or femto-second pulsed UV laser can provide an efficient source for photo-excited charges. In combination it may be possible to create structures that are not only of greater lateral size, but also of greater depth. The use of femto-second laser pulses also allows the creation of photo-excited charge source within the depth of the crystal through two-photon absorption of light within the transparency region. This may be particularly useful in the domain inhibition work where a layer of charge could be formed, which prevents the propagation of domains to the surface, some microns below the surface where the simulations of chapter 5 predict a carbon dioxide laser to heat efficiently. This would put the inhibited domain structures firmly at the depth scales for optical use with guided wave structures. If a femto-second visible source is used it may also be possible to achieve domain inhibition within the bulk of the crystal if an external electric field is applied rather than heating the crystal to create a pyroelectric field. This may achieve full three dimensional domain structuring.

8.2.2 Depth Study

It has not been possible to complete a thorough study of the depth of either the directly written domains of chapter 3 or the inhibited domains of chapter 4. Some indications of and limits to the depths have been made however if future work is to be carried out

a full study on the effects of varying the exposure conditions of power, spot size, scan velocity / dwell time and laser wavelength should be made.

8.2.3 Electrically Variable Planar Diffractive Optics

Through the electro-optic effect oppositely polarised domains will undergo a refractive index change under an electric field of equal magnitude but of opposite sign. Using transparent electrodes to apply a voltage to the domain structures created in chapters 3 and 4 would allow the creation of diffractive planar optics such as diffraction gratings and Fresnel zone plates [R. Cudney, L. Ríos, and H. Escamilla. Electrically controlled fresnel zone plates made from ring-shaped 180° domains. *Opt. Express*, 12(23):5783–5788, 2004.].

8.2.4 Methods of Increasing Domain Depth

Although the depths of the domains in chapters 3 and 4 are not yet fully ascertained, it is appreciated that they are not yet deep enough for efficient use in waveguide PPLN and are certainly not of the depth of the crystal. To make these useful for non-linear frequency conversion the depth of the domains must be increased. This may be achieved through the use of short high voltage pulses or perhaps through combination with LAP or pulsed AOP methods where the UV associated domains may act as seeds for domain growth. The main advantage of this combined approach would be the high degree of freedom and flexibility present in the UV writing stage that is not achievable in the other methods.

Repeated cycling of the poling process has also been seen to have some effect for inhibited domain creation that may be useful for the creation of either increased or full depth structures. It has been seen that, after the initial poling of the crystal following exposure on the $+z$ face, re-poling very fast avoids the problems of the uncorrelated domain growth that is seen when domains nucleate on an exposed region of the $-z$ face. Upon a second forward poling it was seen that bulk domains would nucleate and grow along the line of the exposure with an even greater preference than during the initial poling cycle. These domains, as seen through the visualisation method outlined in chapter 4, are of a bulk nature with a lateral size of around 10 - 20 μm. This increase in poling sensitivity through repeated cycling should be examined further both experimentally and theoretically and may help to give rise to new methods of structured bulk poling in thick (> 5 mm) crystals when combined with other methods such as femto-second LAP.

8.2.5 Structured Poling of Rotated-Cut Crystals

The crystals used in the work of this thesis have almost exclusively been of z cut, meaning that the z axis is normal to the larges faces of the crystal wafer. This cut is desirable for optoelectronic uses for many reasons and particularly for the ability to easily structure an electric field along the z axis for poling. For other uses, other crystal cuts are preferred such as the 127.86°Y-cut and the 64°Y-cut, where the normal to the cut face lies in the yz plane but is rotated about the x axis, which are used in SAW applications to chose the propagation velocity of the surface wave. In crystals such as these it is very difficult to create structured domain patterns since an applied field is generally along the direction normal to the crystal faces. Thus if conventional techniques of electrode structuring are employed the field structure will not be parallel to the z axis as is required for domain propagation. In contrast the methods of domain structuring presented in chapter 4 utilises the inherent symmetry of the crystal structure to create the fields to move photo-excited charges along the z axis. This then creates an electric field which can interact with a propagating bulk domain. The production of bulk domains in crystals of rotated cuts is not difficult and requires only a slightly greater electric field across the wafer such that the component along z exceeds the coercive field. Thus the domain inhibition method of domain structuring allows for micron scale domain structuring on rotated cut crystals unachievable by other methods. This could then be used for the creation of surface acoustic waves using unstructured electrodes.

8.3 Theoretical Work

8.3.1 Heat Flow Model

The laser heating model currently deals only with the solid phase however in the experimental work melting of the crystal is commonly encountered. To better describe the experimental conditions a phase change and thermal model of the liquid phase should be included. This will not be possible analytically however and so will lose the advantage of direct calculation.

The thermal stresses encountered during laser heating may also be an important factor toward experimental results, particularly where fracture may occur or where mechanical stress may couple to electrical phenomena such as UV poling through the piezoelectric effect. An extension to the model would then be to calculate the thermal stresses and strains due to thermal expansion of the crystal during laser heating. This may also help to elucidate the causes for the difficulty in heating LN with focussed beams from carbon dioxide lasers and explain why the crystal often cracks in such cases.

8.3.2 Lithium Diffusion Model

The model of chapter 6 assumed that a model of a continuous concentration field could be used to describe the ionic movement but predicted that the depth of the lithium distributions, produced by the scanning UV laser beam, to be of the order of only 100 nm. This depth corresponds to only around 150 times the Li - Li distance which was taken as the basic diffusive jump length. Thus it may be more realistic to take a discrete approach to the modelling and use a probabilistic particle tracking model rather than a continuous mass flux model. Despite the differences in the characteristic lengths of the diffusion problem and the heating beams an appropriate number of tracer atoms could be taken and then statistics used to give he full picture.

8.3.3 Poling Mechanisms Model

The model of the charge transport which leads to both the UV laser direct poling and the UV laser induced poling inhibition has been formulated but time has not allowed for a numerical evaluation. For future work this should be carried out.

Appendix A

Second Harmonic Generation and Quasi-Phase-Matching

A.1 Development of the SHG intensity

During non-linear second harmonic generation the electric field of the second harmonic at a point l is a linear super-position of the second harmonic fields produced at the points $x < l$. The electric field of the second harmonic at l produced at a point x is given by

$$\begin{aligned} E^{2\omega}(l,x) &\propto \cos(2n_\omega k_\omega x + n_{2\omega}k_{2\omega}(l-x)) \\ &\propto \cos(n_{2\omega}k_{2\omega}l - \Delta k x) \end{aligned} \tag{A.1}$$

where k_ω, $k_{2\omega}$, n_ω and $n_{2\omega}$ are the free-space wave vectors and refractive indices at ω and 2ω respectively and

$$\Delta k = n_{2\omega}k_{2\omega} - 2n_\omega k_\omega. \tag{A.2}$$

The total field of the second harmonic at l is then

$$E^{2\omega}(l) \propto \int_{x=0}^{l} \cos(n_{2\omega}k_{2\omega}l - \Delta k x)\mathrm{d}x' \tag{A.3}$$

$$\propto \frac{\sin(n_{2\omega}k_{2\omega}l) - \sin(\Delta k - n_{2\omega}k_{2\omega}l)}{\Delta k}. \tag{A.4}$$

Using a standard trigonometric relation this can be re-cast as

$$E^{2\omega}(l) \propto \frac{\cos((n_{2\omega}k_{2\omega} + 2n_\omega k_\omega)l/2)\sin(\Delta k l/2)}{\Delta k/2}. \tag{A.5}$$

It can be seen that the electric field contains two spatial frequency components, a high frequency component and a low frequency envelope function. The first factor corresponds to the superposition of the two interacting waves and the second factor describes the power transfer from the fundamental to the second harmonic. The intensity of the second harmonic is proportional to the square of the electric field and is shown in figure A.1. The development of the second harmonic intensity does indeed diminish after one coherence length as stated in section 1.2.2 since the newly created second harmonic is in anti-phase to existing second harmonic due to the difference in phase velocities given by equation A.2. If, however, there was no difference in the refractive indices at ω and 2ω such that $\Delta k = 0$ the system is said to be phase matched and equation A.3 becomes

$$E^{2\omega}(l) \propto \int_{x=0}^{l} \cos(n_{2\omega} k_{2\omega} l) \mathrm{d}x' \tag{A.6}$$

which integrates trivially to

$$E^{2\omega}(l) \propto l \cos(n_{2\omega} k_{2\omega} l) \tag{A.7}$$

where we see that the amplitude envelope of the second harmonic field increases linearly with propagation distance. The intensity of the second harmonic will then increase as l^2. This form of phase matching can be achieved by utilising birefringence within a material and / or temperature tuning the dispersion characteristics.

An alternative way to achieve high second harmonic signals is through quasi phase matching (QPM) whereby the spontaneous polarisation of the crystal in periodically inverted. When the spontaneous polarisation is inverted the sign of the $\chi^{(2)}$ tensor components is inverted also and the phase of the second harmonic being created undergoes a relative phase shift of π, hence adding in phase to the existing second harmonic. A periodically inverted domain pattern with domain widths of nl_c, where n is an integer, can then result in a continually increasing second harmonic field. An expression for the second harmonic field strength after a distance l within the crystal can be derived as follows.

The phase at l of the second harmonic signal produced at the point x is given by

$$\phi^{2\omega} = 2n_\omega k_\omega x + n_{2\omega} k_{2\omega} (l - x) \tag{A.8}$$

where the first factor describes the initial phase which is dependent upon the fundamental and the second factor is the phase accrued whilst traversing from x to l. It is assumed that at $x = 0$ the phase of the fundamental is zero. The electric field at l of

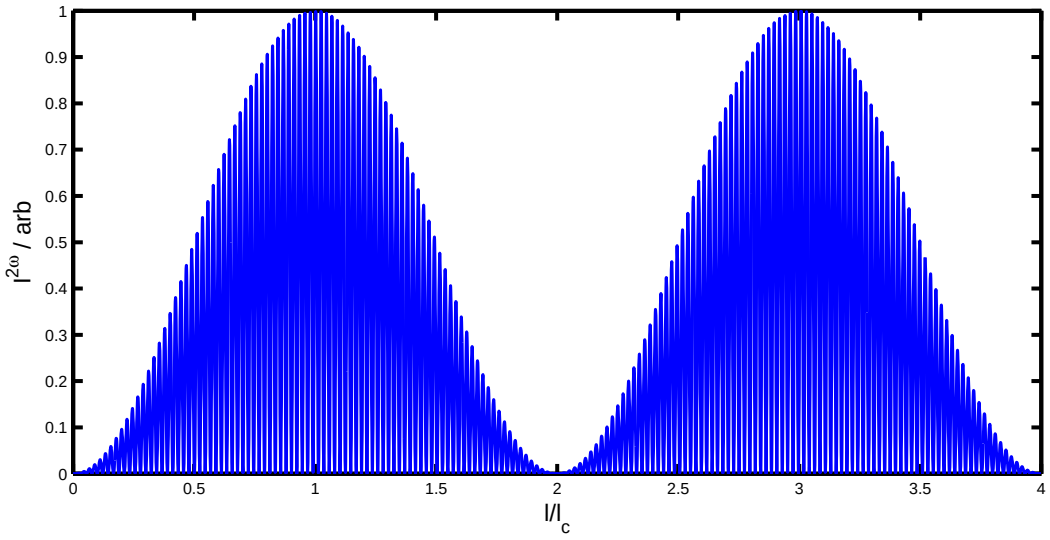

FIGURE A.1: Variation of the second harmonic intensity with propagation distance.

the second harmonic produced at x can then be taken as

$$\begin{aligned} E^{2\omega}(x,l) &\propto \chi^{(2)}(x)\Re\left\{e^{i\phi^{2\omega}}\right\} \\ &\propto \chi^{(2)}(x)\Re\left\{e^{i(2n_\omega k_\omega x + n_{2\omega}k_{2\omega}(l-x))}\right\} \\ &\propto \chi^{(2)}(x)\Re\left\{e^{-i\Delta k x}e^{in_{2\omega}k_{2\omega}l}\right\} \end{aligned} \tag{A.9}$$

where complex exponential form is now used to describe the modulation of the E field, rather than cosine notation, in preparation for easier manipulation. The second harmonic field at l due to the contributions from all x is then

$$E^{2\omega}(l) \propto e^{in_{2\omega}k_{2\omega}l}\int_{x=0}^{l}\chi^{(2)}(x')e^{-i\Delta k x'}\mathrm{d}x' \tag{A.10}$$

If we consider a periodically poled crystal with domain width Λ then the second order susceptibility is given by

$$\chi^{(2)}(x) = \begin{cases} \chi_0^{(2)} & n\Lambda < x < (n+1)\Lambda \quad n = \text{even} \\ -\chi_0^{(2)} & n\Lambda < x < (n+1)\Lambda \quad n = \text{odd} \end{cases} \tag{A.11}$$

where $n = 0, 1, 2, ..n$. Equation A.10 can then be re-written

$$\frac{E^{2\omega}(l)}{e^{in_{2\omega}k_{2\omega}l}} \propto \chi_0^{(2)}\left[\left(\sum_{n=0}^{N-1}(-1)^n\int_{x=n\Lambda}^{(n+1)\Lambda}e^{-i\Delta k x'}\mathrm{d}x'\right) + (-1)^N\int_{x=N\Lambda}^{l}e^{-i\Delta k x'}\mathrm{d}x'\right] \tag{A.12}$$

where

$$N = \lfloor l/\Lambda \rfloor\,. \tag{A.13}$$

Performing the integrations we obtain

$$\frac{E^{2\omega}(l)}{e^{in_{2\omega}k_{2\omega}l}} \propto \frac{-i\chi_0^{(2)}}{\Delta k}\left[\left(\left(e^{i\Delta k\Lambda}-1\right)\sum_{n=0}^{N-1}(-1)^n e^{-i\Delta k\Lambda(n+1)}\right)+ (-1)^N\left(e^{-i\Delta k\Lambda N}-e^{-i\Delta kl}\right)\right]. \quad \text{(A.14)}$$

The series sum

$$\sum_{n=0}^{N-1}(-1)^n\, e^{-ia(n+1)} \quad \text{(A.15)}$$

is given by

$$-\frac{(-1)^N\, e^{-iaN}-1}{1+e^{ia}}. \quad \text{(A.16)}$$

Substituting this result into equation A.14 the second harmonic field after a distance l in a periodically poled crystal is given by

$$\frac{E^{2\omega}(l)}{e^{in_{2\omega}k_{2\omega}l}} \propto \frac{-i\chi_0^{(2)}}{\Delta k}\left[\left(\frac{\left(e^{i\Delta k\Lambda}-1\right)\left(1-e^{-i\Delta k\Lambda N}(-1)^N\right.}{1+e^{i\Delta k\Lambda}}\right)+ (-1)^N\left(e^{-i\Delta k\Lambda N}-e^{-i\Delta kl}\right)\right]. \quad \text{(A.17)}$$

The intensity of the second harmonic can then be given by

$$I^{2\omega}(l) = E^{2\omega}(E^{2\omega})^* \quad \text{(A.18)}$$

which is easily calculated numerically after evaluating equation A.18. Figure A.2 shows the variation of the second harmonic intensity amplitude envelope with propagation distance within the crystal for the situations of no phase matching, perfect phase matching and quasi phase matching with $\Lambda = l_c$ and $\Lambda = 3l_c$.

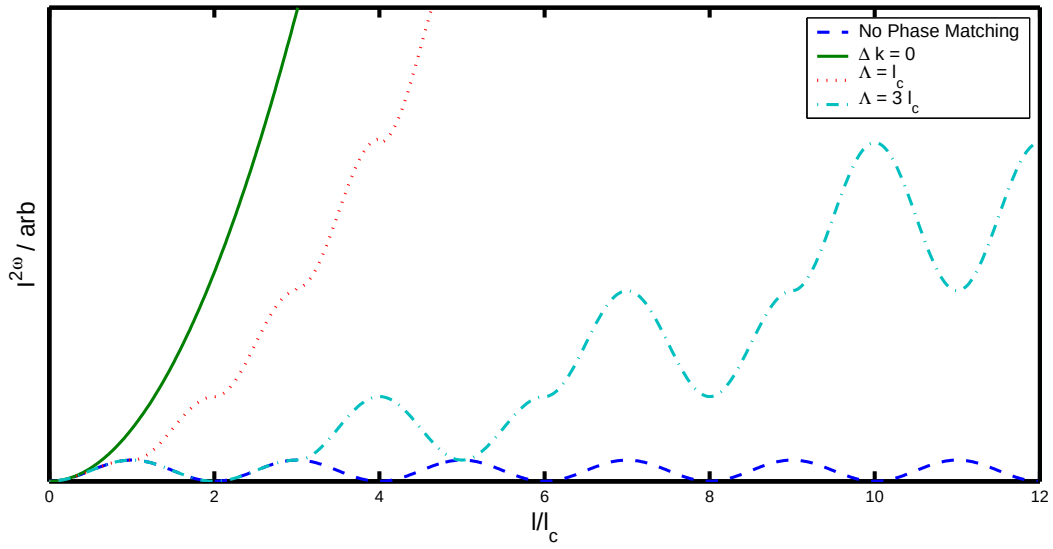

FIGURE A.2: Variation of the second harmonic intensity with propagation distance for the situations of no phase matching, perfect phase matching and quasi phase matching with $\Lambda = l_c$ and $\Lambda = 3l_c$.

Appendix B

Summary of Published Light-Poling Interaction Investigations

B.1 Published Light-Poling Interaction Investigations

The list of papers summarised in the following table does not comprise of all the literature published on light-poling interactions to date, but does give a fair overview of current progress and achievements. Where authors have included hypotheses of the domain formation mechanism, these are summarised also.

Table B.1: Published results of light-poling interaction investigations. Column headers: Ref, reference; λ, wavelength / nm; F, fluence / J cm^{-2}; I, intensity / W cm^{-2}; E_p / mJ; τ_p, pulse length / ns; N, number of pulses; ω, laser spot size / μm; IF, incident face; NF, nucleation face; ΔE_c, change in coercive field; C, crystal; ϕ_l, lateral size / μm; δ, depth / μm; VM, visualisation method. Abbreviations in visualisation method column defined in table B.2.

Ref	λ	**F**	**I**	p	τ_p	**N**	ω	**IF**	**NF**	ΔE_c	**C**	ϕ_l	δ	VM	**Comments**
All Optical Poling															
[1]	248	0.5-10	-	-	20	2-20	-	+z	+z	-	CLN[a]	0.15 - 0.30	2	PFM, HF, SEM	Self-assembled fractal structure following y axes. Surface ablation required.
[2]	248	50-150	-	-	20	2-100	-	-z	-z	-	CLN[a]	0.10	Surface	SEM, HF, PFM	Phase mask exposure, $\Lambda = 726$ nm. Low fluence individual dot domains formed in bright fringes. Dot density increases with fluence till continuous domains seen at mask period. Surface domains could be reversed by high voltage from PFM.
[3]	266	90-150	-	5	10	1-n	-	+z	+z	-	CLN[a]	0.20-0.70	Surface	HF, SEM	Phase mask exposure, grating vector ‖ to x, $\Lambda = 726$ nm. Domains fragmented along y, separation along x is $n\Lambda \approx 2.18-9.4$ μm and along y is ¡ 200 nm. Exposure at T¿100°C results in no fragmentation along y but wider separation along x. Separation distribution independent of laser intensity. No difference in behaviour seen between $\lambda = 266$ nm and 298 nm. Ablation required.
[3]	298	90-150	-	0.5-10.5	7	1-n	-	+z	+z	-	CLN[a]	0.20-0.70	Surface	SEM HF, SEM	Phase mask exposure, grating vector ‖ to x, $\Lambda = 726$ nm. Domains fragmented along y, separation along x is $n\Lambda \approx 2.18-9.4$ μm and along y is ¡ 200 nm. Exposure at T¿100°C results in no fragmentation along y but wider separation along x. Separation distribution independent of laser intensity. No difference in behaviour seen between $\lambda = 266$ nm and 298 nm. Ablation required
[1]	298-306	0.5-10	-	-	~ 7	2-20	-	+z	+z	-	CLN[a]	0.15 - 0.30	2	PFM, HF, SEM	Self-assembled fractal structure following y axes. Surface ablation required.

Continued on next page

[a]Crystal Technology (USA)

Ref	λ	F	I	E_p	τ_p	N	ω	IF	NF	ΔE_c	C	ϕ_l	δ	VM	Comments
[1]	306	7	-	-	~ 7	2-20	-	+z	-	-	CLN[a]	-	-	PFM, HF, SEM	No effect seen at or above $\lambda = 306$ nm.
[4]	308	0.5-1.5	-	-	25	-	3000	+z	+z	-	CLN	0.20	-	PFM, HF, OM	Dots aligned with spacing $\approx$ 400 nm to form rays aligned to y axes. Low fluence - dots only formed. Mid fluence - parallel lines formed. High fluence - self assembled fractal structures. Ray closest approach 0.6 μm, average approach 2.4 μm. Ablation required.
[4]	308	0.5-1.5	-	-	25	-	3000	-z	-z	-	CLN	0.20	-	PFM, HF, OM	Isolated dot domains observed only. Ablation required.
[5]	532	-	-	40-90	5	50	7000	-z	-z	-	CLN	7 mm	Surface	SEM	Crystals heated to 400°C. Fields applied ¡ 75 V mm^{-1}. 10 Hz rep. rate Vacuum 10^{-5} mbar. 90 nm Cu film over illuminated area acts as light-heat transducer and electrode but poling also seen without film.
Light Assisted Poling															
[6]	305, 334, 364, 383, 400, 514.8, 800	-	<1 (305 nm) <100 (334-514 nm) <1000 (800 nm)	-	120-150 fs @250 kHz	-	100-200	-z	-z	41%	CLN	-	Bulk	HF, SEM	All wavelenghs seen to reduce E_c. Reduction depenent upon intensity. More efficient at shorter wavelengths. Domains not limited by crystal symmetry. Surface domains at low exposure conditions.
[6]	305, 334, 364, 383, 400, 514.8, 800	-	<1 (305 nm) <100 (334-514 nm) <1000 (800 nm)	-	120-150 fs @250 kHz	-	100-200	-z	-z	98%	Mg:CLN 5 mol %	-	Bulk	HF, SEM	All wavelenghs seen to reduce E_c. Reduction depenent upon intensity. More efficient at shorter wavelengths. Domains not limited by crystal symmetry. Surface domains at low exposure conditions.
[7]	305	-	0.010 - 0.012	-	c.w.	-	few mm	$\pm$z	-	34%	Mg:CLN[b] 1 mol %	6 mm	Bulk	OI, DC	Domain kinetics seen to change under illumination. Sample Mg:CLN 5 mol %[a] seen to fail structurally during poling plus illumination.
[7]	305	-	0.010 - 0.012	-	c.w.	-	few mm	$\pm$z	-	31%	Mg:CLN[a] 4.9 mol %	6 mm	Bulk	OI, DC	Domain kinetics seen to change under illumination. Sample Mg:CLN 5 mol %[f] seen to fail structurally during poling plus illumination.

Continued on next page

[b] Deltronic (USA)

Ref	λ	F	I	E_p	τ_p	N	ω	IF	NF	ΔE_c	C	ϕ_l	δ	VM	Comments
[7]	305	-	0.010 - 0.012	-	c.w.	-	few mm	±z	-	32%	Mg:CLN [a] 5.5 mol %	6 mm	Bulk	OI, DC	Domain kinetics seen to change under illumination. Sample Mg:CLN 5 mol %[f] seen to fail structurally during poling plus illumination.
[7]	305	-	0.010 - 0.012	-	c.w.	-	few mm	±z	-	2%	CLN[c]	6 mm	Bulk	OI, DC	Domain kinetics seen to change under illumination.
[7]	305	-	0.010 - 0.012	-	c.w.	-	few mm	±z	-	3%	SLN[d]	6 mm	Bulk	OI, DC	Domain kinetics seen to change under illumination.
[8]	305	-	0.04	-	c.w.	-	6 mm	±z	∓z	82%	Mg:CLN 3.2 mol %[d]	-	Bulk	OI	Effect is permanent, E_c remain reduced after illumination stopped. Nucleation on opposit face to illumination. Effect is attributed to position dependent photoconductivity due to reasonable absorption at this wavelength. Charges move within the applied field and build up in areas of low photoconductivity thereby creating the poling field.
[8]	305	-	0.04	-	c.w.	-	6 mm	±z	∓z	74%	Mg:CLN 4.3 mol %[d]	-	Bulk	OI	See above.
[8]	305	-	0.04	-	c.w.	-	6 mm	±z	∓z	82%	Mg:CLN 4.8 mol %[d]	-	Bulk	OI	See above.
[8]	305	-	0.04	-	c.w.	-	6 mm	±z	-	-	Mg:CLN 5.0 mol %[f]	-	-	OI	Sample destroyed during illuminated poling.
[8]	305	-	0.04	-	c.w.	-	6 mm	±z	-	-	Mg:CLN 5.6 mol %[d]	-	-	OI	Sample destroyed during illuminated poling.
[8]	305	-	0.04	-	c.w.	-	6 mm	±z	-	-	Mg:CLN 6.7 mol %[d]	-	-	OI	Sample destroyed during illuminated poling.
[8]	305	-	0.04	-	c.w.	-	6 mm	±z	-	-	Mg:CLN 7.1 mol %[d]	-	-	OI	Sample destroyed during illuminated poling.
[7]	334	-	0.010 - 0.012	-	c.w.	-	few mm	±z	-	27%	Mg:CLN [e] 5.5 mol %	6 mm	Bulk	OI, DC	Domain kinetics seen to change under illumination. Sample used was seen to fail structurally during poling plus illumination of $\lambda = 305$ nm light.

Continued on next page

[c] SZFKI: Research Institute for Solid State Physics and Optics (Budapest, Hungary)
[d] Oxide (Japan)
[e] Yamaju Ceramics (Japan)

Ref	λ	**F**	**I**	$\mathbf{E}_p$	τ_p	**N**	ω	**IF**	**NF**	ΔE_c	**C**	ϕ_l	δ	**VM**	**Comments**
[7]	334	-	0.010 - 0.012	-	c.w.	-	few mm	±z	-	0%	CLN[d] SLN[e] Mg:CLN 5.5 mol %[a] Mg:CLN 1 mol %[c] Mg:CLN 4.9 mol %[a]	6 mm	Bulk	OI, DC	No effect seen.
[9]	334	-	3	-	c.w.	-	-	±z	-	8.5%	CLN[a]	-	Bulk	OI	E_c reduction dependent upon light intensity. Effect persists after illumination stops.
[9]	Multi-line	-	55 (6, $\lambda <$ 334 nm)	-	c.w.	-	-	±z	-	-	CLN[a]	1.5	Bulk	OI	Illumination through 50 % binary mask (Λ = 1 mm) 6 cm from sample through four poling cycles. Illumination stop and forward pole till nucleation. Periodic domains at $\Lambda = 8\mu$m of Fresnel diffraction pattern.
[8]	334	-	0.1	-	c.w.	-	6 mm	±z	-z	52%	Mg:CLN 5.0 mol %[f]	-	Bulk	OI	Effect not permanent, E_c recovers immediately upon stopping illumination.
[8]	334	-	0.1	-	c.w.	-	6 mm	±z	-z	65%	Mg:CLN 5.6 mol %[d]	-	Bulk	OI	Effect not permanent, E_c recovers immediately upon stopping illumination.
[8]	334	-	0.1	-	c.w.	-	6 mm	±z	-z	70%	Mg:CLN 6.7 mol %[d]	-	Bulk	OI	Effect not permanent, E_c recovers immediately upon stopping illumination.
[8]	334	-	0.1	-	c.w.	-	6 mm	±z	-z	75%	Mg:CLN 7.1 mol %[d]	-	Bulk	OI	Effect not permanent, E_c recovers immediately upon stopping illumination.
[10]	351	-	100	-	c.w.	-	150 ∥ z 3 mm ∥ x	+y	-	-	CLT[f]	280	Bulk	PCM, HF, Profiler	Field applied of 2.25 kV mm^{-1}.Beam structured with binary grating amplitude mask. Poling seen to be impeded in illuminated regions.
[9]	351	-	3 - 6	-	c.w.	-	-	±z	-	2-3%	CLN[a]	-	Bulk	OI	E_c reduction dependent upon light intensity. Effect does not persist after illumination stops.
[11]	355	-	0.2	-	c.w.	-	-	±z	-	0	CLN[a]	-	-	OI, DC	Illumination after poling to investigate possible E_c recovery as seen in CLT. No E_c recovery seen.

Continued on next page

[f] Mitsui Corporation (Japan)

Ref	λ	**F**	**I**	$\mathbf{E}_p$	τ_p	**N**	ω	**IF**	**NF**	ΔE_c	**C**	ϕ_l	δ	**VM**	**Comments**
[12]	488	-	$50{\cdot}10^6$	-	c.w.	-	500 nm	$\pm$z	-z	30% @130μm, 20% @surface	CLN[g] Er:CLN $4 \cdot 10^{-4}$ mol %[c]	2	20	Er^{3+} Lum., HF, PCM	Illuminated using confocal microscopy. Stage scanned to write PPLN structures with period down to 8 μm and feature size of 2 μm. Attributed to photo-ionisation of extrinsic $Fe^{2+/3+}$ defects leading to a positively charged focal volume and field required to pole -z face. Two time scales seen corresponding to defects of differnent depths in the band gap.
[13]	488	-	Two beams @ 0.06	-	c.w.	-	-	-	-	31%	Fe:SLN 0.05 mol %	<32	-	OD	Two beam interference creates creates light pattern with grating vector along z. Photo-excited space charge field and external electric field create periodic poling along the z axis of head-to-head domains.
[14]	488	-	$50{\cdot}10^6$	-	c.w.	-	500 nm	-z	-z	30% @130μm, 20% @surface	CLN[h] Er:CLN $4 \cdot 10^{-4}$ mol %[c]	2	20	Er^{3+} Lum., OB	Confocal microscope used. Birefringence between opposite domains seen to increase over distances of 100s of microns from focal spot. Index change due to electro-optic effect. Stark shift of Er^{3+} luminescence used to measure electris field in focal volume. Two responses seen; fast response (<2 ms) proportional to light intensity which suggests an involvement of shallow traps allowing rapid transfer of electrons and a slower response (10 - 100 s) with a rate of change proportional to light intensity but constant saturation relative to fast shift which suggests deeper traps. First process reverts instantly light reduced, second response persists and is almost permanent. $Fe^{2+/3+}$ and niobium antisite defect model proposed.
[15]	488 514 547	-	3000	-	c.w.	-	45 μm	-z	-	31%	CLN[f]	-	Bulk	OB, HF, SEM	Little wavelength dependence seen. Effect attributed to reduced pinning strength of defects.
[15]	488 514 547	-	3000	-	c.w.	-	45 μm	-z	-	89%	Mg:CLN 5.0 mol %[f]	-	Bulk	OB, HF, SEM	Little wavelength dependence seen. Effect attributed to reduced pinning strength of defects.
[6]	514	-	200	-	120-150 fs @250 kHz	-	100-200	-z	-z	-	Mg:CLN 5 mol %	1.3	Bulk	HF, SEM	Field applied of 1.2 kV mm^{-1}. PPLN written with phase mask exposure Λ = 5.25 μm, duty cycle 25/75.

Continued on next page

Ref	λ	F	I	E_p	τ_p	N	ω	IF	NF	ΔE_c	C	ϕ_l	δ	VM	Comments
[15]	514	-	1200	-	c.w.	-	45 μm	-z	-	-	Mg:CLN 5.0 mol %[f]	20-100	Bulk	OB, HF, SEM	Spatial patterning of bulk domains achieved by manually translating stage. Applied field 4 kV mm^{-1}. Effect attributed to reduced pinning strength of defects.
[15]	514	-	-	-	c.w.	-	20 μm	-z	-z	-	Mg:CLN 5.0 mol %[f]	2	Bulk	HF, SEM	Tight focussing with a ×6.3 objective allowed smaller feature size. In-situ monitoring not possible. Effect attributed to reduced pinning strength of defects.
[11]	532	-	1.5	-	c.w.	-	-	±z	-	0	CLN[a]	-	-	OI, DC	Illumination after poling to investigate possible E_c recovery as seen in CLT. No E_c recovery seen.
[5]	532	-	-	40-90	5	50	7000	-z	-z	-	CLN	7 mm	Surface	SEM	Crystals heated to 400°C. Fields applied ¡ 75 V mm^{-1}. 10 Hz rep. rate Vacuum 10^{-5} mbar. 90 nm Cu film over illuminated area acts as light-heat transducer and electrode but poling also seen without film.
[16]	UV Lamp	-	< 0.2	-	c.w.	-	-	±z	-z	-	Mg:CLN 5.0 mol %	< 10.4	Surface	HF, OM	Gratings produced illuminating through $\Lambda = 15.4\mu$m photomask. Illuminating -z face with field of 3.5 kV mm^{-1} for 20 s resulted in domains 500 nm deep. Illuminating -z face with field of 5.4 kV mm−1 for 90 s resulted in bulk domain grating.

Abbreviation	**Description**
PFM	Piezoresponse Force Microscopy
HF	HydroFluoric acid etching
SEM	Scanning Electron Microscopy
OM	Optical Microscopy
OI	Optical Interferometry
DC	Displacement Current measurements
PCM	Phase Contrast Microscopy
OD	Optical Diffraction
OB	Optical Birefringence

Table B.2: Abbreviations used in the visualisation method column of table B.1.

References

[1] C.E. Valdivia, C.L. Sones, J.G. Scott, S. Mailis, R.W. Eason, D.A. Scrymgeour, V. Gopalan, T. Jungk, E. Soergel, and I. Clark. Nanoscale surface domain formation on the +z face of lithium niobate by pulsed ultraviolet laser illumination. *Applied Physics Letters*, 86(2):022906 – 1, 2005.

[2] C.L. Sones, C.E. Valdivia, J.G. Scott, S. Mailis, R.W. Eason, D.A. Scrymgeour, V. Gopalan, T. Jungk, and E. Soergel. Ultraviolet laser-induced sub-micron periodic domain formation in congruent undoped lithium niobate crystals. *Applied Physics B: Lasers and Optics*, 80(3):341 – 344, 2005.

[3] I.T. Wellington, C.E. Valdivia, T.J. Sono, C.L. Sones, S. Mailis, and R.W. Eason. Ordered nano-scale domains in lithium niobate single crystals via phase-mask assisted all-optical poling. *Applied Surface Science*, 253(9):4215 – 4219, 2007.

[4] V.Y. Shur, D.K. Kuznetsov, A.I. Lobov, E.V. Nikolaeva, M.A. Dolbilov, A.N. Orlov, and V.V. Osipov. Formation of self-similar surface nano-domain structures in lithium niobate under highly nonequilibrium conditions. *Ferroelectrics*, 341:85 – 93, 2006.

[5] M. Houe and P.D. Townsend. Thermal polarization reversal of lithium niobate. *Applied Physics Letters*, 66(20):2667 – 9, 1995.

[6] C.E. Valdivia, C.L. Sones, S. Mailis, J.D. Mills, and R.W. Eason. Ultrashort-pulse optically-assisted domain engineering in lithium niobate. *Ferroelectrics*, 340:75 – 82, 2006.

[7] M.C. Wengler, B. Fassbender, E. Soergel, and K. Buse. Impact of ultraviolet light on coercive field, poling dynamics and poling quality of various lithium niobate crystals from different sources. *Journal of Applied Physics*, 96(5):2816 – 2820, 2004.

[8] M.C. Wengler, U. Heinemeyer, E. Soergel, and K. Buse. Ultraviolet light-assisted domain inversion in magnesium-doped lithium niobate crystals. *Journal of Applied Physics*, 98(6):064104 –, 2005.

[9] M. Muller, E. Soergel, and K. Buse. Influence of ultraviolet illumination on the poling characteristics of lithium niobate crystals. *Applied Physics Letters*, 83(9): 1824 – 6, 2003.

[10] G.W. Ross, P.G.R. Smith, and R.W. Eason. Optical control of electric field poling in $LiTaO_3$. *Applied Physics Letters*, 71(3):309 – 11, 1997.

[11] M.C. Wengler, M. Muller, E. Soergel, and K. Buse. Poling dynamics of lithium niobate crystals. *Applied Physics B: Lasers and Optics*, 76(4):393 – 396, 2003.

[12] V. Dierolf and C. Sandmann. Direct-write method for domain inversion patterns in $LiNbO_3$. *Applied Physics Letters*, 84(20):3987 – 9, 2004/05/17.

[13] H.A. Eggert, F. Kalkum, M.C. Wengler, U. Heinemeyer, and K. Buse. Light-assisted generation of tailored ferroelectric domain structures. *Ferroelectrics*, 340: 63 – 7, 2006.

[14] Christian Sandmann and Volkmar Dierolf. The role of defects in light induced domain inversion in lithium niobate. *Physica Status Solidi C: Conferences*, 2(1): 136 – 140, 2005.

[15] C.L. Sones, M.C. Wengler, C.E. Valdivia, S. Mailis, R.W. Eason, and K. Buse. Light-induced order-of-magnitude decrease in the electric field for domain nucleation in MgO-doped lithium niobate crystals. *Applied Physics Letters*, 86(21): 212901 –, 2005.

[16] M. Fujimura, T. Sohmura, and T. Suhara. Fabrication of domain-inverted gratings in MgO:$LiNbO_3$ by applying voltage under ultraviolet irradiation through photomask at room temperature. *Electronics Letters*, 39(9):719 – 721, 2003.

Appendix C

UV-Induced Charge Transport

C.1 UV-Induced Charge Transport

The equations governing the transport of photo-excited charges during focussed UV laser irradiation were given in section 3.5. Here we give the derivation of these equations.

In all transport processes, mass must be conserved for each species undergoing transport. This gives the mass conservation equations

$$\frac{\mathrm{d}\rho_{e,h}}{\mathrm{d}t} = -\nabla \cdot \mathbf{j}_{e,h} + Q_{e,h} \tag{C.1}$$

where ρ is the charge density, t is time, $\mathbf{j}$ is the electric current density, Q is the charge source function and the subscripts e and h refer to electrons and holes respectively. The electric current density for each charge carrier is composed of two contributions, a drift current, $\mathbf{j}_{dr}$, and a diffusion current, $\mathbf{j}_{di}$. The drift current is given by

$$\mathbf{j}_{dr\ e,h} = e\mu_{e,h}c_{e,h}\mathbf{E} \tag{C.2}$$

where q is the electric charge, μ is the mobility, c is the concentration, e is the electronic charge and $\mathbf{E}$ is the electric field. This can be considered more conveniently as a particle flux $\mathbf{f}$, rather than electric current, as

$$\mathbf{f}_{dr\ e,h} = \frac{e}{q_{e,h}}\mu_{e,h}c_{e,h}\mathbf{E} \tag{C.3}$$

where q is the charge of the carrier giving

$$\mathbf{f}_{dr\ e} = -\hat{\mu}_e c_e \mathbf{E} \tag{C.4}$$

and

$$\mathbf{f}_{dr\ h} = \hat{\mu}_h c_h \mathbf{E}. \tag{C.5}$$

The diffusion component of the current density is given by

$$\mathbf{j}_{di\ e,h} = q_{e,h} \mathbf{D}_{e,h} \nabla c_{e,h} \tag{C.6}$$

where $\mathbf{D}$ is the diffusivity. Using the Einstein relation

$$\mathbf{D} = \frac{\hat{\mu} k_B T}{e} \tag{C.7}$$

and, again, dividing by the carrier charge, the diffusion components can be written in terms of particle fluxes as

$$\mathbf{f}_{di\ e} = \frac{-\hat{\mu}_e k_B T}{e} \nabla c_e \tag{C.8}$$

and

$$\mathbf{f}_{di\ h} = \frac{-\hat{\mu}_h k_B T}{e} \nabla c_h. \tag{C.9}$$

The conservation of charge equations can now be written in terms of particle fluxes as

$$\frac{\mathrm{d}c_e}{\mathrm{d}t} = -\nabla \cdot \left(-\hat{\mu}_e c_e \mathbf{E} - \frac{\hat{\mu}_e k_B T}{e} \nabla c_e \right) + Q_e \tag{C.10}$$

and

$$\frac{\mathrm{d}c_h}{\mathrm{d}t} = -\nabla \cdot \left(\hat{\mu}_h c_h \mathbf{E} - \frac{\hat{\mu}_h k_B T}{e} \nabla c_h \right) + Q_h \tag{C.11}$$

where $Q_{e,h}$ now represent particle number sources, rather than explicitly charge sources. Expanding we obtain

$$\frac{\mathrm{d}c_e}{\mathrm{d}t} = \frac{\hat{\mu}_e k_B T}{e} \nabla \cdot T \nabla c_e + \hat{\mu}_e \nabla \cdot c_e \mathbf{E} + Q_e \tag{C.12}$$

and

$$\frac{\mathrm{d}c_h}{\mathrm{d}t} = \frac{\hat{\mu}_h k_B T}{e} \nabla \cdot T \nabla c_h - \hat{\mu}_h \nabla \cdot c_h \mathbf{E} + Q_h. \tag{C.13}$$

Equations C.12 and C.13 are coupled through the electric field E which is itself dependent upon both c_e and c_h and must be solved simultaneously. The electric field can be found by Gauss's law relating the electric displacement $\mathbf{D^E}$ to the free charge,

$$\nabla \cdot \mathbf{D^E} = \rho. \tag{C.14}$$

Including the full form of the electric displacement

$$\mathbf{D^E} = \epsilon \mathbf{E} + \mathbf{P}_s \tag{C.15}$$

where ϵ is the electrical permittivity tensor and $\mathbf{P}_s$ is the spontaneous polarisation, and expressing the vector electric field as the gradient of the scalar electrical potential, V, equation C.14 can be re-written as

$$-\nabla \cdot \epsilon \nabla V + \nabla \cdot \mathbf{P}_s = e(c_h - c_e). \tag{C.16}$$

The above equation can then be readily solved numerically for V and the electric field can be calculated directly for substitution into equations C.12 and C.13 at each point in time.

Appendix D

The Kirchhoff Transform

D.1 Kirchhoff Transform

Many physical problems can be described by either partial or ordinary differential equations such as the heat diffusion equation shown in chapter 5. However, for these equations to be analytically solvable they must be linear, which places restrictions on the extent to which a solution can describe the physical system. In the heat diffusion equation in chapter 5 the non-linearity arises due to the temperature dependence of D, ρ and C and if the equation is to be solved analytically these would have to be approximated with a constant value. In some cases, however, the non-linearity can be encompassed within a new independent variable such that the new equation is linear. In the case of equation 5.5 the term

$$\nabla \cdot D(T)\nabla T$$

can be taken as an example where of course

$$\nabla = \frac{\mathrm{d}}{\mathrm{d}x}\hat{i} + \frac{\mathrm{d}}{\mathrm{d}y}\hat{i} + \frac{\mathrm{d}}{\mathrm{d}z}\hat{k}. \tag{D.1}$$

Taking just the term in x we can introduce a new variable by stating

$$\frac{\mathrm{d}T}{\mathrm{d}x} = \frac{\partial T}{\partial \Theta}\frac{\partial \Theta}{\partial x}. \tag{D.2}$$

The second term in equation 5.5 becomes

$$\frac{\mathrm{d}}{\mathrm{d}x}D(T)\frac{\mathrm{d}T}{\mathrm{d}x} = \frac{\mathrm{d}}{\mathrm{d}x}D(T)\frac{\partial T}{\partial \Theta}\frac{\partial \Theta}{\partial x} \tag{D.3}$$

where it can be seen that if the term is to be linear in the variable Θ then

$$D(T)\frac{\partial T}{\partial \Theta}$$

must be constant. Let the constant be $D(T_0)$, where T_0 is the substrate temperature, then

$$D(T)\frac{\partial T}{\partial \Theta} = D(T_0). \tag{D.4}$$

Rearranging and integrating between T_0 and T, and Θ_0 and Θ where Θ_0 is the value of Θ at T_0;

$$\int_{T_0}^{T} D(T')\mathrm{d}T' = D(T_0)\int_{\Theta_0}^{\Theta} \mathrm{d}\Theta' \tag{D.5}$$

which integrates to

$$\Theta(T) = \Theta(T_0) + \frac{1}{D(T_0)}\int_{T_0}^{T} D(T')dT'. \tag{D.6}$$

This gives the transformation from the real temperature T to a new temperature variable Θ and is known as the Kirchhoff transform.

Appendix E

Solution of the Heat Equation

E.1 Solution of the Heat Equation

In chapter 5 it was shown that the heating of lithium niobate by a scanning UV laser beam can be described by a form of Poisson's equation when the scan speed is slow. Here we describe the full solution.

The heat equation was given by equation 5.13 as

$$\nabla^2\Theta = -\frac{w^2 S(X,Y,Z)}{D(T_0)\rho C}. \tag{E.1}$$

and this was shown to have the solution

$$\Theta(\mathbf{r}) = \frac{w^2}{4\pi D(T_0)\rho C}\int \frac{S(\mathbf{r}')}{|\mathbf{r}-\mathbf{r}'|}\mathrm{d}^3\mathbf{r}'. \tag{E.2}$$

In Cartesian coordinates this can be expressed as

$$\Theta(X,Y,Z) = A\iiint \frac{S(X',Y',Z')}{[(X-X')^2+(Y-Y')^2+(Z-Z')^2]^{\frac{1}{2}}}\mathrm{d}X'\ \mathrm{d}Y'\ \mathrm{d}Z' \tag{E.3}$$

where

$$A = \frac{w^2}{4\pi\rho C D(T_0)} \tag{E.4}$$

to ease notation. Unfortunately this integral cannot be performed because of the form of the denominator. However, we can substitute the relation

$$\frac{1}{[(X-X')^2+(Y-Y')^2+(Z-Z')^2]^{\frac{1}{2}}} = \frac{1}{2\pi^2}\int\!\!\int\!\!\int_{-\infty}^{\infty} \frac{1}{(k_1^2+k_2^2+k_3^2)}\times \exp[i(k_1X+k_2Y+k_3Z)]\ \mathrm{d}k_1\ \mathrm{d}k_2\ \mathrm{d}k_3 \quad \text{(E.5)}$$

into equation E.3 to obtain

$$\Theta(X,Y,Z,) = \frac{A}{8\pi^3}\int\!\!\int\!\!\int_{-\infty}^{\infty}\int\!\!\int\!\!\int \frac{\exp[i(k_1(X-X')+k_2(Y-Y')+k_3(Z-Z'))]}{(k_1^2+k_2^2+k_3^2)}\times S(X',Y',Z')\ \mathrm{d}X'\ \mathrm{d}Y'\ \mathrm{d}Z'\ \mathrm{d}k_1\ \mathrm{d}k_2\ \mathrm{d}k_3. \quad \text{(E.6)}$$

The denominator here still causes problems and so we introduce a further relation

$$\frac{1}{r} = \int_0^{\infty} e^{-r\lambda}\mathrm{d}\lambda \quad \text{(E.7)}$$

to obtain

$$\Theta(X,Y,Z) = \frac{A}{8\pi^3}\int\!\!\int\!\!\int_{-\infty}^{\infty}\int\!\!\int\!\!\int\int_{\lambda=0}^{\infty} \exp[i(k_1(X-X')+k_2(Y-Y')+k_3(Z-Z'))]\times \exp[-(k_1^2+k_2^2+k_3^2)\lambda]S(X',Y',Z')\ \mathrm{d}X'\ \mathrm{d}Y'\ \mathrm{d}Z'\ \mathrm{d}k_1\ \mathrm{d}k_2\ \mathrm{d}k_3\ \mathrm{d}\lambda. \quad \text{(E.8)}$$

The source function, S, can be expressed as

$$S(X',Y',Z') = B\exp[-2(X'^2+y'^2)]\exp(-\alpha w|Z'|) \quad \text{(E.9)}$$

where

$$B = \frac{2P(1-R)\alpha}{\pi w^2} \quad \text{(E.10)}$$

is introduced to ease notation. The integrals in equation E.8 can then be done separately. The X' integral is

$$\exp(ik_1X)\int_{-\infty}^{\infty}\exp(-2X'^2-ik_1X')\ \mathrm{d}X' = \frac{\sqrt{2\pi}}{2}\exp(ik_1X-k_1^2/8) \quad \text{(E.11)}$$

and the Y' integral similarly gives

$$\frac{\sqrt{2\pi}}{2}\exp(ik_2Y-k_2^2/8). \quad \text{(E.12)}$$

Substitution into equation E.8 gives

$$\Theta(X,Y,Z) = \frac{AB}{8\pi^3}\frac{\pi}{2}\iiint_{-\infty}^{\infty}\int_{\lambda=0}^{\infty} \exp[i(k_1X + k_2Y + k_3 + (Z - Z'))]\times$$
$$\exp[-(k_1^2 + k_2^2)/8]\exp[-(k_1^2 + k_2^2 + k_3^2)\lambda]\ \mathrm{d}Z'\ \mathrm{d}k_1\ \mathrm{d}k_2\ \mathrm{d}k_3\ \mathrm{d}\lambda. \quad \text{(E.13)}$$

The k_1 integral is given by

$$\int_{-\infty}^{\infty} \exp(ik_1X - k_1^2/8 - k_1^2\lambda\ \mathrm{d}k_1 = \frac{4\sqrt{\pi}\exp[-2X^2/(1+8\lambda)]}{\sqrt{2+16\lambda}} \quad \text{(E.14)}$$

and the k_2 integral is given similarly by

$$\frac{4\sqrt{\pi}\exp[-2Y^2/(1+8\lambda)]}{\sqrt{2+16\lambda}}. \quad \text{(E.15)}$$

The k_3 integral is given by

$$\int_{-\infty}^{\infty} \exp[ik_3(Z - Z') - k_3^2\lambda]\ \mathrm{d}k_3 = \frac{\sqrt{\pi}}{\sqrt{\lambda}}\exp(-(Z - Z')^2/4\lambda). \quad \text{(E.16)}$$

After substitution into equation E.13 we arrive at

$$\Theta(X,Y,Z) = \frac{AB\sqrt{\pi}}{\pi}\int_{-\infty 0}^{\infty\infty} \frac{\exp[-2(X^2+Y^2)/(1+8\lambda)]}{2+16\lambda}$$
$$\frac{\exp[-\alpha w|Z'| - (Z - Z')^2/4\lambda]}{\sqrt{\lambda}}\ \mathrm{d}Z'\ \mathrm{d}\lambda. \quad \text{(E.17)}$$

The integral over Z' can now be computed and this is given by

$$\int_{-\infty}^{\infty} \exp[-\alpha w|Z'| - (Z-Z')^2/4\lambda]\,\mathrm{d}Z' = \exp[-Z^2/4\lambda]\int_{-\infty}^{0} \exp[Z'^2/4\lambda + Z'(Z/2\lambda + \alpha w)]\,\mathrm{d}Z'$$
$$+ \exp[-Z^2/4\lambda]\int_{0}^{\infty} \exp[Z'^2/4\lambda + Z'(Z/2\lambda - \alpha w)]\ \mathrm{d}Z'. \quad \text{(E.18)}$$

These are error functions of the form

$$\int_{0}^{\infty} \exp[-az^2 - bz]\ \mathrm{d}z = \frac{1}{2}\sqrt{\frac{\pi}{a}}\exp[b^2/4a]\ \mathrm{erfc}[b/2\sqrt{a}] \quad \text{(E.19)}$$

which then gives the integral over Z' as

$$\frac{1}{2}\sqrt{4\pi\lambda}\exp[-Z^2/4\lambda]\left\{\exp[\alpha w - Z/2\lambda]^2\lambda\ \mathrm{erfc}[(\alpha w - Z/2\lambda)\sqrt{\lambda}] + \exp[\alpha w + Z/2\lambda]^2\lambda\ \mathrm{erfc}[(\alpha w + Z/2\lambda)\sqrt{\lambda}]\right\}. \quad \text{(E.20)}$$

Substitution into equation E.18 then gives the final form for Θ as

$$\Theta(X,Y,Z) = \frac{AB}{2}\int_0^\infty \frac{\exp[-2(X^2+Y^2)/(1+8\lambda) - Z^2/4\lambda]}{1+8\lambda}\times \left\{\exp[\alpha w - Z/2\lambda]^2\lambda\ \mathrm{erfc}[(\alpha w - Z/2\lambda)\sqrt{\lambda}] + \exp[\alpha w + Z/2\lambda]^2\lambda\ \mathrm{erfc}[(\alpha w + Z/2\lambda)\sqrt{\lambda}]\right\}\ \mathrm{d}\lambda \quad \text{(E.21)}$$

which must, finally, be computed numerically.

Appendix F

Published Works

F.1 Journal/Book Papers

F.1.1 Modelling the Formation of Optical Waveguides Produced in $LiNbO_3$ by Laser Induced Thermal Diffusion of Lithium Ions.

A. C. Muir, G. J. Daniell, C. P. Please, I. T Wellington, S. Mailis, and R. W. Eason. Modelling the formation of optical waveguides produced in $LiNbO_3$ by laser induced thermal diffusion of lithium ions. *Applied Physics A (Materials Science Processing)*, 83, 389 - 396 (2006).

This publication is the result of the work carried out in chapters 5 and 6.

This paper has received two citations from authors outside of this group that do not have links with this group. The citing papers are

- J. Burghoff, H. Hartung, S. Nolte, A. Tunnermann. Structural properties of femtosecond laser-induced modifications in $LiNbO_3$. *Applied Physics A (Materials Science Processing)*, 86, 165 - 170 (2007)
- J. Burghoff, S. Nolte, A. Tunnermann. Origins of waveguiding in femtosecond laser-structured $LiNbO_3$. *Applied Physics A (Materials Science Processing)*, 89, 127 - 132 (2007)

Appl. Phys. A 83, 389–396 (2006)
DOI: 10.1007/s00339-006-3493-4

Applied Physics A
Materials Science & Processing

A.C. MUIR[1,✉]
G.J. DANIELL[2]
C.P. PLEASE[3]
I.T. WELLINGTON[1]
S. MAILIS[1]
R.W. EASON[1]

Modelling the formation of optical waveguides produced in $LiNbO_3$ by laser induced thermal diffusion of lithium ions

[1] Optoelectronics Research Centre, University of Southampton, SO17 1BJ Southampton, UK
[2] School of Physics and Astronomy, University of Southampton, SO17 1BJ Southampton, UK
[3] School of Mathematics, University of Southampton, SO17 1BJ Southampton, UK

Received: 4 October 2005/Accepted: 9 January 2006
Published online: 15 February 2006 •

ABSTRACT Analytical and numerical modelling of the fabrication of optical waveguides in lithium niobate ($LiNbO_3$) through direct writing with a continuous wave ultraviolet (UV) laser has been performed. It is proposed that the UV illumination induces heating of the surface and subsequent thermal diffusion of lithium which alters the refractive index in accordance with the lithium concentration dependence of the Sellmeier equations.

PACS 61.80.Ba; 66.30.Dn; 77.84.Dy

1 Introduction

$LiNbO_3$ is a widely used optical material due to its high transparency in both the infrared and visible regions [1] and its large non-linear coefficients [2]. The fabrication of optical waveguide structures in $LiNbO_3$ is normally achieved with multiple lithographic and in-diffusion steps [3, 4]. However, it has previously been shown that channel waveguides can be fabricated in $LiNbO_3$ through a simple one step ultraviolet (UV) direct write process [5]. These waveguides can be fabricated with little or no damage to the crystal as evidenced by Raman spectroscopy of the irradiated region. At the time of publication of [5], the waveguide formation mechanism for this direct-write process was not clear, but was suspected to be lithium sideways diffusion, and so modelling techniques were necessary to elucidate the likely causes.

Refractive index structures can be formed via the modification of lithium concentration [6, 7]. $LiNbO_3$ is highly absorbing at the writing wavelength of 244 nm which is below the absorption edge at 300 nm [8, 9] and so the basic assumption for this work was that the optical energy is converted into heat and it is this that subsequently drives the waveguide formation through lithium thermal-diffusion. In a first step the heat flow induced in $LiNbO_3$ by a scanning Gaussian UV laser beam has been modelled. An analytical approach is presented in Sect. 2 using a Kirchhoff transform to include the temperature dependence of the thermal diffusivity and assuming that the density and specific heat are constant. For a physical parameter range of interest a simplified heat equation is then solved in the reference frame of the moving beam. The dependence of temperature distributions and temperature gradients are investigated as a function of the incident power and beam spot size. The heat equation is then solved directly in Sect. 2.3 using finite difference techniques which allow further inclusion of temperature dependent parameters and a discussion of the complementarity of the two methods is given.

A model for diffusive motion in non-uniform temperature fields is derived in Sect. 3 and applied to lithium ions in $LiNbO_3$. The solution of the model is obtained using finite difference techniques and the temperature distributions obtained in section Sect. 2. The resultant lithium concentration profiles are then converted into refractive index profiles through the Li concentration dependent Sellmeier equations [6] and these are compared to the waveguides observed in [5]. The lithium diffusion model is then used to investigate the lifetime of the lithium concentration profiles at room temperature through normal concentration gradient driven (as opposed to thermally driven) diffusion and these are compared to the lifetimes of the waveguides observed in [5].

2 Heat flow modelling

In this section heat flow induced by a scanning laser beam at a highly absorbing wavelength is modelled first analytically, and then numerically using finite difference approximations of the heat equation. In both instances the modelling is performed in the reference frame of the moving beam. The analytical model assumes that the thermal conductivity and thermal diffusivity are the only temperature dependent physical parameters and then uses a Kirchhoff transform to include these in a form of the heat equation that is analytically solvable under certain conditions. The value of the heat capacity used in the analytical model is taken as the average of a fit to experimental data of the Einstein formula for heat capacity, in the temperature range of room temperature to the melting point of $LiNbO_3$. The numerical model uses the full empirical fit of the heat capacity to investigate the assumption of zero temperature dependence and a preferred form of the thermal diffusivity that was not suitable for the analytical model.

2.1 *Non-linear analytical modelling with the Kirchoff transform*

At 244 nm the optical absorption co-efficient has been measured at around $3 \times 10^7\ m^{-1}$ [8] which gives a corresponding absorption depth of around 30 nm. If it is assumed

✉ Fax: +44 (0) 23 8059 3142, E-mail: acm@orc.soton.ac.uk

that the depth of the guiding region is of the order μm as in conventional optical waveguides, it becomes obvious that the index change mechanism cannot therefore be directly optically driven but must instead be driven by thermal effects.

Figure 1 shows the coordinate system used in the model. The coordinates x, y, and z corresponds to the reference frame of the crystal while X, Y and Z corresponds to the reference frame of the moving beam and are given by $(x - vt)/w$, y/w and z/w, respectively, where v is the velocity of the moving beam and w is the $1/\mathrm{e}$ spot size of the laser E-field. For simplicity X, Y and Z are normalised to units of w.

The starting point of the investigation is the heat equation

$$\varrho C_v \frac{\partial T}{\partial t} - \nabla \cdot \boldsymbol{K} \nabla T = S(\boldsymbol{r}, t)\,, \tag{1}$$

where ϱ is the density of the material, C_v is the specific heat at constant volume, T is the temperature in Kelvin, $\boldsymbol{K}$ is the thermal conductivity tensor and $S(\boldsymbol{r}, t)$ is the heat source function. If the specific heat and density are assumed constant with respect to temperature the relation

$$\boldsymbol{D} = \frac{\boldsymbol{K}}{\varrho C_v} \tag{2}$$

can be used, where $\boldsymbol{D}$ is the thermal diffusivity tensor. The heat equation can then be expressed in the isotropic case, where $\boldsymbol{D}$ is a function of temperature only, as

$$\frac{\partial T}{\partial t} - \nabla \cdot D(T) \nabla T = \frac{1}{\varrho C_v} S(\boldsymbol{r}, t)\,. \tag{3}$$

The heat source is the scanning UV Gaussian laser beam which is absorbed near the surface and converted into heat through phonon relaxation within the crystal. The Gaussian intensity profile of the scanning laser and hence the heat source is described by

$$S(x, y, z, t) = \frac{2P(1-R)\alpha}{\pi w^2} \exp\left[-\frac{2((x-vt)^2 + y^2)}{w^2}\right] \times \exp\left[-\alpha |z|\right]\,, \tag{4}$$

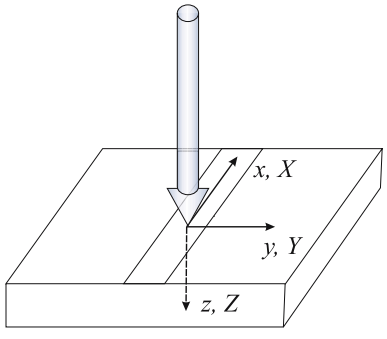

FIGURE 1 Coordinate system used in the models. The coordinates x, y, and z correspond to the reference frame of the crystal and have their origin at the center of the beam on the crystal surface at $t = 0$. X, Y and Z correspond to the reference frame of the moving beam and are normalised in units of the beam spot radius (w). The normalised co-ordinates have their origin at the center of the beam on the crystal surface

where P is the incident optical power, R is the intensity reflectivity at the writing wavelength and α is the optical absorption coefficient. The factor two arises since we reflect the system about the $z = 0$ plane to obtain the boundary condition of zero heat flux.

Since the thermal diffusivity is temperature dependent, (3) is non-linear. The temperature dependence of the thermal diffusivity can, however, be encompassed in a new temperature variable by using a Kirchhoff transform [10]. Using the assumption of constant ϱC_v, we can express the Kirchhoff transform as

$$\Theta(T) = \Theta(T_0) + \frac{1}{D(T_0)} \int_{T_0}^{T} D(T')\,\mathrm{d}T'\,, \tag{5}$$

where Θ is a new temperature variable and $D(T_0)$ is the thermal diffusivity at the substrate temperature T_0. The value of $\Theta(T_0)$ is arbitrary and so can be defined to be zero. Equation (3) is then expressed in terms of the temperature variable Θ in the reference frame of the moving beam as

$$\frac{vw}{D(T(\Theta))} \frac{\partial \Theta}{\partial X} - \nabla^2 \Theta = \frac{w^2 S(X, Y, Z)}{D(T_0) \varrho C_v}\,. \tag{6}$$

If the factor

$$\frac{vw}{D(T)} \tag{7}$$

has a magnitude much less than unity the first term of (3) has a negligible effect. This can be written as a condition on v;

$$v \ll \frac{D(T)}{w}\,. \tag{8}$$

The thermal diffusivity of $LiNbO_3$ between room temperature and the melting point is typically of the order $10^{-6}\ \mathrm{m^2\,s^{-1}}$ [11] and the range of spot sizes used in [5] is between 1.75 μm and 6.6 μm. If a typical spot size of 5 μm is taken it can be seen that the first term will be negligible if

$$v \ll 0.2\ \mathrm{m\,s^{-1}}\,. \tag{9}$$

The maximum scanning velocity used in [5] was $12\ \mathrm{mm\,s^{-1}}$ which is clearly much less than this limit of around $200\ \mathrm{mm\,s^{-1}}$ and so in re-creating the conditions of [5] the first term of (6) can be neglected. The heat equation can then be written as

$$\nabla^2 \Theta = -\frac{w^2 S(X, Y, Z)}{D(T_0) \varrho C_v}\,. \tag{10}$$

This is a form of Poisson's equation which has the familiar solution [13]

$$\Theta(\boldsymbol{r}) = \frac{w^2}{4\pi D(T_0) \varrho C_v} \int \frac{S(\boldsymbol{r}')}{|\boldsymbol{r} - \boldsymbol{r}'|}\,\mathrm{d}^3\boldsymbol{r}'\,. \tag{11}$$

After some algebra and the substitution of (4) (re-expressed in the reference frame of the moving beam) this can be written as

a single integral

$$\Theta(X, Y, Z, \lambda) = \frac{P(1-R)\alpha}{\pi\varrho C_v D(T_0)} \int_0^\infty \frac{1}{1+8\lambda} g(X, Y, \lambda) h(Z, \lambda)\, \mathrm{d}\lambda\,. \tag{12}$$

The function $g(X, Y, \lambda)$ is given by

$$g(X, Y, \lambda) = \exp\left[-\frac{2(X^2+Y^2)}{1+8\lambda}\right] \tag{13}$$

and the function $h(Z, \lambda)$ is given by

$$h(Z, \lambda) = \exp\left(\frac{-Z^2}{4\lambda}\right) \left(\exp\left[\left(\alpha w - \frac{Z}{2\lambda}\right)^2 \lambda\right] \operatorname{erfc}\left[\left(\alpha w - \frac{Z}{2\lambda}\right)\sqrt{\lambda}\right] + \exp\left[\left(\alpha w + \frac{Z}{2\lambda}\right)^2 \lambda\right] \operatorname{erfc}\left[\left(\alpha w + \frac{Z}{2\lambda}\right)\sqrt{\lambda}\right]\right). \tag{14}$$

The final integral must be calculated numerically.

Having obtained a solution for the temperature in terms of Θ, we now find it is necessary to use the Kirchhoff transform again to convert to the real temperature T and so a function $D(T)$ must be generated empirically from experimental data. It is required upon integration of the function $D(T')$ in (5) that $\Theta(T)$ must be a linear one-to-one function of T for $T > T_0$. The most suitable form for $D(T)$ is given by

$$D(T) \propto \frac{1}{T}\,. \tag{15}$$

Figure 2 shows the best fit curve to the data from [11] where the constant of proportionality is found to be $4.173 \times 10^{-4}\ \mathrm{m^2\,s^{-1}\,K}$. Substitution of (15) into (5) gives

$$T(\Theta) = T_0 \exp\left(\frac{\Theta}{T_0}\right)\,. \tag{16}$$

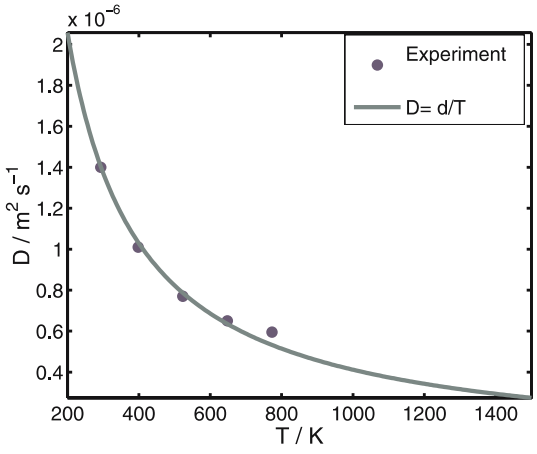

FIGURE 2 Thermal diffusivity of $LiNbO_3$ as function of temperature. The experimental data points obtained from [11]. The *solid curve* shows the fit of the function $D = \frac{d}{T}$ which was used as an empirical formula for D

TABLE 1 Parameter set used in [5]

Parameter	Range
Power P	10–100 mW
Spot Radius w	1.75–6.6 µm
Velocity	0.83–12.00 mm s^{-1}

2.2 *Results and discussion*

The investigation presented here is restricted to the waveguide fabrication parameters of [5], which are given in Table 1. Equations (12) to (14) show that, in the small v regime of $v \ll 0.2\ \mathrm{m\,s^{-1}}$, the velocity has a negligible effect upon spatial temperature distributions in the moving frame.

The specific heat is taken to be the average value of a fit to the data of [2] of the Einstein model [12] between 290 K and 1513 K.

Using (12) and (16) the temperature distributions in arbitrary directions in the reference frame of the moving beam can be calculated. Figure 3a shows the temperature distribu-

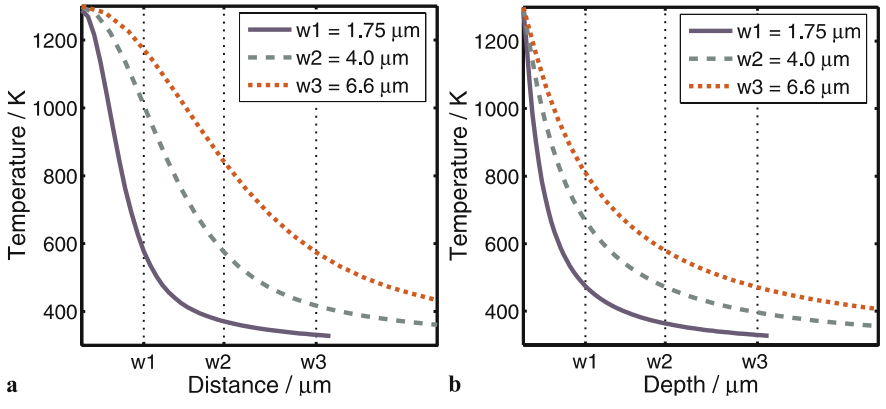

FIGURE 3 (**a**) Temperature rise as a function of distance from the centre of the beam along the crystal surface for writing parameters of $w = 1.75$ µm, $P = 16.8$ mW (*solid line*), $w = 4.0$ µm, $P = 38$ mW (*dashed line*), $w = 6.6$ µm, $P = 62.5$ mW (*dotted line*). (**b**) Temperature rise as a function of depth under the centre of the beam for the same writing parameters as in (**a**)

tion along X axis for three different sets of spot size and laser power. Figure 3b shows the temperature distribution along the Z axis for the same parameters. The combinations of spot size and laser power were chosen to produce the same peak temperature. Figure 3 shows that in all cases the temperature changes are highly localised to the beam spot with the distributions dropping to around one third of the peak temperature rise in the direction parallel to the surface, and around one fifth in the direction normal to the surface, by a distance of one beam radius. The difference in character of the distributions in the two directions can be seen clearly in Fig. 4 which shows the temperature distributions along the X and Z axes. The temperature gradient in the Z direction is much greater than those parallel to the surface (X or Y) due to the fast decay of the z component of the heat source in (4). The localisation of the temperature changes to length scales of order w shows that the crystal is experiencing extremely steep spatial temperature gradients, with temperatures varying by nearly 1000 K in a distance of around 10 μm.

Figure 5 shows the variation of the temperature distribution along the Z axis with incident laser power for a fixed spot size. It is seen that while the spatial extent of the temperature changes does not vary greatly with incident power; the peak temperature increases significantly hence the corresponding temperature gradients increase also. The temperature gradient in the Z direction at the point $(X, Y, Z) = (0, 0, 0)$ varies non-linearly with power as shown in Fig. 6. This can be understood with reference to Fig. 2 which shows the thermal diffusivity of $LiNbO_3$ as a function of temperature. As the power, and hence temperature, increases the thermal diffusivity decreases leading to a confinement of heat in the hotter regions of the crystal.

The flow of lithium ions in the crystal will be due to the spatial temperature distribution induced by the scanning laser beam. The shape of the temperature distribution has been shown to be independent of the scan speed, whether the beam is static in the reference frame of the crystal or moving at a velocity. However, the extent to which a diffusive flow can change the lithium concentration at a point in the crystal depends on the dwell time of the beam at that point and hence the temporal temperature distribution. The temporal temperature distributions at the point $(x, y, z) = (0, 0, 0)$ at the extremes of scan speed in Table 1 are shown in Fig. 7. Even though the velocity is unimportant in the heat flow problem it will clearly be important for the lithium diffusion problem.

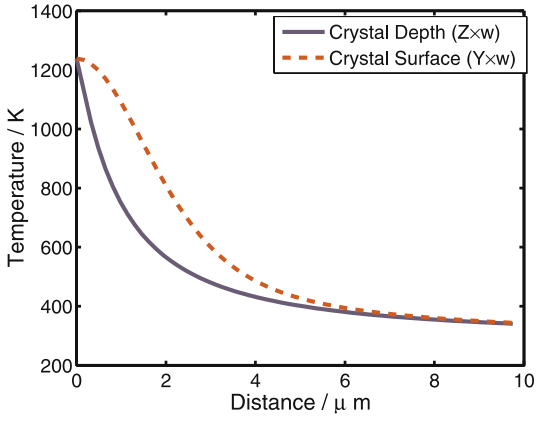

FIGURE 4 Temperature rise with depth (*solid line*) and along the surface (*dashed line*) in the moving frame of the beam for $w = 3.25$ μm, $P = 30$ mW

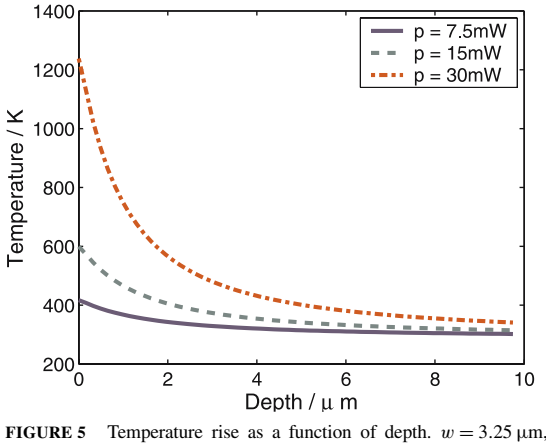

FIGURE 5 Temperature rise as a function of depth. $w = 3.25$ μm, $P =$ 7.5 mW, 15 mW, 30 mW

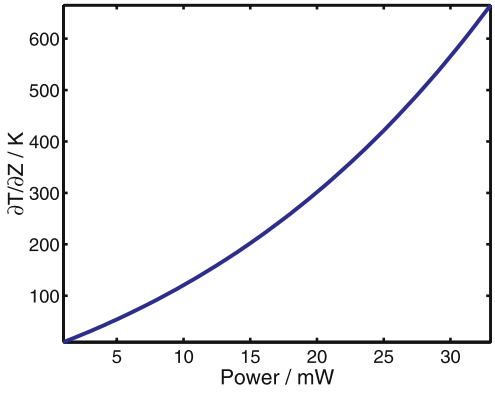

FIGURE 6 Temperature gradient in the Z direction at the point $(X, Y, Z) = (0, 0, 0)$ as a function of laser power. $w = 3.25$ μm

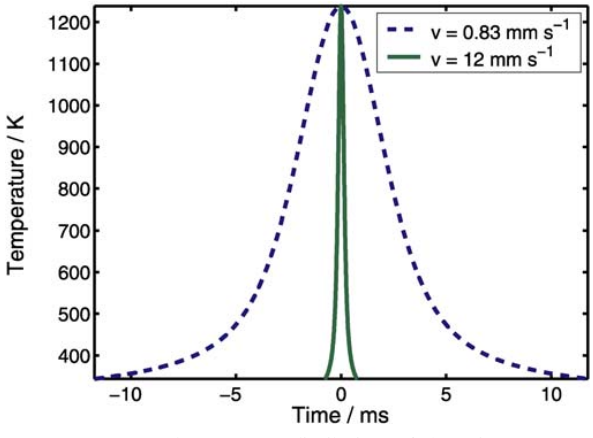

FIGURE 7 Temporal temperature distributions of the point $(x, y, z) = (0, 0, 0)$ at the extremes of scan speed in Table 1, $w = 3.25$ μm, $P = 30$ mW, $v = 0.83$ mm s^{-1}, 12 mm s^{-1}

2.3 *Numerical modelling with finite differences*

An analytical solution to the heat equation can give directly the temperature at any arbitrary point, but suffers from the assumptions required to make a set of equations analytically solvable. In the case of the model of Sect. 2.1, it was required to assume that both the density and specific heat were constant with respect to temperature, that the thermal diffusivity function was of a form that integrated to give a linear one to one function between the temperature variables T and Θ and that the scan speed was negligibly small. Using finite difference techniques to solve the heat equation does not impose any such limitations onto these parameters, and as such the full temperature dependent problem can be solved and the temperature dependence of each parameter can take any form required [15]. However, finite difference techniques cannot give directly a value at any arbitrary point but require that we solve for an entire lattice with the restriction that the conditions at the boundaries are known in advance. This limits the resolution of the obtainable distributions since the demands placed upon the computer time and memory, for three dimensional problems, scale with the cube of the linear density of points in the lattice. The analytical model does not have this restriction and so the two methods can be considered complementary and can be used together to give a clearer understanding of the laser heating process, where the finite difference model can give a full non-linear solution at a restricted resolution and the analytical model can give temperatures directly at arbitrary points.

The finite difference model retains the assumption of negligible v and uses initially the thermal diffusivity function of (15) and constant ϱC_v as were used in the analytical model. The temperature distribution along the Z axis obtained using both the finite difference and analytical models is shown in Fig. 8. The limitation of the finite difference model to include only effects whose spatial extent is greater than the model step size contributes to disagreement of the surface temperature since the optical absorption that takes place on a scale of around $0.01\ w$ appears as a delta function.

The finite difference method can accommodate any form of temperature dependence in the material parameters and so

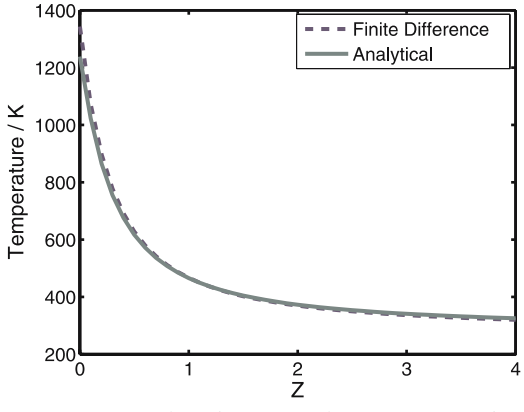

FIGURE 8 Comparison of temperature rise at $X = Y = 0$ as a function of Z position ($Z = z/w$) obtained using analytical and numerical finite difference methods. $P = 30$ mW, $w = 3.25$ μm

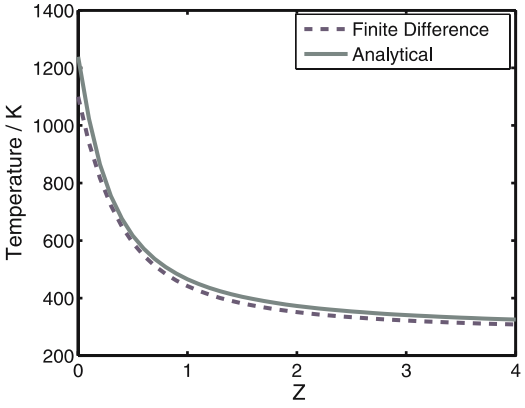

FIGURE 9 Comparison of temperature rise at $X = Y = 0$ as a function of Z position ($Z = z/w$) obtained using analytical and numerical finite difference methods. Finite difference model includes preferred function for thermal diffusivity and temperature dependent heat capacity. $P = 30$ mW, $w = 3.25$ μm

the effect of the constant ϱC_v assumption and the choice of empirical fit for $D(T)$ can be investigated.

A function that gives a better fit to the experimental thermal diffusivity data of [11] but cannot be used in the analytical model is a decreasing exponential of the form

$$D = D_0 + a\,\mathrm{e}^{-bT}\,, \tag{17}$$

where $D_0 = 5.397 \times 10^{-7}\ \mathrm{m^2\,s^{-1}}$, $a = 4.639 \times 10^{-6}\ \mathrm{m^2\,s^{-1}}$ and $b = 5.748 \times 10^{-3}\ \mathrm{K^{-1}}$. Figure 9 shows the temperature distributions obtained using the analytical model with the original form for D and the finite difference model with the above temperature dependence for D and the temperature dependence of C_v given by a fit of data in [2] of the Einstein model for heat capacity. ϱ is known to vary little in comparison to C_v [2] and so the variation of ϱC_v is assumed to be due to C_v only. It can be seen that although the increased heat capacity at high temperatures has lowered the distribution the difference is small and so the approximation in the analytical model of constant ϱC_v and (15) as an empirical fit for D are satisfactory.

3 Lithium ion movement

The governing equations of the thermal diffusion of lithium ions in $LiNbO_3$ are derived under the assumptions that there is no electrostatic interaction between diffusing species and the vacancy density is constant. The equations are solved using finite difference methods and the temperature distributions obtained in Sect. 2 to give the lithium concentration distribution in the y, z plane of the crystal after the passage of the beam. The resultant lithium concentration distribution is converted to a refractive index distribution through the use of the Sellmeier equations for $LiNbO_3$. The light guidance properties of the refractive index distributions are then modelled using a commercial waveguide modelling package for comparison with [5]. The lifetime of the lithium concentration distributions at room temperature are investigated and compared with the lifetimes of the experimental waveguides.

The refractive index of $LiNbO_3$ is dependent upon the concentration of lithium present [6] and waveguides have been produced through the out-diffusion at high temperatures of

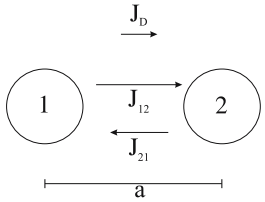

FIGURE 10 Schematic for diffusive flow between sites 1 and 2. J_D is the net flow from site 1 to 2 and J_{ij} is the flow from site i to site j. The two sites are separated by the discrete jump distance a

lithium from the surface of $LiNbO_3$ [7]. However this requires durations of hours at temperatures near the melting point and so is inadequate for situations when heating is only observed for milliseconds. In [7] the temperature was uniform throughout the volume of the $LiNbO_3$ crystal and so no temperature gradients were present but the heating process in [5] has been seen in Sect. 2 to produce very steep temperature gradients and it is proposed that the waveguides observed in [5] were due to the thermal diffusion within the crystal of lithium away from the irradiated regions, driven by the steep temperature gradients.

3.1 *Model derivation*

It is assumed that the ionic diffusivity is isotropic in uniform temperature fields and that concentration changes are small such that vacancies are always present for diffusing species to occupy.

Two sites separated by a distance a as shown in Fig. 10 are considered. There are n_1 particles at site 1 and n_2 particles at site 2. The quantity r is defined to be a rate function that corresponds the average number of times a particle jumps in any direction in unit time and is dependent upon temperature. In one dimension, the flux of particles from site 1 to site 2, and site 2 to site 1 are given by J_{12} and J_{21} respectively where

$$J_{12} = \frac{1}{6} r_1 n_1 \tag{18}$$

and

$$J_{21} = \frac{1}{6} r_2 n_2 \,. \tag{19}$$

The net flux between sites 1 and 2 is then

$$J_D = J_{12} - J_{21} = -\frac{1}{6}\left(r_2 n_2 - r_1 n_1\right) \,. \tag{20}$$

In terms of concentrations

$$J_D = -\frac{a^2}{6}\frac{(r_2 c_2 - r_1 c_1)}{a} \,, \tag{21}$$

where c_1 and c_2 are the concentration of particles at site 1 and 2 respectively. Taking the limit as $a \to 0$

$$J_D = -\frac{a^2}{6}\frac{\partial (rc)}{\partial x} \,, \tag{22}$$

where c is the concentration which will be dependent upon position. The rate of change of concentration is then derived by using (22) to balance the fluxes through the faces of a differential volume in cartesian space. The resulting diffusion equation in the reference frame of the crystal is then

$$\frac{\partial c}{\partial t} = \frac{a^2}{6}\nabla^2 (rc) \,. \tag{23}$$

The temperature dependent expression for r is

$$r = r_0 \exp\left(-\frac{Q}{k_B T}\right) \tag{24}$$

where Q is the activation energy or the energy required for the ion to leave its present position and r_0 is the attempt rate. Q and r_0 were found to be 0.75 eV and $5.024 \times 10^9\ \mathrm{s}^{-1}$ respectively as determined by nuclear magnetic resonance measurements [14].

3.2 *Numerical simulation*

Finite difference techniques have been used to solve (23) with the boundary condition that no concentration change occurs at the edge of the temperature distributions. In the crystal rest frame the temperature distribution and, hence, r are time dependent since the beam is moving. This presents a time dependent three dimensional problem.

The boundary conditions at $|x|$, $|y|$ and $z \gg 0$ are that the concentration should smoothly go to the background value. The boundary at $z = 0$ however is a sharp boundary and the behaviour here is very different to that in the bulk.

The boundary condition at $z = 0$ is that there is no flux of lithium through the surface. There is, of course, no flux into the crystal from the air, and it is assumed that there is no out-diffusion.

The time scale for the diffusive motion is determined by the dwell time of the beam which is given approximately by

$$\Delta t = \frac{w}{v} \,. \tag{25}$$

This gives a corresponding characteristic diffusive distance of

$$\Delta z = \sqrt{\frac{a^2 r}{6}\Delta t} \,. \tag{26}$$

If a is taken to be the lithium–lithium distance of 0.38 nm [14] and r taken to be $r(1000\ \mathrm{K})$, $w = 3.25\ \mu\mathrm{m}$ and $v = 0.83\ \mathrm{mm s}^{-1}$ $\Delta z = 28$ nm. At this length scale the variation of rc is small everywhere except in the z direction at $z = 0$ therefore, from (22) the net flow of lithium will essentially only be away from the surface in the z direction across the length Δz. The one dimensional diffusion equation is then

$$\frac{\partial c}{\partial t} = \frac{a^2}{6}\frac{\partial^2 (rc)}{\partial z^2} \,. \tag{27}$$

This is approximated by finite differences as

$$\frac{c_i^{n+1} - c_i^n}{\delta t} = -\frac{Jz^n_{(i+1/2)} - Jz^n_{(i-1/2)}}{\delta z} \tag{28}$$

where

$$Jz^n_{(i+1/2)} = -\frac{a^2}{4}\frac{(rc)^n_{i+1} - (rc)^n_i}{\delta z} \,. \tag{29}$$

where the superscript n and subscript i refer to temporal and spatial steps respectively. It follows naturally from the derivation of the diffusive flux to take single forward difference approximations in the z direction. The second derivative of (27) is taken explicitly as two first order derivatives to include the crystal surface boundary condition in terms of a particle flux.

3.3 *Results and discussion*

Using the model described in the previous section, we calculated the lithium concentration distribution in the y, z plane after the passage of the writing beam. Figure 11 shows the lithium concentration distribution along the z axis for writing parameters $w = 3.25\,\mu\text{m}$, $v = 0.83\,\text{mm s}^{-1}$, $P = 30\,\text{mW}$ (solid line). The background lithium concentration in $LiNbO_3$ has been normalised to unity for clarity of numbers. The lithium dependent refractive index calculated using the Sellmeier equations for $LiNbO_3$ [6] is also shown (dashed line in the same plot). It can be seen that there is indeed a region of decreased lithium concentration near the surface of the crystal and also that there is an increase in the lithium concentration at a depth of around $0.03\,w$. The model predicts that the lithium ions do indeed move due to the temperature gradient however the concentration change distribution has a far smaller spatial extent than the corresponding temperature distribution.

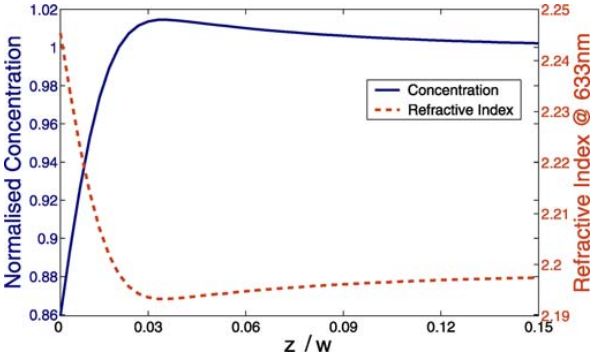

FIGURE 11 Resultant lithium concentration distribution and index distribution along z in the enter of the written channel. $P = 30\,\text{mW}$, $w = 3.25\,\mu\text{m}$, $v = 0.83\,\text{mm s}^{-1}$

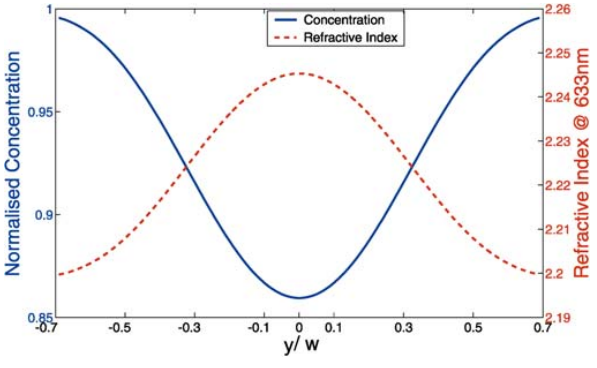

FIGURE 12 Resultant lithium concentration distribution and index distribution along y on the surface of the crystal. $P = 30\,\text{mW}$, $w = 3.25\,\mu\text{m}$, $v = 0.83\,\text{mm s}^{-1}$

Figure 12 shows the lithium concentration distribution in the line along the surface of the crystal. It can be seen again that the dimensions of the concentration distribution are smaller than those of the temperature distribution. In the y direction, however, the difference between the width of the temperature distribution and lithium concentration distribution is less that that in the z direction due gradients in r.

It is possible to include in the finite difference approximation the effects of diffusion in a direction other than z. This has been done for diffusion in the y direction and the correction to the one dimensional case for the same beam parameters as above is shown in Fig. 13. The form of the distribution is, as one would expect, showing movement of lithium from the hot central region to the cooler edges of the beam path. However, it can be seen that the magnitude of the concentration change caused only by diffusion along y is roughly 100 smaller than that caused by diffusion along the z dimension, representing a maximum correction of only around 1% thus validating the assumption that the diffusive flow is essentially one-dimensional.

The finite difference model can also be used to predict the long-term behaviour of the lithium concentration distributions by simulating their subsequent concentration gradient driven diffusion at room temperature following the writing process. The decay of the concentration distribution is shown in Fig. 14 where it can be seen that these distributions are not permanent and will decay on a time scale of months. This is also seen experimentally with the physical guides which gives added strength to the proposition that lithium diffusion is responsible for the index changes seen in [5].

Both Figs. 11 and 12 show the correct refractive index structure for optical guiding: a high-index core region surrounded by a lower index cladding region. Whether these refractive index distributions could support waveguide modes depends on both the magnitude of the refractive index difference between the two regions and the physical size of the high refractive index core region. The refractive index dis-

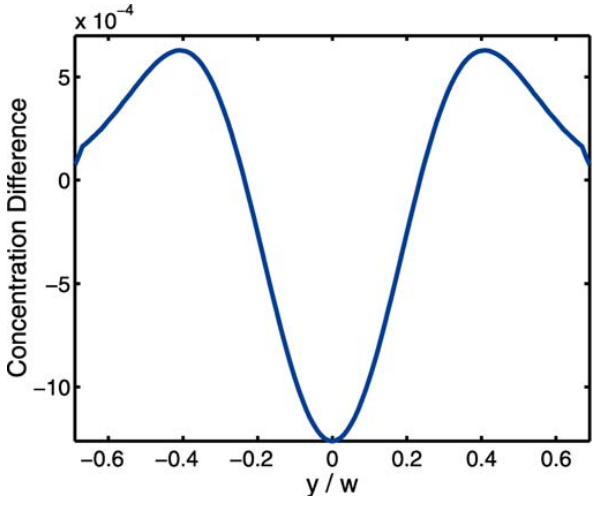

FIGURE 13 Correction to the concentration distribution of Fig. 12 due to the inclusion of flow in the y direction. $P = 30\,\text{mW}$, $w = 3.25\,\mu\text{m}$, $v = 0.83\,\text{mm s}^{-1}$

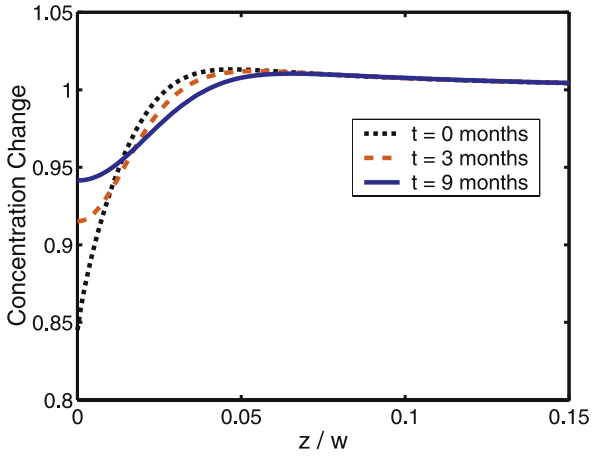

FIGURE 14 Decay of the concentration distribution at room temperature

tributions predicted by the model were inserted into Selene Pro [16], a commercial beam propagation package, but were found however insufficient to support waveguide modes corresponding to those seen in [5]. For comparison it was found that a slab guide with a step index configuration of the minimum and maximum indexes of those seen from the model would require a depth of at least twice that produced by the model to support waveguide modes.

There are, however, many significant physical processes that could be occurring but are not included in the present model. If charge neutrality is not conserved locally a space charge field would be created in the lithium deficient region that could act upon the refractive index through the electro-optic effect. Another possible effect is photo-bleaching during the writing process that would dynamically increase the absorption depth across the beam spot. This would have the effect of pushing the active diffusion region further into the crystal hence increasing the depth of the index change structure.

From this point of view a factor of two in the difference in depth between a guiding and non-guiding structure is not strong enough to rule out thermally driven lithium movement as being the principle cause for the waveguides seen in [5] particularly as the structure lifetime is similar to that of the experimental waveguides.

4 Conclusions

Modelling of the formation of the UV direct-write waveguides in $LiNbO_3$ observed in [5] through thermal diffusion of lithium has been carried out. Heat flow modelling has been performed using both analytical and numerical techniques for heating $LiNbO_3$ with a scanning UV laser beam. The temperature dependence of the thermal diffusivity has been included in the analytical model and the numerical finite difference model has shown that the assumption of constant specific heat represents only a small correction. A model for thermal-diffusion in steep temperature gradients has been derived and applied to lithium ions in $LiNbO_3$ using the temperature distributions obtained in the heat flow model. It was seen that significant diffusive flow occurred in only a thin layer at the crystal surface directly into the crystal. The resultant lithium concentration profile was converted into a refractive index profile using the Sellmeier equations for $LiNbO_3$ but at this stage were seen not to support waveguide modes. The decay of the lithium concentration profile through normal Fickian diffusion was investigated and was seen to agree well with the lifetimes of the experimental guides.

Our results lead us to believe that the thermal diffusion of lithium ions is a primary cause for the waveguides observed in [5]. However the models do not yet include explicitly the charge coupling effects during lithium diffusion or the effect of a possible non-uniform charge distribution on the crystal after illumination. Work is currently in progress to address these omissions, and it is hoped that these will help produce a model which is in consistent agreement with experiment and that could then be used to gain a better understanding of the mechanism with an aim toward determining a process with which to fix the physical waveguides and tune their properties.

REFERENCES

1 M. Lawrence, Rep. Prog. Phys. **56**, 363 (1993)
2 K.K. Wong, *Properties of Lithium Niobate*, Emis Datareview (IEEE 1989)
3 I.E. Barry, G.W. Ross, P.G.R. Smith, R.W. Eason, Appl. Phys. Lett. **74**, 1487 (1999)
4 M.N. Armenise, IEEE Proc. J. Optoelectron. **135**, 85 (1988)
5 S. Mailis, C. Riziotis, I.T. Wellington, P.G.R. Smith, C.B.E. Gawith, R.W. Eason, Opt. Lett. **28**, 1433 (2003)
6 U. Schlarb, K. Betzler, J. Appl. Phys. **73**, 3472 (1993)
7 J.R. Carruthers, I.P. Kaminow, L.W. Stulz, Appl. Opt. **13**, 2333 (1974)
8 A.M. Mamedov, Opt. Spectrosc. **56**, 645 (1984)
9 D. Redfield, W.J. Burke, J. Appl. Phys. **45**, 4566 (1974)
10 J.E. Moody, R.H. Hendel, J. Appl. Phys. **53**, 4364 (1982)
11 R.A. Morgan, K.I. Kang, C.C. Hsu, C.L. Koliopoulos, N. Peyghambarian, Appl. Opt. **26**, 5266 (1987)
12 C. Kittle, *Introduction To Solid State Physics, Fourth Edition* (John Wiley & Sons, New York, 1971) p. 204, Eq. 13
13 R.C. Clive, *Techniques In Partial Differential Equations* (McGraw-Hill, New York, 1971) Sect. 3–11
14 D. Bork, P. Heitjans, J. Phys. Chem. B **105**, 9162 (2001)
15 S. Nakamura, *Applied Numerical Methods In C* (Prentice Hall, Englewood Cliffs, 1993)
16 Selene Pro Version 4.2. Produced by BBV, now part of C2V (www.C2V.nl)

F.1.2 Ultraviolet Laser Induced Submicron Spatially Resolved Superhydrophilicity on Single Crystal Lithium Niobate Surfaces

A. C. Muir, S. Mailis and R. W. Eason. Ultraviolet laser induced submicron spatially resolved superhydrophilicity on single crystal lithium niobate surfaces. *Journal of Applied Physics*, 101, 104916 (2007).

This paper is a result of the work presented in chapter 2 and has been cited by one other paper written by an author outside of this group with no links to this group. The citing paper is

- I. Torchinsky and G. Rosenamnn. Interface modification and bonding of lithium tantalate crystals. *Applied Physics Letters*, 92, 052903 (2008)

Ultraviolet laser-induced submicron spatially resolved superhydrophilicity on single crystal lithium niobate surfaces

A. C. Muir,[a] S. Mailis, and R. W. Eason
Optoelectronics Research Centre, University of Southampton, Hants SO17 1BJ, United Kingdom

(Received 21 February 2007; accepted 29 March 2007; published online 31 May 2007)

Lithium niobate crystal surfaces become superhydrophilic after ultraviolet laser irradiation. The crystal surface hydrophilicity, which was assessed by the contact angle of a sessile drop of de-ionized water, was found to undergo a transition from mildly hydrophobic (contact angle $\theta_E \approx 50°$) to a superhydrophilic state ($\theta_E < 5°$). Patterning of the hydrophilicity at the micron and submicron ranges has been achieved by spatially modulating the illuminating laser beam. © *2007 American Institute of Physics*. [DOI: 10.1063/1.2734539]

I. INTRODUCTION

Lithium niobate (LN) is a material that has found many uses in the optoelectronics industry due to its large electro-optic, acousto-optic, and nonlinear coefficients. In the development of devices which exploit these properties the wettability of the surface is often of great importance either during fabrication[1,2] or as an integral property of the final device.[3] Currently the wetting properties of LN surfaces are altered through the functionalization of the surface with solutions such as $NH_4OH+H_2O_2+H_2O$ (Ref. 1) or by depositing monolayers such as octadecyltrichlorosilane.[3] Structuring of these coatings is currently achieved through the multiple processing steps of photolithography that may disrupt or further complicate the construction of other device components.

In this paper we show that it is possible to achieve a change of the inherent wetting properties of the crystal surface simply by exposing to ultraviolet (UV) irradiation at photon energies exceeding the band gap of the material. It is also shown that the change in wetting behavior can be spatially resolved down to the submicron scale.

II. SESSILE DROP INVESTGATION

A. Experimental details

Experiments characterizing the hydrophilicity change using sessile water drops have been carried out using a range of different lasers [with wavelengths (λ) of 244, 248, and 266 nm] which were either pulsed, with pulse durations ranging from 130 fs to 20 ns, or continuous wave. Ultrafast laser exposures were carried out at $\lambda=266$ nm using the third harmonic of a Coherent Mira oscillator–Legend amplifier system. The laser beam (pulse duration of 130 fs, repetition rate of 1 kHz) was expanded to give an energy fluence of 0.045 mJ cm^{-2} per pulse. Nanosecond laser exposures were carried out at $\lambda=266$ nm (Nd:YVO_4 laser, 20 ns pulse duration, 20 Hz repetition rate) and $\lambda=248$ nm (KrF laser, pulse duration of 20 ns, repetition rate of 10 Hz). The $\lambda=266$ nm beam was expanded to give an energy fluence of 2 mJ cm^{-2} per pulse and the $\lambda=248$ nm beam was truncated by a 6×6 mm^2, square aperture to give an energy fluence at the sample of 40 mJ cm^{-2} per pulse. The exposures using the femtosecond and nanosecond lasers were carried out at ambient laboratory conditions.

The continuous wave exposures were carried out at $\lambda=244$ nm using a frequency doubled argon ion laser, and the slightly elliptical beam provided by the laser was expanded to give a spot with a major axis of 12 mm and minor axis of 10 mm. Exposures were carried out over a range of incident powers from 10 to 60 mW in an environmental chamber which provides a controlled environment of pressure, temperature, and atmosphere. Large glass windows enabled optical monitoring of the surface for the contact angle measurements. The UV illumination of the samples was performed through a fused silica window and the exposure time was controlled by a computer controlled shutter. After UV exposure a 0.5 μl drop of de-ionized (DI) water was immediately placed on the surface and the drop profile was imaged and captured using a charge coupled device (CCD) camera. The contact angle was measured using an image analysis software.[4]

B. Results and discussion

Figure 1 shows the effect of UV irradiation upon the contact angle of a sessile drop and defines the contact angle θ_E as the angle between the substrate surface and the tangent to the drop profile at the line where the solid, liquid, and vapor phases meet. The upper picture [Fig. 1(a)] shows a drop of DI water on an unilluminated surface and the lower

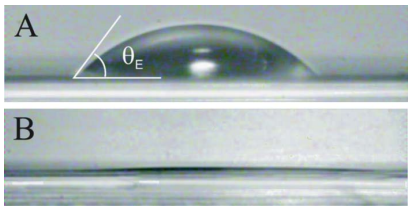

FIG. 1. Effect of the contact angle (θ_E) of a DI water sessile drop on LN after exposure to UV light. (A) shows the contact angle of a drop on an unilluminated surface. (B) shows a drop that has wetted the LN surface after exposure to UV light.

[a]Author to whom correspondence should be addressed; electronic mail: acm@orc.soton.ac.uk

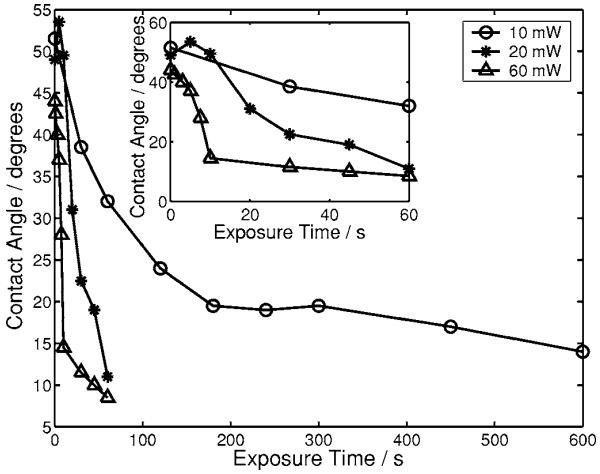

FIG. 2. Change in water contact angle with increasing 244 nm exposure time for powers incident at the chamber of 10, 20, and 60 mW. Inset shows an expanded view of the initial minute. Lines are added to guide the eye.

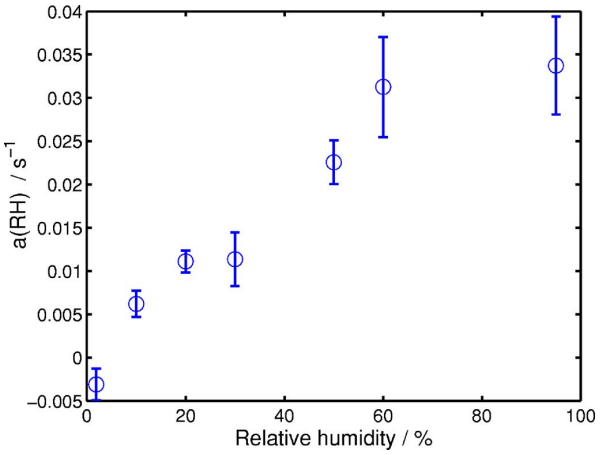

FIG. 3. Change in the parameter a(RH), which describes the strength of the contact angle change, with relative humidity for exposures on the positive z face. Errors are calculated from an error in θ of ±2.8° (P=45 mW).

picture [Fig. 1(b)] shows a drop of the same volume on a preilluminated surface. After sufficient illumination, the contact angle of the drop decreases to a superhydrophilic state ($\theta_E < 5°$) and the surface approaches complete wetting ($\theta_E = 0°$).

All lasers used were seen to produce a change in the hydrophilicity. The $\lambda = 244$ nm laser was chosen for the bulk of the investigation because of the superior quality of its beam profile. Exposures were carried out on both the positive and negative z faces but no significant difference in their behavior was found.

Figure 2 shows the variation of the water contact angle on the positive z face as a function of exposure time with $\lambda = 244$ nm exposure, for powers (measured before the fused silica window of the chamber) of 10 mW (open circle), 20 mW (filled circle), and 60 mW (triangle). The exposures were carried out at a temperature $T = 27$ °C and relative humidity of 55%. It can be seen from the figure that the contact angle change is not a linear function of the total exposure, i.e., the integrated number of photons arriving at the surface, since doubling the incident power does not simply halve the time required to reach a given contact angle. Rather it is seen that the change is a function of both the total exposure and the incident intensity with higher intensities giving a greater change for equivalent exposure.

The contact angle of olive oil was also measured before and after UV exposure; however, the surface was not seen to become oleophillic since no change in the contact angle was seen even after an exposure of 30 mW for 10 min. Prior to application the drop was strongly pulled toward the sample due to the photoinduced surface charging; however, upon contacting the surface no significant change in contact angle was seen.

The atmosphere was observed to have a pronounced effect upon the hydrophilicity change. It was found that when illuminating with the chamber having been evacuated to a pressure of less than 2 mbars, no significant change to the contact angle was seen even for long exposures (15 min) at 45 mW. It was seen particularly that the presence of water during the exposure was important. The relative humidity at constant temperature was lowered within the chamber by purging with dry nitrogen or increased by bubbling air through de-ionized water and measured with a thermohygrometer. The ambient relative humidity in the lab was 38%. The samples were then illuminated under the desired humidity and then returned to atmospheric conditions for the contact angle measurement. As the humidity was increased the change in contact angle was greater for the same exposure. To keep the contact angle large enough to be measureable the exposure time was decresed as the humidity increased. This means that the change in the contact angle needs to be normalized in some way for analysis. Young's equation relates the surface energies at the solid-liquid and solid-vapor interfaces to the contact angle of the three phase system as

$$\gamma_{lv}\cos(\theta_E) = \gamma_{sv} - \gamma_{sl}, \tag{1}$$

where γ is the interfacial energy and the subscripts lv, sv, and sl correspond to the liquid-vapor, solid-vapor, and solid-liquid interfaces, respectively. Since γ_{lv} is a property of the liquid a change in the contact angle will come about only from a change in $(\gamma_{sv} - \gamma_{sl})$. If it can be assumed that the rate of change of this quantity with UV exposure time is constant within our experimental conditions then so too will be $\cos(\theta_E)$ such that

$$\frac{d\cos(\theta_E)}{dt} = a(\mathrm{RH}), \tag{2}$$

where a is dependent upon the relative humidity (RH) and describes the strength of the contact angle change. This leads to

$$a(\mathrm{RH}) = \frac{\cos(\theta_E) - \cos[\theta_E(t=0)]}{t}, \tag{3}$$

where $\theta_E(t=0)$ is the contact angle of unexposed lithium niobate and t is the exposure time. Figure 3 shows the variation of the parameter a(RH) with relative humidity for expo-

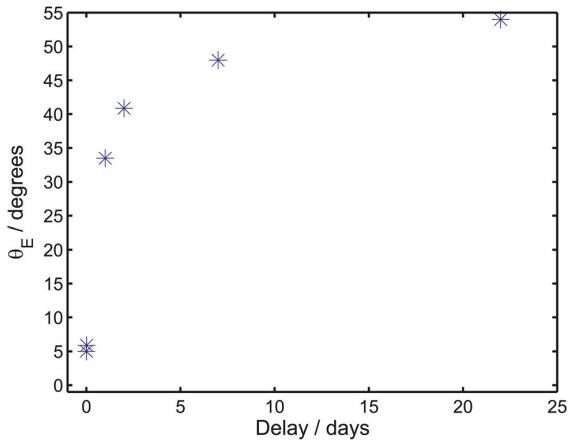

FIG. 4. Recovery of the contact angle with time after exposure of 45 mW for 60 s.

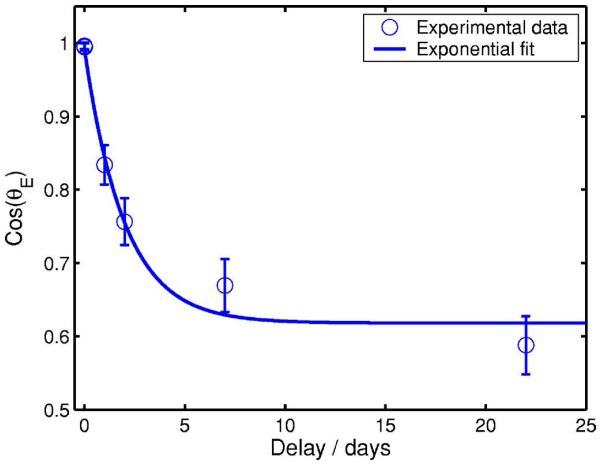

FIG. 5. Decay of the cosine of the contact angle with time after exposure of 45 mW for 60 s. Errors are calculated from an error in θ of ±2.8°.

sures on the positive z face. The error was calculated from the standard deviation (σ) of repeated readings of the contact angle on cleaned unexposed samples, yielding a value of $\sigma = 2.8°$. It can be seen in the figure that there is a linear trend; the change in surface energy being proportional to the number of water molecules present in the atmosphere. The continuation of the trend beyond the ambient humidity, when nitrogen purging was no longer required, indicates that the decrease in UV sensitivity with lowering humidity is indeed due to a reduction in atmospheric water and not due to the displacement of other species by the nitrogen. The value at 95% RH may be reduced due to condensation present upon the sample surface.

In order to study the recovery of the contact angle after exposure a number of samples were exposed at 45 mW for 60 s and then stored individually in polypropelene tubs in the dark. Figure 4 shows that the recovery to the initial contact angle takes around 20 days and that the recovery is not a linear function of time but proceeds at a continuously decreasing rate. If the surface energy change is due to the adsorption of water molecules on the crystal surface, as the humidity dependence suggests, and the thermal desorption of these molecules is a random process with constant probability, then the decay of the surface energy as measured by the cosine of the contact angle should be well modeled by an exponential decay. The decay of the cosine of the contact angle is shown in Fig. 5 with the best fit of the form $y = y_0 + a \exp(-t/\tau)$. The curve fits reasonably well and gives a value of $y_0 = 0.62$ corresponding to a final contact angle of 51.6° which is well within the range of measured unexposed contact angles. The other fit parameters are $a = 0.37$ and $\tau = 2$ days.

From the observed dependence on humidity of the contact angle change after UV exposure it is proposed that the enhanced hydrophilicity is due to dissociative adsorption of atmospheric water onto photoinduced defects creating (hydrophilic) surface hydroxyl groups. The band gap of LN is determined primarily by the properties of the NbO_6 octahedra since the upper level of the valence band is formed by the oxygen electron $2p$ states while the lower level of the conduction band is formed by the d orbitals of the niobium ion.[6] The primary reaction with photons of energy approximately that of the band gap will thus be to create an electron-hole pair bound to a niobium and oxygen ion, respectively. The dissociative adsorption will then proceed as follows:[5]

$$Nb^{5+} + O^{2-} + H_2O \rightarrow Nb^{4+}OH + O^{-}H. \quad (4)$$

The reaction above is similar to that proposed for the UV induced hydrophilicity of TiO_2 (Refs. 7 and 8) and ZnO (Ref. 9) by Watanabe and co-workers. Indeed the band structure of LN is similar to the band structure of TiO_2 since the main building blocks of each crystal are the BO_6 oxygen octahedra with the band gap of TiO_2 being formed by O $2p$ orbitals and Ti $3d$ orbitals and so one may expect the behavior to be similar for $h\nu > E_g$ exposure. This simple hypothesis is, however, shown to be false in Ref. 10, where it is shown that $SrTiO_3$ has no UV induced hydrophilic conversion despite being an ABO_3 oxygen-octahedral dielectric such as LN and having again the similar band structure to both LN and TiO_2. One difference between $SrTiO_3$ and LN, however, is the stacking of the BO_6 octahedra; $SrTiO_3$ is a perovskite-type dielectric that contains corner-sharing oxygen octahedra whereas the LN oxygen octahedra are face sharing. The octahedra in TiO_2 are also face sharing and so this may be another requirement for the hydrophilic conversion process. In Ref. 11, the origin of the UV induced hydrophilic conversion in TiO_2 proposed by Watanabe and coworkers is disputed and attributed solely to the photocatalytic decomposition of organic contaminants which exposes the inherently hydrophilic TiO_2 surface. Although LN also shows a high photocatalytic activity under UV irradiation,[12] our results concerning the humidity dependence of the contact angle change and the fact that no change occurs under vacuum do not support this hypothesis since we see no reason why the photocatalytic decomposition would not occur under these conditions also. In comparison to the hydrophilic conversion in TiO_2 we find that the contact angle change in LN proceeds at a greater rate at the intensities used in this investigation. In Ref. 9, the contact angle change from

the initial angle of 54° to an angle of 10° is seen to take around 5 min for a UV intensity of 50 mW cm^{-2} (λ =365 nm) whereas we see in Fig. 2 that for an exposure of around 20 mW cm^{-2} the change from 55° to 10° is made in just 30 s. In Ref. 11, the change from the initial contact angle (80°) to 15° is seen to take around 18 min for a UV exposure of 13.6 mW cm^{-2} (λ=254 nm) with an initial slope of 4° min^{-1}, whereas in Fig. 2 we see that for an intensity of around 10 mW cm^{-2} the change from 55° to 15° takes around 10 min with an initial slope ($t<200$ s) of around 13° min^{-1}.

Having investigated the behavior of the UV induced hydrophilicity in LN spatial structuring of the surface hydrophilicity, and thus wetting properties was also investigated for possible application in microfluidic devices and sensors.

III. HYDROPHILIC SPATIAL PATTERNING

A. Experimental details

Patterning on the micron scale was achieved by the use of transmission electron microscopy (TEM) hexagonal grids as absorption masks. The grids had hexagonal openings with a diameter of 40 μm (between parallel sides) at a periodicity of 60 μm. The grid was attached to the surface of the sample which was subsequently illuminated under ambient conditions with λ=244 nm light.

Patterning at the submicron scale was achieved either through exposure with an interference pattern of two overlapping beams from the λ=266 nm Nd:YVO_4 laser or by using a phase mask.

Exposures using phase masks were carried out with both the Nd:YVO_4 (λ=266 nm) pulsed source and the λ =244 nm cw source. The phase mask exposures were performed under the same conditions used in the sessile drop experiments. The phase mask used for the λ=244 nm exposures had a period of 1136 nm and the masks used for the λ=266 nm exposures had a period of 1076 nm. The beams used in both cases were divergent and as such the principle modulation of the light intensity pattern at the substrate is expected to be at the phase mask period and not at half of this value as would be expected for a collimated beam.

Visualization of the patterning was achieved through the preferential creation of dew on the exposed areas by cooling the sample in a stream of humid air and visualizing the dew pattern directly using a microscope. The existence of structures was also inferred from diffraction of a He–Ne laser beam from the grating formed by the dew.

B. Results and discussion

Figure 6 shows an optical microscope image of the condensation formed on the $+z$ face after an exposure through the TEM grid (λ=244 nm, 45 mW for 2 min). The sample was cooled by a thermoelectric heat pump to be close to the dew point temperature. The hexagonal lattice which corresponds to the TEM grid pattern can clearly be seen as water vapor from the air preferentially condenses onto the exposed areas. Areas of significant condensation appear darker in the figure while dry areas remain bright. For these exposure conditions the condensation mechanism is seen to be dropwise rather than filmwise.

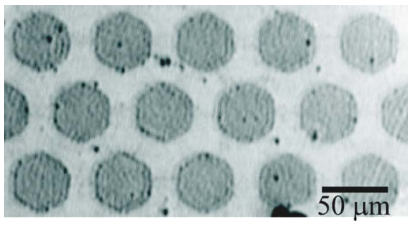

FIG. 6. Condensation pattern formed after cooling in a humid atmosphere. Sample exposed through a TEM grid.

Figure 7(a) shows an optical microscopy image of the preferential condensation of water vapor onto a lithium niobate surface exposed with interfering beams from the Nd:YVO_4 laser. The areas where water is condensing appear dark due to scattering while dry areas appear bright. In this instance it can be seen that the condensation mechanism appears to be filmwise as no discernible drop shapes are present in the condensing areas of the grating pattern. Whether the condensation proceeds as discreet drops or films depends upon the hydrophilicity change that has occurred upon the surface with filmwise condensation occurring for a completely hydrophilic surface (θ_E=0). Since the interfering beams have a Gaussian intensity profile, however, it is possible to view a wide range of illuminating conditions on the same illuminated spot. For example, the microscope image of Fig. 7(b) shows the condensation formed in an area corresponding to lower intensity where the surface does not wet completely and so drops of condensation form. The contrast of the image has been enhanced for clarity and the preferential formation of the drops along the lines of the illuminating interference pattern can be seen clearly.

Diffraction of a He–Ne laser beam (λ=633 nm) was also seen from the submicron structured surfaces due to spatially resolved condensation. The phase mask illuminations create interference patterns with periods of 1136 and 1076 nm for λ=244 nm and λ=266 nm illumination, respectively, giving feature sizes of the hydrophilic patterning of 500 nm. The probe laser beam was incident normally on the sample surface and the diffracted light was measured in transmission. The angles of the m=1 diffracted order in each case were found to be 35.4° for the 1076 nm period mask and 33.9° for the 1136 nm period mask which are within measurement error of the theoretical values of 36.03 ° and 33.9°, respectively.

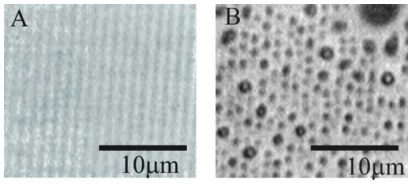

FIG. 7. Condensation patterns formed after an interference pattern exposure: (A) high fluence region with filmwise condensation and (B) low fluence region with dropwise condensation.

We envisage that spatial structuring of the wetting properties with this simple, one step method will enable the creation of microfluidic devices by creating fluid confinement with surface energy barriers, rather than physical barriers such as ridge structures or channels. Since no physical barriers will be present to scatter either optical or acoustic waves, device design can have the flexibility to take full advantage of the many nonlinear optical and acoustic properties for which lithium niobate has become an indispensible material and help create true biological and chemical analysis lab-on-a-chip devices.

IV. CONCLUSION

In conclusion, the hydrophilicity of LN has been seen to undergo a transition from mildly hydrophobic to superhydrophilic under the influence of UV laser light. The hydrophilicity has been shown to be spatially resolvable down to submicron length scale through structuring of the illuminating beam. We propose that the hydrophilic change occurs through the dissociative adsorption of water molecules to form hydrophilic surface hydroxyl groups and this hypothesis has been strengthened by the observation that no change to the hydrophilicity occurs in vacuum and that the hydrophilic change is strongly dependent upon humidity.

ACKNOWLEDGMENT

The authors would like to acknowledge Rutherford Appleton Laboratories Laser Loan Pool for supplying the frequency doubled argon ion laser.

[1]C. L. Sones, S. Mailis, V. Apostolopoulos, I. E. Barry, C. Gawith, P. G. R. Smith, and R. W. Eason, J. Micromech. Microeng. **12**, 53 (2002).
[2]Y. Tomita, M. Sugimoto, and K. Eda, Appl. Phys. Lett. **66**, 1484 (1995).
[3]C. J. Strobl, Z. von Guttenberg, and A. Wixforth, IEEE Trans. Ultrason. Ferroelectr. Freq. Control **51**, 1432 (2004).
[4]Image J: http://rsb.info.nih.gov/ij/; Drop shape analysis plug-in: http://bigwww.epfl.ch/demo/dropanalysis/
[5]M. Maeda, I. Suzuki, and K. Sakiyama, Jpn. J. Appl. Phys., Part 1 **31**, 3229 (1992).
[6]A. M. Prokhorov and Yu. S. Kuz'minov, *Physics And Chemsitry of Crystalline Lithium Niobate* (IOP, Bristol, 1990).
[7]R. Wang, K. Hashimoto, A. Fujishima, M. Chikuni, E. Kojima, A. Kitamura, M. Shimohigoshi, and T. Watanabe, Nature (London) **388**, 431 (1997).
[8]R. Wang, K. Hashimoto, A. Fujishima, M. Chikuni, E. Kojima, A. Kitamura, M. Shimohigoshi, and T. Watanabe, Adv. Mater. (Weinheim, Ger.) **10**, 135 (1998).
[9]R. Sun, A. Nakajima, A. Fujishima, T. Watanabe, and K. Hashimoto, J. Phys. Chem. B **105**, 1984 (2001).
[10]M. Miyauchi, A. Nakajima, A. Fujishima, K. Hashimoto, and T. Watanabe, Chem. Mater. **12**, 3 (2000).
[11]A. Kanta, R. Sedev, and J. Ralston, Langmuir **21**, 2400 (2005).
[12]Z. li, T. Yu, and Z. Zou, Appl. Phys. Lett. **88**, 071917 (2006).

F.1.3 Direct-Writing of Inverted Domains in Lithium Niobate Using a Continuous Wave Ultraviolet Laser

A. C. Muir, C. L. Sones, S. Mailis, R. W. Eason, T. Jungk, A. Hoffmann, and E. Soergel. Direct-writing of inverted domains in lithium niobate using a continuous wave ultraviolet laser. *Optics Express*, 16, 2336 - 2350 (2008)

This paper is a result of the work carried out in chapter 3.

Direct-writing of inverted domains in lithium niobate using a continuous wave ultra violet laser

A. C. Muir*[1], C. L. Sones[1], S. Mailis[1], R. W. Eason[1], T. Jungk[2], Á. Hoffmann[2] and E. Soergel[2]

[1] *Optoelectronics Research Centre, University of Southampton, Hants, S017 1BJ, U.K.*

[2] *Institute of Physics, University of Bonn, Wegelerstrasse 8, D-53115, Bonn, Germany*

Corresponding Author: acm@orc.soton.ac.uk

Abstract: The inversion of ferroelectric domains in lithium niobate by a scanning focused ultra-violet laser beam (λ = 244nm) is demonstrated. The resulting domain patterns are interrogated using piezoresponse force microscopy and by chemical etching in hydrofluoric acid. Direct ultra-violet laser poling was observed in un-doped congruent, iron doped congruent and titanium in-diffused congruent lithium niobate single crystals. A model is proposed to explain the mechanism of domain inversion.

OCIS codes: (160.3730) Lithium niobate; (160.2260) Ferroelectrics; (160.4670) Optical materials; (140.3610) Lasers, ultraviolet

References and links

1. R. S. Weis and T. K. Gaylord, "*Lithium Niobate: Summary of Physical Properties and Crystal Structure,*" Appl. Phys. A **37**, 191 - 203 (1985).
2. A. C. Busacca, C. L. Sones, R. W. Eason, and S. Mailis, "*First-order quasi-phase-matched blue light generation in surface-poled Ti : indiffused lithium niobate waveguides,*" Appl. Phys. Lett. **84**, 4430 - 4432 (2004).
3. F. S. Chen and W. W. Benson, "*A lithium niobate light modulator for fiber optical communications,*" Proceedings of the IEEE **62**(1), 133 - 134 (1974).
4. C. L. Sones, S. Mailis, V. Apostolopoulos, I. E. Barry, C. Gawith, P. G. R. Smith, and R. W. Eason, "*Fabrication of piezoelectric micro-cantilevers in domain-engineered $LiNbO_3$ single crystals,*" J. Micromech. Microeng. **12**(1), 53 - 57 (2002).
URL http://dx.doi.org/10.1088/0960-1317/12/1/308.
5. C. L. Sones, M. C. Wengler, C. E. Valdivia, S. Mailis, R. W. Eason, K. Buse, "*Light-induced order-of-magnitude decrease in the electric field for domain nucleation in MgO-doped lithium niobate crystals,*" Appl. Phys. Lett. **86**, 212901 (2005).
6. C. E. Valdivia, C. L. Sones, S. Mailis, J. D. Mills, and R. W. Eason, "*Ultrashort-pulse optically-assisted domain engineering in lithium niobate,*" Ferroelectrics **340**, 75 - 82 (2006).
URL http://dx.doi.org/10.1080/150190600888983.
7. C. L. Sones, C. E. Valdivia, J. G. Scott, S. Mailis, R. W. Eason, D. A. Scrymgeour, V. Gopalan, T. Jungk, and E. Soergel, "*Ultraviolet laser-induced sub-micron periodic domain formation in congruent undoped lithium niobate crystals,*" Appl. Phys. B **80**(3), 341 - 344 (2005).
URL http://dx.doi.org/10.1007/s00340-005-1731-7.
8. C. E. Valdivia, C. L. Sones, J. G. Scott, S. Mailis, R. W. Eason, D. A. Scrymgeour, V. Gopalan, T. Jungk, E. Soergel, and I. Clark, "*Nanoscale surface domain formation on the +z face of lithium niobate by pulsed ultraviolet laser illumination,*" Appl. Phys. Lett. **86**(2), 022906 (2005).
URL http://dx.doi.org/10.1063/1.1849414.
9. I. T. Wellington, C. E. Valdivia, T. J. Sono, C. L. Sones, S. Mailis, and R. W. Eason, "*Ordered nano-scale domains in lithium niobate single crystals via phase-mask assisted all-optical poling,*" Appl. Surf. Sci. **253**(9), 4215 - 4219 (2007).
URL http://dx.doi.org/10.1016/j.apsusc.2006.09.018.

#90331 - $15.00 USD Received 30 Nov 2007; revised 26 Jan 2008; accepted 27 Jan 2008; published 4 Feb 2008

10. T. Jungk, A. Hoffmann, and E. Soergel, "*Quantitative analysis of ferroelectric domain imaging with piezoresponse force microscopy,*" Appl. Phys. Lett. **89**(16), 163,507 - (2006).
URL http://dx.doi.org/10.1063/1.2362984.
11. E. Soergel, "*Visualization of ferroelectric domains in bulk single crystals,*" Appl. Phys. B **81**(6), 729 - 752 (2005).
URL http://dx.doi.org/10.1007/s00340-005-1989-9.
12. C. L. Sones, S. Mailis, W. S. Brocklesby, R. W. Eason, and J. R. Owen, "*Differential etch rates in z-cut $LiNbO_3$ for variable HF/HNO_3 concentrations,*" J. Mater. Chem **12**, 295 - 298 (2002).
13. A. C. Muir, G. J. Daniell, C. P. Please, I. T. Wellington, S. Mailis, and R. W. Eason, "*Modelling the formation of optical waveguides produced in $LiNbO_3$ by laser induced thermal diffusion of lithium ions,*" Appl. Phys. A**83**(3), 389 - 396 (2006).
URL http://dx.doi.org/10.1007/s00339-006-3493-4.
14. T. J. Sono, J. G. Scott, C. L. Sones, C. E. Valdivia, S. Mailis, R. W. Eason, J. G. Frey, and L. Danos, "*Reflection second harmonic generation on a z-cut congruent lithium niobate crystal,*" Phys. Rev. B **74**(20), 205424 (2006).
URL http://dx.doi.org/10.1103/PhysRevB.74.205424.
15. V. Y. Shur, "*Kinetics of ferroelectric domains: Application of general approach to $LiNbO_3$ and $LiTaO_3$,*" J. Mater. Sci. **41**(1), 199 - 210 (2006).
URL http://dx.doi.org/10.1007/s10853-005-6065-7.
16. V. Y. Shur, D. K. Kuznetsov, A. I. Lobov, E. V. Nikolaeva, M. A. Dolbilov, A. N. Orlov, and V. V. Osipov, "*Formation of self-similar surface nano-domain structures in lithium niobate under highly nonequilibrium conditions,*" Ferroelectrics **341**, 85 - 93 (2006).
URL http://dx.doi.org/10.1080/00150190600897075.
17. M. E. Lines and A. M. Glass, *Principles and Application of Ferroelectrics and Related Materials* (Clarenon Press, 1977).
18. A. M. Mamedov, "*Optical properties (VUV region) of $LiNbO_3$,*" Opt. Spectrosc. **56**(6), 645 - 9 (1984).
19. K. Buse, "*Light-induced charge transport processes in photorefractive crystals. I. Models and experimental methods,*" Appl. Phys. B **64**(3), 273 - 291 (1997).
URL http://dx.doi.org/10.1007/s003400050175.
20. E. M. Bourim, C. W. Moon, S. W. Lee, and I. K. Yoo, "*Investigation of pyroelectric electron emission from monodomain lithium niobate single crystals,*" Physica B **383**(2), 171 - 182 (2006).
URL http://dx.doi.org/10.1016/j.physb.2006.02.034.
21. G. I. Rozenman, "*Photoinduced exoemission from lithium niobate,*" Sov. Phys. Solid State **30**(8), 1340 - 1342 (1988).
22. S. Kim, V. Gopalan, and A. Gruverman, "*Coercive fields in ferroelectrics: A case study in lithium niobate and lithium tantalate,*" Appl. Phys. Lett. **80**(15), 2740 - 2742 (2002).
URL http://dx.doi.org/10.1063/1.1470247.
23. A. N. Morozovska, "*Theoretical description of coercive field decrease in ferroelectric-semiconductors with charged defects,*" Ferroelectrics **317**, 37 - 42 (2005).
24. N. Uchida, "*Optical waveguide loaded with high refractive-index strip film,*" Appl. Opt. **15**, 179 - 182 (1976).

1. Introduction

Lithium niobate (LN) is a ubiquitous material within the optoelectronics industry due to its large electro-optic, acousto-optic and non linear optical properties [1]. It is a ferroelectric crystal with a spontaneous polarisation caused by the displacement of Li^+ and Nb^{5+} cations along the crystallographic c axis thus giving rise to 180° anti-parallel domains that can be switched by the application of a suitable external electric field. It is the orientation of these domains that determines the crystal response to many stimuli, for example the strain or refractive index change resulting from an applied electric field, and so precision scale engineering of domains has become a field of extensive research for application in a large number of areas ranging from harmonic generation through quasi-phase-matched parametric processes [2], signal modulation in telecomunications [3] to the creation of single-crystal microstructures by utilising differential etching [4]. The fabrication of well-defined domain patterns for this range of applications requires a robust method for domain inversion which can achieve the desired spatial ferroelectric domain distributions even on submicron scales and preferably in a flexible, repeatable and easy to apply manner.

Conventional domain engineering is achieved through the application of an external electric field greater than the coercive field of the crystal. The electric field strength is spatially mod-

ulated by applying a structured layer of photo-resist or metal across one surface to produce local screening. The electric field contrast provided by the photoresist layer is, however, relatively poor which limits the width of domain structures to greater than a few microns. Also the conventional method requires multiple fabrication steps and expensive cleanroom facilities.

Recent advances in domain engineering of LN have shown that laser light can be used to influence the domain reversal process and two methods have been identified; light assisted poling (LAP) [5, 6] and all optical poling (AOP) [7, 8, 9]. The LAP approach still uses an external electric field to invert the domains but localised domain reversal is achieved since the coercive field is lowered in the illuminated regions. The AOP approach creates domain inversion without an external electric field by illuminating the crystal with high energy laser pulses. These methods show much promise for domain engineering since the laser light patterns can be structured down to diffraction limited spot sizes and no photolithography is required.

In this paper we present AOP using focused continuous wave (c.w.) ultra-violet (UV) laser light and show that all-optical domain inversion is achievable under exposure conditions entirely different to those used in pulsed AOP and without the need for high peak powers of a pulsed source previously assumed essential. The domain structures created are analysed using piezoresponse force microscopy (PFM) and by chemical etching followed by both surface profiling and scanning electron microscopy.

In the following section the experimental methods used to create the domain patterns and those used to subsequently analyse them are described. In section 3 the experimental results are presented and analysed and a model of the formation mechanism is proposed whereby a poling field is produced by the drift of photo-excited charge carriers in the induced pyroelectric field.

2. Experimental method

A UV laser beam of wavelength 244 nm is provided by a frequency-doubled argon ion laser. The beam is expanded, spatially filtered and collimated before being focused onto a LN sample by a 40 mm focal length lens. The focused spot has a calculated radius of approximately 1.5 μm, however, from the size of damage features seen in a photo-resist covered slide we believe the actual spot radius to be approximately 2.5 μm. The LN samples are mounted upon a three axis computer-controlled stage system (Newport MM2000). The exposure was also controlled by a computer-controlled shutter such that the beam was present only when the stage velocity was constant to ensure uniform exposure along the written lines. The stages were translated to write lines along both the x and y axes at speeds between 50 to 300 μm s^{-1}. Exposures of the above conditions were made at incident powers between 20 and 30 mW, which corresponds to an intensity range of 100 - 150 kW cm^{-2}. At powers below $\sim$ 20 mW no significant effect is seen and at powers higher than $\sim$ 30 mW, although the effect is seen, it is accompanied by excessive surface damage associated with melting of the surface.The samples used were all 500 μm thick, z-cut, optical quality single-crystal wafers. Exposures were carried out on both the positive and negative z faces of iron-doped (0.1 mol % and 0.01 mol %) and un-doped crystals and in duplicate such that identical samples could be analysed by PFM and by etching. Exposures were carried out on the $-z$ face only of titanium in-diffused crystals.

For PFM analysis an atomic force microscope with a conducting tip was used to measure the piezoresponse of the exposed surface by applying an electric field to the surface with the tip and measuring the induced strain by the tip deflection. An overview of the principles of PFM can be found in [10, 11].

Chemical etching in hydrofluoric (HF) acid is a well-established method of domain visualisation in LN due to the fact that the negative z face etches readily whilst the positive z face does not etch at all [12]. Thus if domains are inverted during UV laser irradiation they will present as either a raised ridge in the case of negative z face exposures or as an etched trench in

positive z face exposures. A number of un-doped samples were etched at room temperature in HF acid of 48% aqueous solution for consecutive intervals of 5 minutes, between which they were imaged with an optical microscope and profiled using a KLA-Tencor stylus profilometer. After a cumulative etching time of 1 hr these samples were imaged with a scanning electron microscope (SEM). Other un-doped samples, and both the titanium in-diffused and iron doped samples, were etched for around 15 minutes only before being imaged with an SEM.

Further exposures were performed on a periodically poled LN (PPLN) sample which was analysed by PFM as the PPLN structure gave a benchmark against which to compare any UV laser induced PFM signal.

3. Results and discussion

Figure 1 shows SEM images after etching of exposed areas on the $-z$ face of un-doped congruent LN with scan speeds of 50 and 200 μm s^{-1}. It is clear to see that the behaviour is strongly dependent upon exposure conditions with an abrupt qualitative change occurring at the highest power, splitting the behaviour into two regimes. These two regimes will be referred to as the high power regime and the low power regime, with the understanding that the terms are relative to the somewhat narrow power window of the main investigation. As was mentioned earlier, the effect is seen to occur at higher powers above 30 mW, but is accompanied by undesirable melting and thermal damage, and is not seen at powers considerably below 20 mW. The width of the power window is believed to be due to the strong temperature dependence of the effect and the steep rate of change of temperature with power for these beam parameters as was seen in [13]. In the high power regime the surface is seen to be smooth and resists etching in the crystallographic z direction. The surface contains cracks, due to thermal damage, and is decorated with thin lines that extend along the x axes of the crystal. The features in this regime will be discussed in detail later.

In the low power regime it is seen that etching is also resisted in the exposed regions, resulting in a raised ridge structure. The upper surface of the ridges is seen to consist of densely packed discrete features that have dimensions of around 50-100 nm, an example of this is shown in high magnification in Fig. 2. These features are visible as they resist etching in the vertical direction whilst the $-z$ face they are embedded within does not. Thus the surrounding material etches and the topography of the upper surface of the ridge is revealed.

The change in height with cumulative etching time of the ridges, with respect to the unexposed background $-z$ face, is shown in Fig. 3. The slope of the curve gives the differential etch rate between exposed and unexposed regions. In the high power (solid) curve it can be seen that the gradient is constant and has a value which agrees with the etch rate of virgin LN [12]. As the power decreases it is seen that the etch resistance lasts for a time dependent upon the power and scan speed, but this time decreases with with decreasing power or increasing velocity, until features etch at the same rate as unexposed regions. This may be understood by the mechanism with which the nano-topography of the upper surface of the ridges is revealed: As the surrounding material is etched the sides of these nano-features are revealed to the etchant and they begin to side-etch. The ease at which etchant can enter between the features and attack the sides will, of course, depend upon the packing density. When the side etched distance reaches the radius of the features they will begin to reduce in height and the differential etch rate between the $-z$ crystal face and the exposed region will reduce. At the point at which the the entire depth of these nano-features is revealed side-etching will remove them completely and the differential etch rate will go to zero as the underlying material is revealed. At this point the height of the ridge is preserved.

The widths of the upper surface of the ridges after 15 mins etching is plotted in Fig. 4 as a function of scan speed for powers of 29, 27, 26 and 25 mW. It can be seen that the width is

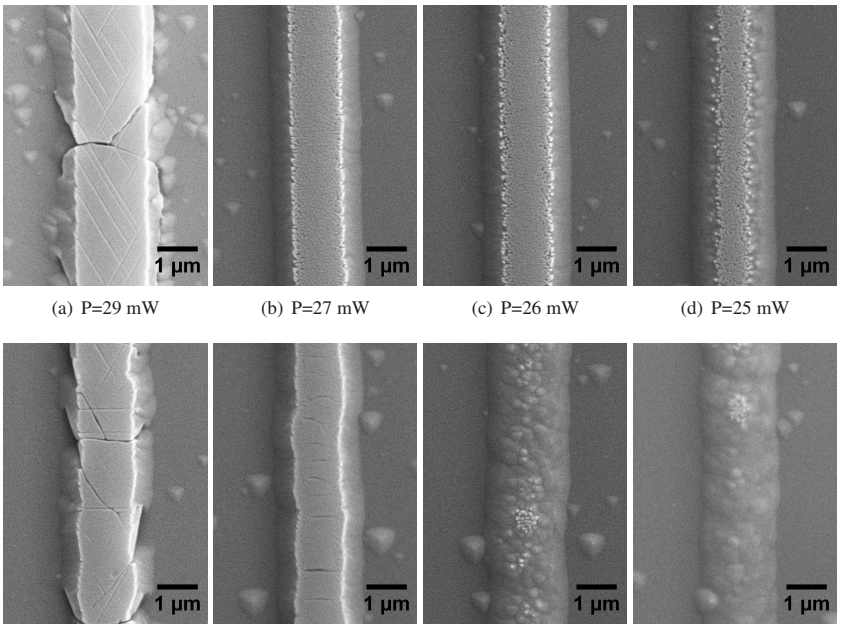

(a) P=29 mW (b) P=27 mW (c) P=26 mW (d) P=25 mW

(e) P=29 mW (f) P=27 mW (g) P=26 mW (h) P=25 mW

Fig. 1. Variation with power of the UV laser-induced layer on the $-z$ face. Lines scanned along the crystallographic y direction. SEM images of structures revealed by HF etching for 15 minutes. (a-d) Scan speed 50 μm s^{-1}. (e-h) Scan speed 200 μm s^{-1}.

strongly dependent upon incident power and only weakly dependent upon the scan speed with the width increasing with increasing power and decreasing with increasing scan speed. Whilst, for a particular scan speed, it is seen that width of the upper layer decreases with decreasing power, the overall width of the ridge left after etching is essentially constant (not shown in Fig. 4). This indicates that this entire width was initially covered in a capping layer of the discrete features described above, but that either the density and/or depth of the features decreased with distance from the center of the beam path such that the outer features were removed by the time the measurements were taken. For higher power exposures the depth and density of features at the outer edges of the beam will be greater and hence more will remain and the width of the upper surface will be greater. Figure 4 then shows that the density and depth of the capping layer vary with power.

In the low power regime, then, an upper layer of discrete features is seen to form that resist etching in the $+z$ direction but do etch in the perpendicular direction. The depth and density of the features is seen to depend upon the position within the exposed region and upon the incident power, with only a weak dependence upon the scan speed.

In the high power regime exposures on the $-z$ face [Fig. 1(a)] are seen to result in an etch resistant layer of quite different topography as compared to low power exposures. The surface of the layer is seen to be very flat, smooth, and rigid as compared to the low power regime where it consisted of discrete features. The edges of the layer are also seen to be sharp and well-defined. Some cracks are present due to thermal damage and these generally span the surface without particular alignment to crystal axes. New features are also revealed by etching

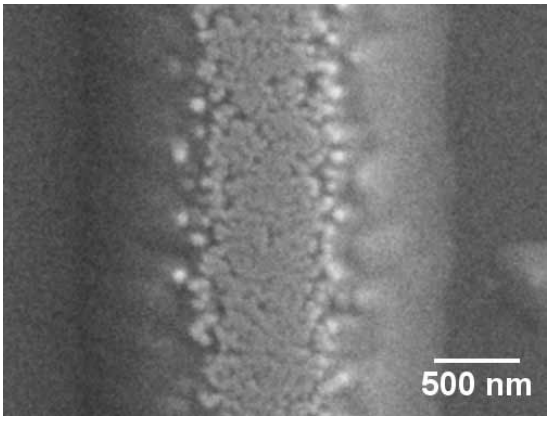

Fig. 2. SEM image of the discrete features seen on the upper surface of the $-z$ face in the low power regime.

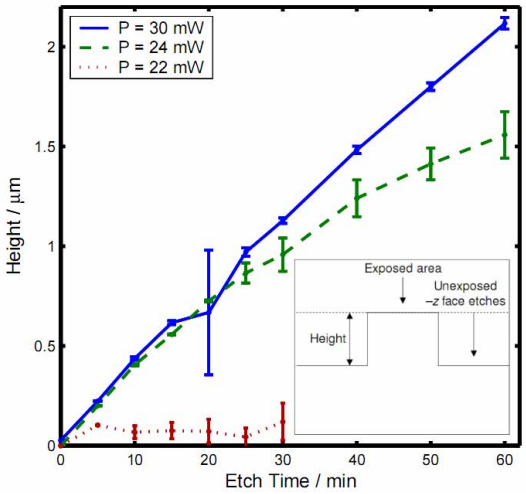

Fig. 3. Change in feature height above $-z$ face with etch time for different power exposures at a scan speed of 100 μm s^{-1}. Flat gradient shows no etch resistance. Error bars obtained as standard deviations of repeated measurements. Insert shows how the height is defined.

that align to the x axes of the crystal and these will be further examined later. Figure 5 shows an SEM image of a high-power exposure after 1 hr etching where the affected layer can be seen to extend to a depth of around 1 μm, whilst the total height of the ridge is just over 2 μm. To investigate better the topography of the features the sample was tilted with respect to the electron beam, about the long axis of the line. The layer is seen to resist etching in the depth direction completely up to etching times of 1 hr as can be seen in Fig. 3, however Fig. 5 shows that the upper layer does etch in the vertical direction from *underneath* as can be seen from the voids where etchant has been permitted to enter through the thermal cracks. Furthermore it can be seen from the symmetric shape of the voids that the etch rate of the layer from underneath,

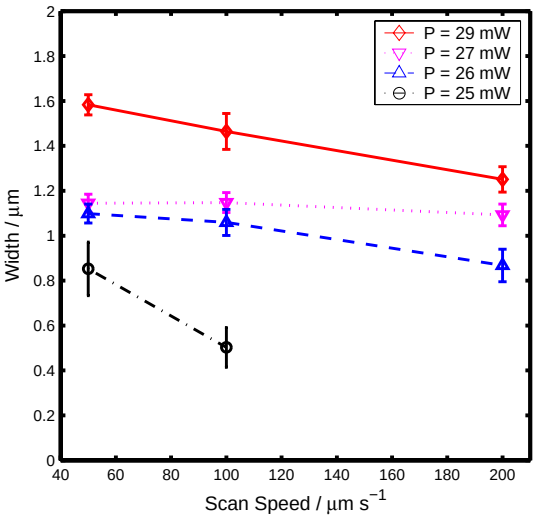

Fig. 4. Variation in the width of the upper surface of the etched ridges with power and scan speed. Error bars obtained as standard deviations of repeated measurements.

toward the surface, is very similar to that of the unaffected crystal beneath.

It was stated in section 2 that the etch characteristics of the $+z$ and $-z$ faces are different [12] and so this fact can be used to determine the ferroelectric polarity. LN also shows anisotropy in the etch characteristics of the y faces [14] and so this also can be used to determine the ferroelectric polarity. Although both y faces etch in HF the $-y$ face etches at a greater rate allowing determination of the direction of the y axes. The etch behaviour of the layer in the y direction of the crystal when the beam is scanned along the perpendicular x axis can be seen in Fig. 6, which shows a high-power exposure after 1 hr etching. The image is taken with no sample tilt. It can clearly be seen that at the top of the figure the layer terminates abruptly whilst at the bottom of the figure the layer terminates with a slope. This indicates that, at the same time as the surrounding crystal has etched downwards in the crystallographic z direction, the layer has etched inwards but only on the lower edge. This asymmetry is not seen when the beam is scanned along the crystallographic y direction as can be seen in Fig. 1(a).

The distinction between a high and low power regime was seen to be made at the same incident powers on the $+z$ face of the crystal. In the low power regime $+z$ face exposures are seen to produce trenches after etching as can be seen in Fig. 7(b). The depths of these trenches, as measured by stylus profiling, was seen to be proportional to the scan speed with depth increasing as the scan speed decreases. The measured depths of the trenches reached some tens of nanometers however the true depth may be greater due to limitations of the profilometer tip to probe such narrow structures. The behaviour of the $+z$ face in the high power regime is different. At high powers etching is not seen to occur over the entire exposed area. This can be seen in Fig. 7(a) that shows an exposure after 1 hr etching. Large cracks [seen horizontally in Fig. 7(a)] caused by thermal effects can be seen (also visible before etching) however new features have been revealed that are aligned with the x crystallographic direction (vertically in the figure).

No difference was seen in the etch behaviour of iron doped samples as compared to un-doped samples since the same corresponding surface topography was present in both the high and low

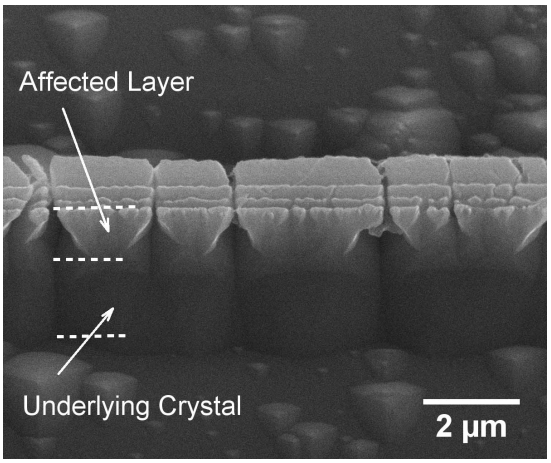

Fig. 5. SEM image of typical features on the $-z$ face after high power UV exposure revealed after 1 hr etching. The x axis of the crystal runs horizontally in the figure. Sample tilted at 30° to the electron beam. The areas indicated by annotations form the upstanding ridge structure and are both in relief of the crystal surface.

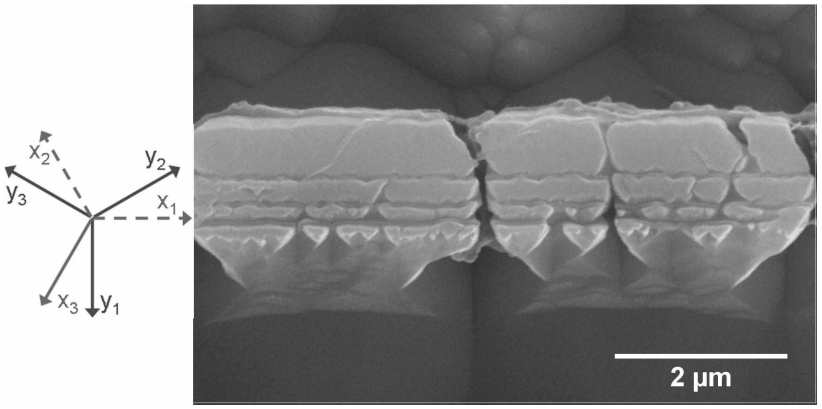

Fig. 6. SEM image of a high-power exposure after 1 hr etching viewed from directly above. The polarity of the affected layer is seen through the differential y etching indicating that the affected layer is of the opposite polarity to the surrounding crystal. Insert shows axes of the underlying crystal.

power regimes. This suggests that defects with energy levels within the band-gap play little role and that the effect is dominated by band-band transitions.

Figure 8 shows an SEM image of a $-z$ face exposure, in the high power regime, on a titanium in-diffused sample after etching in HF acid. It can be seen that the etch behaviour is again similar to that of the exposures on un-doped LN, with a raised ridge being formed. The cracks due to thermal damage can again be seen, however, the features that align to the x axes, that were seen earlier on iron-doped and un-doped LN, are seen with a much lower density. The quality of the edges is reduced due to remnant titanium on the surface.

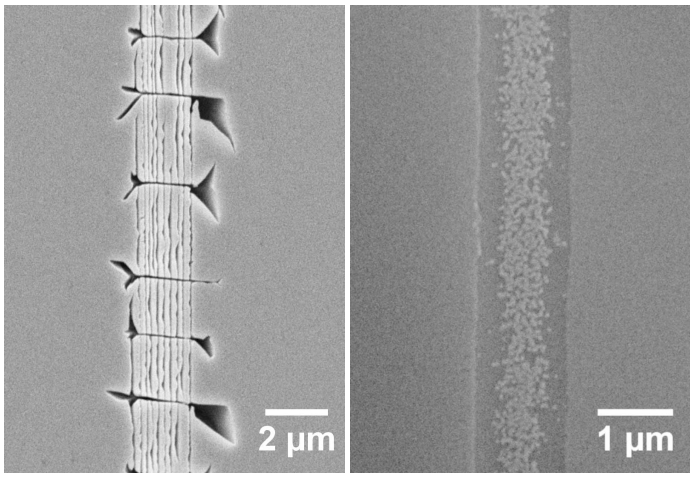

(a) High power (b) Low power

Fig. 7. Typical behaviour of $+z$ exposures in the high and low power regimes. Beams scanned along the crystallographic *x* direction.

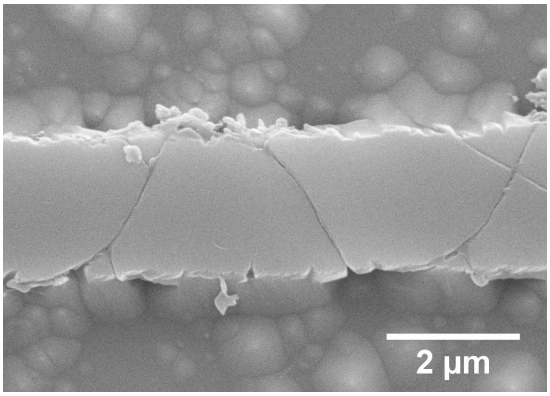

Fig. 8. Typical behaviour of $-z$ exposures in the high power regime on titanium in-diffused LN. Beam scanned along the crystallographic *y* direction.

The etch results of the $-z$ face exposures indicate that the layer formed on the $-z$ face may be crystalline LN with an inverted ferroelectric domain polarity for the following reasons. A domain inverted layer on the $-z$ face would present a $+z$ face to the etchant and so would resist etching in the inward surface normal direction. If the etchant was permitted within or below this inverted layer it would see in the outward surface normal direction a $-z$ face and would so etch accordingly, which is what we see. The etchant which is present at the head-to-head domain boundary between a positive surface domain and an underlying negative bulk domain would be presented with two negative z faces and so would etch in the directions both away from and toward the surface, at the same time as etching sideways, and so a void would be formed. The void would be diamond-shaped in cross-section with opposite vertices on the line

parallel to the surface indicating the depth of the surface domain. This is seen in Fig. 5 and gives the approximate depth of the surface domains as $\sim 1\mu$m. Also, once a domain inverted layer is revealed by the etching of the surrounding crystal, thus forming a ridge structure, it would present either y or x faces to the etchant depending upon the scanning direction and hence geometry of the newly formed ridge. In the case that x faces are presented there would be no asymmetry of the etching since the x axis of LN does not etch differentially. This is the behaviour seen in Fig. 1(a). In the case that the y faces of the crystal are presented to the etchant however an asymmetry is expected since the y axis etches differentially, with the crystal etching at a far greater rate in the $-y$ direction than in the $+y$ direction [14]. The direction of the y axis is of course coupled to the direction of the z axis such that when the z axis is inverted the y axis inverts also [14]. This asymmetry of the etching in the y direction was seen in Fig. 6 which, through the argument above, identifies the y axis of the ridge structure as pointing upward in the figure. The direction of the y axis of the underlying and unexposed LN points downward in the figure. The asymmetries of the etch behaviour thus show that the exposed region is still crystalline and that the direction of the z and y axes is opposite to that of the virgin crystal.

In the case of illuminations on the $+z$ face the etch results suggest that, at low powers, a layer of crystal with a depth of a few tens of nanometers may reverse its polarization. When this occurs a $-z$ face is presented to the etchant which then etches readily, leaving a trench. The etching would stop at the bottom of the domain inverted layer when again a $+z$ face was present. At high powers the entire area is not seen to etch which implies that domain inversion has not taken place across the full beam width.

In the high power regime, on both the $+z$ and $-z$ face, long, narrow, features are formed within the exposed area that etch in contrast to their surrounding material. These have widths of around 50-100 nm and are aligned strictly along the crystal x axes. Such aligned features should not exist in an amorphous material and so further confirms the crystalline nature of the surface. Due to the symmetry of the crystal structure, LN has three pairs of orthogonal x and y axes. The particular x axis that the features dominantly align to depends on the scan direction of the beam. When the beam scans along the y_1 axis, features are seen to appear along the x_2 and x_3 axes but are not seen along x_1, as shown in figures 9(a),9(c) for both the positive and negative z faces. When the beam is translated along the x_1 direction, the features are seen to align to the x_1 axis only as seen in figures 9(b),9(d). We believe that these features are formed by the nucleation of a nanodomain followed by one dimensional growth along the x axis. It is interesting to note that these features span the cracks formed by thermal damage indicating that they were formed before the crystal cracked since any effect within the crystal would not traverse a void. The choice of x axis along which this domain structure will grow will depend upon the stress fields present, due to the electro-mechanical coupling, and upon the screening charge distributions [15]. On the $+z$ face this may represent the only poled region in the exposed area. On the $-z$ face the lines appear as on the the $+z$ face strengthening the hypothesis that the polarity of the $-z$ exposed regions has inverted and that the line features are caused by a fast one dimensional domain growth on the $+z$ face. Self organised domain growth along crystal axes has been seen in previous AOP studies where the growth was along the y axes and had much larger feature size and a larger distance of closest approach of around 1.5 μm [8, 16]. Structures similar to those seen in this paper have been seen during spontaneous backswitching during electric field poling where the alignment has been along either the x or y axes with a feature size of tens of nm [15].

Piezoresponse force microscopy utilises the converse piezoelectric effect to determine the polarity of ferroelectric domains [10]. An electric field is applied to the sample through a conducting atomic force microscopy tip which limits the depth resolution of the technique since the field within the crystal extends to approximately three times the radius of curvature of the

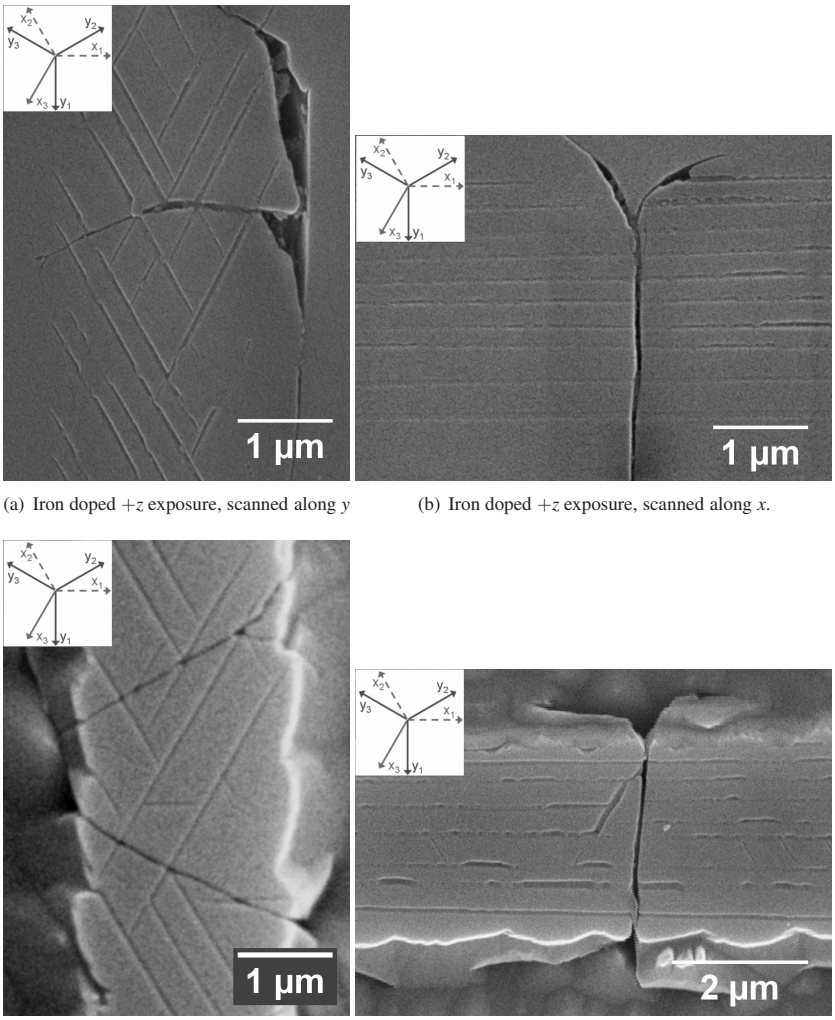

(a) Iron doped $+z$ exposure, scanned along y

(b) Iron doped $+z$ exposure, scanned along x.

(c) Un-doped $-z$ exposure, scanned along y.

(d) Iron doped $-z$ exposure, scanned along x.

Fig. 9. SEM images showing alignment to the x axes of features exposed by etching on the positive and negative z faces after UV exposure in the high power regime.

tip. In our case this corresponds to a depth of around 100 nm. Any domain features with depth greater than this will be seen as bulk domains and give the full piezoresponse amplitude contrast of plus or minus one for positive or negative domains respectively. Domain features with depth less than 100 nm, however, will give the integrated piezoresponse of the sampling volume. This makes identification of shallow domains difficult since both shallow inverted domains and regions of non-piezoelectric material can give the same net PFM response. Figure 10 shows the topography (a) and PFM amplitude (b) of a scanned exposure over a PPLN sample. The PPLN domains run horizontally over the image whilst the UV scanned lines run vertically. The full

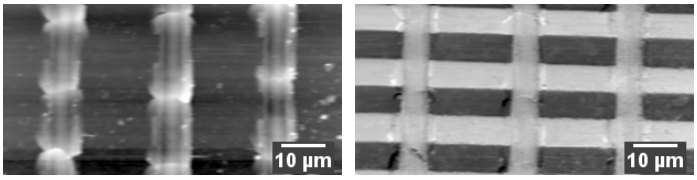

(a) Topography (b) PFM Image

Fig. 10. Topography and PFM amplitude of a scanned UV exposure over PPLN. PPLN domains run horizontally in the images and UV written lines run vertically. In the PFM image $-z$ domains appear black and $+z$ domains appear white. UV scans are seen to invert $-z$ areas of PPLN.

PFM contrast is clearly visible due to the PPLN structure with black areas indicating a $-z$ face and white areas indicating a $+z$ face. It can be seen that the UV exposed areas show the same contrast as the $+z$ areas of the PPLN. This indicates that in the areas of the PPLN that had a $-z$ face, the polarity of the crystal has inverted to a depth greater than the sampling depth of PFM. Where the beam has passed over $+z$ areas of the PPLN no change in the PFM contrast is seen implying that no domain reversal has occurred. This agrees well with the results seen with chemical etching in which a positive domain was seen to be formed on the $-z$ face, and so resisted etching, whilst no large negative domains were seen to form on the $+z$ face since the exposed area did not etch. The PFM results thus corroborate the evidence, given previously by the etch behaviour of the exposed crystals, that inverted domains are formed, in the high power regime, on the $-z$ face but not on the $+z$ face. The minimum depth of the domain formed is given by PFM as $\sim$ 100 nm and a greater estimate of the depth, which may be taken as an upper limit, has been given earlier as $\sim 1\mu$m. Although methods exist to measure the depth of domains, such as side-polishing and etching [15], we do not believe that these are suitable in this instance due to the presumed shallow depth of the structures and the damage of the edge which is caused by mechanical polishing.

PFM has also been used to examine the stability of the domains formed by measuring the piezoresponse of an exposure in the high power regime before and after heating at the crystal 200 °C for four hours. No significant change in the response was seen.

From the results presented above we believe that inverted ferroelectric domains are being formed during UV illumination. The precise mechanism for domain inversion has yet to be discovered however we can justify the UV laser induced ferroelectric domain inversion by considering an electric field formed by the separation of photo excited charges under the following reasoning.

LN is ferroelectric and so possesses a spontaneous electric polarization P_s which has associated with it an electric depolarisation field E_{dep}. At room temperature the unexposed crystal is in equilibrium and E_{dep} is screened by free charges and defects within the crystal [17] which create a compensation field, E_{scr}, with equal magnitude to E_{dep} and aligned parallel to P_s. This is shown schematically in Fig. 11(a). When the UV beam enters the crystal the energy is absorbed within the upper 50 nm ($1/e^2$ intensity absorption depth $\approx$ 30 nm) [18] and is mostly converted into heat, creating temperature distributions with spatial extents of the order of the beam width [13]. When the crystal is heated, P_s and, consequently, E_{dep} are decreased as the Li and Nb cations move toward the para-electric positions. E_{scr} is very slow to react [17] to changes in P_s and so a net field is left as E_{scr} now overcompensates E_{dep}, as shown in Fig. 11(b). At the same time, since the photon energy of the UV beam (5.1 eV) is greater than the LN band gap ($\approx$ 4 eV), photo-excitation occurs creating electron-hole pairs. Most will re-

combine and release their energy as heat. However, a fraction will survive and be free to travel within the crystal under the influence of both electric fields and concentration gradients. These photo-excited charges will see the net electric field, E_{net}, and will drift under its influence with holes moving toward the $+z$ face and electrons moving toward the $-z$ face, as shown in Fig. 11(c). It is worth noting here that charges excited between intrinsic energy bands in LN are not accelerated in the same way as those from defect levels and do not contribute to the bulk photovoltaic currents [19] as do impurity defects with energies within the band gap. The separated photo-excited charges will thus create a photo-induced space-charge field, E_{sc-ph}, anti-parallel to E_{scr}. If drift were the only driving force a maximum steady state photo-induced field would be created that was equal to the vector sum of the E_{dep} and E_{scr} however charges also move by diffusion under the influence of concentration, and possibly thermal [13], gradients which may increase the magnitude of the photo-induced field. The field may also be increased by thermal [20] or photo-induced emission [21] of electrons from the surface. As the beam moves on, the crystal cools and P_s and, consequently, E_{dep} again increase. E_{dep} and E_{scr} now cancel leaving the net field in the crystal equal to E_{sc-ph}. If E_{sc-ph} is greater than the coercive field of LN it is energetically favorable for the spontaneous polarisation to align with the photo-induced field and the polarisation will be reversed. With reference to Fig. 11(e) domain inversion should occur only for $E_{sc-ph} > E_{scr}$ such that alignment of P_s with E_{sc-ph} would lower the total energy of the system. This threshold field for inversion is the coercive field of the crystal, E_c [17]. In the model above where E_{scr} remains constant, with magnitude equal to the room temperature depolarisation field, the estimate of the coercive field is the magnitude of E_{dep} and is given by

$$E_c = \frac{P_s}{\varepsilon} \tag{1}$$

where ε is the permittivity along the z axis. The estimate of the coercive field above evaluates to 28,235 kV cm^{-1} using $\varepsilon = 30\varepsilon_0$ and $P_s = 0.75$ C m^{-2}. This is clearly greater than the experimentally determined coercive field of 210 kV cm^{-1} [17]. However, this overestimate of the coercive field by orders of magnitude is also found in more rigorous derivations [22] and the lowering of the coercive field in ferroelectrics from the theoretical value for perfect crystals has been attributed to charged defects [23] or to mobility of pre-existing domain walls [22]. Regardless of the origin of the reduction in coercive fields it is clear that E_{sc-ph} need not be greater than E_{scr} for domain reversal to be achieved and if $E_{sc-ph} > E_c$ the P_s will invert [Fig. 11(f)].

This model agrees well with the previously seen dependence of the domain width on speed and power as was shown in Fig. 4. It was seen that the width of the domain inverted region had only a weak dependence upon scan speed but a very strong dependence upon power, which indicates that the effect is not simply a function of exposure. Although the model requires photo-excited charges, the number density of which will be a function of exposure, the driving force for charge movement originates from the temperature distribution created by the heating laser. The temperature distribution has been shown to be independent of scan speed for speeds below around 20 cm s^{-1} [13] and hence independent of exposure. The strong temperature dependence and the requirement seen to be reasonably near the melting point can be understood with the model above by considering the steep change of P_s with temperature near the Curie point since $P_s \propto (T_c - T)^{1/2}$, as shown in reference [17], where T_c is the curie temperature.

Anisotropy between the behaviour on the two faces is expected under the following reasoning. The optical absorption depth is around 30 nm at the writing wavelength and so photo-excited charges can only be created within this depth. Thus the source of free charges able to create E_{sc-ph} is essentially two dimensional and located at the surface in a plane parallel to the surface. As can be seen in Fig. 11(c) the field E_{net} in which the photo-excited charges move is directed parallel to P_s regardless of which face is heated. Thus when heating the $+z$ face

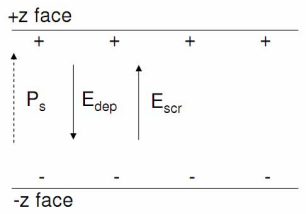

(a) Room temperature equilibrium

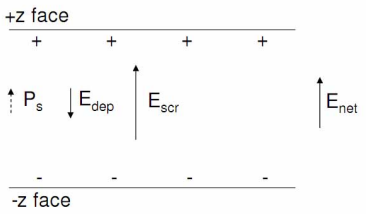

(b) Local heating reduces P_s and hence E_{dep}. E_{scr} is slow to react, thus leaving a net field E_{net}.

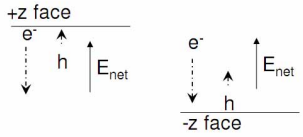

(c) Photo-excited charges at surface move in E_{net}. Electrons trapped at $-z$ face, holes trapped at $+z$ face.

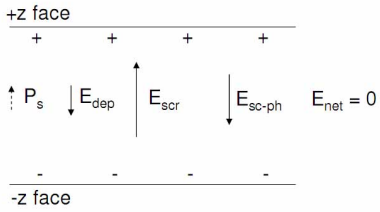

(d) Charge separation produces E_{sc-ph}. Equilibrium reached when $E_{net} = 0$

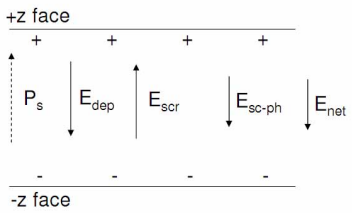

(e) When cool, P_s and hence E_{dep} increase, leaving a net field anti-parallel to P_s.

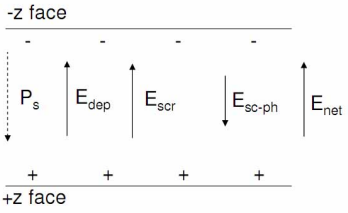

(f) If $E_{sc-ph} > E_c$ then P_s inverts.

Fig. 11. Schematic of the proposed mechanism for domain inversion. Solid arrows represent electric field vectors. Other vectors represented by broken arrows for clarity.

photo-excited holes will be trapped at the surface whilst photo-excited electrons will drift into the bulk of the crystal and, conversely, when the $-z$ face is heated photo-excited holes will drift into the bulk whilst photo-excited electrons will be trapped at the surface. If the mobilities of both electrons and holes were equal then the two situations would be similar and the same E_{sc-ph} would result. However, electron and hole mobilities are in general different with electrons being more mobile than holes with typical semiconductor mobility ratios of 3 (Si) to 23 (GaAs). Thus even from relatively simple consideration an anisotropy between the behaviour on the two z faces is expected.

In the experimental work and modeling described above, a laser wavelength of 244 nm has either been used or assumed for the incident light. As previously mentioned this wavelength has an optical absorption depth of 30 nm [18], which has two pertinent consequences with regard to the model described above. The first of these is that the length scale of the temperature distributions created by the beam are given by the beam radius, since the absorption depth is much less than the beam radius. The second is that the region in which photo-excited charges can be

created is, of course, limited to the absorption depth. Since the ratio of the absorption depth to the beam radius is ≈ 80 the source of charges that can create the field E_{sc-ph} is essentially two dimensional and located at the surface. The limited depth of the charge source limits the distance over which charge separation can occur and hence the depth over which E_{sc-ph} extends. This then, ultimately, result in a limit to the depth of the domain formed. If a laser wavelength at which the optical absorption depth within the crystal is greater than the 30 nm optical absorption depth at $\lambda = 244$ nm, and that still has a photon energy greater than the band-gap, then the charge source will become extended in the depth direction and deeper domains may be able to be formed. The optical absorption coefficient increases rapidly with decreasing wavelength near $\lambda = 244$ nm, so increasing the wavelength will increase the depth of the charge source. The temperature distributions within the crystal, and hence charge driving forces, would remain unchanged until the absorption depth was of equal magnitude to the beam radius.

The full dynamical behaviour of this nonlinear system is complex and subtle and a full numerical investigation of the charge dynamics under UV illumination is currently underway and will be presented in a future communication.

In short we believe that domain formation is due to a space-charge field created by the combined effects of photo-excitation of charge and drift within an electric field, caused by the decrease of spontaneous polarisation at elevated temperatures, and that the different behaviour of the two faces is due to the difference in mobilities of electrons and holes.

4. Conclusion

In conclusion, we have demonstrated domain inversion in congruent lithium niobate, iron-doped congruent lithium niobate and titanium in-diffused lithium niobate by a scanning continuous wave ultra-violet laser operating at a wavelength of 244 nm. The domain structures obtained have been analysed using piezoresponse force microscopy and by chemical etching in hydrofluoric acid, followed by surface profiling and scanning electron microscopy. The positive domains formed on the $-z$ face are also seen to contain self aligned nano-domains of negative polarity which are aligned along the x axes of the crystal. On the $+z$ face domain inversion can be seen at low powers, over the width of the exposed area, by etching. At higher powers domain inversion is not seen over the entire width of the exposure however aligned nano-domains are seen within the exposed area. The domains formed on the $-z$ face at high powers have also been observed by piezoresponse force microscopy. A model is proposed to explain the mechanism of domain inversion whereby the domain inversion is obtained through the action of a space-charge field of photo-excited charges and the differences of behaviour on the positive and negative faces can be explained by different electron and hole mobilities. We believe that by varying the illuminating laser wavelength to tune the optical absorption depth to a greater value the depth of the domains will be increased. Additionally to the numerous technological uses of directly-written domain structures the demonstration of etched ridge structures on titanium in-diffused planar waveguides also makes possible the fabrication of strip loaded waveguides with no photolithography [24].

The authors would like to thank Rutherford Appleton Laboratories Laser Loan Pool for the generous loan of the frequency doubled argon ion laser. We would also like to acknowledge the Engineering Physical Sciences Research Council (EPSRC) for the PhD funding of A. Muir and the EPSRC Portfolio Partnership in Photonics grant (reference EP/C515668/1).

F.1.4 Precision Nanoscale Domain Engineering of Lithium Niobate via UV Laser Induced Inhibition of Poling

C. L. Sones, A. C. Muir, Y. J. Ying, S. Mailis, R. W. Eason, T. Jungk, A. Hoffmann, and E. Soergel. Precision nanoscale domain engineering of lithium niobate via UV laser induced inhibition of poling. *Applied Physics Letters*, 92, 072905 (2008)

This paper is a result of the work carried out in chapter 4.

Precision nanoscale domain engineering of lithium niobate via UV laser induced inhibition of poling

C. L. Sones,[1] A. C. Muir,[1,a)] Y. J. Ying,[1] S. Mailis,[1] R. W. Eason,[1] T. Jungk,[2] Á. Hoffmann,[2] and E. Soergel[2]
[1]*Optoelectronics Research Centre, University of Southampton, Highfield, Southampton, SO17 1BJ, United Kingdom*
[2]*Institute of Physics, University of Bonn, Wegelerstrasse 8, 53115 Bonn, Germany*

(Received 10 December 2007; accepted 31 January 2008; published online 20 February 2008)

Continuous wave ultraviolet laser irradiation at $\lambda = 244$ nm on the $+z$ face of undoped and MgO doped congruent lithium niobate single crystals has been observed to inhibit ferroelectric domain inversion. The inhibition occurs directly beneath the illuminated regions, in a depth greater than 100 nm during subsequent electric field poling of the crystal. Domain inhibition was confirmed by both differential domain etching and piezoresponse force microscopy. This effect allows the formation of arbitrarily shaped domains in lithium niobate and forms the basis of a high spatial resolution microstructuring approach when followed by chemical etching. © *2008 American Institute of Physics*. [DOI: 10.1063/1.2884185]

Domain engineering[1,2] of lithium niobate (LN) is a subject of extensive research and a simple, cheap, and robust method of fabrication of well-defined periodic domain-inverted structures on submicron scales is highly desirable. Spatial domain engineering is used for many optical processes in bulk crystals and waveguides and can also allow for the creation of both freestanding[3] and surface relief structures[4] through the differential etching characteristics of the polar z faces of the crystal. If achievable on the submicron scale, surface structuring through differential etching will allow the implementation of a range of interesting applications such as tunable photonic crystals, ridge waveguide lasers, and multifunctional micromachines.

Previous work has shown that ultraviolet (UV) and visible laser light can either directly invert[5] or assist the domain inversion process in LN.[6–9] In this paper, however, a different effect is presented whereby illumination of the $+z$ face with UV light at $\lambda = 244$ nm (with photon energy greater than the LN band gap) *inhibits* domain inversion in illuminated areas during subsequent electric field poling (EFP). Of major importance, the inhibited domains are not restricted in their shape or alignment with the crystal x or y axes, hence, arbitrarily shaped domains can be formed. Some initial results of this effect and its applicability in the creation of micro/nano structures in LN are presented.

A beam from a frequency-doubled Ar-ion laser was focused to a spot size of ~ 2.5 μm on the $+z$ or $-z$ face of either an undoped congruent or 5 mol % MgO-doped LN crystal. Positioning and exposure control of the crystal was achieved by a computer-controlled, three-axis stage system coupled with a mechanical shutter.

For dynamic exposures, sets of parallel lines were drawn on the z faces of the crystals along the crystallographic x or y directions by moving the stages at speeds ranging from 0.05 to 0.3 mm s^{-1}. For static exposures, arrays of illuminated spots with identical exposure times, ranging from a few milliseconds to a few tens of seconds, were formed. The separation between the edges of adjacent illuminated spots in the arrays varied from 0 to 6 μm which permitted us to verify if any proximity effect existed such as that observed in pulsed laser direct poling[5] where the closest approach observed there was of order ~ 2 μm, irrespective of illuminated pattern resolution. For both types of exposures, the power was varied between 20–28 mW.

A two-beam interference scheme that allowed the formation of periodic structures over larger areas of the crystal via single exposures was also investigated. The incident interference fringe pattern had a period of 700 nm and extended over an area of around 2000 μm^2. As with previous experiments, several different exposure times, ranging from tens of milliseconds to tens of seconds, and a range of incident powers were tried.

Each set of illumination conditions was duplicated for both $+z$ and $-z$ face illuminations, to allow a direct comparison of the resultant effects on each of these polar faces. The samples were then poled using the EFP setup described in Ref. 6. The voltage was ramped at 2 kV/min to a value of ~ 10.1 kV, corresponding to an electric field of 20.2 kV/mm across the 0.5 mm thick sample. This value of the applied electric field ensures that domain inversion occurs slowly, which is desirable since the kinetics of the domain wall motion is seen to influence greatly the shape and quality of the resultant structures.

Etching of the poled crystal in aqueous HF acid solution then allows visualization of the formed domain structures through the different etch rates of the two z faces.[10] Piezoresponse force microscopy[11] (PFM) was also used to verify the domain nature of these structures. Lastly, the samples were imaged with a scanning electron microscope (SEM).

Figures 1 and 2 show SEM images of the structures produced by illumination of the single focussed UV beam on the $+z$ face followed by EFP and etching. The images show smooth, continuous unetched sections which correspond to the UV illuminated area of the surface. The etched background is the newly domain inverted area which presents a $-z$ face to the acid and hence etches. Further observation of the SEM images shows that the edges of the structures are

a)Author to whom correspondence should be addressed. Electronic mail: acm@orc.soton.ac.uk.

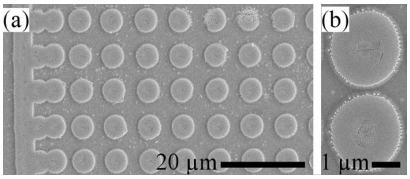

FIG. 1. (a) SEM image of a poling inhibited dot array. Scale bar 20 μm. (b) SEM image of two closely spaced poling inhibited dots.

slightly jagged, possibly due to the Gaussian intensity profile of the illuminating beam.

Interestingly, exposures on the $-z$ face, done for the purpose of comparison, were not seen to inhibit domain inversion. On the contrary, domain inversion was seen to initiate in the illuminated regions and was then followed by domain propagation through the crystal in a random and disorderly fashion. Hence, all the results discussed in this letter correspond to $+z$ face illuminations that result in domain inhibition.

Arrays of dots, such as the ones shown in Fig. 1(a), which are produced by static exposures, can have arbitrary dot separations and no interaction between dots was observed even when the separation between them was less than one micron, Fig 1(b). When illuminated areas overlapped, the regions of inhibited domain inversion merged. This can be seen on the left hand side of Fig. 1(a), where stage backlash distorted the array by reducing the dot spacing. Additional UV exposure of a specific area was not observed to produce any further effect. This can be seen in Fig. 2(a) where a cross-hatched pattern is shown as a result of sequential line scans along the x and y crystallographic axes. A higher magnification SEM image that shows the quality of the overlapped exposure is shown in Fig. 2(b). The sample was tilted by 45° during the SEM scan which allows the observation of the quality of the sidewall of the poling inhibited domain. The SEM images shown in Fig. 2 were obtained after prolonged etching (39 h). As a result, high aspect ratio structures were produced underlining the potential of this method for surface microstructuring.

The potential of this technique to form precisely positioned structures without proximity restrictions demonstrates the practicality of this technique in the implementation of devices such as couplers, y junctions, ring microresonators, and photonic crystals. The width of the area over which inhibition occurs is seen to be dependent upon both the incident power and the dwell time/scanning velocity of the beam with larger domains formed with longer dwell or lower scan speeds. This functionality reiterates the capability of this technique.

The quality of the poling inhibited regions was observed to be dependant upon the domain wall kinetics during the EFP step. It was seen that when the wall movement was smooth and reasonably slow, the inhibition process produced continuous domains. In congruent crystals when the wall movement can be fast, expanding in a "jerky" manner,[1,12] the poling inhibited regions appeared fragmented or did not exist at all in areas corresponding to fast domain wall motion. In the MgO doped crystals where EFP is known to be slower[13,14] and smoother, the inhibited domains appeared to be smooth and continuous everywhere.

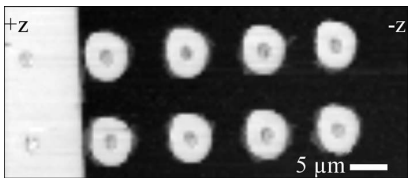

FIG. 3. PFM image of poling inhibited dot array. White=$+z$ face, black=$-z$ face as indicated. White area to left of image is an unpoled bulk domain.

In order to investigate the stability of the inhibited domains the crystal was thermally annealed for 1 h at 215 °C after the EFP step of the process. SEM investigation of the HF etched annealed crystal showed that the poling inhibited domains survived the brief annealing process without any significant change apart perhaps from the fact that after annealing there seems to be a slight improvement on the quality of the edges.

The domain orientation of the inhibited domains was further investigated by PFM which confirmed the observations deduced from chemical etching. Figure 3 shows a PFM image of an area of the crystal that carries a set of static spot illuminations and has also been partially poled (only a fraction of the area was domain inverted). Full contrast is associated with opposite ferroelectric domains where a $+z$ face appears white (left section of the image) while a $-z$ face appears black (right larger section of the image). The dots which appear white in a black background of the PFM image correspond to the UV exposed areas which have maintained their original domain orientation ($+z$) while the surrounding area has been inverted ($-z$) and appears black. The depth sensitivity of the PFM is ~100 nm (Ref. 15) which gives the lower limit to the depth of the inhibited domains. Preliminary investigations of the etched y face indicated that the depth of the domain inhibited area was in the range of 0.5–1 μm, however a systematic investigation will be presented in a future communication.

Interferometric exposures were at much lower laser intensity than single beam exposures due to the larger spot size. Exposure of the $-z$ face, followed by brief etching in HF, resulted in no topographical contrast. Exposure of the $+z$ face followed by bulk EFP and etching produced a periodic relief structure which is shown in the SEM image of Fig. 4.

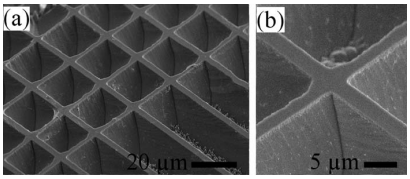

FIG. 2. (a) SEM image of poling inhibited hatched lines after 39 h of HF etching. Sample tilt 45°. (b) High magnification SEM image of a crossing point in (a).

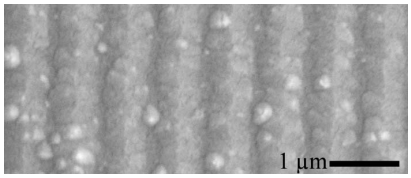

FIG. 4. SEM image of $+z$ face after interferometric exposure, EFP and brief etching.

The SEM image shown in Fig. 4 is qualitatively different to the ones produced at higher intensity. We believe that the surface relief pattern shown in Fig. 4 as revealed by chemical etching is a single domain structure which has originated from a periodic poling inhibited structure. Due to the low intensities used in this experiment the initial poling inhibited areas are expected to be very narrow and shallow hence easily removed by the acid via side etching. However, by using higher UV laser intensities it should be possible to obtain deeper periodic domain structures at the highly desired submicron scale.

We believe that the inhibition of the domain reversal is due to redistributed charges under the crystal surface which increases the coercive field locally. UV illumination leads to photoexcitation of charges and heating of the crystal.[16] A pyroelectric field is formed which drives electrons into the bulk of the crystal and holes toward the surface, producing a short range dipolar electric field distribution, which increases the coercive field locally. When a domain nucleates on the $-z$ face and propagates toward $+z$ face, inversion will not occur in this region where the coercive field is increased and domain propagation will be impeded, leaving a $+z$ surface domain island on a $-z$ background. This mechanism has some similarities to that described by Dierolf and Sandmann[7] for confocal light-assisted poling. However, in our case the driving field for the electrons is created by local heating of the crystal and not an external voltage and is opposite in direction to that of Dierolf and Sandmann,[7] leading to domain inhibition rather than domain inversion. Also, the mechanism we describe is latent and does not require application of the external field during illumination as in their case.

As a method of surface structuring UV poling inhibition followed by etching is simple, inexpensive, and flexible to implement. The shape/size and the quality of the fabricated structures is determined by the incident exposure conditions, in combination with the subsequent EFP parameters and the annealing steps, respectively. Additionally, as the crystallographic symmetry is not observed to impose limitations on the orientations of the created structures, any desired shapes can be achieved. Also the single domain nature of these structures provides the necessary requirement for implementation of efficient nonlinear, piezoelectric, and other domain-orientation-sensitive devices.

In conclusion, exposure of the $+z$ surface of congruent LN single crystals via UV laser radiation at $\lambda = 244$ nm is shown to inhibit domain inversion locally during subsequent EFP and, hence, results in the creation of UV illumination controlled two-dimensional surface structures. Domain inhibition was further verified by PFM and differential wet etching. UV light-induced poling inhibition is attributed to the redistribution of photoexcited charges in the electric field created when the laser heats the crystal, thus, producing a space-charge field which repels the propagating bulk domains during the subsequent EFP step. Finally, this effect, in conjunction with wet etching, was demonstrated to provide an easy alternative method for fabricating useful domain and surface relief structures.

The authors are grateful to the Engineering and Physical Sciences Research Council, UK, and the EU for research funding under Grant No. EP/C515668 and STREP 3D-DEMO respectively.

[1] V. Y. Shur, Ferroelectrics **340**, 3 (2006).
[2] B. J. Rodriguez, R. J. Nemanich, A. Kingon, A. Gruverman, S. V. Kalinin, K. Terabe, X. Y. Lui, and K. Kitamura, Appl. Phys. Lett. **86**, 012906 (2005).
[3] C. Sones, S. Mailis, V. Apostolopoulos, I. E. Barry, C. Gawith, P. G. R. Smith, and R. W. Eason, J. Micromech. Microeng. **12**, 53 (2002).
[4] S. Mailis, G. W. Ross, L. Reekie, J. A. Abernethy, and R. W. Eason, Electron. Lett. **36**, 1801 (2000).
[5] I. T. Wellington, C. E. Valdivia, T. J. Sono, C. L. Sones, S. Mailis, and R. W. Eason, Appl. Surf. Sci. **253**, 4215 (2007).
[6] C. L. Sones, M. C. Wengler, C. E. Valdivia, S. Mailis, R. W. Eason, and K. Buse, Appl. Phys. Lett. **86**, 212901 (2005).
[7] V. Dierolf and C. Sandmann, Appl. Phys. Lett. **84**, 3987 (2004).
[8] M. Müller, E. Soergel, and K. Buse, Appl. Phys. Lett. **83**, 1824 (2003).
[9] M. C. Wengler, U. Heinemeyer, E. Soergel, and K. Buse, J. Appl. Phys. **98**, 064104 (2005).
[10] C. L. Sones, S. Mailis, W. S. Brocklesby, R. W. Eason, and J. R. Owen, J. Mater. Chem. **12**, 295 (2005).
[11] T. Jungk, Á. Hoffmann, and E. Soergel, Appl. Phys. Lett. **89**, 163507 (2006).
[12] V. Gopalan, Q. X. Jia, and T. E. Mitchell, Appl. Phys. Lett. **75**, 2482 (1999).
[13] A. Kuroda, S. Kurimura, and Y. Uesu, Appl. Phys. Lett. **69**, 1565 (1996).
[14] K. Nakamura, J. Kurz, K. Parameswaran, and M. M. Fejer, J. Appl. Phys. **91**, 4528 (2002).
[15] T. Jungk, Á. Hoffmann, and E. Soergel, New J. Phys. **10**, 013019 (2008).
[16] A. C. Muir, G. J. Daniell, C. P. Please, I. T. Wellington, S. Mailis, and R. W. Eason, Appl. Phys. A: Mater. Sci. Process. **83**, 389 (2006).

F.1.5 Ultraviolet Light Induced Single Step All-Optical Poling in Lithium Niobate

C. L. Sones, A. C. Muir, S. Mailis, and R. W. Eason. Ultraviolet light-induced single step all-optical poling in lithium niobate. *Central Laser Facility Annual Report III 2006/2007*, 151 - 153.

This paper was published in the 2006 - 2007 annual report of the Central Laser Facility at the Rutherford Appleton Laboratories. The paper is a result of the work presented in chapter 3.

Ultraviolet light induced single step all-optical poling in lithium niobate

C. L. Sones, A. C. Muir, S. Mailis and R. W. Eason
Optoelectronics Research Centre, University of Southampton, Highfield, Southampton, S017 1EN, UK

Main contact email address **cls@orc.soton.ac.uk**

Introduction

Precision-scale engineering of domains in ferroelectric lithium niobate crystals is a subject of extensive research recently due to the numerous applications that this material has in optical telecommunications, nonlinear optics and optical sensing. The fabrication of well-defined periodic domain structures for this range of applications requires a robust method for ferroelectric domain inversion which can achieve the desired spatial ferroelectric domain distributions even on submicron scales. Furthermore, this method must be flexible, repeatable, and easy to apply.

So far the most popular method for ferroelectric domain reversal, referred to as E-field poling, involves the application of an external electric field across the two opposite *z* faces of the crystal at room temperature. Spatially selective ferroelectric domain reversal is achieved by covering one *z* face with photolithographically patterned photoresist or metal which provides the necessary spatially selective electric field contrast. However, the electric field contrast provided by the patterned photoresist is rather poor and consequently widths of ferroelectric domain produced by this method are limited to greater than a few microns.

We have directed considerable effort to the end goal of establishing a simple and reliable domain inversion technique that can circumvent the limitations of simple E-field poling. We have been experimenting with two different light-induced ferroelectric domain engineering approaches which we refer to as all-optical poling[1] (AOP) and light-assisted electric field poling[2] (LAP). The main feature in both methods is that the E-field contrast provided by the presence of patterned electrodes is now no longer necessary. The AOP approach attempts to achieve the required control over the formation of micron and submicron scale periodic domains via the use of a patterned optical field instead of the patterned electric field in the conventional technique of E-field poling. The LAP approach is a modified E-field poling technique wherein domain inversion is achieved under the combined influence of a patterned optical field and an un-patterned E-field. In this method the simultaneous presence of light results in a reduction of the field required to achieve domain inversion in the crystal, and hence eases the requirement of an otherwise extremely high electric field (~22 kV mm^{-1}) for conventional domain inversion.

Several groups have also studied the interaction between illuminating laser light and ferroelectric crystals, using c.w. light at different wavelengths (305 & 334 nm[3], 514 nm[4]) for domain inversion in undoped lithium niobate. Domain patterning in MgO-doped lithium niobate crystals using ultraviolet light from a Hg-lamp has also been reported.[5] Our earlier LAP experiments have demonstrated light-controlled micron scale domain patterning in congruent and MgO-doped single crystal material through an interaction with c.w. and pulsed laser light. We have reported an order-of-magnitude reduction in the electric field required for domain nucleation in lithium niobate crystals induced by illumination from a focused c.w. laser beam at wavelengths of 514, 488 and 457 nm.[2] We have also observed reduction in the nucleation field via use of ultra-short laser pulses (~120-150 fs) of near-ultraviolet (305 nm) to near-infrared (800 nm) wavelengths.[6]

Our AOP experiments conducted at the LSF in RAL and also at the ORC with the NSL-4/5 lasers using a ns UV (298-329 nm) light have also resulted in submicron AOP surface domains.[1,7] We have been exploring other wavelengths which are highly absorbed by the crystal with an end goal of pushing the AOP domain further in the crystal, and possibly achieving better control on the growth and the formation of the AOP domains. This has been possible with the CWL1 continous wave (c.w) frequency-doubled argon-ion laser from CLF-RAL laser loan pool that provides a wavelength range of 229-264 nm.

Our recent studies using this c.w source have interestingly revealed that AOP is achievable even without the high peak intensities, previously assumed essential, of a pulsed source. Some of the initial results from these experiments are described here later.

Experiments and results

The experimental set-up involved a 5 cm focal length lens that focused a spatially-filtered and collimated beam from the frequency doubled Ar-ion laser on the *z* face of the *z*-cut undoped congruent lithium niobate crystals. The beam was focused to a measured spot diameter of ~5 µm. The selected incident laser wavelength was 244 nm, at which the lithium niobate crystals are known to be highly absorbing. The incident power was varied from 20-28 mW, yielding an intensity range of 125-175 kW cm^{-2}.

The crystals used in the study were 0.5 mm thick, optically polished *z*-cut, undoped congruent lithium niobate wafers supplied by Crystal Technology, USA.

The crystals were mounted on motorised translational stages which not only allowed for the precise positioning of the illuminated *z* face at the point of focus, but also allowed for the motion of the illuminated *z* faces along the two directions lateral to the incident beam. Crystal faces were illuminated either by translating the stage at a uniform speed relative to the static incident beam, or just leaving it stationary, thereby inscribing structures in the shape of straight lines or circular dots.

Lines were drawn on the *z* faces of the crystals along the crystallographic *x* or *y* directions by moving the stages at speeds ranging from 0.05-0.3 mm s^{1}. A range of different speeds was tried to observe its effect on the widths and the depths of the directly written domain structures.

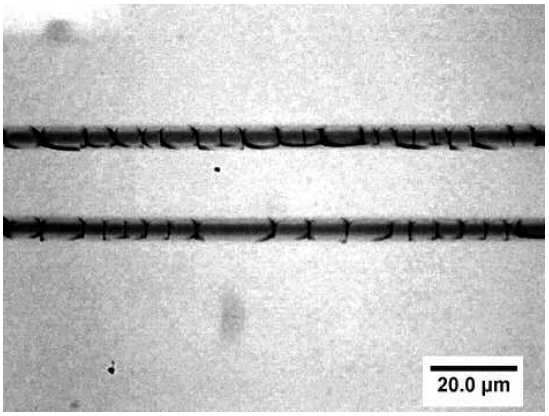

Figure 1. Unetched UV exposed + z face, showing line scanned at incident power 30 mW and scan speed 50 µm s^{-1}. Two distinct features can clearly be seen; a central darkened region and a wider surface damaged region.

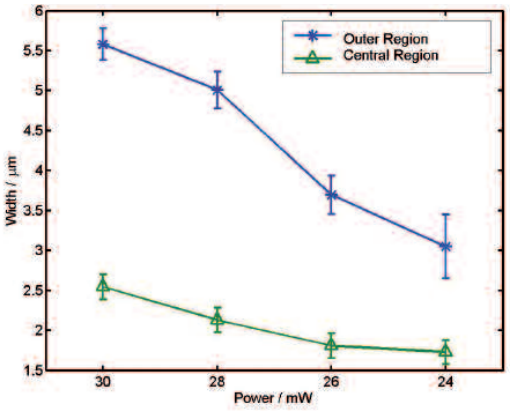

Figure 2. Plot showing variations of the widths of the total affected regions and (asterix) and central darkened (triangle) regions of the UV exposed lines.

For static exposures, (when the stages were not moving), the total time for which a particular position on the crystal face is illuminated was controlled using a shutter positioned along the path of the beam. The set of different exposure times ranging from a few milliseconds to one second were investigated to study the effect of the illumination time on the formation of the domain features. For a particular exposure time, an array of illuminated spots was formed by successively illuminating several equidistant positions on the crystal face. The separation between the edges of adjacent illuminated spots in the arrays varied from a few microns to zero microns. This permitted us to verify whether the proximity effect observed in pulsed AOP, (which forbids the merging of isolated domains with those in their near proximity, and hence prevents the formation of continuously joined domains), would also be an obstacle in the c.w AOP case.

Each of the explored illumination conditions was duplicated for a set of complementary *z* faces, thus allowing for a direct comparison of the AOP effect on each of those faces.

Initial examination of the illuminated faces was performed with an optical microscope between cross polarisers. Routinely employed domain visualisation techniques of wet chemical etching (in HF acid), and Piezorespsonse Force microscopy (PFM) were used for establishing the domain nature of directly written structures. Further measurements and characterisation of the domain inverted structures was done with a surface profiler and scanning electron microscope (SEM).

Initial examination of the UV scanned lines using a microscope revealed that in the case of both faces, lines written at higher powers (above 24 mW) and slower speeds result in damaged surfaces. The lines were seen to be composed of two distinct regions; a central region where the crystal is seen to undergo some darkening, and an outer lighter region with cracks resulting from thermal deformations and melting along its lengths. In all these lines the widths of the darkened regions (ranging from 1.4-2.5 µm) were significantly less than the $1/e^2$ beam diameter of 5 µm. A high magnification optical microscope image of Fig. 1 shows the extent of damage on the illuminated surfaces, and also clearly shows the two distinct affected regions. Surfaces of lines scanned at lower powers however appeared smooth and free of any of the randomly orientated cracks and voids associated with lines written at higher powers. The surface topography of these lines studied using a surface profiler confirm the absence of surface damage. A preliminary study of the variation in the widths of the scanned lines revealed a dependence on the writing/scanning conditions, namely the incident power/intensity and the scan speeds, with the larger widths corresponding to lines scanned at higher powers and or slower speeds. The measured widths of the total affected regions agree with those predicted by our previous thermal model[8]. Fig. 2 shows the width variation of affected regions with power for a set of lines scanned at identical speeds.

After the initial assessment the samples were studied using a PFM to determine if domain inversion had occurred in the illuminated regions. Fig. 3a, b show piezoresponse images of lines scanned on either of the *z* faces, with the dark lines in the image corresponding to the UV written lines. Interestingly, the contrast in the acquired PFM images for the scanned lines, improved with the incident power, which points to a difference in depth of the affected region. After a first set of PFM measurements, samples were annealed at 200˚C for 4 hours to eliminate the traces of residual charge, if any, from the illumination. The second set of measurements after the annealing step did not produce any change in the observed contrast of the piezoresponse images, which then verifies the piezoelectric nature of the domain inverted lines.

Moreover as shown in Fig. 3c a fortuitous accident with the tuning of the writing stages has also shown that the creation of the domains is not hindered by the imposed symmetry of the crystal (as in case of conventional poling techniques where domains will preferentially grow along the x or y axes of the crystal) but that domains can be created with arbitrary shape.

The samples were finally etched in pure HF acid to ascertain their domain nature via the established *z* face differential etch mechanism, which is know to selectively etch on the - *z* faces of lithium niobate. The samples were first briefly etched for a period of 5mins to determine the

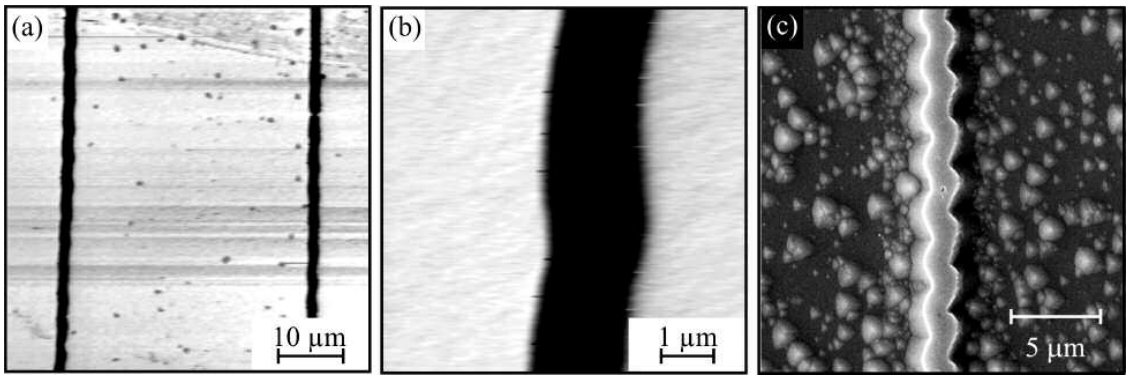

Figure 3. a, b) PFM images of written lines. c) SEM image showing a similar domain inverted line after etching.

profile of the etched domain inverted scanned lines. Etched structures with complementary shapes were observed for the two *z* faces, namely domain inverted lines on the + *z* face revealed etched trenches, whereas a similarly inverted lines on the – *z* face were etched out to reveal surface relief ridges. The samples were further etched (in steps of 5 min for about an hour), and subsequently imaged and profiled in order to determine the depths of the inverted domains. The shallow depths of the domain inverted regions were obvious from the scanning electron microscope (SEM) images seen in Fig. 4. Fig. 4a shows an SEM micrograph of an etched domain inverted trench formed on a + *z* face. Fig. 4b shows a SEM micrograph of an etched domain inverted ridge (revealed on an etched - *z* face). The gradients of the upper and lower edges of the ridge structure in Fig 4b, provides further evidence of its domain inverted nature. The upper edge of the ridge does not display any side etching whilst the lower surface displays a shallow gradient indicating side etching. Inversion of the *z* axis also results in the inversion of the *y* axis, and the differential etching mechanism of the *y* faces then results in these differing gradients. This has also been observed on domain structures written on - y faces through the differential etching behaviour of the *z* faces. Fig 5 shows an SEM micrograph of etched domain inverted ridges (revealed on an etched - *z* face) imaged from their sides at an angle of 49°. The thin film like layer with a thickness of ~ 1µm, suspended above the pyramid like structures observed on etched - *z* faces, corresponds to the UV induced domain inverted layer.

Conclusions

In summary we have demonstrated AOP via use of a c.w. light at 244 nm from a frequency doubled Ar-ion laser (CWL-1) on loan from the CLF-RAL. Domain inversion

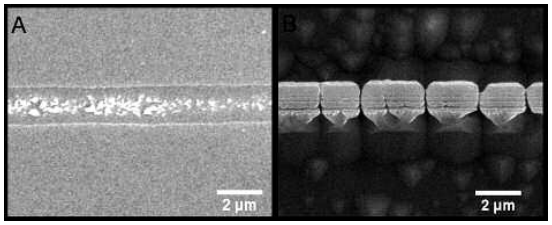

Figure 4. a. SEM image of an etched - z domain on a + z face. Incident power was 20 mW, and scan speed was 50 µm s^{-1}. b. SEM image of an etched + z domain on a - z face. Incident power was 26 mW and scan speed was 50 µm s^{-1}.

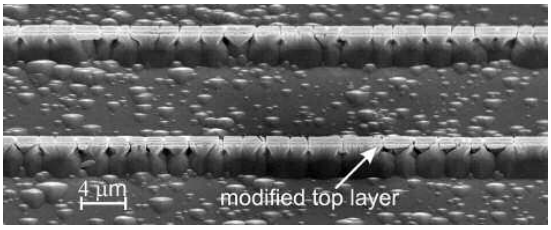

Figure 5. SEM image of an etched + z domain on a - z face. Incident power was 26 mW, and scan speed was 50 µm s^{-1}. Stage tilted by 49° to view sides of etched ridges.

was achieved for illumination on both the *z*-faces. The domain inverted regions, had widths comparatively smaller than those of the scanning laser beam, implying the possibility of sub-micron domain formation. The shapes of the inverted regions strictly adhered to those of the incident beam, which meant that it is possible to fabricate domains with arbitrary shape. The depths of the inverted domains are not quite those desired for guided wave interaction, however, we are confident that simple, post illumination processing can increase the domain depth whilst retaining the advantages of a direct-write system. In conclusion c.w AOP presents a single step versatile approach to domain inversion in lithium niobate.

References

1. C. E. Valdivia, C. L. Sones, J. G. Scott *et al., Applied Physics Letters* **86** (2), 022906 (2005).
2. C. L. Sones, M. C. Wengler, C. E. Valdivia *et al., Applied Physics Letters* **86** (21), 212901 (2005).
3. M. Muller, E. Soergel, and K. Buse, *Applied Physics Letters* **83** (9), 1824 (2003).
4. V. Dierolf and C. Sandmann, *Applied Physics Letters* **84** (20), 3987 (2004).
5. A. Fujimura, T. Sohmura, and T. Suhara, *Electronics Letters* **39** (9), 719 (2003).
6. C. E. Valdivia, C. L. Sones, S. Mailis *et al.,* in *ISDS* (Ekaterinburg Russia, 2005).
7. I. T. Wellington, C. E. Valdivia, T. J. Sono *et al., Applied Surface Science* **253** (9), 4215 (2007).
8. A.C. Muir, G. J. Daniell, C. P. Please *et al., Applied Physics A-Materials Science & Processing* **83** (3), 389 (2006).

F.1.6 Progress in Ferroelectric Domain Engineering at the Micro / Nanoscale

R. W. Eason, S. Mailis, C. L. Sones, A. J. Boyland, A. C. Muir, T. J. Sono, J. G. Scott, C. E. Valdivia,and I. T. Wellington. *Progress in ferroelectric domain engineering at the micro / nanoscale.* In, Schwartz, Robert W. (ed.) Electroceramic Materials and Applications. Chichester, UK, Wiley, 93-108. (Ceramic Transactions, 196) (2005)

This paper was includes results from the work presented in chapters 5 and 6. The paper was first presented at the sixth PAC RIM [Pacific Rim] meeting of the American Ceramic Society, held September 2005 in Hawaii, and then published as above.

PROGESS IN FERROELECTRIC DOMAIN ENGINEERING AT THE MICRO/NANOSCALE

Robert W. Eason, Sakellaris Mailis, Collin L. Sones, Alexander J. Boyland, Alistair C. Muir, Tleyane J. Sono, Jeffrey G. Scott, Christopher E. Valdivia, Iain T. Wellington.

Optoelectronics Research Centre
University of Southampton
Southampton, Hampshire, SO17 1BJ, UK.

ABSTRACT

Ferroelectric materials such as lithium niobate (LN) or lithium tantalate (LT) are examples of an extremely versatile class of optical crystals. In bulk single crystal, single domain format, these crystalline hosts find numerous applications in nonlinear optics, optical storage, photorefraction, surface acoustic wave devices, optical waveguides, piezoelectric and pyroelectric devices and electro-optic modulation. Single domain crystals can be subsequently engineered via spatially selective poling to yield domain structures whose size can lie in the region of a few tens of μm to sub-μm, for applications and device fabrication that are impossible to implement in single domain geometry.

This paper discusses our progress to date in micro- and nanostructuring of such materials, for applications in nonlinear optics, switching and deflection, and 3-dimensional sculpting for possible MEMS use. The techniques and benefits are discussed of using both light-assisted and direct optical poling for achieving controllable domains that can be irregular or periodic, bulk or surface, at sizes that approach the 100 nm scale. For surface inversion, domain features can be produced that lack the otherwise characteristic crystal symmetry imposed hexagonal shapes observed in conventional electric field poling.

INTRODUCTION

Ferroelectric materials play an extremely important role across many scientific and technological disciplines due to their wide range of intrinsic properties such as piezoelectricity, pyroelectic, electro-optic and photorefractive behaviour and are currently finding widespread use in periodically poled geometries for efficient quasi-phase-matched interactions[1]. Two widely used and commercially available materials are lithium niobate (LN) and lithium tantalate (LT) which are usually purchased in the form of single domain, pre-poled wafers of typically up to 3 inch diameter and thickness of order 1 mm or below.

For both LN and LT that have been congruently grown, the coercive, or poling, field at room temperature is ~21 kV mm^{-1} for forward poling[2], a value which is high, but manageable for producing periodically poled structures at periods of order 4-5 μm or larger in bulk crystals of thicknesses ~1 mm. Another variant of these crystals, termed stoichiometric, have poling fields of order one hundredth[3], of this value and there is currently great interest in the routine commercial availability of high quality stoichiometric crystal materials. As well as their much reduced coercive fields, stoichiometric crystals have far fewer intrinsic defects such as lithium vacancies, and nonlinear optical experiments have shown that they possess much greater resistance to optical damage by almost four orders of magnitude as compared to their congruent counterparts[4].

These crystals can be poled using electric fields to produce domain patterns that can be bulk (throughout the entire crystal thickness) or surface (some few μm depth) in nature, and such spatially selective domain patterning adds greatly to their functionality and areas of application.

While periodically poled lithium niobate (PPLN) in particular has found application in nonlinear optical harmonic and parametric generation, achieving high quality samples with periods of less than the ~4 μm value is experimentally challenging. It is therefore of considerable importance to investigate methods for realising μm scale periodicity, and below, for applications in tunable Bragg structures, filters and gratings, backward wave parametric generation, and other areas such as optical memory that involve domain patterning at the experimental limit which is of order ~10 nm.

This paper discusses recent progress in both physical structuring, using the technique of laser direct writing, and also domain engineering, to produce spatially selective domain patterns at feature sizes of ~100 nm and above, in both congruent and MgO doped stoichiometric materials. A generic end goal of our work to date may be summarised by the following schematic shown in figure 1 which concerns the idea of a functional lab-on-a-chip, using an active material such as LN rather than glass, polymers or silicon. Once the toolbox of techniques for structuring in 3D is complete, then arbitrary designs are possible for the manipulation of objects such as biological cells, micro-beads, or single molecules around the surface of such a chip. The added value of using a functional material such as LN compared to glass lies in the ability to integrate electrodes into the structure, thereby accessing the material's intrinsic piezoelectric, pyroelectric and electro-optic effects.

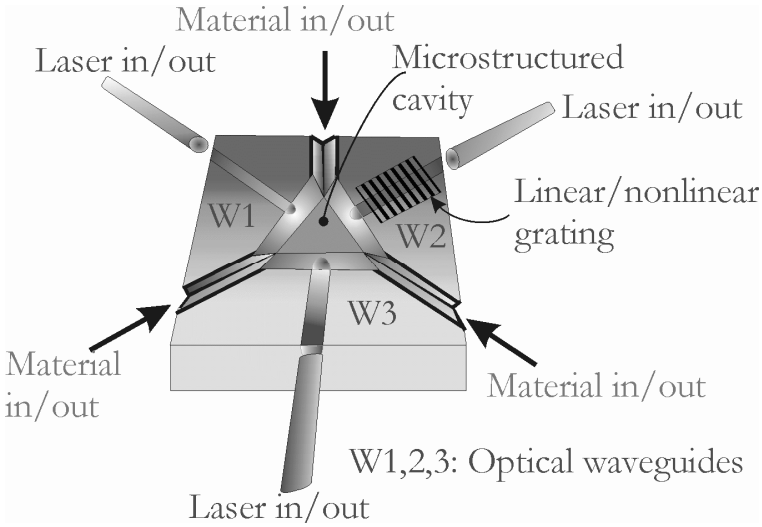

Figure 1. Schematic of physical structuring processes required for fabrication of a lab-on-a-chip.

PHYSICAL STRUCTURING PROCESSES

A range of physical structuring processes exists for generating surface profiles such as gratings, holes, vias and optical waveguides. Of prime importance however is that the processed crystal has a high quality finish, and that the number of processing steps is minimized. While laser ablation for rapid processing of LN may satisfy the second criterion, problems of direct laser machining such as debris, cracking and redeposition in single crystal materials are difficult to overcome. Secondly, conventional photolithographic processing which requires cleanroom access involves numerous sequential steps such as cleaning, photoresist spinning, patterning, baking, development, with subsequent diffusion, etching or other methods of spatially selective material removal or overgrowth. While these processes are to a large extent routine, and may be

automated, there is clearly an opportunity here for faster single-step processing technology using for example laser direct writing and two such techniques are briefly discussed here.

Surface UV irradiation plus wet etching.

For writing of gratings, two-beam interferometry or the use of phase masks are the preferred routes. If UV light is used, and the energy density is kept below the ablation threshold, then although little physical damage may be evident, the exposed regions may have undergone latent damage and these areas can be subsequently removed in a smooth and precise manner with an etchant such as hydrofluoric acid (HF). This technique has been successfully used to form surface gratings with a period of 360 nm onto both the + z face of LN, and x-cut titanium indiffused LN channel waveguide structures[5]. The method has the advantage of rapid processing, as a single 20 ns duration pulse from an excimer laser is all that may be required, and subsequent etching reveals a faithful replica of the initial irradiation pattern. Precise depth control of the grating profile is somewhat harder to achieve however leading to a consequent reduction in the performance (linewidth and grating strength) of such devices in comparison to, for example, fiber Bragg gratings.

Direct writing of channel waveguides

A second technique that we have been exploring involves a process by which a scanned focused c.w. UV laser operating at a wavelength of 244 nm can be used to rapidly heat the surface of a LN crystal, inducing localized Li ion diffusion which can lead to the formation of optical waveguiding structures[6]. Since the first report of this technique, we have subsequently modeled the process using both analytical and finite difference techniques to determine the maximum temperature rise, spatial and temporal temperature gradients and consequent Li ion diffusion achieved in both lateral and depth directions[7]. The inset of figure 2 shows the results of an analytical model we have developed, which indicates that a transient temperature rise of almost 1000 °C is possible via scanned UV laser heating. Noteworthy is the fact that the extremely small absorption depth of ~30 nm at this wavelength produces a distinct difference in temperature profiles for surface (x or y) compared with depth (z) directions. The difference in temperature gradients greatly affects the Li ion diffusion process, and diffusion does not occur to any great extent in the depth direction, as shown in figure 2. Even though the index change associated with Li diffusion away from the heated regions is high enough to produce guided wave structures, as have been produced experimentally, the modeling performed so far indicates that the diffusion depths achievable are insufficient to support even single mode guidance. This discrepancy, which may have its origins in either the fundamental model assumptions or details associated with some unknown physical parameters, is currently under further investigation.

DOMAIN BASED STRUCTURING

An alternative technique that we have been pursuing for several years concerns the use of micro and nanostructuring based on domain engineering. For some applications, the domain patterning produced is subsequently converted into a corresponding topographical structure as in case for PPLN, the presence of the domain structure alone is all that is required. We show below a simple example of the application of a single domain boundary in deflection and switching, using the principle of voltage controllable total internal reflection (TIR) at an interface between opposite polarity domains.

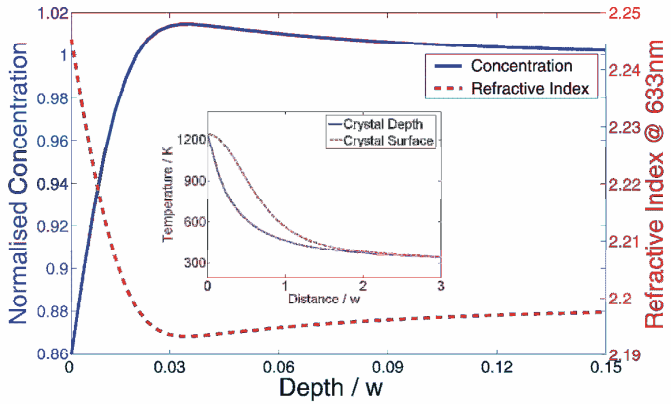

Figure 2. Modelled lithium concentration and associated refractive index distribution along the depth (z) direction for identical beam parameters as in the inset of this figure. Note that the induced Li concentration does not extend very far into the crystal depth, and peaks at a distance of order 0.03 of the incident laser spot size. The depth axis has been normalized relative to the beam width. Inset: Modelled temperature distributions on the surface (x or y directions) and in depth (z) for UV beam writing parameters of spot size $w = 3.25\ \mu m$, incident laser power $P = 30$ mW and writing speed $v = 0.83$ mm s^{-1}.

TIR deflection and switching.

Shown in figure 3 is a schematic of a miniature TIR device that we have fabricated in congruent LN, with dimensions of $5 \times 13 \times 0.3$mm in x, y, z directions[8]. One half of the wafer has been re-poled to produce a boundary between anti-parallel domains. On application of a voltage across this boundary region, the local refractive index is increased on one side of the boundary, and decreased on the other. A laser beam incident on the boundary from the elevated index side will experience deflection via Snell's law proportional to the applied voltage, and subsequently TIR when the induced index change exceeds the value required for the particular value of incident angle.

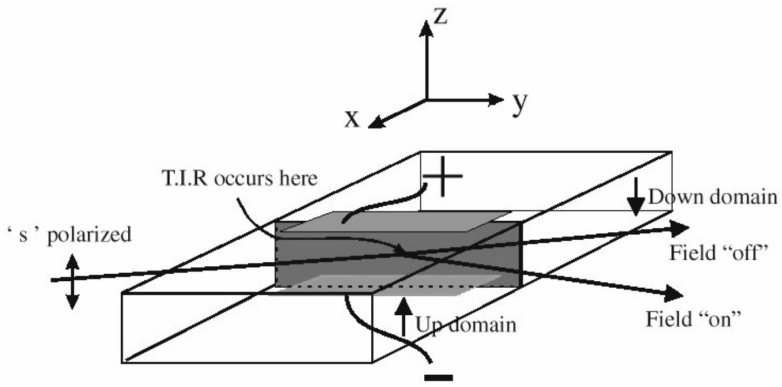

Figure 3. Schematic of TIR deflection and switching device with poled anti-parallel domains.

In practice, for *s* polarized light incident at an angle of ~88°, a voltage of ~1kV is required for TIR to occur, utilizing the r_{33} electro-optic coefficient. Deflection will also occur for *p* polarized light, which can access the r_{13} coefficient, but this requires an applied voltage roughly

three times higher. If the exit facet of the device is cut at an appropriate angle, Snell's law can magnify the final deflection achievable to produce a ~10° swing of the exiting beam, and this can be further extended to 20° by reversing the polarity of the applied field across the interface. For an extended device length of 50 mm, modeling shows that the device is capable of achieving 300 resolvable spots. Further extensions of this technique allow both RGB colour separation and also 2-dimensional scanning operation.

Cantilevers

Micro-structuring in LN has been achieved via a process of spatially selective poling, crystal bonding and subsequent etching in HF. Such techniques permit full 3-dimensional structuring[9] in single crystal material which is a fundamental requirement if device implementation requires subsequent use of electro-optic or piezoelectric coefficients. Shown in figure 4 is an example of such sculpting used to produce a cantilever of transverse and height dimensions ~50 µm, and length of 5 mm. The gap between the cantilever and the substrate is afew µm, and during focused ion beam writing of electrodes on the side of the structure, without the use of a compensating electron flood beam to neutralize any surface charging, the cantilever experienced deflection to a height of ~15 µm, showing that such single crystal geometries are capable of flexure and bending, and hence suitable for MEMS based applications.

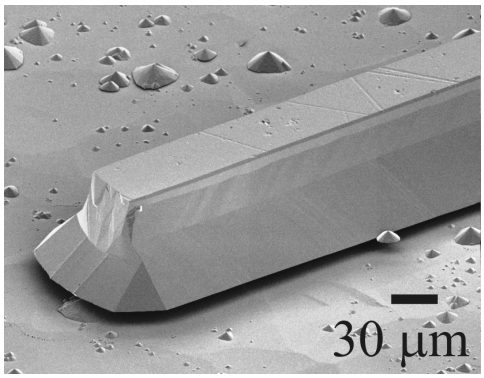

Figure 4. SEM image of a free-standing cantilever in LN (dimensions of ~50 µm×~50 µm ×5 mm).

Surface poling (overpoling).

As well as poling in bulk materials, where domain inversion is required throughout the full crystal thickness of ~500 µm to 1 mm, for waveguide geometries inversion is strictly only required throughout the waveguide depth of a few µm. As noted earlier, fabrication of small period gratings (Λ ~few µm) is far from routine, particularly when trying to achieve uniformity throughout a ~1 mm LN sample. Surface poling[10], alternatively termed overpoling, has been used recently to fabricate periodic structures with a domain size of ~0.5 µm, and period of 1 µm. Using a grating period of 2.5 µm, first order quasi-phase-matched harmonic generation from λ= 825 nm to λ=412.5 nm has been achieved in a Ti:indiffused LN channel waveguide[11], producing an overall output power of 6 mW, and an efficiency of ~10%.

Overpoling refers to a technique in which conventional photolithographic periodic patterning in photoresist is followed by the application of an electric field such that the charge delivered during poling exceeds the nominal charge Q calculated via:

$$Q = 2 A P_s EF \quad (1)$$

where A is the area to be poled, P_s is the spontaneous polarization for LN (0.72μC mm^{-2}) and EF is an empirical poling factor.

For an EF of ~1, normal bulk poling is achieved, while for an EF of >10 for example, the entire crystal poles, with domain wall spreading occurring throughout the crystal volume. For intermediate values (EF~4-6), while the bulk crystal experiences poling throughout its volume, regions directly below the photoresist do not, due most likely to trapped charge directly beneath the insulating photoresist layer. These regions of unpoled material can extend to depths of some few μm to perhaps 10 μm, dependent on both the periodicity chosen and the value of EF used. Figure 5 shows an example of such surface domains, taken via scanning force microscopy (SEM) on a polished and etched y face. For this example a periodicity of 6.5μm was used, and it can be seen that although some domains extend to beyond 10 μm depth, the degree of depth uniformity is poor. For waveguide applications however, as noted earlier, all that matters is that the minimum depth exceeds the waveguide dimension.

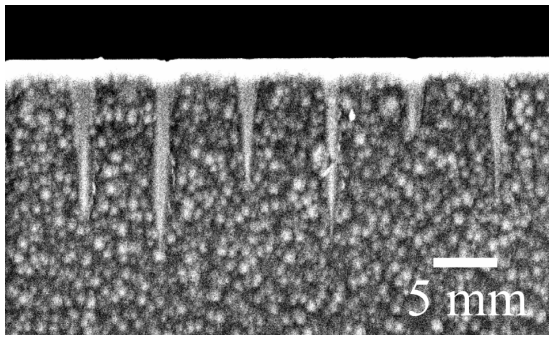

Figure 5. SEM image of an etched y-face showing typical surface domain profile (for Λ = 6.5 μm).

Even shorter period (Λ = 1.0 μm) surface domains have been realized, with a minimum domain feature size of ~0.5 μm, as shown in figure 6. A problem which is evident in this technique however, and can be clearly seen in figure 5, is that the mark/space ratio of domain inverted material differs from the ideal 50/50 value.

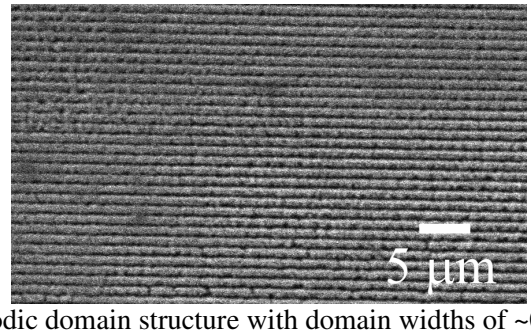

Figure 6. Surface poled periodic domain structure with domain widths of ~0.5 μm.

While we have tried to address this problem, success to date in achieving the 50/50 ratio is limited, and remains a problem for routine high quality surface domain structuring. For SHG

experiments therefore, the trade-off that exists concerns the mark-space ratio efficiency reduction versus the efficiency increase achieved by operating in first order.

Nanotips.

The final example in this section on domain-based structuring relates to the fabrication of arrays of domain inverted tips on the surface of a LN wafer[12]. Applications for this technique lie in the area of SHG, atomic force microscopy and piezoelectric nano-devices. Figure 7 shows an SEM of a typical array, formed via photolithographic patterning, poling and etching in HF at a temperature of 60 °C. Tips with the characteristic 3-fold symmetry form due to the differentialnature of y-face etching. As etching proceeds in the –z direction, the simultaneous y-face etching will result in the formation of pyramids, shown from a top view in figure 7. Also seen in the inset is a highly magnified view of a single tip, from which it is apparent that the tip apex is essentially of nm scale.

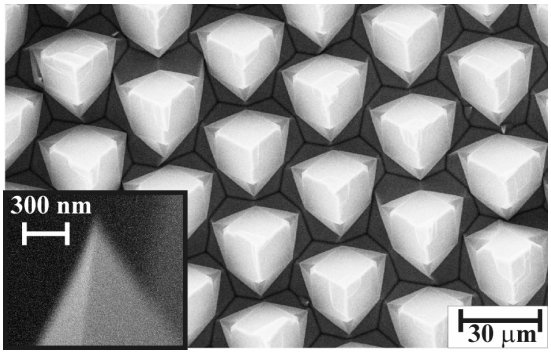

Figure 7. SEM picture of nanotip array formed on the –z face of LN. Tip dimensions are ~30 μm at their base, and ~100 μm high. Inset shows that the tip apex is of ~nm dimensions.

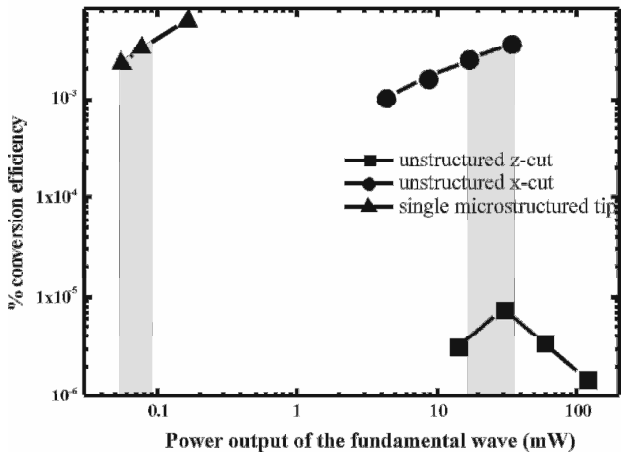

Figure 8. SHG conversion efficiency within nanostructured LN tips compared to unstructured x- and z-cut crystal samples.

Experiments have been performed using ~130 fs laser pulses at 800 nm to generate SHG at 400 nm from these tips, to investigate the efficiencies achievable from interactions within LN in a non-phase matched geometry under the extremely high power densities present in the vicinity

of the tip. Figure 8 shows our first results, from which it can be seen that the harmonic conversion efficiency is dramatically enhanced, compared to that achievable with either unstructured x- or z -cut LN samples. This enhanced efficiency may be due to a combination of factors such as increase of the light intensity within the tip, access to nonlinear coefficients unavailable in the unstructured material, surface enhanced or surface phase-matched interaction, or even modification of the basic ferroelectric structure itself within these extreme crystal geometries. Whatever the predominant cause, highly efficient SHG has been achieved in an otherwise non-phase matched geometry. These investigations are ongoing, and material characterization is underway to determine whether the crystal structure within such tips has been modified with respect to that of bulk material.

LIGHT-INDUCED ETCH FRUSTRATION, LIGHT-ASSISTED POLING AND ALL-OPTICAL POLING.

We now address the area of laser light interaction with LN for investigation of the effects of light-induced frustrated etching (LIFE), light-assisted poling (LAP), and all-optical poling (AOP), using c.w. ion lasers operating in the UV and visible (244 nm, 488 nm, 514 nm, 532 nm), ns UV pulsed lasers (excimer, frequency quadrupled YAG and doubled dye) and finally 100 fs pulsed Ti:sapphire (from 305 nm to 800 nm). The work here spans several years, and we have investigated a range of ferroelectric hosts including congruent LN and LT (CLN, CLT), Fe:doped congruent LN (Fe:CLN), MgO:doped congruent LN (MgO:CLN) and MgO:doped stoichiometric (MgO:SLN). Table (I) summarises the experiments to date, and the abbreviations used.

Table I. Classification of light-assisted interactions in ferroelectric host materials.

Laser	Wavelengths	*CLT*	*CLN*	*Fe:CLN*	*MgO:CLN*	*MgO:SLN*
c.w.	UV	LAP	**LIFE**[b]	LIFE		
	visible	LAP	LAP	**LIFE**[a]	LAP	**LAP**[d]
pulsed	UV ns		**LIFE**[c] **AOP**[f]	LIFE	AOP	
	UV, visible fs		**LAP**[e]		**LAP**[e]	

(The abbreviations in **bold** and superscripts refer to subsequent sub-headed sections in the text)

Light induced frustrated etching (LIFE[a])

This has been investigated under two dissimilar experimental regimes. The first experiments were conducted with Fe:doped CLN only[13], with Fe dopant concentrations varying between 0.01 wt% and 0.2 wt%. The experimental arrangement involved the exposure of the –z face for periods ranging from 30 s up to one hour to an incident c.w. laser beam at wavelengths of 488 nm or 532 nm in the presence of an HF acid environment.

Initially, these experiments were performed in the expectation that this photoelectrochemical etching procedure would produce a dramatically enhanced etch rate, as had been seen previously for a range of semiconductor materials. In fact, the reverse effect was observed, namely the presence of the light totally inhibited any etching at the highest focused light intensity used (~1 kW cm^{-2}), and partially frustrated the etching at intensities between 1 kW cm^{-2} and ~1 W cm^{-2}. Within this partially frustrated regime[14], a spatially complex and visually dramatic patterning

resulted, forming line features that followed the intrinsic crystallographic axes, with linewidths of order ~0.5 µm. An example of these surface features is shown in figure 9.

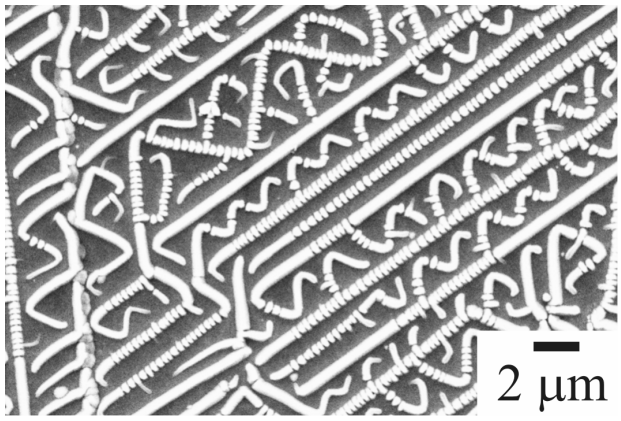

Figure 9. LIFE patterning in Fe:doped CLN using c.w. 532 nm laser light.

Although these results are artistically appealing, it has proved impossible to produce any useful degree of surface ordering. The intrinsic scale-lengths of the LIFE process appear to be almost ideal however, falling as they do in the sub-µm region. It has further proved difficult to uniquely classify the nature of these raised non-etched line features. While the temptation to refer to them as domains is considerable, there is as yet no clear evidence that this is the case, unlike our results for all-optically poled CLN which are discussed in a later section.

Light induced frustrated etching (LIFE^{b}).

The second set of experiments that fall within the LIFE category have been performed using c.w. focussed UV light at 244 nm from a frequency doubled Ar-ion (FRED)laser. The set-up is essentially identical to that used for direct writing of channel waveguides in the –z face of undoped LN as described earlier. Laser powers of between 20 mW and 50 mW at a focused spot size of 1.7 µm were used, at a reasonably fast scanning speed of 50 mm s^{-1} to ensure that no significant surface damage or melting occurred. The results shown in figure 10 reveal that the laser-exposed regions proved to be highly etch resistant[15]. One dimensional ridge features of height 1.7 µm as well as 2-dimensional square lattice patterns were written with good uniformity and reproducibility. Micro-Raman studies of the etch resistant structures revealed no departure from identical unexposed material, indicating that the UV laser writing process had neither damaged nor melted the crystal surface. As with the results for LIFE^{a} above, it is tempting to conclude that these features are laser-written inverted domains, but there is no direct evidence for this however. An equally plausible explanation might involve surface charge modification. Following laser writing, if the sample was annealed at a temperature of ~200 °C for one hour, then subsequent HF exposure did not reveal any etch-resistant features. Techniques such as scanning force microscopy (SFM), discussed in a subsequent section, cannot be easily used here once the sample has been etched. All such scanning probe techniques are also sensitive to sample topography, and both of these LIFE^{a,b} techniques result in highly textured topographical surfaces. The technique is simple, direct and fast however, and can result in feature sizes of a few µm.

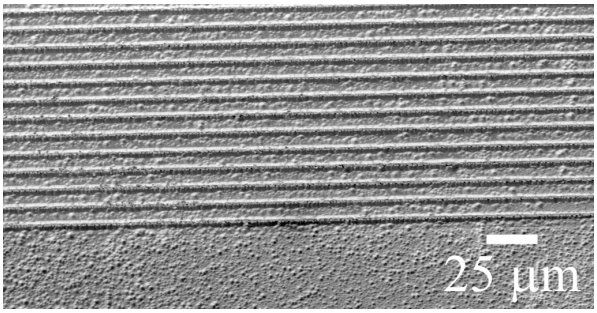

Figure 11. SEM of –z face after scanned laser exposure and 1 hour of HF etching. The separation between each track was 9 µm.

Light induced frustrated etching (LIFE[c])

The final example of this surface structuring process can be seen in figure 11 below. A range of experiments was performed, using between one and ten laser pulses, followed by HF etching. A TEM grid that had multiple hexagonal openings of ~50 µm width, was loosely attached to the –z face of CLN samples[16]. Following exposure, the samples were etched in HF, and then examined by SEM. The level of detail and self-ordering in the surface topography is extremely interesting, suggesting that a similar process may be operating to that seen in LIFE[a], but in a time frame of ns rather than in minutes or hours. The surface features (as seen in the inset of figure 11b) are remarkably uniform, at a similar size of ~0.5 µm to previous LIFE[a] results. In the present case, it is also extraordinary that the etch frustration process appears to be inordinately sensitive to the local irradiance.

The etch pattern in figure 11b shows the result of exposure from a near-field (Fresnel) diffraction pattern produced by lack of perfect contact between the mask and the LN crystal surface. Although the variation of light intensity towards the edges of the irradiated area can only be slight (few % to perhaps few 10's of %), this variation is clearly sufficient to produce an equivalent modulation of the frustration effect. Indeed, towards the centre of the irradiated area, where the intensity modulation can only be minimal, it is still apparent that the frustration modulation and ordering persists. It would be very surprising if the frustration phenomena could be that sensitive to local intensity, or perhaps intensity gradient, but this is what appears to happen.

Even though the precise explanation is not yet apparent, it is clear that such a technique may be eminently suitable for precision surface topography manipulation.

Light-assisted poling (LAP[d])

There have been several reports to date of the role of incident light in modifying coercive fields for both forward and backward poling, and there appear to be at least two somewhat contradictory processes occurring. The first of these LAP processes concerns the modification of the recovery of the coercive field in CLT following a forward poling step[17]. Directly after a forward poling (some few seconds), the field required for reverse poling is considerably lower than the field needed to reverse pole perhaps one hour after the initial forward poling step. The internal field that plays an important role in such congruent crystals takes time to adjust itself to the new direction of spontaneous polarization. The recovery process is far from simple, and at

least three distinct rate constants have been identified in the recovery mechanism, with time constants ranging from ~1s to more than one year. After one hour for example, the field required

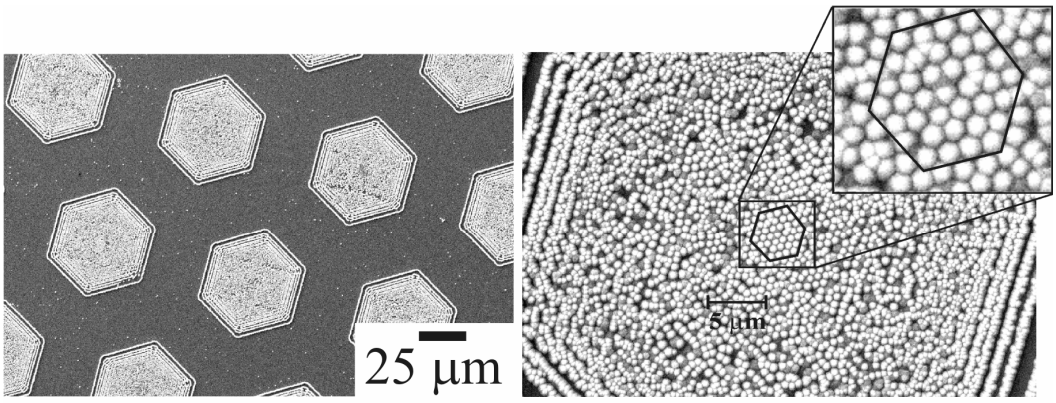

Figure 11. SEM images of etch frustrated hexagonal patterns induced on the –z face of LN via exposure through a TEM grid using a KrF excimer laser operating at 248 nm, 20 ns pulse duration.

for reverse poling in CLT remains some 35% lower than for the initial forward poling process.

During this coercive field recovery process, light in the visible spectral region, specifically at the Ar ion wavelengths of 488 nm and 514 nm, which is incident on the crystal, can enhance this rate of recovery. If the incident light is patterned, or structured, then by judiciously choosing the value of field applied during illumination, selected unilluminated areas can undergo reverse poling, whereas illuminated areas, where the coercive field has recovered faster, will not. Achieving the balance between poling and not poling in unilluminated and illuminated areas respectively is clearly difficult, particularly considering that all such local coercive fields are themselves time-dependent. Periodic patterning has been achieved however via this technique with a periodicity of ~6 μm, but over a very limited spatial extent, using 351nm UV illumination from an Ar ion laser.

The second of these processes appears to be the direct opposite of the first: during re-poling, incident light in the near-UV[18] or visible region[19] can dramatically reduce the local coercive field, by as much as 34% and 90% respectively in either MgO:CLN or MgO:SLN. Figure 12 shows a plot of the ratio of coercive field with and without illumination as a function of the irradiance for three crystal samples: CLN, MgO:CLN and MgO:SLN. For the latter two crystal types, the reduction is dramatic, and saturates at a value of only 10% of the field required for an unilluminated sample. One difference to note in these experiments however is that the field recorded here is not the conventionally defined coercive field, but the 'nucleation field', defined as the field at which the first evidence of poling occurs. The laser wavelength of 514 nm was chosen for these experiments as this line contained the highest power, but all other available Ar laser wavelengths in the visible of near UV produced substantially similar results. These experiments were greatly assisted through the use of a purposely designed transparent sample cell, shown in figure 13, which allowed the application of an electric field while simultaneously illuminating the LN sample with two different laser wavelengths: one for control of the coercive field and a second for viewing domain nucleation and growth.

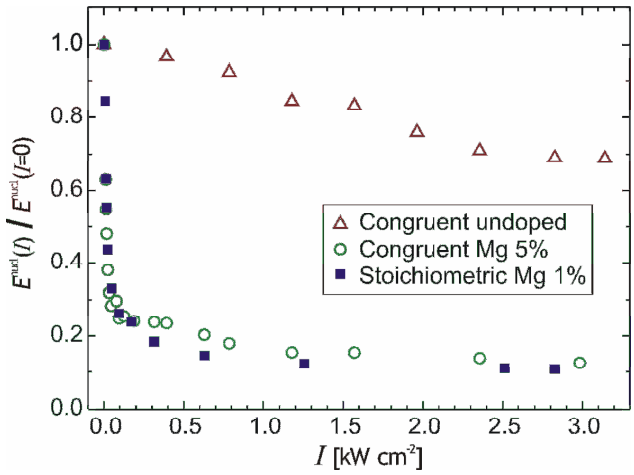

Figure 12. Nucleation field versus incident c.w. Ar ion laser irradiance at a wavelength of 514 nm.

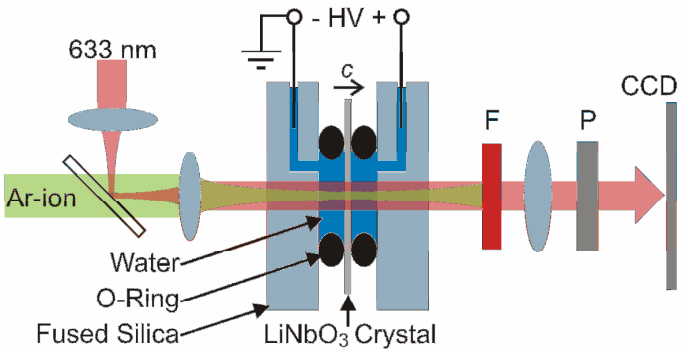

Figure 13. Transparent sample cell for simultaneous application of optical and electric fields.

Light-assisted poling (LAP[e]).

At the other extreme of laser exposure conditions, recent results have been obtained using a Ti:sapphire 100 fs laser source to investigate the process of LAP under very high peak power density. Figure 14 shows the result after etching in HF, in which a ~100 µm diameter domain has been formed in MgO:CLN at the remarkably low electric field of 100 V mm^{-1}, a value of less than 2% of the normal unilluminated nucleation field. These domains are not as easily visualized as those for the LAP[d] process, and are only revealed via HF etching after the LAP process. The laser average laser power was ~100 µW, for ~100 fs duration pulses at a repetition rate of 1 kHz. Light of wavelength 334 nm was used for figure 14, although a range of other wavelengths between 305 nm and 800 nm also process efficient LAP processing.

For the lowest wavelength of 305 nm, the incident power could be reduced to the extremely low value of 100 nW, a factor or 1000 less than used for figure 14. These experiments are ongoing, and hold considerable promise for further precise LAP experiments.

A final result in this fs LAP section is shown in figure 15, which was recorded in CLN. The letters were written by manually moving the position of the incident beam, hence the precision is less than can ultimately be achieved.

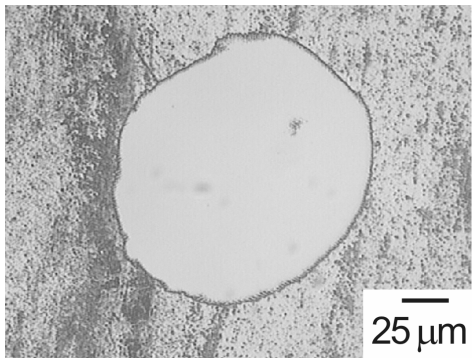

Figure 14. LAP domain formation on the –z face in 5-mol% MgO:CLN.

The domains are bulk, not surface as for other techniques, and an interesting and useful point concerns the lack of evidence of any crystal- imposed hexagonal symmetry. Deleterious post-formation domain spreading did not occur, indicating a very promising route for further study in formation and build-up of arbitrary 2-d domain patterns.

Figure 15. Domain patterning via fs LAP in CLN at a bias field of 16 kV mm^{-1}. Average power was 120 mW at a pulse repetition rate of 250 kHz.

All optical poling (AOP^{f}).

The final technique in this section relates to domain formation using direct laser addressing only, without the requirement for any simultaneous externally applied electric field[20]. If this approach can be perfected, and controllable domain features produced, this would represent a significant step in precision domain engineering.

Three laser sources have been used for this technique. The first was a Q-switched 10ns duration frequency quadrupled diode-pumped Nd:YAG operating at $\lambda = 266$ nm, with good beam quality and up to 5 mJ output energy per pulse. The second was a KrF excimer laser, with poor beam quality, operating at $\lambda = 248$ nm and up to 300 mJ per pulse. Finally, a frequency-doubled Q-switched Nd:YAG laser pumping a dye laser, which was subsequently also frequency doubled, producing mJ level output at ~7 ns duration, but tuneable over the wavelength region of ~292 nm to 329 nm. This last source was valuable for its tunability, as the output wavelength straddles the absorption edge of undoped CLN which lies around >310 nm. In all cases, selected parts of the incident beams were chosen to maximise available uniformity.

Figure 16a shows a representative example of a laser-exposed sample subsequently HF etched, in which the typical three-fold symmetry is immediately apparent. Exposures were made in undoped and MgO-doped congruent lithium niobate using fluences ranging from 100 mJ/cm^2 up to 10 J/cm^2, applying 1 to 1000 pulses. In all instances where any ablation or laser-induced surface topography was observed, similar UV-induced surface domains were formed. Figure 16b shows a magnified view of the central area, from which it is apparent that this patterning technique produces features that are far from random. We have used SFM techniques to investigate these patterns, and conclude from studies of laser-exposed, but unetched samples, that they are surface domains. Using focussed ion beam milling to probe the sub-surface region, the domain depths extend to almost 2 μm. These UV-induced surface domains are uniform, regular, of linewidths as small as 100 nm, and curiously grow along the –y directions only, never in the +y direction.

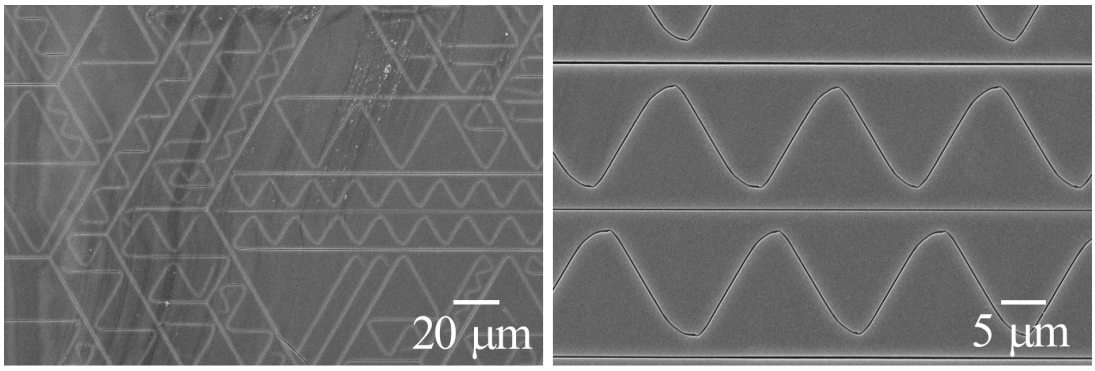

Figure 16. MgO-doped congruent lithium niobate exposed to 2 pulses of a KrF excimer laser at λ = 248 nm. (a) Large area self-organized UV-induced surface domains which extend across the entire laser-exposed region. (b) ~200 nm domain lines deflect away from other lines during growth, reliably reproducing similar features at each turn.

Detailed examination of figure 16b shows that the triangular domain regions situated between the three horizontal domain lines are incredibly self-similar. During growth, they have exactly the same closest-approach to the previously formed straight domains. Their shape on turning away from these lines is effectively identical. Their gradient and degree of curvature are identical. There is clearly ordered behaviour here, and from their growth habit, it is most likely that growth is electrostatically controlled. Fourier transformation shows some degree of preferred spatial feature size, and further work is in progress here on analysis of this behaviour.

The final part of this section concerns ordered periodic line features, and we have used phase masks to structure the incident laser light to try to achieve this. In figure 17 below, a phase mask with a period of ~750 nm was used to examine ordered domain growth along the y axis. It is clear that domain formation has only occurred at every fifth or sixth intensity maximum produced from the phase mask, another indication of perhaps an underlying electrostatic control mechanism. As earlier, these studies are being continued, to both elucidate the mechanism, and improve the fidelity, uniformity and spatial resolution.

CONCLUSION

Our progress to date in physical and domain engineering in doped lithium niobate has been presented. Applications where appropriate have been given and some recent experiments on laser-assisted and direct laser-written structures have been described. Domain features as small as

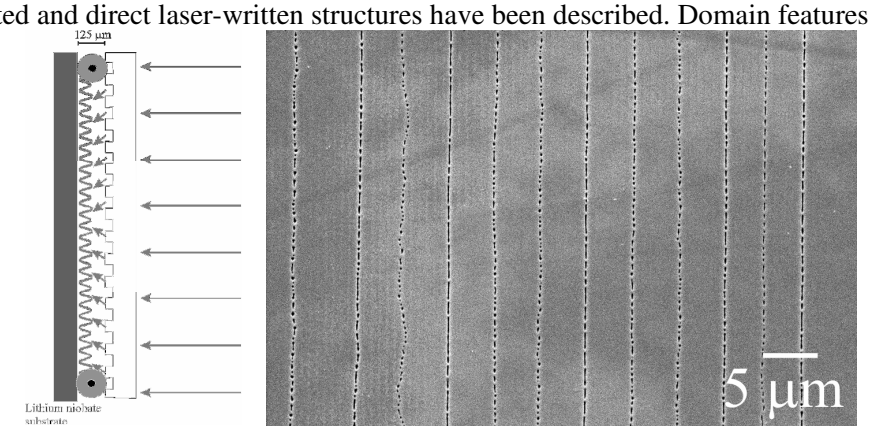

(a) (b)

Figure 17. +z face exposure from frequency doubled dye laser at a fluence of ~250 mJ cm^{-2} at λ= 297.5 nm. The contrast in figure (b) has been stretched to show underlying intensity maxima resulting from the phase mask producing a period Λ = 726 nm.

100nm in width have been achieved and progress made towards ordered, periodic arrays. While there is still more work required, laser-assisted techniques are seen to hold considerable promise for both domain patterning and also materials surface processing.

ACKNOWLEDGMENTS

The authors are grateful to the following for collaborative work within this programme: D. A. Scrymgeour and V. Gopalan, Penn State University, USA, for PFM work on surface domain analysis. T. Jungk, E. Soergel, M. C. Wengler, K. Buse, University of Bonn, Germany, for supply of the transparent poling cell, and DC-EFM domain analysis. I. Clark, CCLRC Rutherford Appleton Labs, UK, for laser access within the LSF laser programme. The Engineering and Physical Science Research Council, UK, (EPSRC) for research funding.

REFERENCES

[1] R. L. Byer, *J.Nonliner Opt. Phy. Mater*., "Quasi-phasematched nonlinear interactions and devices," **6(4)**, 549-92 (1997)

[2] V. Gopalan, T. E. Mitchell, Y. Furukawa, and K. Kitamura, "The role of nonstoichiometry in 180° domain switching of $LiNbO_3$ crystals," *Appl. Phys. Lett*., **72(16)**, 1981-3 (1998).

[3] L. Tian, V. Gopalan, and L. Galambos, "Domain reversal in stoichiometric $LiTaO_3$ prepared by vapour transport equilibration," *Appl. Phys. Lett*., **85(19)**, 4445-47 (2004).

[4] Y. Furukawa, K. Kitamura, S. Takekawa, K. Niwa, and H. Hatano, "Stoichiometric Mg:$LiNbO_3$ as an effective material for nonlinear optics," *Opt. Lett*., **23(24)**, 1892-94 (1998).

[5] S. Mailis, G. W. Ross, L. Reekie, J. A. Abernethy, and R. W. Eason, "Fabrication of surface relief gratings on lithium niobate by combined UV laser and wet etching," *Electron. Lett.,* **36(21)**, 1801-3 (2000).

[6] S. Mailis, C. Riziotis, I. T. Wellington, P. G. R. Smith, C. B. E. Gawith, and R. W. Eason, "Direct UV writing of channel waveguides in congruent lithium niobate single crystals," *Opt. Lett.,* **28(16)**, 1433-5 (2003).

[7] A. C. Muir, G. J. Daniell, C. P. Please, I. T. Wellington, S. Mailis, and R. W. Eason, "Modelling of UV laser-induced optical waveguide formation via lithium ion thermal-diffusion in $LiNbO_3$," to be submitted to Appl. Phys. A.

[8] A. J. Boyland, S. Mailis, J. M. Hendricks, P. G. R. Smith, and R. W. Eason, "Electro-optically controlled beam switching via total internal reflection at a domain-engineered interface in $LiNbO_3$," *Opt. Commun.,* **197(1-3)** 193-200 (2001).

[9] C. Sones, S. Mailis, V. Apostolopoulos, I. E. Barry, C. B. E. Gawith, P. G. R. Smith, and R. W. Eason, "Fabrication of piezoelectric micro-cantilivers in domain engineered $LiNbO_3$ single crystals," *J. Micromech. Microeng.,* **12(1)**, 53-7 (2002).

[10] A. C. Busacca, C. L. Sones, V. Apostolopoulos, R. W. Eason, and S. Mailis "Surface domain engineering in congruent lithium niobate single crystals: a route to sub-micron periodic poling," *Appl. Phys. Lett.*, **81(26)**, 4946-8 (2002).

[11] A. C. Busacca, C. L. Sones, R. W. Eason, and S. Mailis, "First-order quasi-phase-matched blue light generation in surface-poled Ti-indiffused lithium niobate waveguides," *Appl. Phys. Lett.,* **84(22)**, 4430-2 (2004).

[12] S. Mailis, P. G. Lagoudakis, M. Paturzo, J. D. Mills, J. Feldmann, and R. W. Eason, "Second harmonic generation enhancement in lithium niobate micro-tips," *CLEO/QELS 2005,* CMN4, (2005).

[13] A. J. Boyland, S. Mailis, I. E. Barry, R. W. Eason, and M. Kaczmarek, "Latency effects and periodic structures in light induced frustrated etching of Fe:doped $LiNbO_3$," *Appl. Phys. Lett.,* **77(18)**, 2792-4 (2000).

[14] J. G. Scott, A. J. Boyland, S. Mailis, C. Grivas, O. Wagner, S. Lagoutte, and R. W. Eason, "Self ordered sub-micron structures in Fe-doped $LiNbO_3$ formed by light-induced frustration of etching (LIFE)," *Appl. Surf. Sci.,* **230(1-4)**,138-50 (2004).

[15] S.Mailis, C.Riziotis, P.G.R.Smith, J.G.Scott, R.W.Eason, "Continuous wave ultra violet radiation induced frustration of etching in lithium niobate single crystals," *Appl. Surf. Sci.,* **206(1-4)**, 46-52 (2003).

[16] S. Mailis, C. L. Sones, J. G. Scott, and R. W. Eason, "UV laser-induced ordered surface nanostructures in congruent lithium niobate single crystals," *Appl. Surf. Sci*., **247(1-4)**, 497-503 (2005).

[17] P. T. Brown, G. W. Ross, R. W. Eason, and A. R. Pogosyan, "Control of domain structures in lithium tantalate using interferometric optical patterning," *Opt. Commun.,* **163**, 310-6 (1999).

[18] M. C. Wengler, B. Fassbender, E. Soergel, and K. Buse, "Impact of ultraviolet light on coercive field, poling dynamics and poling quality of various lithium niobate crystals from different sources," *J. Appl. Phys*, **96 (5)**, 2816-20 (2004).

[19] C. L. Sones, M. C. Wengler, C. E. Valdivia, S. Mailis, R. W. Eason, and K. Buse, "Light-induced order-of-magnitude decrease in the electric field for domain nucleation in MgO-doped lithium niobate crystals," *Appl. Phys. Lett.*, **86(21)**, 212901 (2005).

[20] C. E. Valdivia, C. L. Sones, J. G. Scott, S. Mailis, R. W. Eason, D. A. Scrymgeour, V.Gopalan, T. Jungk, E. Soergel, and I. Clark, "Nanoscale surface domain formation on the +z face of lithium niobate by pulsed UV laser illumination," *Appl. Phys. Lett.*, **86(2),** 022906 (2005).

F.1.7 Design and Performance of a ZnSe Tetra-Prism for Homogeneous Substrate Heating using a CO_2 Laser for Pulsed Laser Deposition Experiments

T.C. May-smith, A. C. Muir, M. S. B. Darby, and R. W. Eason. Design and Performance of a ZnSe Tetra-Prism for Homogeneous Substrate Heating using a CO_2 Laser for Pulsed Laser Deposition Experiments. *Applied Optics*, **47**, (pages not yet designated) (2008).

During my time working on this thesis I was approached by the Pulsed Laser Deposition group for help in the modelling of the effectiveness of a novel substrate heating system for pulsed laser deposition experiments. The system comprised of a CO_2 laser and a prism that could split and translate the four quadrants of the laser beam such that they could be incident on the substrate as a square homogeneous beam which was named the tetra-prism. My role in the work was to model the heat source provided by the beam and the subsequent heating of the substrate, taking into account the losses at the substrate faces through radiative emission. The effect of interference and diffraction within the source function was investigated to various degrees which created three different source functions for investigation, one with no interference or diffraction effects, one with Fresnel diffraction from the sharp interfaces of the prism and one with both Fresnel diffraction and interference. Other heat sources of an un-transformed Gaussian beam, a raster-scanned focused beam and a fully homogenised beam were also compared. It was found that interference effects were insignificant but that diffraction effects were not and that the tetra-prism actually produced the ideal beam shape since it could compensate for the increased losses at the substrate corners where the surface area to volume ratio is highest.

This paper has been accepted for publication in Applied Optics, however at the time of writing the page proofs are still being produced by the publishers.

Design and performance of a ZnSe tetra-prism for homogeneous substrate heating using a CO_2 laser for pulsed laser deposition experiments

T. C. May-Smith,* A. C. Muir, M. S. B. Darby, and R. W. Eason

Optoelectronics Research Centre, University of Southampton, Highfield, Southampton, SO17 1BJ, UK.

*Corresponding author: tcms@orc.soton.ac.uk

Received 6 August 2007; revised 9 January 2008; accepted 26 February 2008;
posted 29 February 2008 (Doc. ID 85908); published 0 MONTH 0000

We report on the design and performance of a ZnSe tetra-prism for homogeneous substrate heating using a continuous wave CO_2 laser beam in pulsed laser deposition experiments. We discuss here three potential designs for homogenizing prisms and use ray-tracing modeling to compare their operation to an alternative square-tapered beam-pipe design. A square-pyramidal tetra-prism design was found to be optimal and was subjected to modeling and experimental testing to determine the influence of interference and diffraction effects on the homogeneity of the resultant intensity profile produced at the substrate surface. A heat diffusion model has been used to compare the temperature distributions produced when using various different source intensity profiles. The modeling work has revealed the importance of substrate thickness as a thermal diffuser in producing a resultant homogeneous substrate temperature distribution.

OCIS codes: 310.0310, 310.1860, 220.0220, 230.0230, 230.5480.

1. Introduction

Substrate heating is critical to the pulsed laser deposition (PLD) process if high quality epitaxial crystal growth is to be achieved without the need for postannealing. For films to be of a consistent quality both across the substrate and throughout the film depth, a suitable technique must be adopted which is capable of heating substrates homogeneously. Poor spatial homogeneity can result in variable quality growth in selective areas, which can increase stresses in the film and can also lead to areas of film with a higher propagation loss (in the case of optical films) and/or areas of film where the laser-ion valence state is not as desired (in the case of doped films). Temporal instability can also lead to the occurrence of distinct layers within a thick film (≥ tens of micrometers) where the crystal structure or even phase may vary from layer to layer. Such unintended layered growth can cause problems of increased fragility when the film is subsequently polished in preparation for waveguiding experiments, and waveguide mode distortion may occur if the problem is significant enough that the refractive index varies appreciably from layer to layer. The use of long deposition runs (>2 h with our apparatus) places a requirement on the efficiency of substrate heating systems; leakage of radiation resulting in heating of the chamber walls must be minimal to avoid outgassing from any previously deposited material and/or thermal expansion of the chamber, which can lead to degradation and eventual cracking of vacuum windows.

The requirements placed on any substrate heating system make a remote radiative technique the obvious choice. CO_2 lasers make excellent heat sources because the infrared wavelengths (e.g., 10.6 μm) are absorbed well by most materials and the heat is highly directional, allowing it to be steered only to where it is needed with high efficiency. CO_2 laser heating holds a significant advantage over resistive wire and lamp-based techniques when heating relatively small substrates (e.g., 10 mm × 10 mm). The

0003-6935/08/120001-01$15.00/0

power required to reach ~1373 °K (1100 °C, needed to grow Al_2O_3 in the alpha-alumina sapphire phase) with such small sized substrates is only ~25 W and is easily obtainable with commercially available CO_2 lasers. Achieving the same temperature using resistive wire or lamp-based techniques is practically impossible without significant chamber heating, filament burnout, or oxidation occurring.

However, two problems need to be overcome before a CO_2 laser can be used as part of a reliable and flexible substrate heating system. First, the substrate must be held so that heatsinking is minimized or else the resultant temperature variation may lead to cracking because of differential thermal expansion. Second, the CO_2 laser beam must be transformed to produce an ideally flat-top square intensity profile so that homogeneous heating occurs. These two problems have been circumvented in the past by using metallic blocks [1,2] as substrate holders and heating the blocks with the CO_2 laser. The blocks act as heat diffusers and allow substrates to be heated homogeneously, but this method then loses some of the advantages of the indirect heating approach. In particular, the substrate temperature obtainable will be limited because of the large surface area of the block, and the laser powers required to reach typical deposition temperatures may become so high as to result in significant chamber heating.

Our solution to the substrate holder problem is to machine a cradle out of alumina ceramic tubing. For vertically held substrates, the design shown in Fig. 1 has been optimized so that substrates can be heated without any significant adverse heatsinking occurring. The cradle also allows a large amount of the substrate surface to be utilized and only two small notches (each approximately 1 mm × 1 mm) where film does not grow occur on each side of the substrate.

The problem of beam homogenization is certainly not a new one, and there have been several previous reported attempts at a solution using various approaches. If the problem is simplified to the requirement of a circular flat-top intensity beam, a combination of aspheric lenses [3] or cylindrical lenses [4] may be used to produce a suitably homogenized beam. The addition of a square aperture can allow a square beam to be produced using this approach, but this would then lead to a significant amount of radiation being wasted. Homogenous heating of sapphire substrates using a reflective square-tapered beam-pipe for PLD experiments has been reported [5], and this technique is modeled and discussed later on as a standard to be reproduced. A considerable problem with this technique however is that substrates must be held very close to the beam-pipe aperture (few millimeters separation). This means that it is generally inevitable that the beam-pipe must be placed inside the deposition chamber, where it gradually gets coated by stray deposit, and continuous repolishing of the internal faces is necessary for efficient operation to be maintained. A slightly more advanced approach is to use a square beam-pipe in a kaleidoscope arrangement [6]. Such a setup can make a very effective beam homogenizer, but in general cannot be placed close to the substrate inside a deposition chamber where gradual coating of the optical surfaces will be unavoidable.

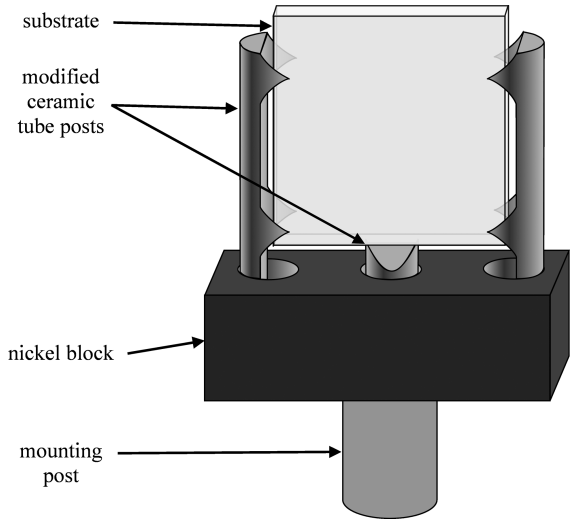

Fig. 1. Diagram of a vertical substrate holder design based on machined alumina ceramic tubes.

Our solution to the problem of beam homogenization has previously been to use a two-axis mirror scanner to raster scan the CO_2 laser beam over the back face of the substrate [7], leaving the front substrate face available for deposition and effectively using the substrate itself as a thermal diffuser. The delay for each scanning point can be adjusted so that the beam spends slightly more time around the edges to counteract the higher rate of radiative emission caused by the increased surface area to volume ratio. As an example of how effective the combination of substrate cradle and raster-scanning mirrors has been, depositions have been performed at ~1073 °K (800 °C) for a continuous period of up to 6 h with no apparent chamber heating throughout the deposition runs. While we have used this technique successfully, the capital cost of such a system is relatively high and it is perhaps unnecessarily complicated, especially when compared to the simpler alternative technique of beam transformation presented here.

Where a homogeneous intensity profile is required without any significant intensity modulation (that can result from interference, for example), a diffractive optical element consisting of a binary surface relief phase grating structure can be used [8]. Such a structure can be made to map sections of the input beam continuously to make a homogeneous output beam unaffected by interference. Since, however, it is known that a certain degree of heating beam intensity modulation can be tolerated from our experience with raster-scanned mirror setups, such a complicated optical structure should not be necessary for

the production of a square beam for substrate heating purposes. The concept of beam folding has recently been discussed in detail as a simple passive optical route to achieving a homogeneous flat-top intensity profile [9]. A suitable combination of biprisms can be used to section an input beam and translate the sections so that they sum at an output plane to give the desired intensity profile [10]. Where a square profile is required, as opposed to a rectangular profile, the optical arrangement can be simplified by using a prism with four facets [11]. It is well known that the beam folding approach suffers from the effects of interference and Fresnel diffraction, but, as we will go on to discuss later, this is not necessarily a problem for the application intended here.

The solution presented here uses a beam folding prism to convert the Gaussian intensity profile of a standard CO_2 laser beam into a square approximately flat-top intensity profile optimal for heating square substrates. A material transparent at a wavelength of 10.6 μm, such as ZnSe, can be used, and the prism can additionally be antireflection coated for the CO_2 laser wavelength for improved efficiency. The prism can be designed to produce the square intensity distribution at any specified distance from the substrate (limited only by intensity modulation caused by interference), and this may be outside the chamber to avoid undesirable coating during depositions. As with the raster-scanning laser heater used previously, the prism directs heat onto the back face of the substrate. This is important because of interference effects that could otherwise lead to an inhomogeneous deposition face temperature if it were not for the role of substrate thickness as a thermal diffuser. When substrate rotation is desired, the prism can even be mounted as a vacuum window, allowing a suitable rotary vacuum feed-through system to simultaneously rotate substrate and prism. This latter mode of operation is highly desirable and would be challenging to achieve via alternative methods.

Three potential prism facet designs have been considered and ray-tracing modeling has been used to assess the basic incoherent operation of each design compared to a more conventional square-tapered beam-pipe. A heat diffusion model has been constructed to compare the substrate temperature homogeneity achieved with different beam homogenizing devices. An untransformed Gaussian laser beam is modeled to illustrate the need for beam homogenization. The source functions produced by a square-tapered beam-pipe and raster scanning are modeled to set the benchmark of temperature homogeneity that must be reproduced with a prism. The most favorable prism design, a square-pyramidal tetra-prism, is then modeled with and without coherence effects, and the results from experimental testing of a prototype device are presented. Finally, the importance of the substrate thickness acting as a thermal diffuser is illustrated by a comparison of source intensity modulation to substrate temperature inhomogeneity for a range of different substrate thicknesses.

2. Device Design

A. Ray-Tracing Modeling

The beam propagation modeling software package ZEMAX has been used to model the averaged intensity beam profiles shown in the following sections. A large number of rays (1 000 000 was sufficient to produce relatively clear intensity profiles) were propagated through the prisms with start and end positions recorded for each ray. The rays, all initially travelling parallel to the optical axis, were randomly generated with different intensities to simulate the Gaussian beam of the CO_2 laser. It is important to note that this initial ray-tracing modeling work does not account for the effects of diffraction or interference because the initial interest is in the problem of producing an averaged intensity flat-top square profile. The effects of diffraction and interference will be discussed in Section 3.

B. Square-Tapered Beam-Pipe Comparison

A square-tapered beam-pipe has been used with good success in the past [5] and the averaged intensity profile from such a device represents an effective benchmark that needs to be equalled or bettered using a prism. Although beam-pipe designs represent a good solution as a beam homogenizer, they have a short working distance that restricts their use to inside the chamber only. Any optical device that can only be used inside the chamber has the obvious practical limitation that it will be gradually coated over time from the deposition process and its performance will degrade as a consequence. Crucially, the proposed prism designs can have longer working distances (many tens of centimeters) that allow them to be used outside the chamber and this is why one of these designs is targeted as the proposed end device (it should be noted here, however, that intensity modulation due to interference may become a significant issue at much greater distances since it is dependent on the incident angle of the intersecting beam sections).

A beam-pipe was made out of four trapezoidal brass sections and the internal sides were optically polished. A cross section of the beam-pipe device is shown in Fig. 2(a) with some rays drawn to indicate its basic operation. A map of how the device reflects different parts of the beam onto the substrate is shown in Fig. 2(b). Since the beam-pipe aperture is necessarily much larger than the laser beam size, the beam was expanded before entering the beam-pipe. We have operated the device with it butted as close to the substrate holder assembly as possible at a distance of about 1 mm from the substrate surface. The modeled averaged intensity profile produced at this distance is shown in Fig. 3(a). It can be seen that the beam-pipe is quite effective in producing a homogeneous square intensity profile.

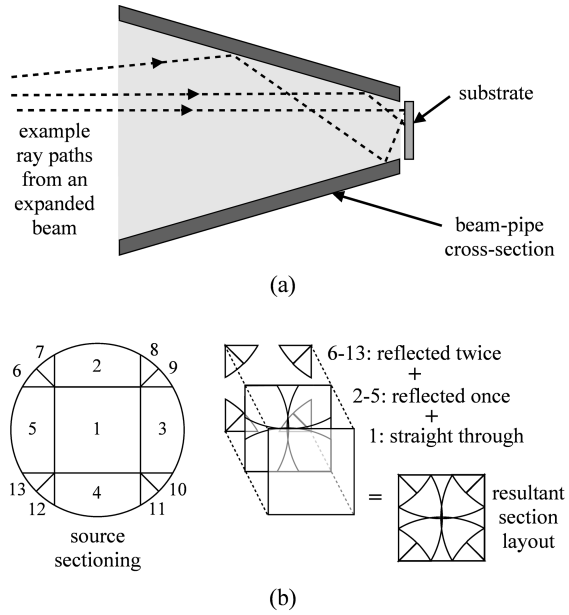

Fig. 2. (a) Cross section of a square-tapered beam-pipe with some rays drawn to indicate its basic operation. (b) Map showing how the beam-pipe device reflects different parts of the beam onto the substrate.

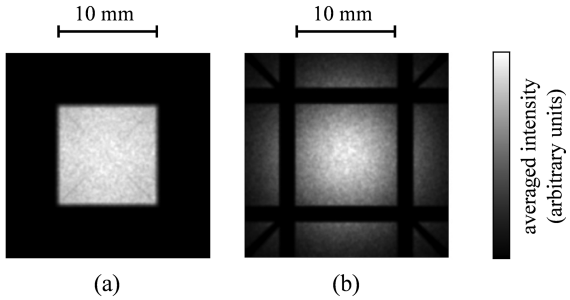

Fig. 3. Modeled averaged intensity beam profiles at (a) 1 mm and (b) 40 mm from the end of the square-tapered beam-pipe.

However, the output from the beam-pipe is highly divergent and hence the device has a very limited working distance. The modeled averaged intensity profile shown in Fig. 3(b) clearly illustrates how the beam profile diverges rapidly as the distance from the substrate is increased to 40 mm. The actual intensity profile on the substrate will also depend on interference effects, but since the prism intensity profiles will also be affected by interference, it is not of concern at this initial stage of comparison.

C. Prism Designs Under Consideration

A selection of custom ZnSe prisms with differently cut facets are now discussed as an alternative method of beam homogenization. There are two things to consider when designing such a prism. First, the basic choice and arrangement of facets will determine how the beam will be translated from a Gaussian profile into a flat-top square profile. Second, the facet angles will determine the working distance of the prism (defined as the distance from the prism at which the optimum averaged intensity profile is achieved). Choices for facet arrangements will be discussed first and facet angle considerations will be discussed afterward for the prism design chosen as the end device in Subsection 2.D. The angles for different facets on each prism design should be optimized to make the working distance the same for each design. However, for this initial comparison the facets can all be made with the same angle and different distances can be examined to find the optimum value for each design. Intensity profiles that are achieved at 50%, 100%, and 150% of this optimum working distance can then be compared. This makes a fair comparison of how the different designs transform the beam, but without the need for more complex facet designing.

The first prism under consideration is the simplest, with only four facets used for beam transformation. This tetra-prism shape is shown in Fig. 4(a) and a map of how the device sections and translates the beam is shown in Fig. 4(b). The addition of a square facet at the apex of the tetra-prism produces the second design for consideration and is referred to as a 'square-top tetra-prism' and shown in Fig. 5(a). A map of how this second device translates the beam is shown in Fig. 5(b). The square-top tetra-prism is limited in that it produces wings outside of the main homogeneous square. The addition of four further facets allows this problem to be overcome and this third design, referred to as a 'square-top octa-prism,' is shown in Fig. 6(a). A map of how this final device

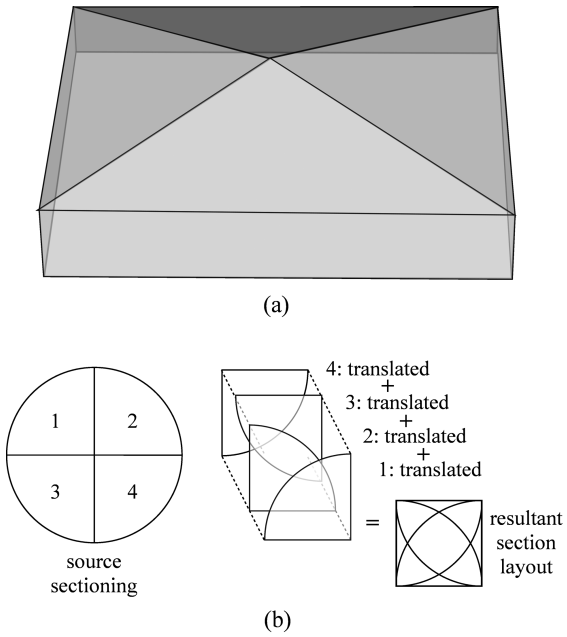

Fig. 4. (a) Line drawing of the tetra-prism. (b) Map showing how the tetra-prism translates different parts of the beam.

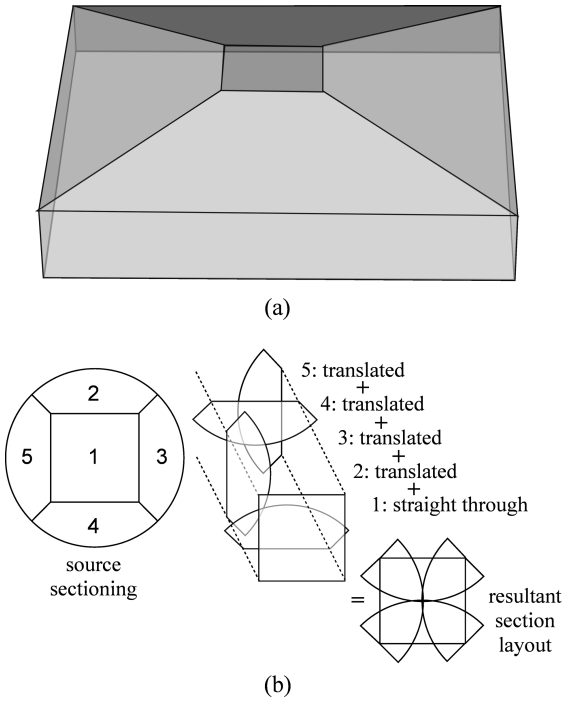

Fig. 5. (a) Line drawing of the square-top tetra-prism. (b) Map showing how the square-top tetra-prism translates different parts of the beam.

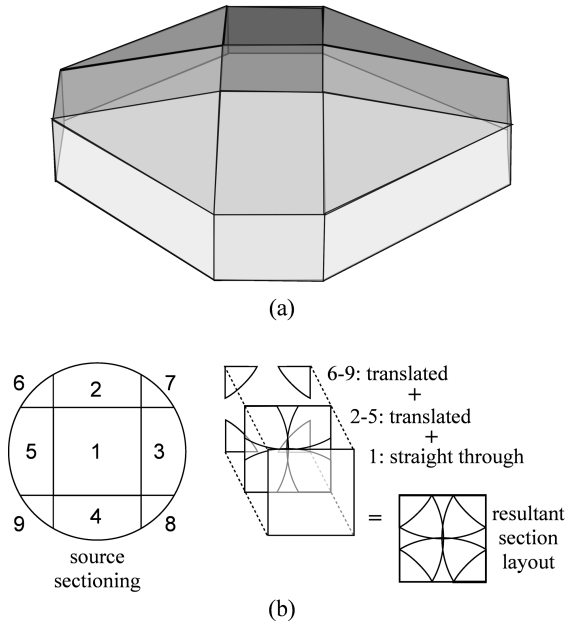

Fig. 6. (a) Line drawing of the square-top octa-prism. (b) Map showing how the square-top octa-prism translates different parts of the beam.

under consideration translates the beam is shown in Fig. 6(b).

D. Comparison Using Ray-Tracing Modeling

Averaged intensity profiles for each prism design under consideration have been modeled at 50%, 100%, and 150% of the working distance in each case and these profiles are shown in Fig. 7(a)–7(c) for the tetra-prism, square-top tetra-prism, and square-top octa-prism, respectively. The modeled averaged intensity profiles in Fig. 7 show that the tetra-prism and the square-top octa-prism are both effective at generating a homogeneous square profile. The only difference is the way that the square profile is constructed; the tetra-prism makes a square from quadrants of the beam, whereas the square-top octa-prism makes a square from some straight-through radiation combined with translated sides and corners.

A comparison of the prism efficiencies can be made by measuring how much of the power incident on each prism subsequently reaches the desired central square area (10 mm × 10 mm for our substrates) at the working distance. Modeling revealed these efficiencies to be 95%, 91%, and 99% for the tetra-prism, the square-top tetra-prism, and the square-top octa-prism, respectively. Although the square-top octa-prism would appear to be the best design because it transfers incident power with a significantly higher efficiency into the desired homogeneous heating square, the tetra-prism design is preferable because it offers a significant advantage over the other two designs. The facets for both the square-top designs would have to be specified for a fixed working distance, beam waist, and substrate size, and the usefulness of the prisms outside of these design parameters would be limited. The tetra-prism design is, however, more practical because the distance from the prism to the substrate can be changed to heat different sized substrates if the beam waist is adjusted accordingly to reoptimize the profile produced. Because of this advantage and the relative simplicity of the design and manufacture, the tetra-prism design has been selected as the optimum.

E. Determination of Facet Angles for Square-Pyramidal Tetra-Prism

The desired working distance and size of substrate determine the facet angle required. For simplicity only a nondivergent input laser beam is considered here. Once the working distance and substrate size have been decided, the required angle of the tetra-prism facets can be calculated using Eq. (1), where n_1 is the refractive index of the tetra-prism material (=2.4 if ZnSe is used) at the laser wavelength (=10.6 μm for the CO_2 laser in our experimental setup), n_2 is the refractive index of the surroundings (=1.0 if air), θ is the angle of the tetra-prism facets, h is the substrate width, and D is the working distance. The small angle approximation of $\sin(x) = x$

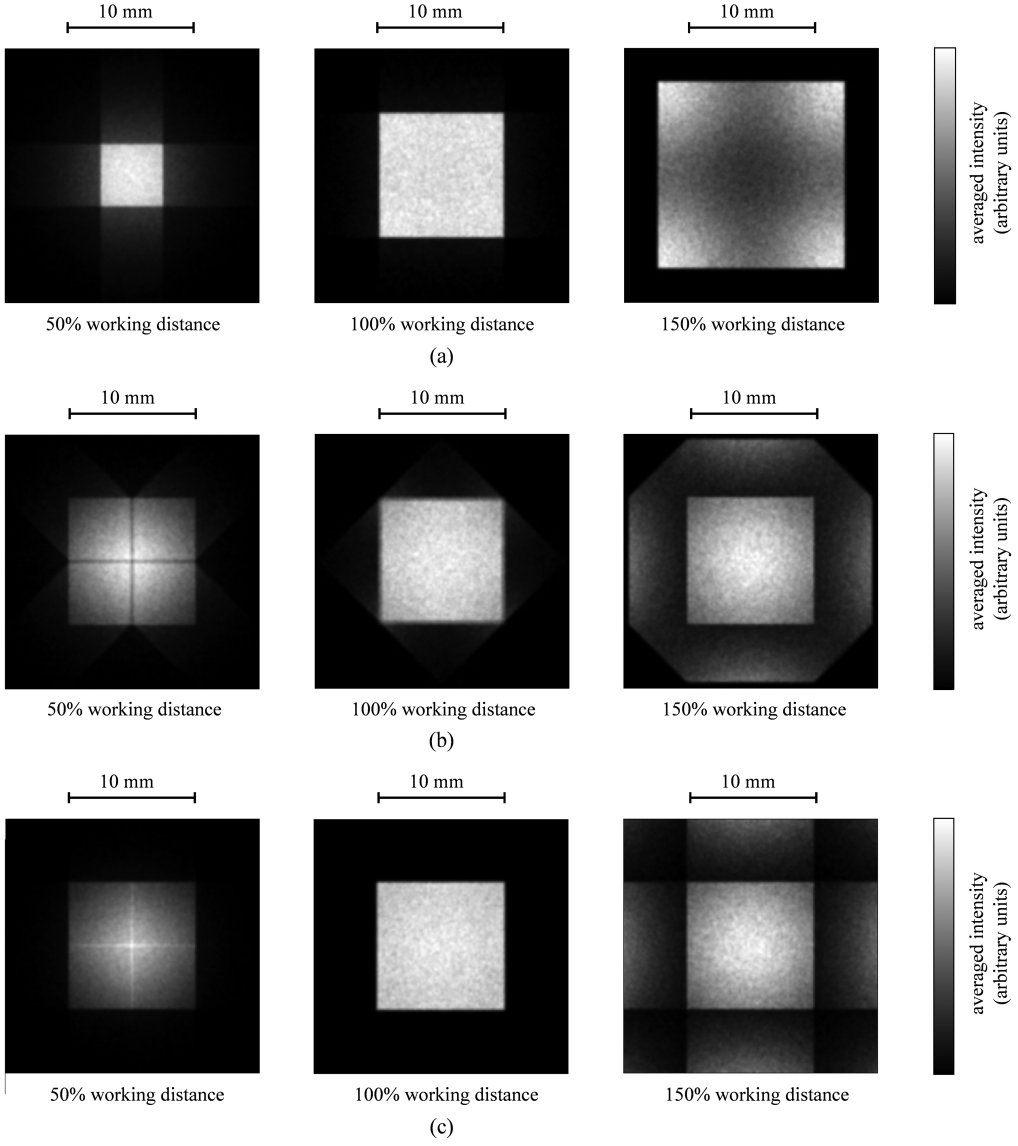

Fig. 7. Averaged modeled intensity profiles for each prism design under consideration at 50%, 100%, and 150% of the working distance in each case: (a) tetra-prism, (b) square-top tetra-prism, and (c) square-top octa-prism.

has been used to derive Eq. (1). The various parameters can be seen in Fig. 8.

$$\sin^{-1}\left(\frac{n_1\theta}{n_2}\right) - \theta = \tan^{-1}\left(\frac{\sqrt{2}h}{2D}\right) \qquad (1)$$

The actual performance of the tetra-prism (i.e., the flatness of the averaged intensity profile) must finally be optimized by changing the initial beam waist and can also be tuned by allowing the beam to diverge slightly if desired. The averaged intensity profiles shown in Fig. 9 are for three different initial beam waists (radius at $1/e^2$ intensity), 3.0 mm, 9.0 mm, and 27.0 mm for (a), (b), and (c), respectively, to illustrate the effect of changing beam size. A beam waist that is too small results in an unusable heat source intensity profile that would lead to an inhomogeneous substrate temperature distribution,

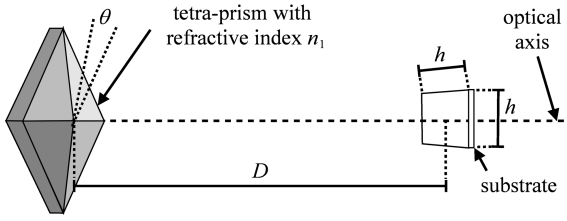

Fig. 8. Illustration of parameters used in Eq. (1).

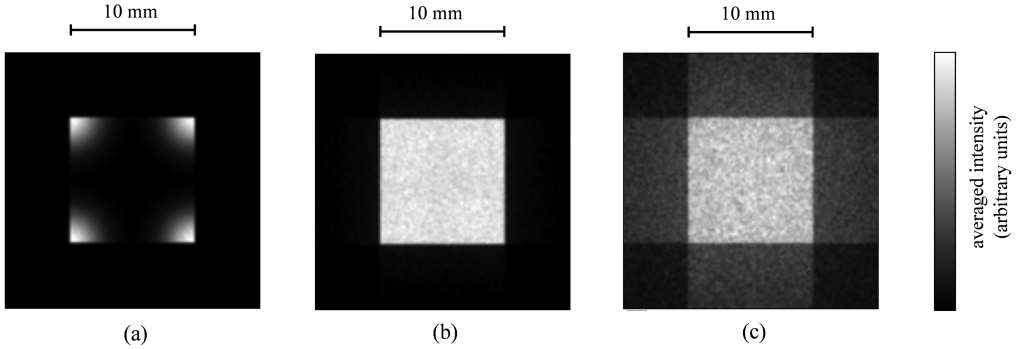

Fig. 9. Averaged modeled intensity profiles for three different initial beam waists to illustrate the effect of changing beam size: (a) 3.0 mm, (b) 9.0 mm, and (c) 27.0 mm.

whereas, a beam waist that is too large leads to a significant increase in wasted radiation, though the central square may still be usable in this case. Once the design has been fixed, the initial beam waist and the distance from the tetra-prism to the substrate can be changed to adjust the profile to heat different sized substrates.

A tetra-prism was fabricated using ZnSe to allow us to further evaluate the design and experimental performance. We used 10 mm × 10 mm sized substrates and the chamber dimensions required a working distance of about 30 cm. The required tetra-prism facet angle was calculated to be approximately 1.0° using Eq. (1). The tetra-prism fabrication was subject to normal manufacturing tolerances and the four facet angles were polished to an angle of $1.0 \pm 0.1°$. This tetra-prism setup has been modeled in Section 3 and has been used for testing in Section 4 on experimental tests.

3. Three-Dimensional Heat Diffusion Modeling with Various Source Functions

A. Three-Dimensionsal Substrate Heat Diffusion Model

The commercial finite element modeling software package COMSOL MULTIPHYSICS has been used to construct a three-dimensional (3D) computer model describing the heat flow in a $Y_3Al_5O_{12}$ (YAG) substrate (10 mm × 10 mm × 0.5 mm) that results from CO_2 laser heating with various different source intensity distributions. The model has been used to evaluate and compare the ability of different heat source intensity functions to produce homogeneous temperature distributions on the substrate deposition face when heating the opposite back face of the substrate.

The heat flow within the substrate is governed by the heat diffusion equation, which, in the steady state with constant thermal conductivity, is given by

$$-k\nabla^2 T = Q, \tag{2}$$

where k is the thermal conductivity (k=3.5 $Wm^{-1}K^{-1}$ at 1073 °K [12]), T is the temperature in Kelvin, and Q is the heat source function. For simplicity, and since the substrates are heated in vacuum, it can be assumed that heat loss at the substrate surfaces is due only to radiative emission. This gives the nonlinear boundary equations for the model of

$$\mathbf{n} \cdot (k\nabla T) = \varepsilon\sigma(T_{\text{amb}}^4 - T^4), \tag{3}$$

where $\mathbf{n}$ is a unit vector directed with the inward normal to the surface, ε is the emissivity = 0.45, σ is the Stefan-Boltzmann constant, and T_{amb} is the ambient temperature around the substrate=293 °K. Emissivity is not well documented for YAG at high temperatures so the value above was estimated from a separate calibration of temperature involving the melting of thin, high purity metal foils on a YAG substrate. The effect of a small error in this would be to alter the power values calculated for reaching specific substrate temperatures and would not significantly affect the qualitative assessment of temperature distributions. The fact that the right hand side of Eq. (3) is negative for $T > T_{\text{amb}}$ indicates that the heat flux direction will be out of the surface.

Zero heat flux boundary conditions were introduced on the internal boundaries so that the four-fold rotational symmetry of the substrate could be utilized to make a reduced geometry, allowing the computational modeling to be performed on one substrate quadrant and then copied to make the full size source profiles and temperature distributions. The final requirement for the modeling is the heat source function which will depend upon the beam homogenization technique under consideration and will be introduced in the respective following sections.

For the modeling of different source functions that follows, the power of the incident beam was varied such that $T = 1073 \pm 0.5$ °K at the center of the substrate deposition face and the beam waist was varied along with any source specific parameters such that the standard deviation of the substrate temperature distribution was minimized. The minimum standard deviation, range, and mean of the temperature distribution across the deposition face were then taken to quantify the substrate temperature homogeneity. These conventions were used to enable direct comparisons between the source functions and the respective resultant substrate temperature distributions. The same temperature range has been used for

all of the shaded temperature contour plots to allow the various distributions to be compared directly. The only exception to this rule is the case of the temperature distribution produced by the untransformed Gaussian source, which had a significantly greater range than the other distributions.

B. Untransformed Gaussian

Initially, to clearly illustrate the need for any beam homogenization device, the temperature distributions produced by an untransformed Gaussian beam have been calculated for a range of beam waists. In this case the heat source function is given by

$$Q = \frac{2P}{\pi w^2} \exp\left[-2\frac{(x^2+y^2)}{w^2}\right]\delta(z), \tag{4}$$

where P is the power of the incident laser beam, w is the beam waist, x and y are Cartesian axes, and it has been assumed that the optical absorption can be modeled as a delta function, since the absorption depth is much less than the substrate thicknesses under consideration here (an absorption coefficient of $200\,\mathrm{cm}^{-1}$ at a wavelength of $10.6\,\mu\mathrm{m}$ [13] gives a $1/e$ absorption depth of $50\,\mu\mathrm{m}$). The investigation has been limited to beam waists up to half the width of the substrate (5.0 mm) because beam waists larger than this are not practical, since they would result in significant wastage of radiation and heating of the chamber and other chamber parts. As an example, the amount of beam wastage with a waist of 5.0 mm is 4.4%, giving this untransformed Gaussian model a comparable heat transfer efficiency to the tetra-prism discussed in Section 2.

The minimum standard deviation of 43 °K was found to occur for a beam waist of 5.0 mm and a power of 5.6 W with a corresponding mean temperature of 978 °K and a temperature range of 173 °K. A profile of the untransformed Gaussian source function is shown in Fig. 10(a) and the deposition face temperature distribution is shown in Fig. 10(b). It can be seen in Fig. 10(b) that most of the substrate surface is at a temperature more than 50 °K below that of the substrate center. Such an inhomogeneous temperature distribution would result in severely reduced quality crystal growth in the cooler areas and would not be acceptable for use in PLD experiments. This clearly indicates the requirement for a beam homogenization technique if a CO_2 laser is to be successfully used as a heat source.

C. Square-Tapered Beam-Pipe

The beam profile obtained from the square-tapered beam-pipe discussed in Section 2 can be used in the heating model as an initial benchmark of beam homogenizer performance. The beam-pipe is highly effective at creating a homogeneous intensity profile at its working distance and so can be modeled by a source function with a constant energy density profile, as shown in Fig. 11(a). Figure 11(b) shows the resultant deposition face temperature distribution using such a flat source function with a power of 7.2 W. The standard deviation of the temperature distribution was found to be 7.1 °K with a mean temperature of 1063 °K and a range of 34 °K. This is a significant improvement on the untransformed Gaussian beam case, which had a standard deviation approximately six times greater and a temperature range about five times greater. However, it is clear that improvement may be made here by altering the heat intensity at the substrate edges, and, since this cannot be done with the beam-pipe, this illustrates the limitation of this device.

D. Raster-Scanned Gaussian

The second initial benchmark to compare the operation of the tetra-prism against is a raster-scanned Gaussian beam. Such a system has been experimentally optimized previously to use a grid of 6×6 scanning points spaced evenly across the substrate surface. Rather than model the high speed movement of one beam across the substrate, we can instead approximate the process by dividing the laser power into the grid points and making them constant in time. This approximation is valid when the scan speed is fast (<100 ms to scan one complete cycle, which is faster than the thermal diffusion time in YAG) and the grid point dwell time is significantly longer than the transit time of the beam between grid points. In this case, the source function can be built without coherence effects because in reality there is only one laser beam and one spot at any one time. The source can be described by

$$Q = \frac{2P}{36\pi w^2}\sum_{i,j=1}^{3}\left[\begin{array}{l}\exp\left(-\frac{2}{w^2}\{[x+(i-0.5)d]^2+[y+(j-0.5)d]^2\}\right)\\ +\exp\left(-\frac{2}{w^2}\{[x+(i-0.5)d]^2+[y-(j-0.5)d]^2\}\right)\\ +\exp\left(-\frac{2}{w^2}\{[x-(i-0.5)d]^2+[y+(j-0.5)d]^2\}\right)\\ +\exp\left(-\frac{2}{w^2}\{[x-(i-0.5)d]^2+[y-(j-0.5)d]^2\}\right)\end{array}\right], \tag{5}$$

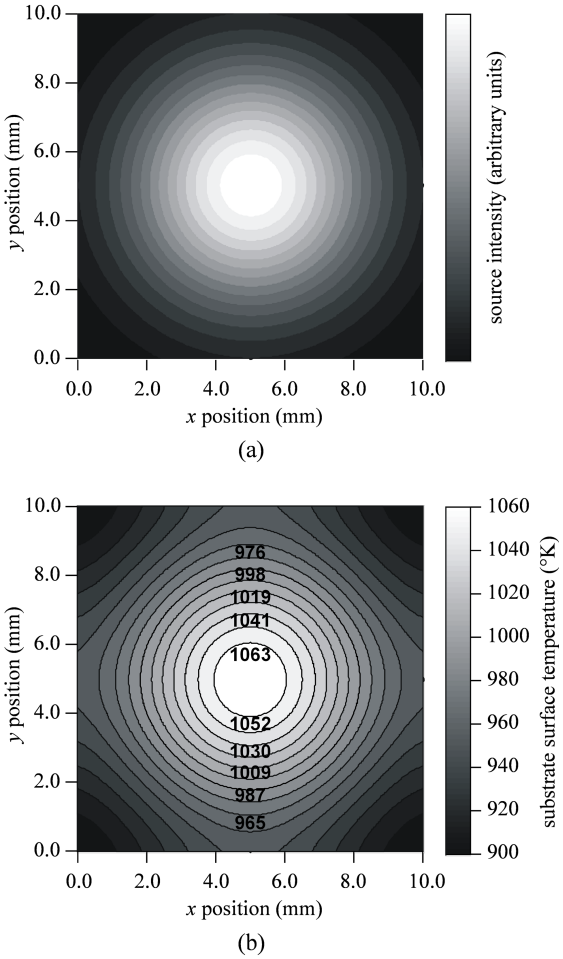

Fig. 10. (a) Untransformed Gaussian beam source function with $w = 5.0\,\text{mm}$ and $P = 5.6\,\text{W}$. (b) Resultant modeled temperature distribution of the substrate deposition face, standard deviation = 43 °K, mean = 978 °K, and range = 173 °K.

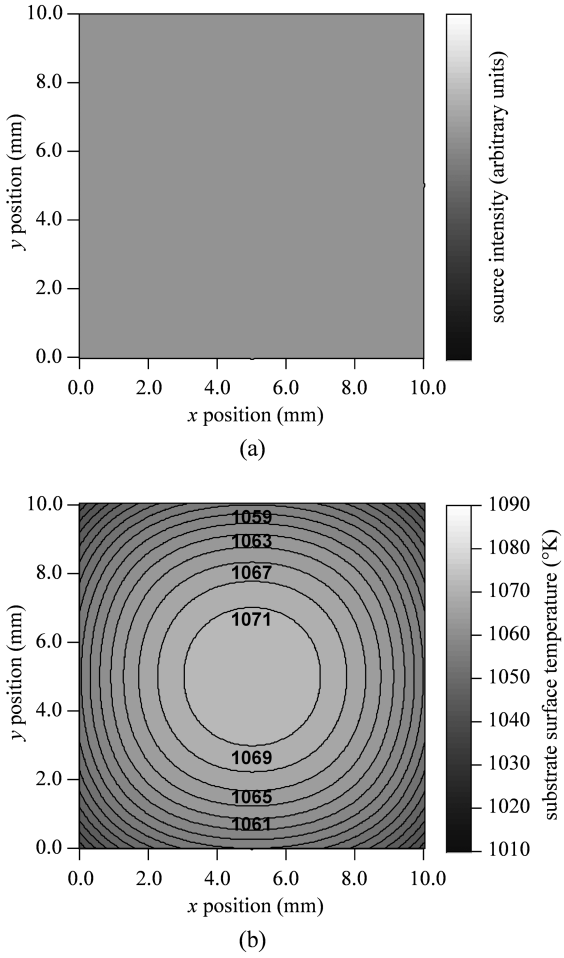

Fig. 11. (a) Flat intensity heat source function with $P = 7.2\,\text{W}$. (b) Resultant modeled temperature distribution of the substrate deposition face, standard deviation = 7.1 °K, mean = 1063 °K, and range = 34 °K.

where d is the separation between neighboring scanning points along the x and y axes and i and j are indices to be summed over.

The range of beam waists used for this analysis was $1.0\,\text{mm} < w < 3.5\,\text{mm}$ and the scanning point separation was varied from $1.0\,\text{mm} < d < d_{\max}$, where $d_{\max}$ was chosen such that the outermost scanning point was a distance w from the substrate edge to minimize wastage of radiation outside of the central heated square. The minimum standard deviation of 14 °K was found for $d = 1.6\,\text{mm}$ and $w = 1.0\,\text{mm}$ with a power of 6.9 W. The mean temperature for these parameters was 1052 °K and the range was 63 °K. The heat source profile used is shown in Fig. 12(a) and the resultant substrate deposition face temperature distribution is shown in Fig. 12(b). The raster scanner has not performed as well as the beam-pipe in our modeling. This is attributed to the reduced heat intensity at and near the substrate edges due to the constraints we placed on the modeling to minimize heat wastage. For the raster scanner to compare to the beam-pipe, the scanning points at the edges would have to be set closer to and perhaps even overlap the edges to enable the intensity there to be increased. Another method of tuning the temperature distribution with the raster scanner, and one that has been successfully employed previously, would be to increase the dwell time for scanning points around the outside of the heated square. This would allow the average intensity at the edges to be increased without leading to a decrease in power efficiency.

E. Recombined Incoherent Gaussian

The heat source function obtained from the addition of four incoherent beam quadrants is now considered as an initial assessment of the heating profile produced by the tetra-prism. The incoherent operation of the tetra-prism has been simulated directly

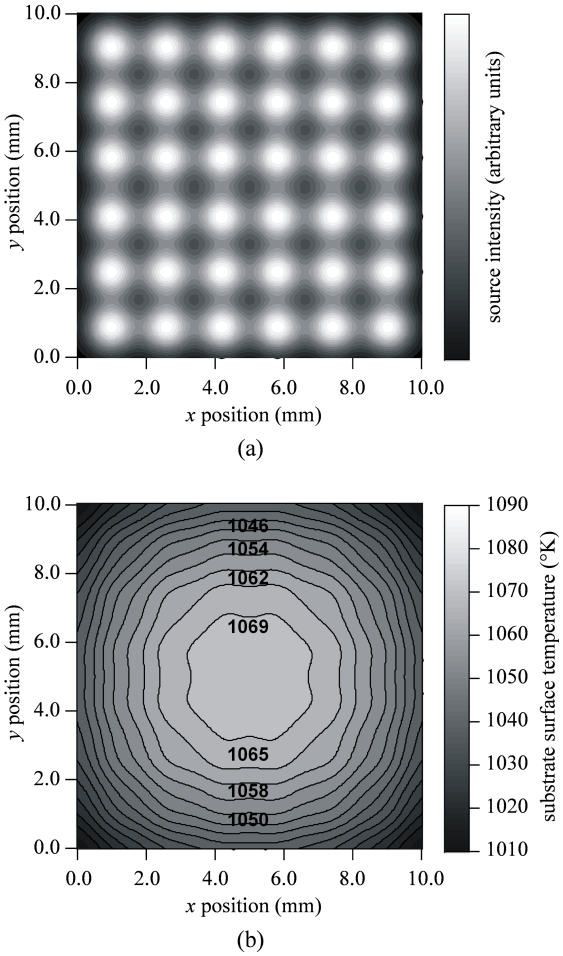

Fig. 12. (a) Raster-scanned beam source function with $w = 1.0\,\text{mm}$, $d = 1.6\,\text{mm}$, and $P = 6.9\,\text{W}$. (b) Resultant modeled temperature distribution of the substrate deposition face; standard deviation = 14 °K, mean = 1052 °K, and range = 63 °K.

in Section 2 using ray-tracing methods, but for the purposes of the temperature modeling it is simpler to generate the heat source function from the superposition of four appropriately truncated Gaussians. To investigate the effect of changing working distance D for a fixed tetra-prism angle ($\theta = 1.0°$), a quadrant separation parameter a is introduced. The source function is then given by

$$Q = \frac{2P}{\pi w^2}\begin{pmatrix} \exp\left\{-\frac{2}{w^2}[(x+a)^2+(y+a)^2]\right\} & (x > -a, y > -a) \\ +\exp\left\{-\frac{2}{w^2}[(x+a)^2+(y-a)^2]\right\} & (x > -a, y < a) \\ +\exp\left\{-\frac{2}{w^2}[(x-a)^2+(y+a)^2]\right\} & (x < a, y > -a) \\ +\exp\left\{-\frac{2}{w^2}[(x-a)^2+(y-a)^2]\right\} & (x < a, y < a) \end{pmatrix}. \quad (6)$$

The parameter range $3.0\,\text{mm} < a < 5.0\,\text{mm}$ and $1.0\,\text{mm} < w < 10.0\,\text{mm}$ was modeled over to achieve a combination that results in the most homogeneous temperature distribution. A minimum standard deviation of 2.7 °K was found to occur for $a = 5.0\,\text{mm}$ and $w = 7.7\,\text{mm}$ using a power of 7.7 W. The mean temperature obtained with these parameters was 1076 °K and the temperature range was 16 °K. A profile of the source function generated by the above parameters is shown in Fig. 13(a) and the deposition face temperature distribution is shown in Fig. 13(b). It is interesting to note from Fig. 13(a) that in contrast to the source functions produced by the previous homogenizer devices, the parameters above do not produce the flattest average intensity source function possible, which would occur for slightly different parameters ($a = 5.0\,\text{mm}$ and $w = 9.6\,\text{mm}$). However, this slightly inhomogeneous heating profile does result in the most homogeneous temperature distribution. This is because above average heat supplied at and near the substrate edges compensates for the higher rate of radiative emission from these areas because of the larger surface area to volume ratio. This highlights the fact that the goal of a square heating beam homogenizer is not actually to produce a perfectly flat intensity square beam, but rather an overall flat intensity beam with an increased level of heat at the corners and around the edges. This is key to the success of the tetra-prism design, which enables the level of increased intensity at the substrate edges to be controlled without the consequence of reduced efficiency. The temperature distribution shown in Fig. 13(b) clearly illustrates the improvement in homogeneity over the untransformed Gaussian case and the two alternative homogenizer device benchmarks. Such a homogeneous temperature distribution is ideal for PLD experiments and the remaining challenge is for the tetra-prism to reproduce a similar degree of homogeneity despite the diffraction and interference effects that apply in the real-world case.

F. Recombined Gaussian with Fresnel Diffraction

Fresnel diffraction will produce a larger periodic modulation of intensity than interference for the tetra-prism setup under consideration and will therefore be the dominant factor in determining the substrate temperature inhomogeneity, allowing the

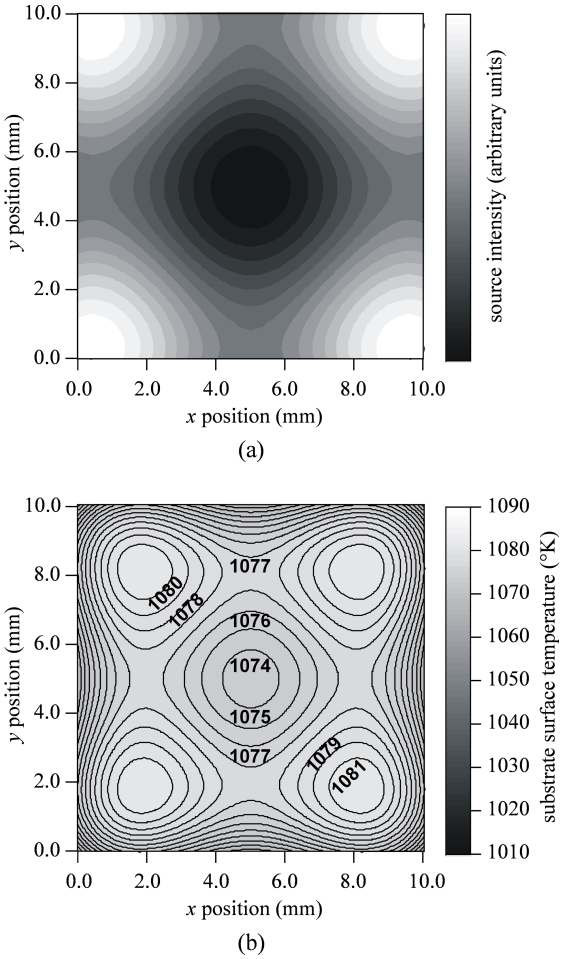

Fig. 13. (a) Recombined incoherent Gaussian beam source function with $w = 7.7$ mm, $d = 5.0$ mm, and $P = 11.0$ W. (b) Resultant modeled temperature distribution of the substrate deposition face, standard deviation = 2.7 °K, mean = 1076 °K, and range = 16 °K.

source intensity modulation due to interference to be neglected here for simplicity.

Since the diffraction by a straight edge cannot be solved analytically, numerical Fourier transform methods were employed using the numerical computing software package MATLAB. The resulting source matrix was then imported into COMSOL MULTIPHYSICS for subsequent heat diffusion modeling. To calculate the source function, a single quadrant of a Gaussian E-field was considered and then propagated in free space using Fourier optics methods. The independence of the diffraction of each quadrant from the others then allowed the result for the initial single quadrant to be rotated to give the pattern produced by the other three quadrants. The four resultant E-field distributions could then be summed to build the complete source function.

The Fresnel diffraction was seen to have three noticeable effects on the heat source compared to the incoherent function analyzed in the previous section. An intensity modulation in both the x and y directions was introduced with a period variable at the millimeter scale length and the effective edge of the source was softened and moved toward the center of the substrate.

The recombined beam quadrant parameters were varied as in Subsection 3.E to find the parameters that produce the most homogeneous substrate temperature distribution. The minimum standard deviation of 2.2 °K in this case was found to occur with $a = 5.6$ mm and $w = 9.5$ mm with a power of 9.5 W. The mean temperature was found to be 1076 °K and the temperature range was 14 °K. Figure 14(a) shows the source function for these parameters. The diffraction has produced an intensity modulation of varying period between about 0.5 mm and 1.5 mm along the x and y axes. Figure 14(b) shows the resultant substrate deposition face temperature distribution. Compared to the incoherent

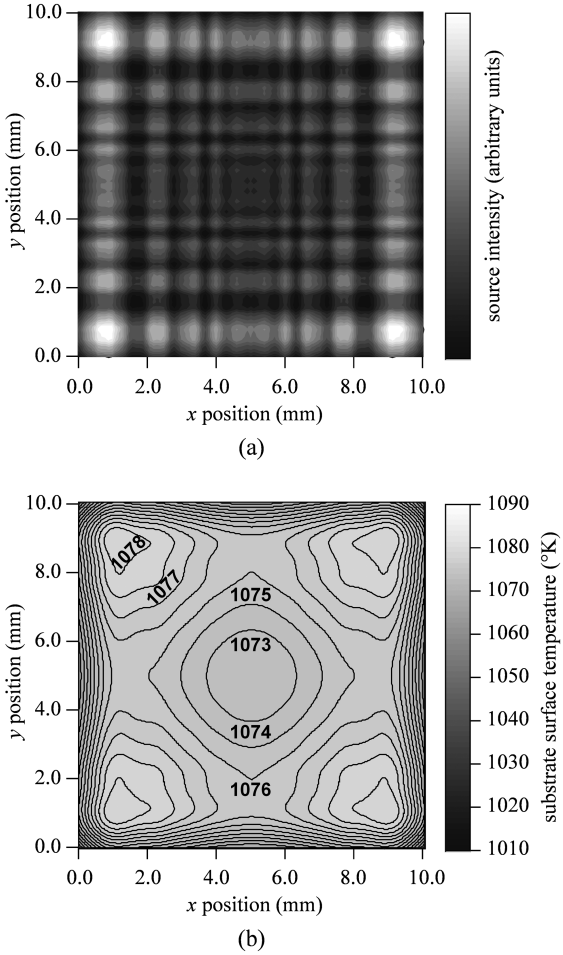

Fig. 14. (a) Recombined Gaussian with Fresnel diffraction with $w = 9.5$ mm, $d = 5.6$ mm, and $P = 9.5$ W. (b) Resultant modeled temperature distribution of the substrate deposition face, standard deviation = 2.2 °K, mean = 1076 °K, and range = 14 °K.

Table 1. Summary of Modeling Results for the Different Homogenization Techniques Under Consideration

Beam homogenization technique	Power (W)	Surface temperature properties (°K)		
		Standard deviation	Mean	Range
Untransformed Gaussian	5.6	43	978	173
Square-tapered beam-pipe	7.2	7.1	1063	34
Raster-scanned 6 × 6 grid	6.9	14	1052	63
Recombined incoherent Gaussian	7.7	2.7	1076	16
Recombined Gaussian with Fresnel diffraction	9.5	2.2	1076	14

recombined Gaussian case, the beam waist and quadrant separation have increased to compensate for the shift of the effective edge that results because of Fresnel diffraction. Despite the additional modulation, however, a temperature distribution with comparable homogeneity to the incoherent case is still achieved. It is clear therefore that the tetra-prism design and experimental parameters can be optimized simply by using incoherent modeling in the case that has been studied here, but it would be useful to know how much the heating beam intensity can be modulated due to diffraction or interference before the temperature distribution is significantly affected. A simple two-dimensional (2D) model has been used in Section 5 to investigate this and give an indication of the role of substrate thickness as a thermal diffuser in the achievement of homogeneous temperature distributions.

The modeling results from all of the different homogenization techniques are summarized in Table 1.

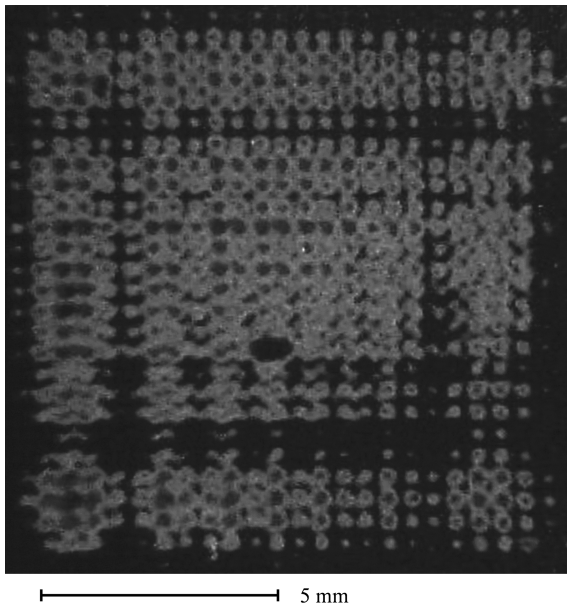

Fig. 15. Picture of the intensity profile generated by a square-pyramidal tetra-prism using temperature sensitive liquid crystal film. Note that some saturation has occurred in the center of the most intense spots shown.

4. Experimental Tests

A. Experimental Observations of Diffraction and Interference Effects

A temperature sensitive liquid crystal film was used as a viewing screen on a large metal heatsink with the CO_2 laser operating at low powers to achieve an experimental indication of the real-world period of intensity modulation. A picture of the film is shown in Fig. 15. Different periods can be clearly seen that can be attributed separately to the effects of diffraction and interference. A constant period of approximately 400 μm can be observed along the x and y axes, which is attributed to interference. A larger period that varies between ~1.0 and 2.0 mm can also be observed, which is attributed to diffraction. This agrees approximately with the source function that included diffraction generated using a square aperture in the previous section. The image also has some distortion that is due to manufacturing imperfections in the device.

B. Thermocouple Measurements of Substrate Surface Temperature

Thermocouple measurements were made of the substrate surface temperature to confirm the validity of the heat diffusion modeling. An accurate measurement is technically difficult to achieve because the thermocouple acts as a heatsink and reduces the substrate temperature where the measurement is made. However, a very thin thermocouple can be used to minimize this problem. A 0.25 mm diameter type-K thermocouple was used with its insulating outer layer stripped off and a very small amount of thermally conductive indium paste was used on the tip to make a good contact with the substrate.

The temperature was measured to be ~1073 °K with an absorbed heating power of about 10 W. The heat diffusion model predicted that the substrate surface temperature would be ~1073 °K for an absorbed power of 9.5 W using the recombined Gaussian source function with diffraction included. The comparison of absorbed power here allows us to use the power value from the modeling produced by a square aperture source function. We can therefore conclude that the model is working with sufficient accuracy to be valid as an indicator of the substrate temperature achievable by using different heat source functions and powers.

5. Substrate Thickness as a Thermal Diffuser

A. Two-Dimensional Substrate Cross Section Heat Diffusion Model

In order to generate simple rules for describing the influence of source intensity modulation on the homogeneity of substrate temperature, we can simplify by using a 2D thermal model. A cosine-squared modulation can serve as an approximation of the actual source intensity modulation for this simple modeling. Eqs. (2) and (3) still describe the heat flow within the 2D domain and the heat source is given by

$$Q = \frac{Ak_f}{k_f h + \cos(k_f h)\sin(k_f h)} \cos^2(k_f y)\delta(z), \quad (7)$$

where A is a parameter similar to the beam power and can be varied to adjust the temperature, y is the direction parallel to the heating face, z is the direction perpendicular to the heating face, and $k_f = \pi/\Lambda$, where Λ is the heat intensity modulation periodicity that results from using the cosine-squared function. The nonlinear heat equations were solved using COMSOL MULTIPHYSICS.

B. Modeling Results

Simulations were carried out over a range of substrate thicknesses and heat intensity modulation periodicities. For simplicity, the heat intensity periodicities were chosen such that the modulation was symmetric about the substrate center. The parameter A was varied to give a temperature of 1073 ± 0.5 °K at the center of the substrate deposition face. To isolate the effect of changing the heat intensity modulation from temperature inhomogeneity that results from the substrate edges, the parameter Δ shown as Eq. (8) has been used, where T_{mod} is the temperature for the modulated heat intensity case and T_{flat} is the temperature for the unmodulated heat intensity case.

$$\Delta = [T_{\text{mod}}(y) - T_{\text{flat}}(y)]_{\text{max values}} - [T_{\text{mod}}(y) - T_{\text{flat}}(y)]_{\text{min values}} \quad (8)$$

Figure 16 shows Δ plotted for a range of heat intensity modulation periodicities from 0.2 mm up to 5.0 mm and for substrate thicknesses of 0.1, 0.25, 0.5, and 1.0 mm. The temperature inhomogeneity due to source modulation increases rapidly with increasing heat intensity modulation periodicity and decreasing substrate thicknesses. This highlights the role of substrate thickness as a thermal diffuser for the heat source function. Thicker substrates allow more homogeneous temperature distributions to be produced because more thermal diffusion can take place between the heated face and the opposite deposition face. Figure 16 can be used as a guideline for how inhomogeneous a heat source can be before it has a significant impact on the temperature homogeneity of substrates with different thicknesses.

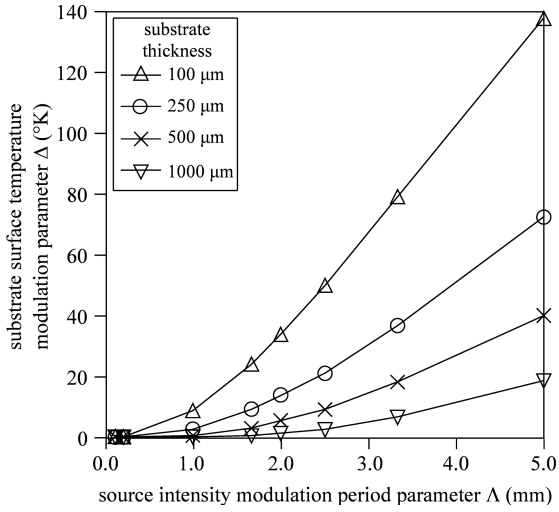

Fig. 16. Variation of the temperature inhomogeneity due to source modulation for substrate thicknesses of 0.1, 0.25, 0.5, and 1.0 mm.

6. Conclusions

A new remote substrate heating setup utilizing a ZnSe tetra-prism in combination with a CO_2 laser has been described for pulsed laser deposition (PLD) experiments. Three initial prism designs and their operation were considered and compared to a more conventional square-tapered beam-pipe and the best design was chosen for further discussion and subsequent experimental testing. Three-dimensional heat modeling was performed using various source functions representing a simple Gaussian beam, a square-tapered beam-pipe, a raster-scanning mirror setup, and the most favorable prism design, the tetra-prism, with and without diffraction. Experimental tests were performed on a 1.0° tetra-prism made out of ZnSe to indicate the actual intensity pattern that results from combined diffraction and interference effects. Finally, the role of substrate thickness as a thermal diffuser was highlighted by modeling the temperature inhomogeneity that results from source functions with different intensity modulation periods using substrates with a range of different thicknesses.

The modeled substrate temperature distributions that result from different source functions in turn indicated the necessity for such a beam homogenization device and then the limited impact of coherence effects for the tetra-prism setup dimensions under consideration. It was shown that out of the possible beam homogenization techniques available (beam-pipe, prisms, and raster scanning) the tetra-prism was not only the simplest and most convenient method but also the most effective since the beam shape was easily tailored to compensate for increased heat loss via radiative emission at the substrate edges and corners. When taking diffraction

into account, the modeling predicted an ideal homogeneous deposition face temperature distribution for use in PLD experiments, with a standard deviation of just 2.2 °K and a mean temperature of 1076 °K.

Experimental testing verified the accuracy of the modeling work and showed that it may be used in the future to predict substrate temperature that results from a certain heat intensity source profile and absorbed power. The influence of source modulation on temperature homogeneity was found to be negligible for substrates greater than a few hundred micrometers thick at modulation periods less than a few millimeters. In conclusion, a ZnSe tetra-prism has been presented as a highly effective low-cost beam shaping tool for substrate heating in PLD experiments.

5 The authors acknowledge the support of the Engineering and Physical Sciences Research Council (EPSRC) for funding under grant EP/C515668. A. C. Muir and M. S. B. Darby also acknowledge the receipt of EPSRC studentships, and M. S. B. Darby acknowledges the receipt of an industrial CASE award from QinetiQ.

References

6
1. K. H. Wu, C. L. Lee, J. Y. Juang, T. M. Uen, and Y. S. Gou, "In situ growth of $Y_1Ba_2Cu_3O_{7-x}$ superconducting thin films using a pulsed neodymium:yttrium aluminium garnet laser with CO_2 laser heated substrates," Appl. Phys. Lett. **58**, 1089–1091 (1991).
2. P. E. Dyer, A. Issa, P. H. Key, and P. Monk, "A cw CO_2 laser substrate heater for superconducting thin-film deposition," Supercond. Sci. Technol. **3**, 472–475 (1990).
3. T. Hirai, K. Fuse, M. Shiozaki, T. Okada, K. Ebata, and H. Nanba, "Characteristics of ZnSe aspheric beam homogenizer for CO2 laser," SEI Tech. Rev. **55**, 71–77 (2003).
4. J. A. Hopkins, F. A. Schwartz, M. H. McCay, T. D. McCay, N. B. Dahotre, and J. B. Bible, "Apparatus and method for producing an improved laser beam," U.S. patent 6,016,227 (18 January 2000).
5. A. A. Anderson, R. W. Eason, M. Jelinek, C. Grivas, D. Lane, K. Rogers, L. M. B. Hickey, and C. Fotakis, "Growth of Ti:sapphire single crystal thin films by pulsed laser deposition," Thin Solid Films **300**, 68–71 (1997)
6. A. Delmas and J. C. Li, "Study of an optical device used to homogenize a laser beam. Application to emissivity measurements on semitransparent materials at high temperature," Int. J. Thermophys. **24**, 1427–1439 (2003).
7. S. J. Barrington and R. W. Eason, "Homogeneous substrate heating using a CO_2 laser with feedback, rastering, and temperature monitoring," Rev. Sci. Instrum. **71**, 4223–4225 (2000).
8. D. K. Fork, "Single binary optical element beam homogenizer," U.S. patent 5,986,807 (16 November 1999).
9. M. A. Dakhil, Y. M. Hassan, and A. M. Samour, "Folding of Gaussian beam and a proposal for an optical device," Opt. Commun. **238**, 163–168 (2004).
10. J. P. Sercel and M. von Dadelszen, "Practical UV excimer laser image system illuminators," in *Laser Beam Shaping Applications*, F. M. Dickey, S. C. Holswade, and D. L. Shealy, eds. (CRC Press, 2006), pp. 113–156.
11. Y. Kawamura, Y. Itagaki, K. Toyoda, and S. Namba, "A simple optical device for generating square flat-top intensity irradiation from a Gaussian laser beam," Opt. Commun. **48**, 44–46 (1983).
12. N. P. Padture and P. G. Klemens, "Low thermal conductivity in garnets," J. Am. Cerm. Soc **80**, 1018–1020 (1997).
13. G. A. Slack, D. W. Oliver, R. M. Chrenko, and S. Roberts, "Optical absorption of $Y_3Al_5O_{12}$ from 10 to 55 000 cm^{-1} wave numbers," Phys. Rev. **177**, 1308–1314 (1969).

F.2 Conference Papers

F.2.1 Modelling of UV Direct-Write Waveguides in Single Crystal Lithium Niobate

A. C. Muir, I. T. Wellington, G. J. Daniell, R. W. Eason, S. Mailis, and C. P. Please. Modelling of UV direct-write waveguides in single crystal lithium niobate. *CLEO/Europe 2005* Munich 12-17 June 2005

Modelling of UV Direct-Write Waveguides In Single Crystal Lithium Niobate

A. C. Muir, I. T. Wellington, G. J. Daniell, R. W. Eason, S. Mailis
Optoelectronics Research Center and School of Physics & Astronomy, University of Southampton, SO17 1BJ, United Kingdom.
C. P. Please
School of Mathematics, University of Southampton, SO17 1BJ, United Kingdom.

It has been shown that waveguide structures can be directly written into single crystal $LiNbO_3$ through the influence of a focussed c.w. laser source at a wavelength of 244nm scanned across the surface [1]. A possible cause for this effect is the thermally induced diffusion of Li ions away from the regions heated by the laser beam leading to a local decrease in the refractive index which is dependant upon the Li concentration [2]. Figure 1 shows a schematic of this process.

The diffusion of heat within the crystal has been modelled initially by analytical methods which include a Kirchhoff integral transform to include the effect of a temperature dependant thermal diffusivity. Using this analytical model we have investigated the characteristics of the temperature distribution in the vicinity of the scanning beam with variation of exposure parameters such as beam spot size, incident optical power and scanning speed. It has been found that the temperature distribution in the reference frame of the moving beam is independent of the scan speed for all practical speeds.

A finite difference model has also been constructed for a static beam and the results compare very closely with the analytical model. The finite difference model has allowed the inclusion of a temperature-dependant heat capacity as well as a temperature-dependant thermal diffusivity. It has been found however, that the temperature-dependant heat capacity has only a small additional effect and so this justifies the use of the analytical model where only the thermal diffusivity is temperature-dependant.

The equations describing diffusion of Li ions in a dynamic, spatially non-uniform, temperature distribution have been derived and used to extend the finite difference temperature model into a model of Li diffusion induced by the scanning beam. For an incident power of 80mW, scan speed of $8 \times 10^{-4} ms^{-1}$ and spot size of 3.25μm a peak Li concentration change was calculated to be about 1% in the preliminary results. Calculations of the refractive index changes based on these predicted Li concentration changes will be presented and compared with measured values achieved via direct waveguide writing.

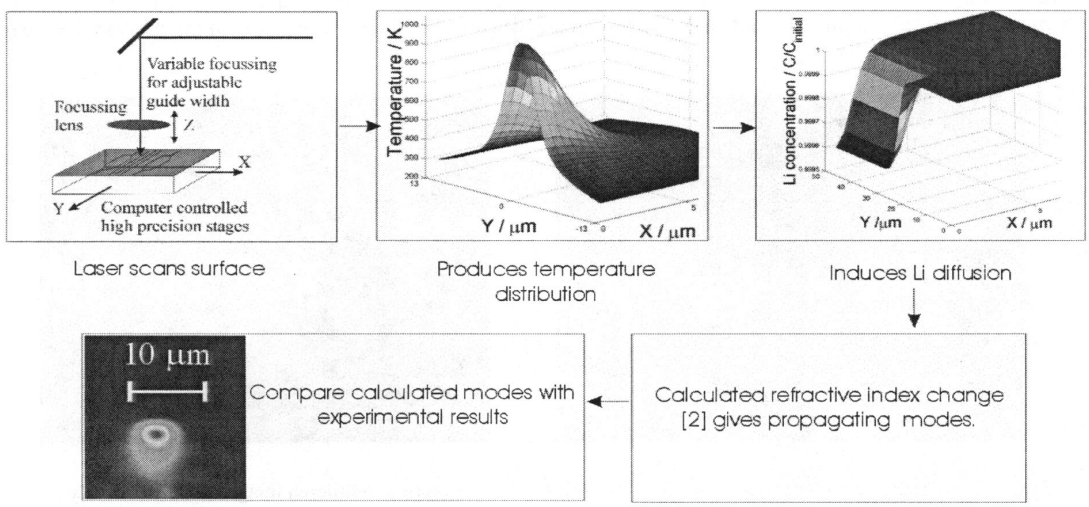

Figure 1: Schematic of guide writing and modelling process.

[1] S. Mailis, C. Riziotis, I. T. Wellington, P. G. R. Smith, C. B. E. Gawith and R.W. Eason *"Direct ultraviolet writing of channel waveguides in congruent lithium niobate single crystals"* Opt. Lett, **28**, 16, 1433-1435, (2003).

[2] U. Schlarb and K. Betzler, *"Refractive indices of lithium niobate as a function of wavelength and composition."*, J. Appl. Phys. **73**, 7, 3472-3476, (1992).

0-7803-8974-3/05/$20.00 ©2005 IEEE

F.2.2 UV Radiation-Induced Surface Wetting Changes in Lithium Niobate Single Crystals

S.Mailis, C.L.Sones, C.E.Valdivia, I.T.Wellington, A.C.Muir, J.G.Scott, and R.W.Eason. UV radiation-induced surface wetting changes in lithium niobate single crystals. *CLEO-Europe 2005* Munich 12-17 Jun 2005

UV radiation-induced surface wetting changes in lithium niobate single crystals

S. Mailis, C. L. Sones, C. E. Valdivia, I. T. Wellinghton, A. C. Muir, J. G. Scott, R. W. Eason

Optoelectronics Research Centre, University of Southampton,
Highfield, Southampton SO17 1BJ,
UK

The interaction between highly absorbed UV laser radiation and the z-faces of lithium niobate single crystals has been reported to induce modification of the surface reactivity with chemical etching agents such as hydrofluoric acid (HF) [1,2]. This effect has been attributed to the photo-excitation of charges which are subsequently trapped in defect sites producing a spatial charge distribution that corresponds to the illuminating pattern.

In this contribution we show that the UV laser-induced surface charge distributions interact sufficiently with the polar molecules of various solvents to increase their attachment to the surface hence changing the wetting behaviour of the surface without changing the surface topography (surface roughness). The wetting modified area corresponds strictly on the illuminated surface areas. We have observed such wetting modifications even in submicron regions (0.7 μm) after illumination through an appropriate phase mask. Figure 1 shows the spreading of a de-ionized water droplet on a) non-exposed and b) pulsed laser exposed areas. The contact angle of the droplet with respect to the surface before UV illumination was of order 110°. After UV illumination the contact angle became 180° as shown in figure 1b. Finally, the UV laser induced wetting modification of the surface recovers completely after a few days at room temperature or faster by thermal annealing at ~200° C for 2 hrs.

Pulsed and c.w. laser radiation from a KrF excimer laser (248 nm) and frequency-doubled argon-ion laser (244 nm) respectively were used to illuminate the +/- z surfaces of commercially available lithium niobate single crystal wafers. Selective attachment of (various amphiphilic molecules, organic dyes, quantum dots, metallic/polymer nano-paticles) on pre-illuminated surfaces will be presented. Lithium niobate is a nonlinear ferroelectric material possessing very useful physical properties. Additionally it is an excellent host for active and passive optical waveguides. The ability for precise spatial arrangement of organic/inorganic molecules and nano-particles has the potential to offer valuable solutions to device fabrication.

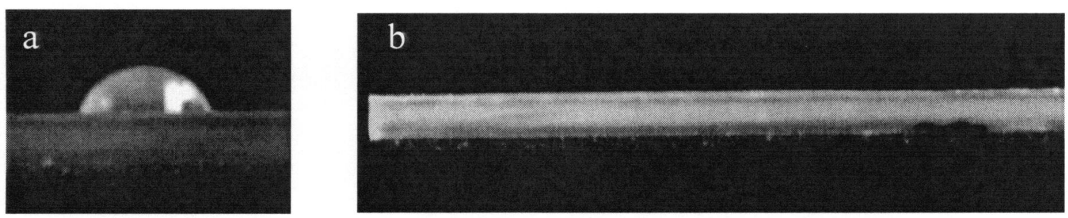

Figure 1 a) de-ionized water droplet on the +z face of a lithium niobate single crystal wafer, the contact angle is ~110° b) after UV exposure the same volume of water spread readily on the illuminated surface

1. S. Mailis, C. Riziotis, P. G. R. Smith, J. G. Scott, and R. W. Eason, "Continuous wave ultraviolet radiation induced frustration of etching in lithium niobate single crystals."Appl. Surf. Sci. **206** (1-4), 46 (2003).
2. S. Mailis, P. T. Brown, C. L. Sones, I. Zergioti, and R. W. Eason, "Etch frustration in congruent lithium niobate single crystals induced by femtosecond ultraviolet laser irradiation." Appl. Phys. A **74** (2), 135 (2002).

0-7803-8974-3/05/$20.00

F.2.3 UV Laser-Induced Ferroelectric Domain Structures Investigated by Piezoresponse Force Microscopy

T.Jungk, A.Hoffmann, E.Soergel, S.Mailis, A.C.Muir, I.T.Wellington, C.E.Valdivia, C.L.Sones, and R.W.Eason. UV laser-induced ferroelectric domain structures investigated by piezoresponse force microscopy *CLEO-Europe/IQEC 2007* Munich 17-22 Jun 2007 CE7-4-THU

UV laser-induced ferroelectric domain structures investigated by piezoresponse force microscopy

T. Jungk, A. Hoffmann, E. Soergel
Institute of Physics, University of Bonn, Wegelerstraße 8, 53115 Bonn, Germany

S. Mailis, A. C. Muir, I. T. Wellington, C. E. Valdivia, C. L. Sones, R. W. Eason
Optoelectronics Research Centre, University of Southampton, Highfield, Southampton SO17 1BJ, UK

Ferroelectric domains have been generated on the +z and the −z faces of congruent undoped lithium niobate ($LiNbO_3$) single crystals by direct UV writing using a continuous wave (c.w.) frequency doubled argon ion laser ($\lambda = 244$ nm). The width of the domains was observed to depend on the intensity of the laser beam. Interestingly, also the contrast of the domains seen by piezoresponse force microscopy (PFM) [1] was observed to increase with higher laser intensity. The contrast difference could be attributed to a difference of the depth of these surface domains as the depth sensitivity of the PFM is ~ 1 µm for $LiNbO_3$.

After the first set of PFM scans the samples underwent thermal annealing at 200 °C for 4 hours, thereby eliminating any residual charge distributions from the writing process. The second set of PFM scans (after thermal annealing) did not show any changes in the images a fact that ensures that the observed contrast is of piezoelectric origin. Surface topography scans obtained simultaneously with the piezoresponce images showed no surface damage for most of the writing conditions. Figure 1 (a,b) shows two piezoresponce images obtained from the –z face of a UV exposed sample. The dark tracks correspond to the illumination tracks while the corrugation of the line is due to mechanical vibrations during the direct writing process. Subsequent etching in hydrofluoric acid showed differential etching following the UV illumination track, as expected from an inverted ferroelectric domain. A scanning electron microscopy imaged of the etched sample is shown in Fig 1(c)

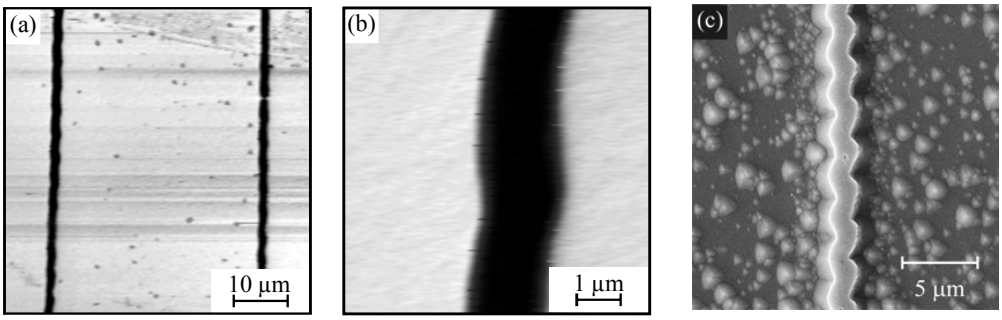

Fig. 1 Piezoresponse force microscopy images (a, b) of a UV laser-induced domain structure in congruently melting $LiNbO_3$. Writing parameters: laser power of 30 mW on a 5 µm spot diameter, scanning velocity 0.2 mm/s. (c) Scanning electron microscopy image of the etched UV illuminated –z face.

The crucial question remains: what is the formation process? UV laser irradiation of $\lambda = 244$ nm in known to strongly heat the crystal locally since the crystal has an extremely small absorption depth of <<1micron at this wavelength [2]. The temperature being above T_c, ferroelectric order is abolished and the crystal becomes electrically conductive in this volume. Thus UV light can travel deeper into the crystal volume. This light is absorbed in crystalline $LiNbO_3$ and generates free electrons. Due to the bulk photovoltaic effect a space charge field arises which has an opposite direction with respect to the polarization field. Now – if after illumination the temperature decreases below T_c the orientation of the polarization axis is defined via this space charge field. This results in the observed surface domains. Note that this process for the domain formation works for both, the +z and the –z face in the same manner.

We will further discuss this phenomenon during the presentation.

References

1. T. Jungk, A. Hoffmann, and E. Soergel „Quantitative analysis of ferroelectric domain imaging with piezoresponse force microscopy," Appl. Phys. Lett. **89**, 163507 (2006)
2. A. C. Muir, G. J. Daniell, C. P. Please, I. T. Wellington, S. Mailis, R. W. Eason „Modelling the formation of optical waveguides produced in $LiNbO_3$ by laser induced thermal diffusion of lithium ions," Appl. Phys. A, **83,** 389-396 (2006)

F.2.4 Surface Domain Inversion in $LiNbO_3$ by Direct UV Writing

T.Jungk, A.Hoffmann, E.Soergel, S.Mailis, A.C.Muir, I.T.Wellington, C.E.Valdivia, C.L.Sones, and R.W.Eason. Surface domain inversion in LiNbO3 by direct UV writing. *EMF 2007* Bled, Slovenia 3-7 Sep 2007

Surface Domain Inversion in $LiNbO_3$ by Direct UV Writing

T. JUNGK[1], Á. HOFFMANN[1], E. SOERGEL[1*], S. MAILIS[2], A. C. MUIR[2], I. T. WELLINGTON[2], C. E. VALDIVIA[2], C. L. SONES[2], AND R. W. EASON[2]

[1]*Institute of Physics, University of Bonn, Wegelerstraße 8, 53115 Bonn, Germany*
[2]*Optoelectronics Research Centre, University of Southampton, Highfield, Southampton SO17 1BJ, UK*
**E-mail address: soergel@uni-bonn.de*

Ferroelectric domain inversion has been achieved on the +z and the −z faces of congruent undoped lithium niobate ($LiNbO_3$) single crystals by direct UV writing using a continuous wave (c.w.) frequency doubled argon ion laser ($\lambda = 244$ nm). The width and the depth of the domains were observed to depend on the intensity and the spot size of the laser beam as well as the writing speed. The inverted domain structures were investigated by scanning electron microscopy (SEM), after HF acid differential etching, and piezoresponse force microscopy (PFM) [1]. UV laser inverted domains directly written on a multi domain crystal (PPLN) show that the PFM contrast of the UV written domains is lower as compared to the bulk domains (Fig. 1b). This indicates that the UV written domains are shallower than 1 µm because any domain depth exceeding ~ 1 µm in $LiNbO_3$ would appear as bulk in PFM imaging. This is consistent with the extremely small absorption depth of << 1 µm at $\lambda = 244$ nm [2].

Although shallow these UV laser written domains can be also remarkably narrow and also they can be fabricated onto any surface independent of the crystal orientation. Driving these surface domains deeper in the crystal by optical or electric field post processing. is currently under investigation.

.

(a) (b)

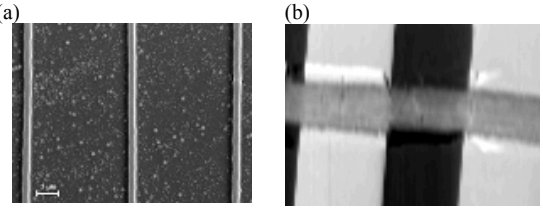

Fig. 1: (a) Scanning electron microscopy image of the HF etched UV laser inverted domain lines. (b) Piezoresponse force microscopy image of UV-induced domain structures written on a previously periodically poled $LiNbO_3$ substrate ($\Lambda = 8$ µm). The relative contrast indicates that the depth of the UV-written domains is << 1 µm..

[1] T. Jungk, Á. Hoffmann, and E. Soergel, Appl. Phys. Lett. 89, 163507 (2006).
[2] A. C. Muir, G. J. Daniell, C. P. Please, I. T. Wellington, S. Mailis, R. W. Eason, Appl. Phys. A, 83, 389 (2006)

F.2.5 Latent Ultrafast Laser-Assisted Domain Inversion in Congruent Lithium Niobate

S. Mailis, C. E. Valdivia, C. L. Sones, A. C. Muir, and R. W. Eason. Latent ultrafast laser-assisted domain inversion in congruent lithum niobate. *CLEO-Europe/IQEC 2007* Munich 17-22 Jun 2007 CE7-2-THU

Latent ultrafast laser-assisted domain inversion in congruent lithium niobate

S. Mailis, C. E. Valdivia, C. L. Sones, A. C. Muir, R. W. Eason

Optoelectronics Research Centre, University of Southampton, Highfield, Southampton, SO17 1BJ, U.K.

The combination of light with external electric fields has been successfully used for the domain engineering of ferroelectric lithium niobate crystals [1,2]. It has been shown that *simultaneous* illumination and application of an external electric field can achieve, e.g. in the case of MgO-doped lithium crystals, coercive field reduction up to 98% using fs-pulsed light [2].

In the case of undoped congruent lithium niobate, however, it has been observed and it is reported here that *photo-induced coercive field reduction also occurs in a latent manner* whereby the application of the electric field is delayed with respect to the illumination of the crystal. Furthermore, the local coercive field reduction becomes fixed after the first poling cycle. Hence, the initially illuminated and domain inverted regions will re-invert at lower voltages for subsequent poling cycles. The most significant implication of the latency is the decoupling of the laser illumination and E-field application steps which significantly simplifies the experimental setup and allows for high resolution light patterning, e.g. using a phase mask.

The second harmonic of the ultra-fast laser system (Coherent: Mira oscillator, RegA amplifier, repetition rate of 250 kHz, pulse duration ~130 fs) at λ = 400 nm was focused onto the –z face of the crystal to a spot size of approximately 45 μm. The average power of the illuminating laser beam was 10 mW, 20 mW and 40 mW which correspond to a peak intensity of 4.5 GW/cm^2, 9 GW/cm^2 and 18 GW/cm^2 respectively. Congruent lithium niobate samples of 500 μm thickness were initially "conditioned" by a sequence of five "dark" poling cycles before illumination to ensure consistency of the forward and reverse values of the intrinsic coercive field. In this investigation a transparent cell was used for the illumination and poling of the crystals which allowed *in situ* observation of the domain formation (via stress-induced birefringence and electro-optic refractive index contrast at the inverted domain boundaries).

The latent laser-assisted inverted ferroelectric domains, shown in Figure 1a, have all been poled at the same voltage. They correspond however to different time delays between the illumination time and the voltage application time, with the far right being the most recent. It is obvious from this figure that the domain spreading is a function of the illumination-voltage time delay. Figure 1b plots the results of a more comprehensive investigation of the resulting domain area (measured after brief etching of the crystal in HF acid) as a function of the time delay before the application of voltage. Each spot was illuminated for 30s, with a 30 s delay between subsequent illuminations. 30 s after the last exposure, the voltage was ramped at a rate of ~130 V/s, maintained at the maximum voltage V = 4 kV for 300 s and finally ramped down to 0 kV at a rate of ~130 V/s.

A full study of the latent coercive field modification and domain expansion dynamics will be presented.

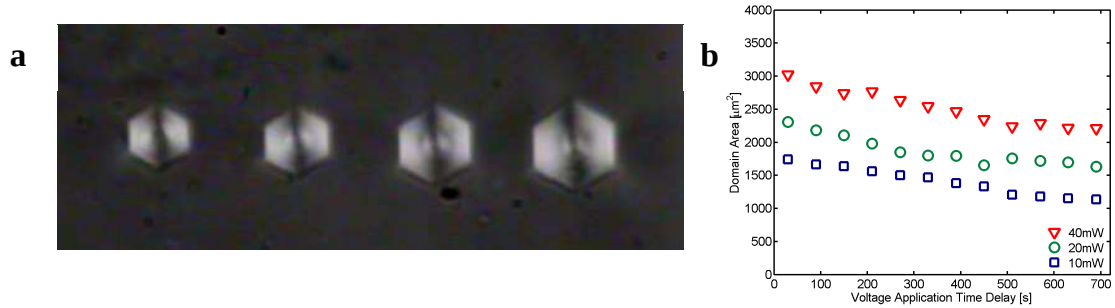

Figure1: (**a**) Ferroelectric domains of different areas corresponding to different time delays between illumination and voltage application, the far right being the most recent. (**b**) Ferroelectric domain area vs. voltage application time delay for three different illuminating powers with an applied voltage of 4 kV.

References.

[1] M. Fujimura, T. Sohmura, and T. Suhara, "Fabrication of domain-inverted gratings in MgO:$LiNbO_3$ by applying voltage under ultraviolet irradiation through photomask at room temperature," Electron. Lett., **39**, 719-21 (2003).

[2] C.E. Valdivia, C.L. Sones, S. Mailis, J.D. Mills, and R.W. Eason, "Ultrashort-pulse optically-assisted domain engineering in lithium niobate," Ferroelectrics, 340, 75-82 (2006).

F.2.6 UV Laser Radiation Inhibits Domain Inversion in Lithium Niobate.

S. Mailis, A. C. Muir, Y. J. Ying, C. L. Sones, R. W. Eason, T. Jungk, A. Hoffmann, E. Soergel. UV Laser Radiation Inhibits Domain Inversion in Lithium Niobate. *CLEO/QELS 2008* San Jose 4 - 9 May 2008 CWG-3-WED

UV laser radiation inhibits domain inversion in lithium niobate

S. Mailis, A. C. Muir, Y. J. Ying, C. L. Sones, R. W. Eason
Optoelectronics Research Centre, University of Southampton
Highfield, Southampton, SO17 1BJ, U.K.
T. Jungk, A. Hoffmann, E. Soergel
Institute of Physics, University of Bonn, Wegelerstrasse 8, 53115 Bonn, Germany

Abtract: Continuous wave UV laser (λ=244 nm) irradiation of the +z face of lithium niobate single crystals inhibits ferroelectric domain inversion in the volume of the crystal which lies immediately below the UV exposed surface.

1. Introduction.

Ferroelectric domain engineering in lithium niobate (LN) is a subject of extensive research mainly for the fabrication of quasi-phase-matched (QPM) nonlinear optical devices, for the performance improvement of linear devices and for microstructuring.

Laser illumination of LN crystals has been observed to assist the electric field ferroelectric domain inversion process by reducing locally the value of the coercive field (E_c). Reduction of E_c up to two orders of magnitude has been observed in Light Assisted Poling (LAP) experiments [1,2]. The laser radiation which has been used in LAP is normally not significantly absorbed by the crystal (λ=350 nm - 800 nm) and the inverted ferroelectric domains typically extend throughout the thickness of the crystal.

Here we present UV laser induced *inhibition* of ferroelectric domain inversion where spatially selective pre-exposure of the +z face of LN crystal inhibits domain inversion in the UV exposed area during electric field poling at a later stage. In these experiments the two steps of i) UV illumination and ii) E-field application are separated; the application of the external electric field can take place long (days) after the UV illumination.

2. Experimental procedure

The experimental arrangement for the UV exposure consisted of a set of computer controlled x-y-z translation stages on which 500 μm thick crystal samples (source; crystal technology Inc USA) are mounted and scanned in front of the focussed UV laser beam. The laser source was a frequency doubled Ar: ion laser at λ=244 nm which was focussed down to a spot size of ~2.5 μm. A computer controlled mechanical shutter was also used to control the exposure time. In the experiments presented here two types of exposures were performed always on the +z face of the samples: i) arrays of linear tracks where the crystal is translated linearly at a constant speed and the length of these tracks varied between 0.5mm to 5mm and ii) arrays of exposures where the crystal was static during the exposure, the duration of which was controlled by the mechanical shutter.

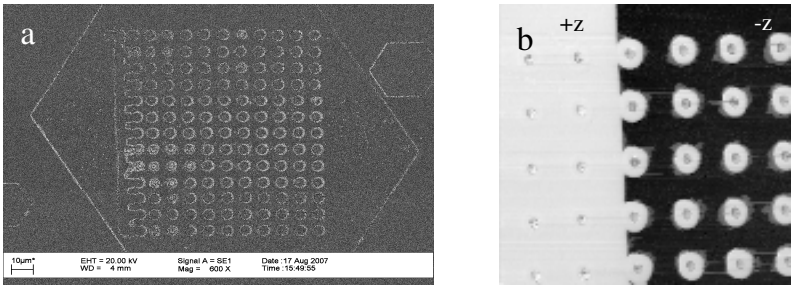

Figure1. a) SEM image of the HF-etched +z face of a UV exposed and poled congruent LN sample. The array of dots correspond to the UV exposed areas. b) Piezoresponse map of the +z face of a UV dot-exposed and partially poled LN sample. The black and white areas correspond to –z and +z faces respectively. The PFM scan size is 58μm x 58μm

After UV illumination the crystal sample was domain inverted by applying a uniform external electric field exceeding the E_c which for congruent LN crystals is $E_c \approx 22$ kV/mm. The inverted domain topography of the UV exposed face was investigated by scanning electro microscopy (SEM) after brief etching (~15 minutes) in pure HF acid. Figure 1a shows an array of upstanding dots which corresponds to static exposures and seems to have maintained their original domain orientation. The area surrounding these features is domain inverted and now corresponds to a –z face. This is shown clearly in figure 1a where the dot array appears to be surrounded by the newly poled hexagonally shaped domain.

Piezoresponse force microscopy (PFM) was used to verify the ferroelectric domain polarity of the features which were observed in the SEM images. The PFM scan which is presented in figure 1b shows the domain mapping of a spot illuminated surface that has been partially domain inverted. In the PFM image the white area corresponds to a +z face and the black area corresponds to a –z face as indicated in the figure. The right part of the image has been domain inverted and appears black. The white dots observed within the black background corresponds to UV illuminated spots which have resisted poling and show the same contrast as the left part of the image which has also not been domain inverted. The vertical contrast divide corresponds to the domain wall between the newly poled domain on the right hand side and the original domain on the left. The dot-exposed array extends on both sides of the domain wall. Interestingly the area in the centre of the exposed dots appears grey indicating the presence of an amorphous layer as a result of surface melting in the more intense central area of the Gaussian intensity profile of the laser spot.

3. Discussion

The results presented here show that the effective coercive field increases in the UV exposed areas which is opposite to what has been observed in all LAP experiments. The difference in this case is that short wavelength UV radiation which is highly absorbed by the crystal is used. UV radiation at λ=244 nm is absorbed in the first few 10s of nanometers [3] in LN and it is capable of producing photo-excited charge and heat. Our hypothesis is that the photo-excited charges diffuse through the affected volume and get trapped in crystal defects thus creating suitable electrostatic termination points for the propagating bulk domain which has nucleated on the original –z face (during the poling process) and propagates towards the original +z face. As a result of this process the surface and the volume of the crystal below the UV exposed areas maintain the original domain polarity.

The depth of this non-inverted part is unknown. However, observation of the PFM scan in figure 2 shows that the non-inverted domains on the right hand side have the same contrast as the bulk non-inverted domain on the left hand side of the image. The depth sensitivity of the PFM is of order ~100 nm which is roughly 3 times the radius of curvature of the AFM tip which is used [4]. Any domain deeper than ~100 nm would appear as bulk hence this corresponds to a minimum depth for the domain inverted features which we observe.

4. Conclusions

The exposure of the +z surface of congruent lithium niobate single crystals to UV laser radiation (λ=244 nm) is shown here to inhibit domain inversion locally during the process of E-field poling. The effect was investigated by SEM of HF etched samples which showed differentially etched features corresponding to the UV irradiated areas. The domain inhibition was further verified by piezoresponse microscopy. PFM also provides a minimum depth of these non-inverted domains of ~100 nm as deduced from the depth sensitivity of the instrument. UV induced poling inhibition is attributed to the redistribution of diffused photo-induced charges and subsequent trapping in crystal defect sites which provide electrostatic termination points for propagating bulk domains during the E-field poling process.

Depending on the depth of these domain structures they can be used in nonlinear waveguide devices (waveguide PPLNs) however, this effect when combined with chemical etching provides a very versatile tool for the fabrication of surface micro/nano-structuring of excellent optical quality in lithium niobate.

5. References

[1] C.L.Sones, M.C.Wengler, C.E.Valdivia, S.Mailis, R.W.Eason, K.Buse, "Light-induced order-of-magnitude decrease in the electric field for domain nucleation in MgO-doped lithium niobate crystals" Appl. Phys. Lett. **86**, pp.212 (2005)

[2] C.E.Valdivia, C.L.Sones, S.Mailis, J.D.Mills, R.W.Eason "Ultrashort-pulse optically-assisted domain engineering in lithium niobate" Ferroelectrics **340**, pp.75-82 2006

[3] A. M. Mamedov, "Optical properties (VUV region) of $LiNbO_3$," Optics and Spectroscopy **56**, pp 645 – 649 (1984)

[4] T. Jungk, A. Hoffmann, and E. Soergel "Impact of the tip radius on the lateral resolution in piezoresponse force microscopy" arXiv:cond-mat/0703793v1

List of Figures

List of Tables